

Lightweight Materials

VEHICLE TECHNOLOGIES OFFICE

2012

annual progress report

Contents

A. Acronyms and Abbreviations

Acronyms and Abbreviations	A-1
----------------------------------	-----

1. Introduction

Introduction.....	1-1
-------------------	-----

2. Automotive Metals

A. Properties and Manufacturability - Oak Ridge National Laboratory	2-1
B. Properties and Manufacturability - Pacific Northwest National Laboratory	2-15
C. Industrial Scale-Up of Low-Cost Zero-Emissions Magnesium by Electrolysis: Metal Oxygen Separation Technologies	2-40
D. Modeling and Computational Materials Science - Oak Ridge National Laboratory	2-46
E. Modeling and Computational Materials Science - Pacific Northwest National Laboratory	2-57
F. Multi-Material Enabling - Oak Ridge National Laboratory	2-63
G. Multi-Material Enabling - Pacific Northwest National Laboratory.....	2-100

3. Carbon Fiber and Polymer Composites

A. Predictive Tools for Carbon Fiber Composites - Pacific Northwest National Laboratory	3-1
B. Low-Cost Carbon Fiber Development - Oak Ridge National Laboratory	3-7
C. Carbon Fiber Technology Facility - Oak Ridge National Laboratory	3-22
D. Development and Commercialization of a Novel Low-Cost Carbon Fiber - Zoltek Companies, Inc.	3-30

4. United States Automotive Materials Partnership LLC Cooperative Research

A. Advanced Metals	4-1
B. Non-Destructive Evaluation	4-23

5. Crosscutting

A. Demonstration Project for a Multi-Material Lightweight Prototype Vehicle - Vehma International of America, Inc.	5-1
B. Safety Data and Analysis - Lawrence Berkeley National Laboratory.....	5-7

Acronyms and Abbreviations

°C	Celsius
µm	micrometer (micron)
2D	two dimensional
3D	three dimensional
2T	two layer
3T	three layer

A

AC	alternating current
AHSS	advanced high-strength steel
Al	aluminum
AM	aluminum-manganese
AMO	Advanced Manufacturing Office
AMSA	Autodesk Moldflow Structural Alliance
AMTEC	Advanced Materials Training and Education Center
APS	Advanced Photon Source
AR	as received
ASMI	Autodesk Simulation Moldflow Insight
ASPPRC	Advanced Steel Processing and Products Research Center
ASTM	American Society for Testing and Materials
AWS	American Welding Society

B

BIW	body-in-white
B-M	Boltzmann-Matano

C

C	carbon
CAD	computer aided design
CAE	computer aided engineering
CAFE	Corporate Average Fuel Economy
CALPHAD	CALculated PHAse Diagrams
CF	carbon fiber

CFTF	Carbon Fiber Technology Facility
CMS	computational materials science
CP	crystal plasticity
CPIE	close proximity indirect exposure
CRADA	Cooperative Research and Development Agreement
CTF	constrained thermal fatigue
Cu	copper
CUV	crossover utility vehicle
CZM	cohesive zone model

D

D	deuterium
DC	direct current
DIC	digital image correlation
DOE	U.S. Department of Energy
DP	dual phase (steel)
DSC	differential scanning calorimetry

E

EBSD	electron backscattered diffraction
EERE	Office of Energy Efficiency and Renewable Energy
EMF	electromagnetic forming
EMTA	Eshelby-Mori-Tanka Approach
EMTA-NLA	Eshelby-Mori-Tanka Approach to Non-linear analysis
EPMA	electron microprobe analysis
ESC	electronic stability control
ESPEI	extensible self-optimizing phase equilibrium infrastructure

F

FARS	Fatality Analysis Reporting System
Fe	iron
FE	finite element
FEA	finite element analysis
FEM	finite element modeling, finite element method

FiB	focused ion beam
FSSW	friction stir spot weld/welding
FSW	friction stir welding
FTIR	Fourier transform infrared
FY	fiscal year

G

GB	grain boundary
GCIP	generic closure inner panel
Gen I	first generation
Gen II	second generation
Gen III	third generation
GHG	greenhouse gas
GM	General Motors
GMAW	gas metal arc welding

H

H	hydrogen
HAZ	heat-affected zone
HSBS	hot stamped boron steel
HVAC	heating, ventilating, and air conditioning

I

ICME	Integrated Computational Materials Engineering (USAMP) program
ICWE	integrated computational weld engineering
IPS	initial plastic strain
IR	infrared

L

L-direction	longitudinal direction
LBNL	Lawrence Berkeley National Laboratory
LFT	long fiber thermoplastic
LM	Lightweight Materials
LTT	low transformation temperature

M

MAP	microwave-assisted plasma
MC	Monte Carlo
MD	molecular dynamics
MENA	Magnesium Elektron North America
MFERD	Magnesium Front End Research and Development
Mg	magnesium
MgO	magnesium oxide
MIE	Major Item of Equipment
MMLV	multi material lightweight vehicle
Mo	molybdenum
MTR	Multiple Tow Reactor
MY	model year

N

Nd	neodymium
NDE	nondestructive evaluation
NHTSA	National Highway Traffic Safety Administration
NPRM	Notice of Proposed Rulemaking
NVH	noise, vibration, and harshness

O

O	oxygen
OD	outside diameter
OEM	original equipment manufacturer
OPF	oxidized polyacrylonitrile (PAN) fibers
ORNL	Oak Ridge National Laboratory

P

PA	polyamide
PAN	polyacrylonitrile
PCBN	polycrystalline cubic boron nitride
PES	precursor evaluation system
PNNL	Pacific Northwest National Laboratory

PP	polypropylene
PPF	pulse pressure forming
PSI	pounds per square inch

Q

Q&P	quenching and partitioning
-----	----------------------------

R

R&D	research and development
RD	rolling direction
RE	rare earth
RSCC	Roane State Community College

S

SEM	scanning electron microscope
Si	silicon
SIMS	secondary ion mass spectrometry
SNS	Spallation Neutron Source
SPR	self-pierce riveting, self-piercing rivet
SUV	sports utility vehicle
SVDC	super vacuum die cast
SWE	spot weld element

T

T-direction	transverse direction
TEM	transmission electron microscopy
TGA	thermal gravimetric analysis
TRIP	transformation-induced plasticity
TWB	tailor-welded blanks

U

UHSS	ultra-high strength steels
U.S.	United States of America
USAMP	U.S. Automotive Materials Partnership
UTS	ultimate tensile strength

V

VMT	vehicle mile traveled
VTO	Vehicle Technologies Office

X

XPS	x-ray photoelectron spectroscopy
-----	----------------------------------

Z

Zn	zinc
Zr	zirconium

1. Introduction

As part of the U.S. Department of Energy's (DOE's) Vehicle Technologies Office (VTO), the Lightweight Materials activity (LM) focuses on the development and validation of advanced materials and manufacturing technologies to significantly reduce light and heavy duty vehicle weight without compromising other attributes such as safety, performance, recyclability, and cost. Because it takes less energy to accelerate a lighter object, replacing cast iron and traditional steel components with lightweight materials such as high-strength steel, magnesium, aluminum, and polymer composites can directly reduce a vehicle's fuel consumption. For example, a 10% reduction in vehicle weight can result in a 6%–8% fuel economy improvement. Reducing vehicle weight has other benefits such as allowing cars to carry advanced emissions control equipment, safety devices, and integrated electronic systems without becoming heavier. Lightweight materials are especially important for improving the efficiency and range of hybrid electric, plug-in hybrid electric, and electric vehicles because they offset the weight of power systems such as batteries and electric motors.

In the short term, vehicle weight reduction can be achieved by replacing heavy steel components with materials such as high-strength steel, aluminum, or glass fiber-reinforced polymer composites. The properties and manufacturing of these materials are well established, but better, more cost effective technologies and processes are needed for joining, modeling, and recycling them. In the longer term, even greater weight savings are possible (50%–75% weight reduction for some components) through use of advanced materials such as magnesium and carbon fiber reinforced composites. However, more extensive research and development (R&D) is needed to better understand the properties of these materials and reduce their costs.

Research and development work conducted within the LM activity is broken down into three categories: Properties and Manufacturing, Modeling and Computational Materials Science (CMS), and Multi-material Enabling. Work within Properties and Manufacturing aims to improve properties (such as strength, stiffness, or ductility) and manufacturability (such as material cost, production rate, or yield) of a variety of metal and polymer composite materials. The focus of the Modeling and CMS and Multi-material Enabling work is to provide supporting technologies necessary for full system implementation such as joining methods, corrosion prevention techniques, predictive models, and other computational tools. This introduction summarizes the highlights of the program in all of these areas during the 2012 fiscal year.

Carbon Fiber and Polymer Composites

Carbon fiber reinforced polymer composites have the potential to reduce component weight by more than 60%, however, there are significant technical and cost barriers to their widespread introduction onto vehicles. The cost of input material (precursor) and the carbonization process contribute significantly to the total cost of carbon fiber; hence, significant focus has been provided to these areas. Oak Ridge National Laboratory (ORNL) has been seeking to reduce the cost of carbon fiber through different low cost starting materials including textile grade polyacrylonitrile (PAN), lignin, and polyolefins, and through advanced processing techniques for stabilization and oxidation as well as carbonization/graphitization that promise to improve the rate and cost of conversion to carbon fiber. The process improvements are enabling validation of successfully converting larger volumes (tows) of precursor to carbon. As reported here, Zoltek Companies, Inc. is developing processes and materials to produce a blended lignin/PAN precursor to produce carbon fiber suitable for lightweight automotive structures. ORNL is working on a project to scale and transition low cost carbon fiber (CF) technology through the ORNL Carbon Fiber Technology Facility (CFTF). This project, reported here, is cofunded by the DOE VTO and the Advanced Manufacturing Office (AMO). It supports the DOE Office of Energy Efficiency and Renewable Energy's (EERE's) technology deployment agenda, specifically with respect to advanced lightweight materials in high volume energy applications

Magnesium Alloys

Magnesium (Mg) alloys, with the lowest density of all structural metals, have the potential to reduce component weight by greater than 60%. However, significant technical barriers limit the use of Mg to approximately 1% of the average vehicle by weight. These barriers include high raw material cost and price volatility, relatively low specific stiffness, difficulty in forming sheet at low temperatures, low ductility of finished components (such as in [Figure 1](#)), and a limited alloy set, among others. In addition, using Mg in multi-material systems introduces joining, corrosion, repair, and recycling issues that must be addressed.

Ongoing work in the LM activity is supporting the wider application of Mg components by addressing some of these technical gaps. As documented in this report, ORNL is exploring combinations of twin roll casting and asymmetric rolling as a means to produce lower cost, more formable magnesium sheet. An exciting project documented in this report from Pacific Northwest National Laboratory (PNNL) has demonstrated a non-rare earth containing magnesium extrusion with properties that offer a 20% mass savings over conventional 6061 aluminum on an energy-absorbed basis. Work reported here from Metal Oxygen Separation Technologies (MOxST), now INFINUM, offers a potential route towards domestically produced, low-cost primary magnesium. Combined, these examples and the other magnesium projects documented in this report continue to improve the readiness of Mg processing, integration, and modeling towards wider application and significant vehicle weight reduction.



Figure 1. Mg extrusion exhibiting low ductility failure.

Aluminum Alloys

Aluminum (Al) alloys represent a middle-ground in the structural light metals spectrum. Years of development within the aerospace, construction, and automotive industries have led to a well-developed and reasonably well understood alloy and processing set. Applications of Al within automotive design include hoods and panels, power train components, and even entire vehicle body-in-white (BIW) structures. There are several barriers to the increased use of Al in vehicle weight reduction applications such as material cost, room temperature formability, and limitations within the existing manufacturing infrastructure. As with Mg, the addition of significant amounts of Al to the automotive manufacturing stream presents added multi-material challenges in joining, corrosion, paint and coatings, repair, and recycling.

Aluminum research and development supported by the LM activity focuses on addressing the manufacturing and integration technology gaps described above. PNNL reports several accomplishments in Al research this year including demonstration of a sequential hot/room-temperature forming process for heavy-duty truck components that offers superior strength and useful formability, and continued development and understanding of high-rate forming processes for Al sheet. Combined with several other Al-focused projects, activities documented in this report continue to support wider application of Al throughout passenger and commercial vehicles.

Advanced High Strength Steel (AHSS)

Conventional iron and steel alloys are prominent in existing vehicle architectures, making up about 45% of the weight of a vehicle. Despite the relatively high density of iron based materials, the exceptional strength and ductility of advanced steels offers the potential for efficient structural designs and reduced weight. Application of a new generation of AHSSs has the potential to reduce component weight by up to 25%, particularly in strength limited designs. Steel components are also generally compatible with existing manufacturing infrastructure and vehicle materials, making them a likely candidate for near-term weight reduction. Steel development and research in the LM activity is focused on introducing the so-called “3rd generation advanced high strength steels.” As shown in [Figure 2](#), 3rd generation AHSS are targeted to properties in between 1st and 2nd generation AHSS with high strength, improved ductility, and low cost.

The LM activity supports a variety of projects focusing on 3rd Generation AHSS. Examples include in-situ characterization of the austenite-ferrite transition during heating and deformation, and several projects that are addressing joining challenges in AHSS. ORNL reports on a project to improve the weld fatigue strength of arc-welded advanced high strength steels. PNNL reports on a project investigating the chemical and microstructural contributors to improved austenite stability and performance in advanced steels. A combination of process, performance, and joining research in the LM portfolio helps to accelerate development and eventual deployment of 3rd generation advanced high strength steels.

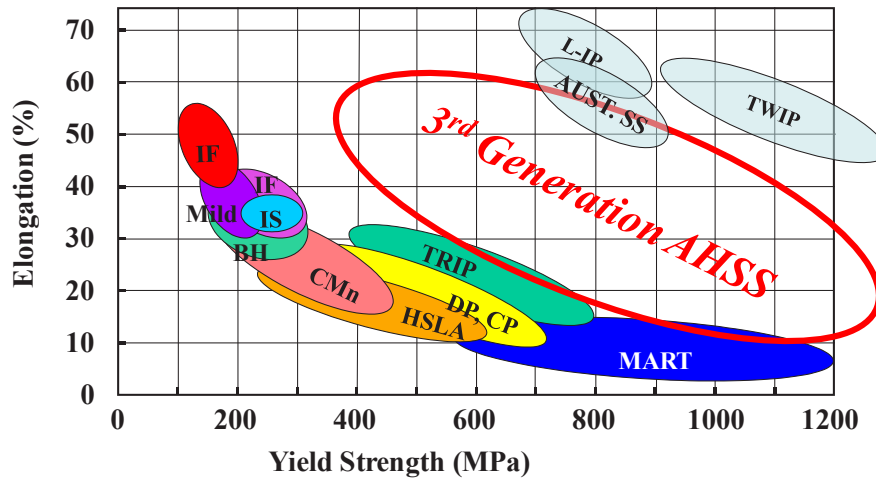


Figure 2. Yield strength versus uniform elongation for a variety of steel types.

Modeling and Computational Materials Science

Developing new, lightweight vehicle structures will require advances in areas such as structural design, processing, and alloy chemistry. Classical approaches to these advancements such as experimental, analytical, or Edisonian techniques can often yield the desired results but with limited efficiency. Computational approaches to materials engineering offer the potential to “short-circuit” the development cycle through predictive engineering and simulated experimentation. Advanced modeling techniques can also be used to optimize designs in well-established materials, further reducing component weight. By reducing the time and resources necessary to advance lightweight materials towards vehicle applications it is possible to introduce relatively immature materials such as magnesium without the decades (or centuries) of development applied towards conventional steel and aluminum. A National Research Council report on integrated computational materials engineering (ICME) identifies vehicle weight reduction as an area likely to benefit from ICME techniques. In addition, The Office of Science and Technology Policy white paper outlining the Materials Genome Initiative, an interagency effort to support the development of ICME and accelerated materials development/deployment, has also identified vehicle weight reduction as a promising area for application of ICME techniques.

Many of the projects supported by the LM activity include an element of computational materials science, while other projects focus almost exclusively on ICME techniques. ORNL combines exceptional experimental work with sound theory to generate diffusion and mobility data for Mg alloy simulations. PNNL reports a project focused on applying computational techniques towards a better understanding of the mechanisms driving low ductility in magnesium die castings. Further computational materials science and ICME work reported in this document provides insight to the potential of these techniques as well as their need for further development.

Looking Forward

The following reports provide a detailed description of the activities and technical accomplishments of the LM activity during the 2012 fiscal year. The work shown here has produced technologies that make today’s vehicles more efficient, safe, and affordable. In collaboration with industry, universities, and national laboratories, VTO continues to develop the next generation of lightweight components. These efforts are building the foundation of technologies—and technology manufacturers—that tomorrow’s vehicles need to achieve ultra-high efficiency and resulting reductions in petroleum use and greenhouse gas emissions.

2. Automotive Metals

A. Properties and Manufacturability - Oak Ridge National Laboratory

Field Technical Monitor: C. David Warren
Oak Ridge National Laboratory
1 Bethel Valley Road; Oak Ridge, TN 37831
(865) 574-9693; fax: (865) 574-6098; e-mail: warrencd@ornl.gov

Technology Area Development Manager: William Joost
U.S. Department of Energy
1000 Independence Ave., S.W.; Washington, DC 20585
(202) 287-6020; fax: (202) 856-2476; e-mail: william.joost@ee.doe.gov

Contractor: Oak Ridge National Laboratory (ORNL)
Contract No.: DE-AC05-00OR22725

Executive Summary

Metals make up about 80% of all the materials used for light vehicle construction, and by a wide margin, the largest fraction of the metals is steels (Schnatterly, 2007; Schultz, 2007). Steels represent about 62% of average vehicle weight. Of the various steel mill products used for auto construction, about 70% of the total, or 839 kg of the average light vehicle weight of 1,970 kg, is supplied as flat-rolled carbon steel for chassis parts and body panels. Magnesium (Mg) alloys and advanced high-strength steels (AHSSs) are two candidate materials for replacing mild steels in future automotive designs to obtain significant mass reduction.

The traditional sheet steels used for chassis and body constructions are the so-called “mild” steels. The combined interests of improving crash worthiness and reducing vehicle weights were at least partially responsible for the development of first generation (Gen I) AHSSs. A second generation (Gen II) of AHSSs was developed, offering much greater strength and ductility but at a premium price which is too high for many automotive applications. The first effort in this report is aimed at developing a fundamental understanding of the microstructural development in AHSSs to facilitate development of a third generation (Gen III) of AHSSs which will preserve many of the performance advantages of Gen II AHSSs but at costs more commensurate with the needs of the domestic automotive industry.

The low density of Mg alloys makes them good candidates for lightweight construction of components in the automotive industry. However, they exhibit much more complex mechanical behavior and significantly less ductility than more commonly used automotive materials. The second task in this report examines one approach to controlling the microstructural texture in magnesium alloys and thus increasing the ductility of those materials.

Activities and Developments

R&D Fundamental Study of the Relationship of Austenite-Ferrite Transformation Details to Austenite Retention in Carbon Steels

Principal Investigator: Zhili Feng, ORNL
(865) 576-3797; fax: (865) 574-4928, e-mail: fengz@ornl.gov

Project Team: Zhenzhen Yu, Rozaliya Barabash, Oleg Barabash, Ke An, Harley Skorpenske, ORNL; Wenjun Liu, Advanced Photon Source, Argonne National Laboratory

Accomplishments

- Successfully applied a novel in situ neutron diffraction technique to quantify the phase transformation kinetics and the role of alloying element partitioning during intercritical temperature annealing of DP980 steel.
- Experimentally determined the two predominant phases responsible for the excellent mechanical properties of DP980, ferrite and martensite, by means of synchrotron microdiffraction. The microscopic strain distribution within individual grains is the root cause of deformation incompatibility phenomena between the ferrite and martensite phases.

Future Directions

- Probe in situ the nonequilibrium allotropic phase transformations in AHSSs including dual-phase (DP) and transformation-induced-plasticity (TRIP) steels during fast transient heating and cooling conditions.
- Resolve the microscopic strain distribution in the fine-grained AHSSs, including DP and TRIP steels, as well as the strain partitioning between ferrite (soft phase) and martensite (hard phase) in AHSSs.
- Develop polycrystalline plasticity deformation and formability model for selected AHSSs.

Technology Assessment

- Target: Develop science-based solutions to overcome the property degradation in the current generation of AHSSs during thermomechanical fabrication and manufacturing processes, and enable the development of more ductile AHSSs (Gen III).
- Gap: Fundamental understandings of the nonequilibrium phase transformation kinetics and the microscopic strain partition mechanisms in AHSSs are quite limited and offer an obstacle to developing the next generation of AHSSs needed by the automotive industry.

Introduction

Steel has been an important material for body construction of motor vehicles for decades. Steels, especially AHSSs, are expected to remain as a primary auto body structural material in the foreseeable future. The use of Gen I AHSS is prevalent in many of today's vehicles, providing designers with excellent crash management and considerable weight reduction opportunities. The automotive industry, steel industry, and government are working together to pursue Gen III AHSSs that will offer even greater potentials for weight reduction and safety enhancement with manufacturability and affordability acceptable for future generation vehicles. Gen III AHSSs would have specific strengths (strength-to-weight ratios) on a par with or even higher than those of aluminum alloys and Mg alloys. Controlling costs will likely require that Gen III AHSSs be modestly alloyed when compared to Gen I AHSSs.

The Gen I AHSSs and several promising Gen III AHSS concepts rely on allotropic phase transformation (i.e., decomposition of austenite to various low temperature phases) and solution strengthening to achieve a balance of strength and ductility. This approach stems from the unique and versatile phase transformation characteristics of the iron-carbon (Fe-C) alloy system. By varying the amounts of alloying elements and controlling the thermomechanical processing routes in steel making, the volume fractions, grain sizes, and morphologies of different phases can be tailored to meet the strength and ductility specifications of different grades of steels. The resulting microstructures produced in this way are essentially a mixture of hard phases such as martensite and bainite and soft phases such as ferrite and retained austenite, with the sizes of the constituent phases on the order of micrometers (10^{-5} – 10^{-6} m). Under load, the hard phases and soft phases deform differently, which is known as the incompatible deformation phenomenon. Plastic strains are preferably accumulated in the soft phase grains under continued loading. The localized strain concentration in soft phase grains causes nucleation and coalescence of microvoids at the grain boundaries, which accelerates fracture during deformation.

The primary aim of this project is to use unique facilities like the Advanced Photon Source (APS) at Argonne National Laboratory and the ORNL Spallation Neutron Source (SNS), available through the DOE Office of Science, to characterize in situ AHSSs with emphasis on (1) the austenite-ferrite phase transformation behavior under the rapid heating/cooling conditions typical of modern sheet steel production and (2) microscopic and macroscopic deformation and failure processes. The fundamental knowledge on the phase transformation and deformation/failure will provide the scientific underpinnings to support the ongoing development of Gen III AHSSs at steelmakers, auto original equipment manufacturers (OEMs), and research organizations.

Approach

Highly engineered and carefully controlled thermomechanical processing routes are used to achieve the desired microstructures in AHSSs (Wagoner, 2006). The phase transformation processes are complex and nonequilibrium in nature. A novel, in situ neutron diffraction experiment was developed to directly measure and quantify the nonequilibrium phase transformation processes under the heating and cooling conditions representative of AHSS thermomechanical processing (Feng, 2011). An electrical resistance-heating device was designed and built to enable controlled heating and cooling. The subsecond time resolution necessary for direct in situ measurement of nonequilibrium phase transformations of AHSS was achieved through (1) optimizing special sample configurations that maximize the diffraction volume to increase the intensity of the diffraction pattern and at the same time minimize the temperature gradient (less than 3°C) within the diffraction volume to maintain measurement accuracy and (2) applying the stroboscopic technique unique to the time-of-flight pulsed neutron source to drastically increase the diffraction intensity. The newly developed neutron diffraction experiment makes it possible for bulk volume averaged measurement, thereby avoiding the complications of the surface effects experienced in our previous synchrotron x-ray experiments. Furthermore, neutron diffraction directly detects and measures the different phases present in the material to eliminate the uncertainties in dilatometer measurement caused by the alloying element concentration induced volumetric changes associated with the nonequilibrium phase transformation (Yu et al., 2012). The neutron diffraction experiments were performed at the SNS VULCAN beam line.

There have been a number of studies on the macroscopic strain-stress partitioning between different phase constituents in polycrystalline alloys. In situ synchrotron x-ray and neutron diffraction experiments measure the lattice strains of the respective constituent phases at different stress levels. Since the gage volume typically ranges from cubic millimeters to cubic centimeters, the lattice strains measured from these diffraction experiments are macroscopic ones averaged over hundreds to thousands grains. They are unable to resolve the microscopic strain variations inside a grain. In this work, the synchrotron x-ray microdiffraction technique was used to probe in situ the three dimensional “distribution” of the microscopic strain distribution within the individual grains of DP AHSS under tensile loading to provide insights on the microscopic deformation incompatibility and stress partitioning between the hard and soft phases. A special differential aperture x-ray microscopy technique was applied to probe the microscopic deformation process underneath the surface (Larson et al., 2002; Liu et al., 2004). The in situ microscopic deformation study was conducted at the APS high-energy x-ray microdiffraction 34-ID-E beam line.

Results and Discussion

DP980 steel, a ferrite-martensite DP AHSS, was used for both in situ neutron diffraction phase transformation study and in situ synchrotron microscopic deformation study. The FY 2012 effort concentrated on developing the baseline experimental procedures and demonstrating the usefulness of both techniques.

(1) In situ neutron diffraction study of the nonequilibrium phase transformation

The on-heating phase transformation in the intercritical temperature region was the focus of the in situ neutron diffraction experiment in FY 2012, since annealing in such a temperature region is typically the first step in thermomechanical processing of AHSS to achieve the desired final microstructure [4]. DP980 was heated to different intercritical temperatures, with heating rates ranging from 0.1 to 30°C/s, and then held at the target temperatures for from 0-1,000 s. Figures 1 and 2 present the kinetics of isothermal phase transformation at two different intercritical temperatures, 732°C and 772°C respectively, obtained from the in situ neutron diffraction experiment. In both cases, the samples were heated at 30°C/s to the target temperature and isothermally held for up to 1,000 s. As shown in the figures, the austenite phase continued to form during the initial stage of the isothermal holding at both temperatures. But the rates of the isothermal phase transformation were very different. At 732°C, it took about 600 s to complete the austenite formation, whereas it took about half that time at 772°C. More importantly, the lattice spacing of the newly formed austenite also continued to decrease. Since the lattice spacing of the austenite is a function of the alloying element concentration, especially the carbon concentration, the change in lattice spacing provides direct experimental evidence that the formation of austenite during isothermal annealing in the intercritical temperature region is controlled by the diffusion of alloying elements. The in situ neutron diffraction experiment provides, for the first time, a means of quantitatively correlating the kinetics of the austenite formation to the alloying diffusion and partitioning process in a complex multiphased steel.

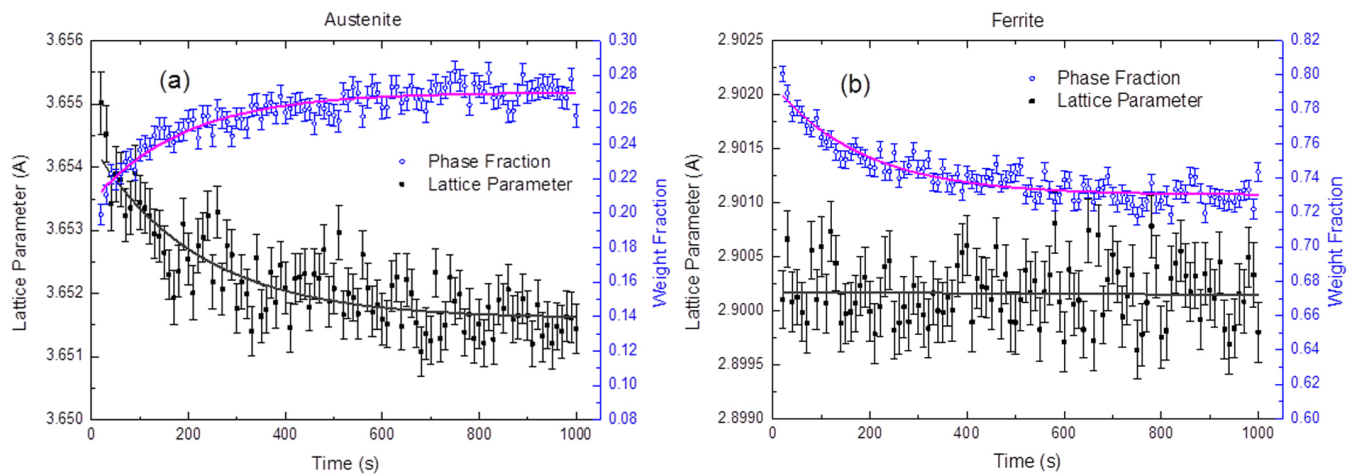


Figure 1. Variation of phase fractions and lattice parameters of (a) austenite and (b) ferrite phases as a function of holding time at an intercritical temperature of 732°C.

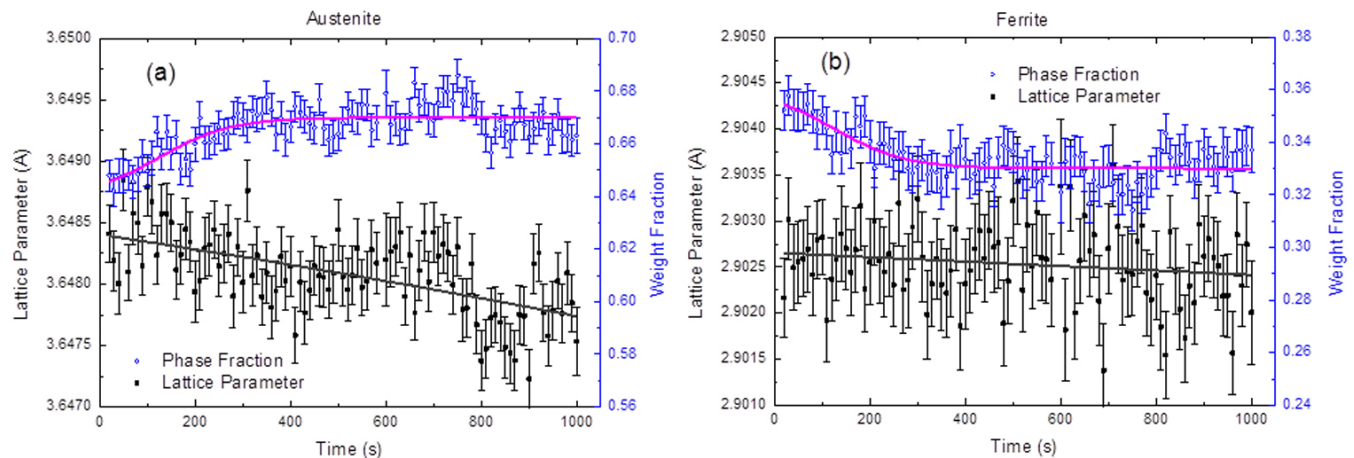


Figure 2. Variation of phase fractions and lattice parameters of (a) austenite and (b) ferrite phases as a function of holding time at an intercritical temperature of 772°C.

2) *In situ* synchrotron microbeam study of the microscopic deformation process

The microdiffraction beam facility at APS allowed the investigation of strain-stress partitioning between the ferrite and martensite phases during tensile loading inside individual grains. Figure 3 shows the evolution of the lattice strain (i.e., elastic strain) distribution in a selected ferrite grain (labeled as G1 in the figure). The different grains and their orientations were identified from the polychromatic microbeam scan. The elastic strain distribution inside grain G1 was determined by means of monochromatic diffraction. The x-axis in the figure is parallel to the tensile loading direction of the sample, whereas the y-axis is parallel to the depth direction. Hence, the figure reveals the grains *underneath* the surface of the sample. Different colors within the map indicate the variation in grain orientations.

The ferrite grain G1, located from 8 to 25 μm underneath the sample surface, was mapped for microscopic strain distribution as a function of the applied macroscopically average strain. The lattice strain component normal to the surface of the sample was determined through the d-spacing change of crystallographic plane (211). At global strain $\epsilon = 0$, the average strain level of (211) was about 0.05% ~ 0.07%, indicating the residual stress present from the steel making process. Because the measured strain component is normal to the applied stress direction, it is generally negative as the grain is subjected to stress. As shown in the figure, the strain distribution inside the grain is highly nonuniform. Furthermore, the overall microscopic strain was the highest when the applied strain was 0.23%. Increasing the applied strain to 0.30% actually reduces the overall microscopic strain in the grain. As the applied strain further increased to 0.46%, the microscopic strain distribution didn't vary much from that at 0.30%.

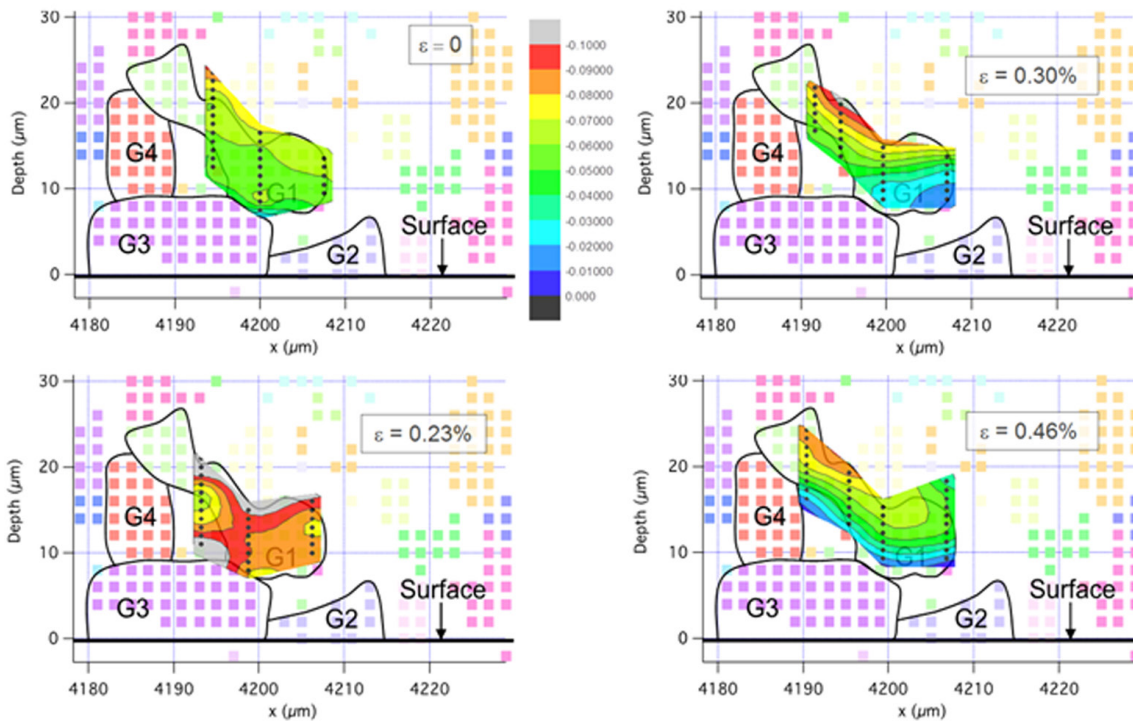


Figure 3. Microscopic strain evolution as a function of global strain level (ϵ) within a ferrite grain (marked as G1). The x-axis is parallel to the tensile loading direction, and G2 is located roughly at the sample center.

Therefore, it can be concluded that the ferrite grain yielded in between 0.23% and 0.30% of the applied strain, well before the general yielding of the material that occurs at 0.7%. There should be localized strain accumulation within the martensite grains after the ferrite grain yielded. Also, as shown in Figure 3, at global strain levels above 0.30%, the blue color at the shallower grain boundary of G1 indicates that voids may be forming between the soft (ferrite) and hard (martensite) phases due to the deformation incompatibility.

The strain distributions in the other grains as well as the plastic strains are being analyzed.

Technology Transfer Path

The primary aim of this project is to use unique facilities like APS and SNS, available through the DOE Office of Science, to characterize in situ AHSSs with emphasis on (1) the austenite-ferrite phase transformation behavior under the rapid heating/cooling conditions typical of modern sheet steel production and (2) microscopic and macroscopic deformation and failure processes. The fundamental knowledge on the phase transformation and deformation/failure will provide the scientific underpinnings to support the ongoing development of Gen III AHSS at steelmakers, auto OEMs, and research organizations. The results of this work will be published at national and international conferences and made available to the steel industry and steel alloy development researchers. This information can then be used to design Gen III high strength steels by those organizations.

Conclusions

In FY 2012, a novel in situ neutron diffraction experiment was developed to directly measure and quantify the nonequilibrium phase transformation processes under the heating and cooling conditions representative of AHSS thermomechanical processing. Changes in both the phase fractions and the lattice spacing can be measured continuously during rapid heating and isothermal holding in the intercritical temperature region. It was observed that the on-heating phase transformation kinetics in DP980 steel are strongly dependent on the alloying element diffusion and partition, and the initial microscopic heterogeneity in the DP microstructure plays a major role in the phase transformation process. Future work will be focused on providing further understanding of the microscopic heterogeneity and its effects on the kinetics of austenite decomposition under conditions of controlled cooling, which will greatly enhance understanding of phase transformation kinetics in modern steels with complex microstructures.

Synchrotron microbeam diffraction experiments provided direct experimental evidence that highly nonuniform microscopic strain distribution develops within individual phases under loading. Such measurement has significant importance for understanding the deformation incompatibility phenomena between the soft and hard phases.

Low Cost Magnesium Sheet Production Using the Twin Roll Casting Process and Asymmetric Rolling

Principal Investigator: G. Muralidharan, Oak Ridge National Laboratory
(865) 574-4281; fax: (865) 574-4357; e-mail: muralidhargn@ornl.gov

Principal Investigator: B. Radhakrishnan, Oak Ridge National Laboratory
(865) 241-3861; fax: (865) 576-4944; e-mail: radhakrishnb@ornl.gov

Collaborator: Prof. Sean Agnew, University of Virginia
(432) 924-0605; fax: (432) 982-5660, e-mail: sra4p@eservices.virginia.edu

Collaborator: Dr. Bruce Davis, Magnesium Elektron North America
(618) 709-5023; fax: (618) 452-7929, e-mail: Bruce.Davis@Magnesium-ElektronUSA.com

Collaborator: Dr. Mark Kozdros, CANMET
(905) 645-0695, e-mail: Mark.Kozdras@NRCan-RNCan.gc.ca

Accomplishments

- Demonstrated that the texture of AZ31B sheet is modified during asymmetric rolling.
- Demonstrated that annealing of an asymmetrically rolled sheet results in a favorable reduction in the severity of basal texture.
- Incorporated twinning deformation modes for Mg alloy AZ31 in a crystal plasticity (CP) framework model of asymmetric rolling.
- Received an R&D 100 award for the development of the asymmetric rolling mill. The development and procurement of the rolling mill, along with initial research to establish texture control, was funded by the Advanced Manufacturing Office of DOE and the alloy specific research work using the mill was funded by the Vehicle Technologies Office of DOE.
- Modeled texture development in the presence of combined compression and shear loads during rolling.
- Developed a model for the recovery of deformation substructure and incorporated the model within the CP Monte Carlo framework to model static recrystallization in AZ31 following shear combined with compression rolling.

Future Directions

- Evaluate effect of annealing parameters on texture evolution of asymmetrically rolled AZ31B sheet.
- Complete asymmetric rolling of twin roll cast sheet and evaluate texture evolution after annealing.
- Evaluate formability of shear rolled and annealed twin roll cast sheet.
- Combine deformation and annealing models to predict texture and grain size evolution during dynamic recrystallization of AZ31 during asymmetric rolling.
- Develop deformation history inputs for the microstructure simulations at various sheet depths using finite element (FE) simulations of the shear rolling process.

Technology Assessment

- Target: Identify the effect of shear rolling on texture and formability of twin roll cast sheet. Develop a predictive simulation tool for microstructure and texture during shear rolling of Mg alloys.
- Gap: Although the literature shows that asymmetric rolling (or shear rolling) of Mg sheet is successful in modifying the strong basal texture and improving formability, very little is known about the effect of process parameters on the extent of texture modification and on the magnitude of the improvement of the formability. Integrated computational materials engineering based process optimization of shear rolling should be applied to optimize material microstructure and texture.

Introduction

The higher cost of sheet production and the lower formability relative to steel and aluminum are two major factors inhibiting the widespread use of Mg in automotive applications. The conventional production route for Mg sheet from direct chill casting of slab is time, energy, and labor intensive due to multiple steps involved in the production route. A modern sheet production technology, called twin roll casting, that is currently used for aluminum has been applied to Mg on a laboratory scale in an attempt to reduce the energy consumption of the process and reduce its cost. This technology involves the solidification of a liquid metal stream in the gap between cooled rolls. By doing this, a strip 3–8 mm thick can be produced directly from the molten state. In comparison to the conventional method of sheet production, this is significantly more energy efficient. This sheet can then be finish rolled using two to three passes to achieve a final gage of 1.5–2 mm. This eliminates losses from scalping, resource consumption associated with breakdown rolling, and a number of warm rolling passes to reach the 3 mm gage thickness that would be required by the conventional process route.

The other major cost factor is Mg's lower formability. Mg's lower formability is associated with its hexagonal close-packed crystal structure. This reduces the relative number of slip systems that are active to accommodate deformation. Furthermore, conventionally rolled Mg sheet has a strong basal texture component that results in anisotropy of tensile properties. The rolling process aligns the basal texture component parallel with the rolling plane, with a 5–10 degree tilt forward and aft of the rolling direction. It is this tilt that produces the anisotropy. Weakening or randomization of the basal texture in Mg sheet will reduce this effect and improve formability.

Several approaches have shown the feasibility of randomizing the texture in Mg alloys. The addition of rare earth elements has been proven to randomize the texture in Mg alloys and improve formability. Asymmetric rolling (or shear rolling of Mg sheet) has also been shown to be successful in modifying the strong basal texture and improving formability. However, very little is known about the effect of process parameters on the extent of texture modification and on the magnitude of improvement of formability. The primary objective of this project is to evaluate the feasibility of modifying the texture and the formability of twin roll cast Mg alloy sheet through shear rolling, thereby enabling the production of low cost Mg sheet.

Approach

A synergistic experimental and computational modeling approach, as shown in Figure 4, was used in this project. Two types of shear rolling mills were available for the execution of this project: a four high shear mill with 3 : 1 sized work roll (with shear ratios limited to a single value of 3 : 1), shown in Figure 5(a); and a new two high shear rolling mill with equal diameter rolls capable of continuously variable shear ratios, shown in Figure 5(b). To understand the effect of process parameters on the texture developed after shear rolling, several shear-rolled sheets were characterized as described below.

1. Sheet preheated to temperature and then rolled using cold rolls with the four high mill.

Shear rolled using the two high mill with 1 : 1 sized warm rolls, but capable of differential speeds.

- a. RP6 (Normal rolled, 1 : 1, 200°C, 25% reduction)
- b. RP9 (Shear rolled, 1 : 1.35, 200°C, 25% reduction)
- c. RP12 (Shear rolled, 1 : 3, 200°C, 40% reduction)

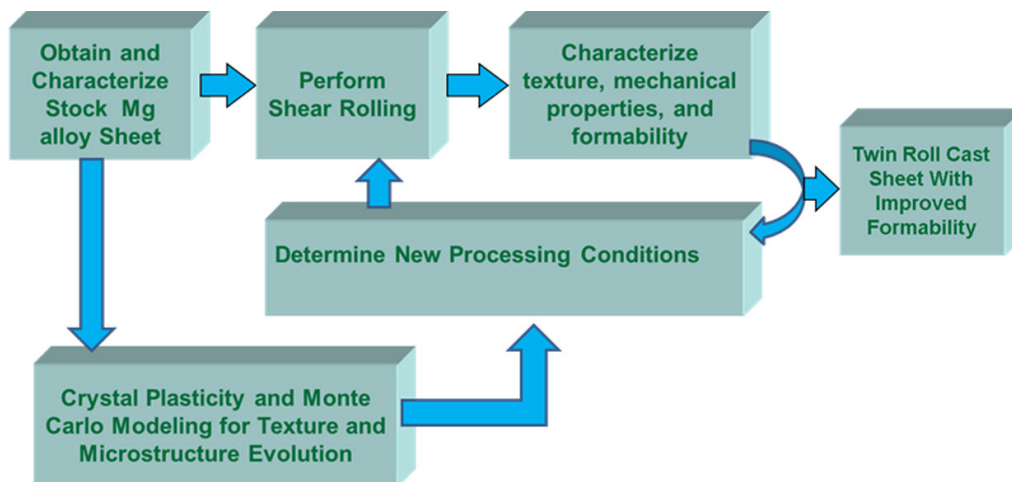


Figure 4. Schematic of the overall approach used in this project.

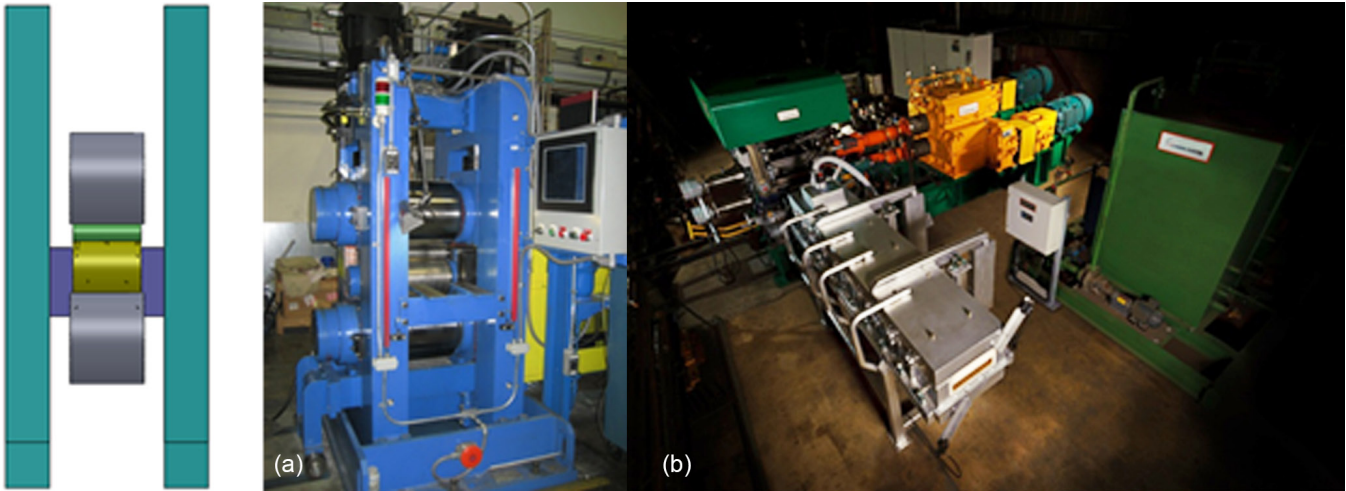


Figure 5. Two types of shear rolling mill available for process development: (a) four high shear mill and (b) two high shear mill.

The objective of the modeling effort is to use an integrated mesoscale modeling capability to develop a fundamental understanding of the mechanisms that contribute to microstructure and texture evolution during shear rolling and annealing of Mg alloys. The effort will guide the optimization of process and microstructural parameters to achieve the target performance. The existing modeling framework based on coupling a CP-based deformation model with a Monte Carlo (MC)-based annealing model is being modified for simulating the dynamic recrystallization that occurs during shear rolling at hot/warm rolling temperatures. The effort involves extending the CP-MC simulations to dynamic recrystallization by breaking down the hot deformation into a series of deformation and annealing steps and applying the current simulation capability for static recrystallization at each step in a sequential fashion. Techniques will be developed for mapping the microstructural domain between the deformation and annealing simulations and establishing the deformation step and the annealing time corresponding to a given strain rate. Based on this approach, it will be possible for the first time to predict both microstructure and texture evolution during dynamic recrystallization as a function of strain, strain rate, deformation path, and the input microstructure and texture.

The following two-step modeling approach is being pursued. First, the deformation of the twin rolled strip during subsequent shear deformation will be modeled using a continuum FE code such as ABAQUS. The goal of this effort is to quantify the influence of process parameters such as reduction ratio, roll geometry, roll speed, deformation temperature, strain rate, and the operating friction coefficient on the deformation gradient within the sheet. Second, the deformation path experienced by a volume element at different through-thickness locations will be used as input to the mesoscale code to simulate the microstructure and texture evolution. Such an approach has been developed previously at ORNL for shear rolling of steel sheets.

Results and Discussion

Figure 6 shows the texture obtained from the centerline of AZ31B sheet (a) in as-received condition, (b) symmetrically rolled isothermally at 200°C, (c) shear rolled isothermally at 200°C, and (d) shear rolled using preheated sheet. Note that the basal texture is modified using shear rolling with the maximum intensity in the basal plane tilting away from the sheet normal. A more random distribution of the basal pole intensities is achieved.

Figure 7(a) shows the engineering stress-strain curves, while Figure 7(b) shows the elongation to failure obtained from the sheets processed using different processing routes. As seen from Figure 7(b), sheets with the textures shown in Figures 6(b) and 6(c) obtained through shear rolling show good ductility (RP6 and RP9) compared to the typical as-processed sheet. Further work is being performed to prepare sheets of greater width with the texture shown in Figure 6(d) using the new shear rolling mill to enable formability testing.

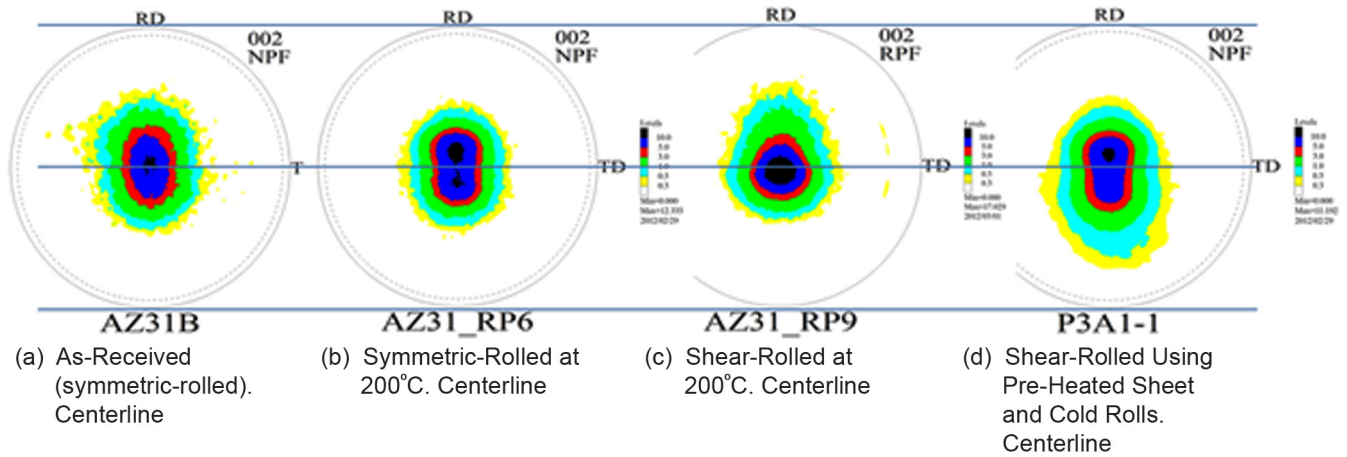


Figure 6. (0002) pole figures from the sheet centerline show that shear rolling (c, d) modifies the basal texture.

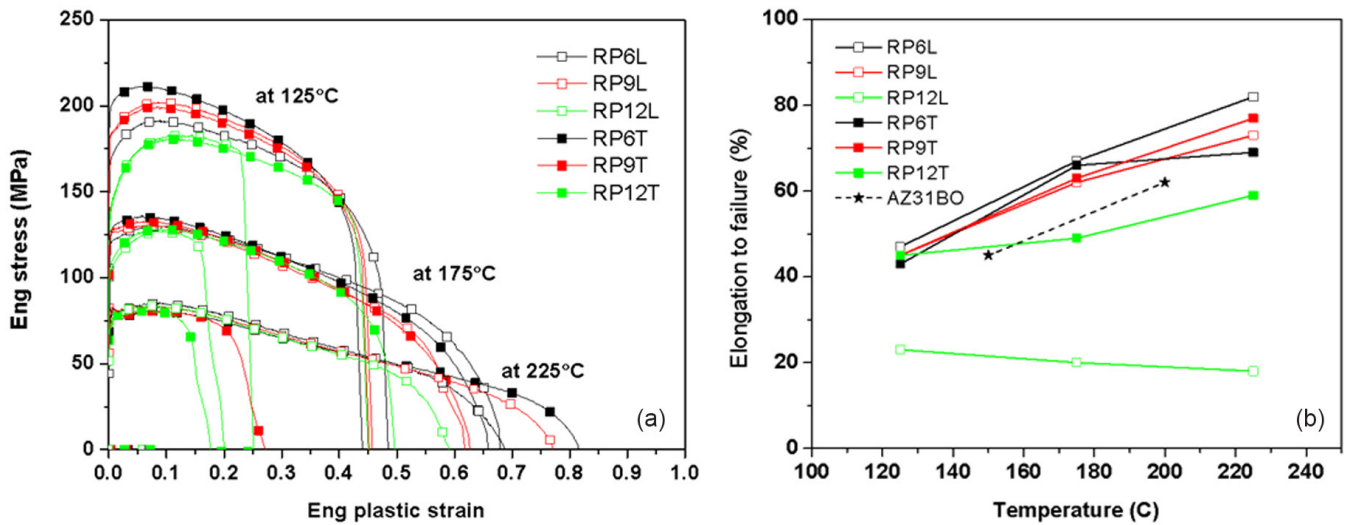


Figure 7. Stress-strain curves obtained from the AZ31B sheets processing using different routes (a). Note that L indicates longitudinal and T indicates transverse orientation of the specimens. Elongation to failure (b) obtained from the stress-strain curves in (a).

Computational modeling is being used to identify the most promising routes to achieve sheets with the desired texture and improved formability. The CP-based deformation model has been modified so that it can handle all the existing slip-based and twin-based deformation modes that are demonstrated during the deformation of the wrought Mg alloy AZ31. The deformation model is based on the neighborhood compliance model developed by Sarma and Dawson (1996). The model is a scheme for partitioning the strain between volume elements within a microstructure subjected to an external loading path. The model was applied to an external velocity gradient consisting of varying ratios of compression and shear representing the local deformation conditions during asymmetric rolling. The model parameters that include the critical resolved shear stress and hardening parameters for various slip and twin systems were obtained from published data for AZ31B (Choi et al., 2010). In addition, a twinning model based on the predominant twin reorientation model proposed by Choi (2010) was also integrated into the CP model. The CP model was used to investigate the effect of shear to compression ratio on the initial texture, which is predominantly basal. The evolution of the deformation texture for various values of shear superimposed on compression is shown in Figure 8. The results indicate that increasing the shear rate is helpful in reducing the intensity of the initial basal texture and rotating the basal poles away from the sheet normal direction up to a shear to compression ratio of about 1.0. However, continued increase in the shear rate is not beneficial as it leads to an increase in the basal texture intensity and a rotation of the peak back toward the normal direction. The results show the importance of choosing the proper shear to compression ratio based on the initial texture and deformation conditions such as temperature and overall strain level to optimize the final texture of the rolled sheet to obtain improved formability.

A model for microstructure and texture evolution during static recrystallization of the Mg alloy AZ31 has been developed by coupling the CP-based microstructural deformation model with a Monte Carlo based annealing model (Radhakrishnan et al., 1998) that simulates thermally activated microstructural evolution associated with recovery and recrystallization. The recovery model is based on the assumption that the extent of local substructure recovery leading to the formation of sub-grain boundaries (through the reorganization of the geometrically necessary dislocations) is proportional to the misorientation of a volume element with respect to its surroundings and the local stored energy. A hybrid model (Rollett and Raabe, 2001) was integrated into the mesoscale modeling framework. The coupled CP-annealing model is able to capture the texture weakening associated with recovery of the deformation substructure obtained by shear rolling as shown in Figure 9. In the model, a velocity gradient was used as input with different values for the shear and the compression. The shear to compression ratio was systematically varied. In the actual shear rolling process, however, there could be a variation in the amount of shear through the thickness of the sheet. Such variation was found in previous studies of shear rolling of Fe-3% silicon (Si) steel, where pins of Fe-3Si were embedded in the sheet and the shape change observed after shear rolling. Therefore, in the actual shear rolling process, the final texture could be a superposition of several of the model results. In addition, the microstructures used in the simulation are not truly representative of the input microstructure for shear rolling. To be more accurate, significantly larger microstructures that accurately capture the initial grain orientations more accurately should be taken in the model. At this point, the model results are qualitative, but can be improved when combined with a better process model for shear rolling. The biggest unknowns in the process model are the operating shear and the constitutive behavior under shear rolling conditions, which need to be input into a continuum code.

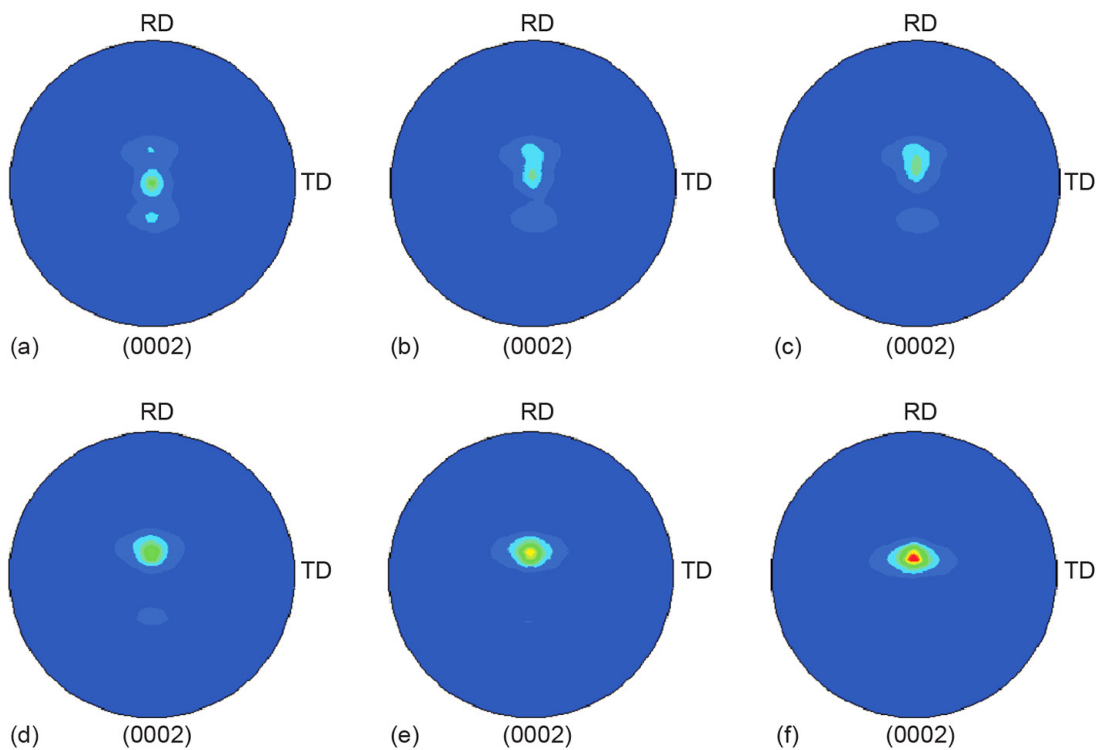


Figure 8. (0002) pole figures from deformation simulations for different shear rates Y : (a) 0.0, (b) 0.15, (c) 0.25, (d) 0.5, (e) 1.0, and (f) 2.0.

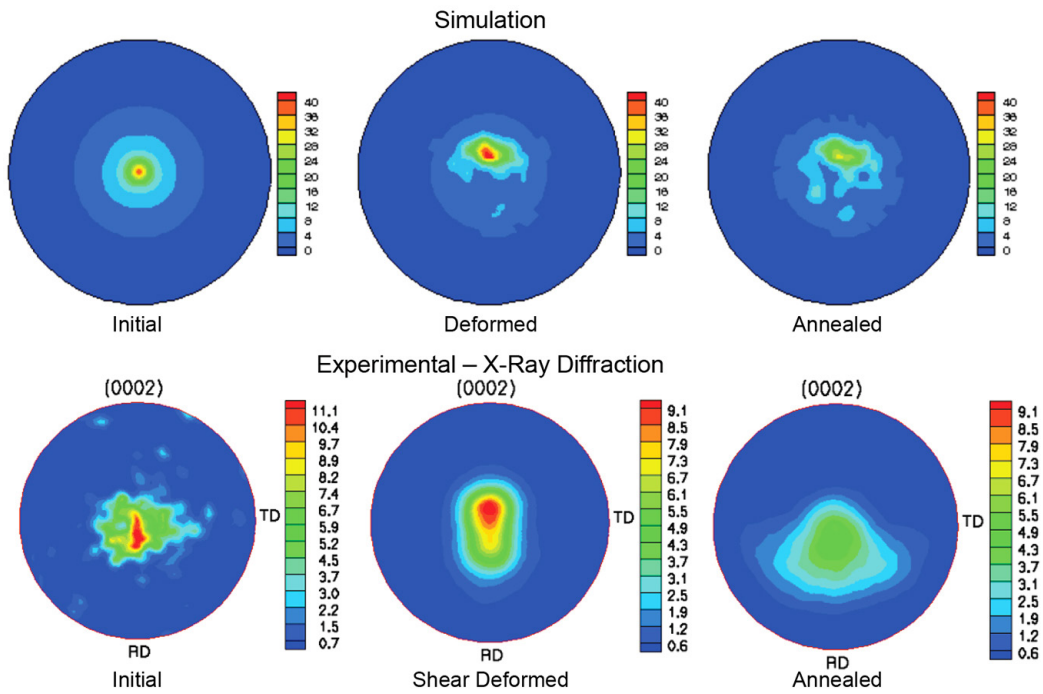


Figure 9. CP-FE modeling of static recrystallization following shear rolling of AZ31 showing texture weakening (top), and experimental validation using x-ray diffraction (bottom).

The extent of weakening also depends on the extent of recovery, the amount of initial deformation, and the shear to compression ratio during shear rolling, as shown in Figure 10.

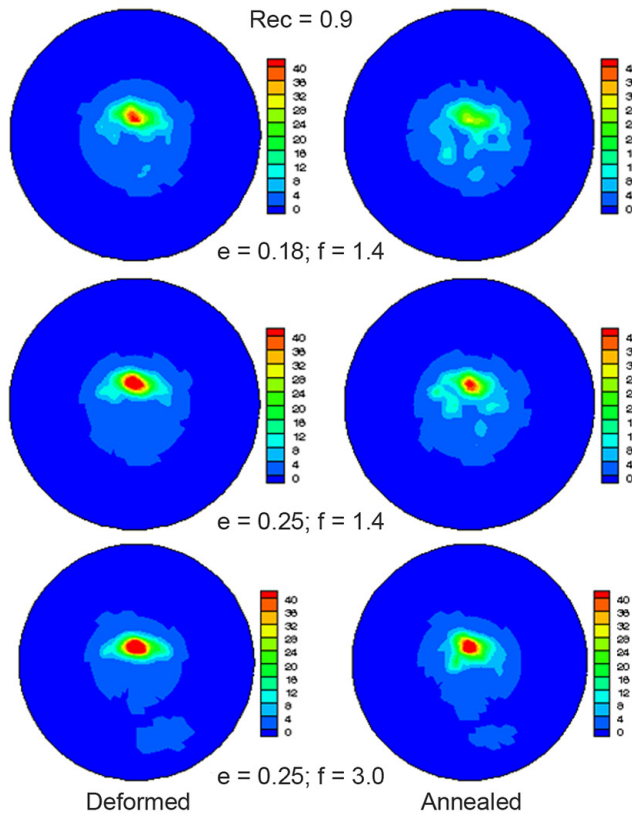


Figure 10. CP-MC simulations showing the effect of initial deformation and the shear : compression ratio on texture weakening during static recrystallization

Technology Transfer Path

Currently there are a number of paths forward for technology transfer, including the following.

1. ORNL interacts with FATA Hunter, the fabricator of the asymmetric rolling mill. Since FATA Hunter is commercializing a large scale mill, processing methods developed as part of the project could be commercialized by licensing them to FATA Hunter.
2. Processing technology could also be transferred through Magnesium Elektron North America, another collaborator on this project.

Conclusions

Using experimental work and computational modeling, it has been demonstrated that shear rolling combined with annealing has the potential to decrease the intensity of basal pole texture in AZ31B. Further work will focus on evaluating the formability of sheets with modified texture with the aim of improving formability.

Conclusions

In FY 2012, a novel in situ neutron diffraction experiment was developed to directly measure and quantify the nonequilibrium phase transformation processes under the heating and cooling conditions representative of AHSS thermomechanical processing. Both the phase fractions and the lattice spacing changes can be continuously measured during rapid heating and isothermal holding in the intercritical temperature region. It was observed that the on-heating phase transformation kinetics in DP980 steel are strongly dependent on the alloying element diffusion and partition, and the initial microscopic heterogeneity in the DP microstructure plays a major role in the phase transformation process. This information will be made available to the scientific community for designing Gen III AHSSs.

Using experimental work combined with computational modeling, it has been demonstrated that shear rolling combined with annealing has the potential to increase the ductility of AZ31B. Further work to confirm these results is planned.

Presentations/Publications/Patents

Sarma, G.; Radhakrishnan, B. Effect of Shear to Compression Ratio on Texture Evolution During Differential Speed Rolling of Magnesium (submitted to *Materials Science and Engineering A*).

Yu, Z.; Barabash, R.; Barabash, O.; Liu W.; Feng, Z. Microscopic Deformation in Individual Grains in an Advanced High Strength Steel. *JOM* (in press).

Yu, Z.; Feng, Z.; An, K.; Zhang, W.; Specht, E. D.; Chen, J.; Wang, X. L.; David, S. In-Situ Neutron Diffraction Study of Non-Equilibrium Phase Transformation in Advanced High-Strength Steels. In *Trends in Welding Research, Proceedings of the 9th International Conference*, Chicago, IL, June 4-8, 2012; Babu, S.; Bhadeshia, H. K.; Cross, C. E.; David, S. A.; DebRoy, T.; DuPont, J.; Koseki, T.; Liu, S. Eds.; ASM International: 2013.

References

Choi, S. H.; Kim, D. H.; Lee, H. W.; Shin, E. J. Simulation of texture evolution and macroscopic properties in Mg alloys using the crystal plasticity finite element method. *Materials Science and Engineering A* **2010**, 527, 1151–1159.

Feng, Z. Material Degradation Phenomena and Mitigation for Nuclear Reactor Life Extension, Oak Ridge National Laboratory, Oak Ridge, TN, 2011.

Larson, B. C.; Yang, W.; Ice, G. E.; Budai, J. D. and Tischler, J. Z. Three-dimensional X-ray Structural Microscopy with Submicrometre Resolution. *Nature* **2002**, 415, 887–890.

Liu, W. J.; Ice, G. E.; Larson, B. C.; Yang, W. G.; Tischler, J. Z.; Budai, J. D. The three-dimensional X-ray crystal microscope: A new tool for materials characterization. *Metall Mater Trans A* **2004**, 35A, 1963–1967.

Radhakrishnan, B.; Sarma, G.; Zacharia, T. Modeling the kinetics and microstructural evolution during static recrystallization-Monte Carlo simulation of recrystallization. *Acta Mater.* **1998**, 46, 4415–4433.

Rollett, A. D.; Raabe, D. A hybrid model for mesoscopic simulation of recrystallization. *Computational Materials Science* **2001**, 21, 69–78.

Sarma, G. B.; Dawson, P. R. Texture predictions using a polycrystal plasticity model incorporating neighbor interactions. *International Journal of Plasticity* **1996**, 12, 1023–1054.

Schnatterly, J. Steel Content of North American Vehicles. Presented at the Great Designs in Steel seminar, 2007. (<http://www.autosteel.org/~media/Files/Autosteel/Great%20Designs%20in%20Steel/GDIS%202007/20%20-%20Steel%20Content%20of%20North%20American%20Vehicles.pdf>)

Schultz, R. A. Metallic Material Trends for North American Light Vehicles. Presented at the Great Designs in Steel seminar, 2007. (<http://www.autosteel.org/~media/Files/Autosteel/Great%20Designs%20in%20Steel/GDIS%202007/21%20-%20Metallic%20Material%20Trends%20for%20North%20American%20Light%20Vehicles.pdf>)

Wagoner, R. H. Advanced High Strength Steel Workshop, organized jointly by National Science Foundation, Department of Energy and American Iron and Steel Institute, Arlington, VA, October 23–26, 2006.

Yu, Z.; Feng, Z.; An, K.; Zhang, W.; Specht, E. D.; Chen, J.; Wang, X. L.; David, S. Comparative Study of Steel Phase Transformation Behavior by Dilatometry Method and In-Situ Neutron Diffraction. In *Trends in Welding Research, Proceedings of the 9th International Conference*, Chicago, IL, June 4-8, 2012; Babu, S.; Bhadeshia, H. K.; Cross, C. E.; David, S. A.; DebRoy, T.; DuPont, J.; Koseki, T.; Liu, S. Eds.; ASM International: 2013.

B. Properties and Manufacturability - Pacific Northwest National Laboratory

Field Technical Monitor: Dean Paxton
Pacific Northwest National Laboratory
902 Battelle Boulevard; P.O. Box 999; Richland, WA 99352
(509) 375-2620; e-mail: dean.paxton@pnnl.gov

Technology Area Development Manager: William Joost
U.S. Department of Energy
1000 Independence Ave., S.W.; Washington, DC 20585
(202) 287-6020; e-mail: william.joost@ee.doe.gov

Contractor: Pacific Northwest National Laboratory (PNNL)
Contract No.: DE-AC05-00OR22725 & DE-AC06-76RLO1830

Executive Summary

The Properties and Manufacturability project consists of five tasks focused on R&D activities advancing the basic mechanical properties, manufacturability, and cost of lightweight materials towards the levels needed for increased implementation in automotive applications. These tasks include the following:

- Deformation Fundamentals in Advanced Lightweight Materials
- Aerodynamic Lightweight Cab Structures
- Non-Rare Earth High-Performance Wrought Mg Alloys
- Enhanced Room-Temperature Formability in High-Strength Aluminum Alloys Through Pulse Pressure Forming
- Aluminum Formability Extension Through Superior Blanking Process

The following sections outline specific task work conducted at PNNL in the area of properties and manufacturability of lightweight metals. Each task supports one or more goals within the Properties and Manufacturability Agreement as outlined below.

Activities and Developments

Microstructure Deformation Fundamentals in Advanced Lightweight Materials

Principal Investigator: Xin Sun, Pacific Northwest National Laboratory
(509) 372-6489; fax: (509) 372-6099; e-mail: xin.sun@pnnl.gov

Principal Investigator: David K. Matlock and John Speer, Advanced Steel Processing and Products Research Center (ASPPRC), Colorado School of Mines
(303) 273-3775; fax: (303) 273-3016; e-mail: dmatlock@mines.edu
(303) 273-3897; fax: (303) 273-3016; e-mail: jspeer@mines.edu

Accomplishments

- Identified materials and quenching and partitioning (Q&P) parameters to generate properties in the “3rd generation advanced high strength steel (AHSS)” property range. (FY 2012)
- Produced four different types of Q&P steel samples for tensile testing, hole expansion testing, and stretch-bending testing. (FY 2012)
- Performed static tensile testing to evaluate the macroscopic tensile properties and the microstructure for the in-plane and through-thickness directions. (FY 2012)
- Performed electron backscattered diffraction (EBSD) on two Q&P steels to distinguish the phase fractions and morphologies. (FY 2012)
- Initiated nano-indentation testing with Q&P steels to quantify hardness differences for different phases after a preliminary test with a commercial Q&P steel. (FY 2012)

Future Directions

- Perform the stretch-bending testing with Q&P steels. A strategy to test sub-sized samples is currently being developed.
- Complete EBSD and nano-indentation testing on Q&P steels.
- Perform microstructure-based finite element analyses using the results of microstructure analyses and nano-indentation testing for property prediction and future directions for property improvement.
- Develop new processing parameters based on the computational results for further property improvement.

Technology Assessment

- Target: Develop 3rd generation AHSS products with 1200 MPa ultimate tensile strength (UTS) and 30 percent total elongation.
- Gap: Reduced alloying and lower cost are important considerations for the development of 3rd generation AHSS. In addition, the automotive steel industry still lacks an overall understanding of the key material parameters controlling the mechanical properties of AHSS

Introduction

AHSS represents an important technology in efforts to reduce vehicle weight for improved fuel efficiency and occupant safety. These steels have evolved with new alloying and processing strategies to tailor microstructures containing various mixtures of ferrite, martensite, bainite, and retained austenite. Following previous development of 1st and 2nd generation AHSS, 3rd generation AHSS concepts are being pursued to identify lower alloy steels that achieve ultra-high strength properties in combination with formability sufficient for implementation in automotive production. Relative to the 2nd generation steels, reduced alloying and lower cost are the focus of these steels.

This project is focused on experiments and theoretical analyses based on microstructural-based modeling designed to improve the overall understanding of the variables which control austenite stability against straining, and thus mechanical properties of new AHSS products. The results of these analyses will be used to accelerate the development of 3rd generation AHSS products. It is envisioned that steels with 1200 MPa UTS and 30 percent total elongation will be the property goal, along with a consideration of cost target of this class of material anticipated by the global automotive and steel industry. The proposed effort will also focus on improved understanding of the relationship between AHSS microstructural features and the effects of microstructure on global and local deformation mechanisms. Thus 3rd generation AHSS developed in this effort will possess good localized deformation capacity for automotive forming and trimming operations.

Approach

Because the Q&P process has been identified as a potential process to generate 3rd generation AHSS properties, the first round of material development focused on Q&P steels. Q&P, which is a process recently developed by ASPPRC, involves an initial cooling step to a temperature between M_s and M_f to create controlled fraction of martensite and austenite, followed by a thermal treatment intended to promote carbon diffusion from supersaturated martensite to austenite, thereby stabilizing some of the austenite to room temperature. **Figure 1** shows a diagram of the Q&P process. First, the materials and Q&P processing parameters were identified to generate the model Q&P steels which may be in 3rd generation AHSS property range. Here, the materials are enriched with carbon and manganese to obtain the desired austenite volume fraction and stability, and processing parameters (e.g., the temperature and time for the initial reheating, quenching and partitioning). Four different types of Q&P tensile samples were produced, based on different processing parameters. In addition, the same materials and Q&P processing parameters were employed to produce samples for hole expansion and stretch-bending testing. Static tensile testing was then completed with the four Q&P steels using ASTM E-8 samples for both rolling and transverse directions.

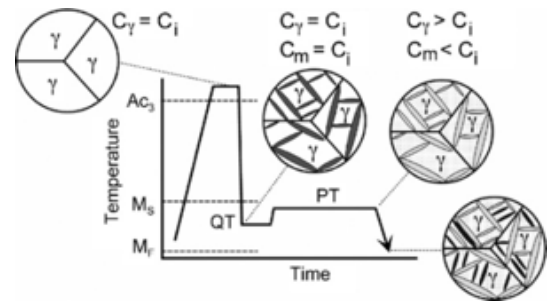


Figure 1. Schematic diagram of the Q&P process (De Moor et al., 2011)

Microstructure analyses were performed on all the Q&P samples using scanning electron microscopy (SEM). SEM pictures were obtained from the in-plane and through-thickness cross-sections along the rolling and transverse directions. Due to the complex microstructures generated by the Q&P process, EBSD techniques have been implemented on two selected Q&P steels for phase identification. In addition, nano-indentation tests have been initiated with the Q&P steels to identify the hardness numbers of the different constituent phases. The images from EBSD, together with the SEM images for the same location and the hardness data obtained from indentation test, are expected to be used for the microstructure-based finite element modeling that will be used for property prediction and improvement.

Results and Discussion

The chemical compositions of two selected materials (0.2~0.3C-3Mn-1.6Si) are given in **Table 1**. The material was received as a 1-mm-thick cold rolled sheet. Test samples were machined from the sheet and then heat-treated using the Q&P heat-treating parameters listed in **Table 2**. Different annealing temperatures were employed based on Thermo-Calc® thermodynamic calculations to generate different microstructures (i.e., an intercritical microstructure with 50 percent volume fraction of ferrite (MAT4) or a fully austenitized microstructure (MAT1, MAT2, MAT3)). **Figure 2** shows the microstructures of the four different Q&P samples. The four materials show some difference in their detailed microstructures depending on the employed Q&P processing parameters. In general, these materials have very small grains (<3 μm) and quite complex microstructures with several different phases (i.e., austenite, tempered/untempered martensite, bainite) and phase properties. MAT1–3 have quite homogeneous microstructures along all directions while MAT4, due to the employment of different annealing temperatures, shows inhomogeneous and banded microstructures depending on the directions.

Table 1. Chemical composition of the prepared steel grades (wt%)

	C	Mn	Si	Al	P	S	N
0.3C-3Mn-1.6Si	0.29	2.95	1.59	0.06	0.01	0.0028	0.0039
0.2C-3Mn-1.6Si	0.20	3.00	1.60	0.06	0.01	0.0031	0.0041

Table 2. Heat treating parameters for four different types of Q&P steel samples

Name	Chemistry	Annealing Temps/Time (°C/s)	Quenching Temps/Time (°C/s)	Partitioning Temps/Time (°C/s)
MAT1	0.3C-3Mn-1.6Si	820/120	180/10	400/100
MAT2	0.2C-3Mn-1.6Si	840/120	250/10	400/10
MAT3	0.2C-3Mn-1.6Si	840/120	250/10	400/100
MAT4	0.2C-3Mn-1.6Si	725/120	185/10	450/10

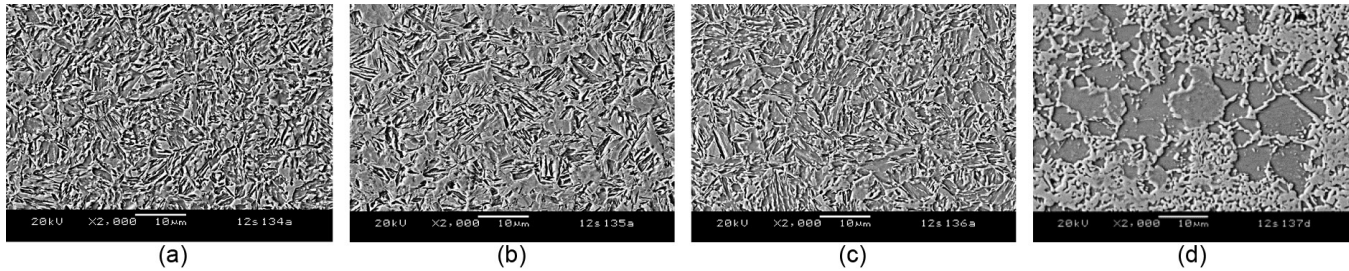


Figure 2. Microstructures of the four Q&P steels (in-plane view). (a) MAT1, (b) MAT2, (c) MAT3 and (d) MAT4

Figure 3 shows the stress-strain curves for the four Q&P samples along the rolling and transverse directions and compares their macroscopic tensile properties to different steels. In Figure 3(a), MAT1–3 show consistent stress-strain behaviors along the rolling and transverse directions due to their homogeneous microstructures whereas MAT4 shows different behaviors for each direction. In general, the four materials have very high UTSs (>1300 MPa) and relatively good ductilities (>10 percent). The properties of these materials in the context of overall 3rd generation AHSS property requirements are summarized in Figure 3(b). To meet the property target for this project (i.e., 1200 MPa UTS and 30 percent total elongation), additional focus must be put on improving the total elongation. As MAT1 and MAT2 have similar UTS but different ductility, these two materials were selected as the base materials for the subsequent investigation on the effects of microstructure features on the properties of Q&P steels, especially ductility.

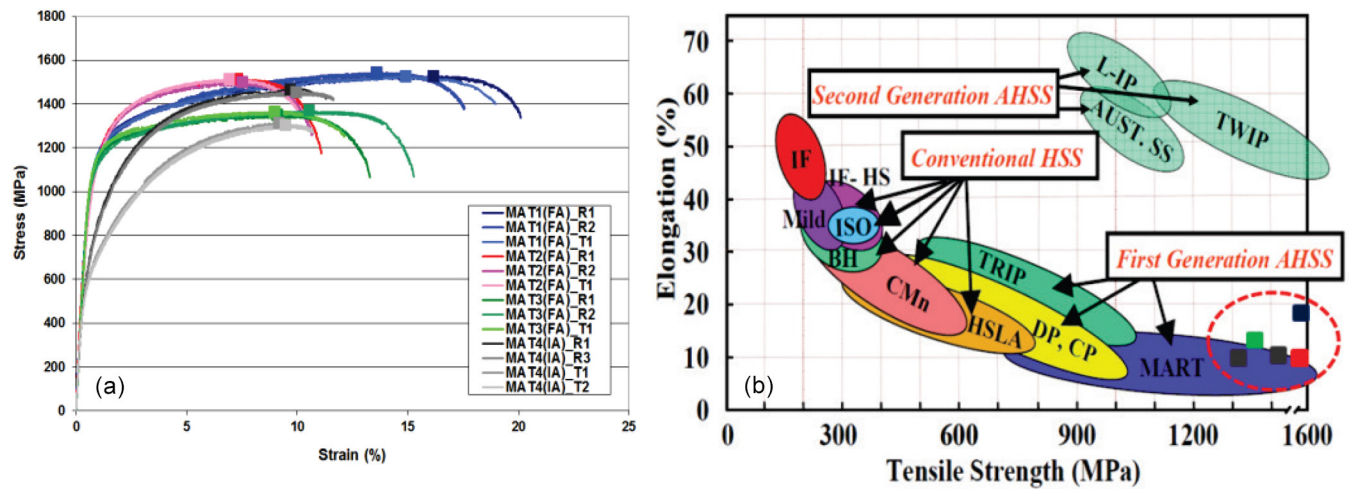


Figure 3. (a) Stress-strain curves for the Q&P steels and (b) tensile properties of the Q&P steels compared to other steels

Due to their complex microstructures, much effort has been spent on EBSD experiment with these Q&P steels in obtaining the useful results for the subsequent microstructure-based modeling works. Figure 4 shows the grain orientation map and phase map for MAT2, which indicates the complex microstructures and small grains of this type of materials. SEM analysis is being performed on the same location where EBSD was performed, and nano-indentation testing has been initiated to obtain the hardness data for different phases. Figure 5 shows the microstructure of a commercial Q&P steel of 1000 MPa UTS grade and its hardness histogram with average hardness values for the constituent phases obtained from a preliminary nano-indentation test. Detailed methodology was established based on the preliminary test to obtain the meaningful results at the microstructural scale of interest.

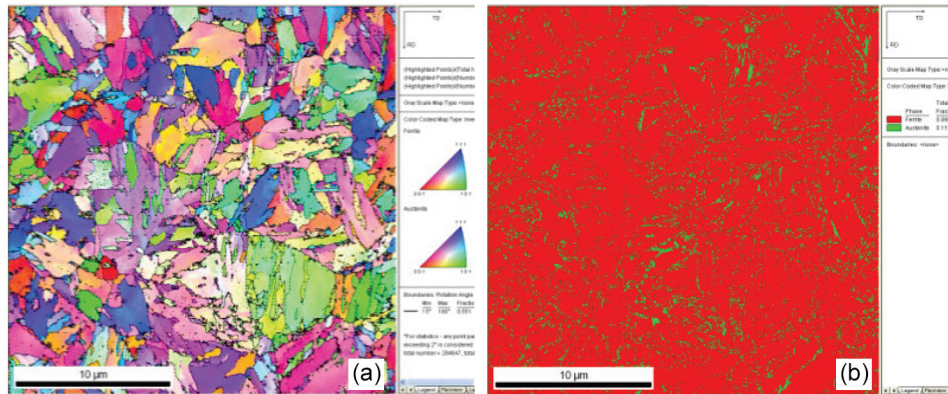


Figure 4. (a) Grain orientation map and (b) phase map of Q&P steel (MAT2)

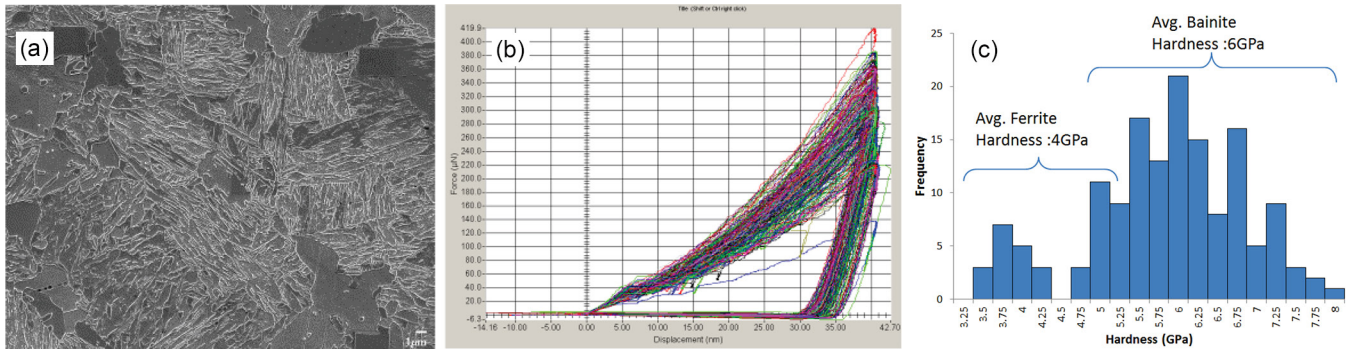


Figure 5. (a) Microstructure of a commercial Q&P steel, (b) 225 force-displacement curves from nano indentation test and (c) histogram of measured hardness data

Additional samples for hole-expansion and stretch-bending testing were recently heat-treated based on the same Q&P processing parameters. Due to the limited dimensions of the heat-treating furnace sub-sized samples with dimensions of 25 mm × 250 mm were developed for stretch-bending testing. The samples were then spot welded to strips of DP980 materials with dimensions of 50 mm × 50 mm, and the joint configuration is currently being optimized.

Technology Transfer Path

The deliverables of this projects will be transferred to the participants (original equipment manufacturers) and steel producers through the industry/university cooperative research center (ASPPRC at Colorado School of Mines) during regularly scheduled semi-annual review meetings.

Conclusions

Q&P steel was selected as our initial model steel for the development of 3rd generation AHSS and to provide an overall understanding of microstructure deformation fundamentals of AHSS. Four different Q&P steels were produced, based on different chemistry compositions and heat-treating parameters. Tensile test results indicate that all Q&P steels have properties in the lower range of the 3rd generation AHSS property map. Even though the overall property improvement trend is encouraging, further elongation improvements are needed in the next iteration to meet the requirements for this project. In general, the produced Q&P steels have very small size grains and quite complex microstructures, which necessitates EBSD and SEM analysis for phase identification. Further nano-indentation tests will identify the mechanical strength of the different phases. Microstructure analyses and nano-indentation tests will be employed in subsequent modeling efforts to identify possible directions for future property improvements.

Publications/Presentations/Patents

Choi, K.S.; Soulam, A.; Li, D.; Sun, X.; Khaleel, M.A.; Xu, L.; and Barlat, F. Relationship Between Material Properties and Local Formability of DP980 Steels, SAE Technical Paper no. 2012-01-0042, SAE 2012 World Congress, April 24–26, 2012, Detroit, Michigan, USA.

Sun, X.; Soulam, A.; Choi, K.S.; Guzman, O.; and Chen, W. Effects of Sample Geometry and Loading Rate on Tensile Ductility of TRIP800 Steel. *Mat. Sci. Eng. A*, **2012**, *541*, 1–7.

Taylor, M.D.; Matlock D.K.; Packard C.E.; and Sun, X. Applicability of Nanomechanical Testing to Commercially Produced Advanced High-Strength Steels. Materials Science and Technology, Pittsburgh, PA, October 2012.

Taylor, M.D.; Matlock D.K.; Speer J.G.; and De Moor E. Effect of Microstructure on the Fracture Response of AHSS. Spring 2012 Advanced Steel Processing and Products Review Meeting, Golden, CO, March 2012.

Taylor, M.D.; Matlock D.K.; Speer J.G.; and De Moor E. Effect of Microstructure on the Fracture Response of AHSS. Fall 2012 Advanced Steel Processing and Products Review Meeting, Golden, CO, September 2012.

Xu, L.; Barlat, F.; Lee, M.G.; Choi, K.S.; and Sun, X. Hole Expansion of Dual Phase Steels. 6th International Conference on High Performance Structures and Materials, June 18–20, 2012, New Forest, Hampshire, UK.

Reference

De Moor, E.; Speer, J.G.; Matlock D.K.; Kwak J.-H.; and Lee S.B. Effect of Carbon and Manganese on the Quenching and Partitioning Response of CMnSi Steels. *ISIJ Intl.* **2011**, *51*, pp 137–144.

Aerodynamic Lightweight Cab Structure Components

Principal Investigator: Mark T. Smith, PNNL
(509) 375-4478; e-mail: mark.smith@pnnl.gov

Nona Larson, PACCAR Technical Center
(360) 757-5365; e-mail: nona.larson@paccar.com

Accomplishments

- Completed aluminum (Al) sheet forming sequences using a prototypical “A-pillar” tray forming tool. The forming sequence included hot preforming of an Al sheet blank followed by room-temperature (RT) forming into the final deep tray shape. Forming required levels of deformation that significantly exceeded the forming capability of the baseline Al sheet.
- PACCAR completed adhesive bonding qualification tests on Al sheet coupons that had been processed through a simulated hot/RT-forming sequence. These tests established that the thermal exposure of the simulated forming process does not have a detrimental effect on the application of production coatings and finishes.
- PACCAR and the PNNL established an initial technical partnership with Magna International, a leading supplier for the commercial vehicle industry. In conjunction with PACCAR, a Class 8 truck cab aerodynamic component was selected for prototype development using the enhanced elevated-temperature forming process. (FY 2012)

Future Directions

- Complete fabrication of prototype aerodynamic formed components for testing by PACCAR.
- Conduct material property and finish system characterization of formed trays and prototype components to confirm the ability to meet PACCAR materials and manufacturing specifications.
- Establish production feasibility for Al components in conjunction with Magna International and PACCAR.

Technology Assessment

- Target: Develop an elevated-temperature hot-forming process, combined with a cold-finish forming process that can increase the useable elongation and formability to the equivalent of over 40 percent for a 6000-series Al sheet alloy. In general, RT-forming limits for current generation, automotive grade 6000-series alloys are limited to the equivalent of 18 to 20 percent tensile elongations, depending on component geometry and part complexity.
- Target: Demonstrate the feasibility of hot-forming complex Al sheet components requiring overall formability levels of up to 40 percent equivalent tensile elongation, while meeting mechanical property and finish requirements for exterior cab component applications.
- Gap: Current 6000-series Al sheet alloys have desirable strength levels and surface finish characteristics, but lack sufficient formability (>18–20 percent tensile elongation) to allow their use in the manufacture of many aerodynamic cab components and structures.
- Gap: Existing Al hot-forming processes typically result in formed sheet tensile properties below 100 MPa yield strength levels. This limits the use of hot-formed Al sheet in applications that require higher strengths (150 MPa) for long-term fatigue and dent resistance.
- Gap: RT Al forming processes result in mechanical properties with insufficient final-formed ductility. This limits applications where residual ductility is required for riveting and hemming assembly operations.

Introduction

The objective of this project is to demonstrate lightweight materials manufacturing methods that will increase the efficiency of Class 8 trucks by enabling more widespread use of mass-saving Al and enabling aerodynamic styling through the use of a new approach to Al sheet forming. The project will develop forming technology that will enable Al sheet to replace sheet steel and molded fiberglass reinforced composite panels and components, providing individual panel and component weight savings of approximately 40 percent.

Approach

The project will use an elevated-temperature forming process, to be developed at PNNL, to demonstrate enhanced formability in 6000-series Al alloy sheet. The high-ductility forming process will enable PACCAR member companies to design prototype cab components with aerodynamic features that would otherwise not be feasible for manufacturing. PNNL will develop and optimize a hot-forming + cold-forming process using sheet tensile specimens and PACCAR will evaluate surface conditions and corrosion behavior for formed specimens. Based on the selected process parameters, PNNL and PACCAR will design and build a prototype component for laboratory testing. The technology for the process developed at PNNL will be transferred to a Tier 1 supplier and project partner, Magna International, who will build full-scale prototype components for PACCAR, which will then finish the parts and perform durability testing (e.g., fatigue and corrosion testing). Planned technical steps and milestones include conducting elevated-temperature tensile tests at various strain rates on the alloy provided by PACCAR to develop a constitutive materials relation for use in forming analysis. These data will provide a basis for selection of the temperature and strain rates for subsequent forming trials.

Assuming a process route can be established, the full-scale component will be modeled at PNNL to determine the optimum forming process cycle. Depending on component size and forming requirements, a prototype die will be constructed and parts fabricated at either PNNL or Magna International. Given the high-temperature processing involved in the proposed forming

approach, PACCAR will perform surface-oxide characterization and evaluate the e-coat process development to ensure good adherence through optimized parameters.

Several prototype panels will be made and PACCAR will process the parts through the cab assembly and coating process and perform component testing. Component testing will include a durability test (possibly on a cab shake system); corrosion testing; and mechanical properties testing, including tension and fatigue testing.

Technology Transfer Path

This task is primarily focused on demonstration of the development of a thermomechanical forming process that can achieve significantly enhanced levels of formability in Al sheet materials. PACCAR and its two truck companies have multiple applications where high formability and good post formed properties of the Al sheet would allow them to replace low-strength glass fiber composites in highly shaped aerodynamic panels and components. The project includes participation by Magna International, a major supplier of truck cab structures and components, that will facilitate transfer of the technology to a Tier 1 supplier.

Results and Discussion

The second phase of this project has focused on demonstrating the hot/ RT-forming process on a 3 dimensional prototypical “A-pillar” tray part (Figure 6) that requires levels of formability that exceed conventional Al sheet forming methods. A series of hot preforming experiments were conducted to evaluate different forming temperatures and post-forming cooling steps. These experiments narrowed the hot-forming step to two temperatures (500 and 540°C) and post-forming cooling by forced air and by water quenching. The hot-forming temperature combined with the post-forming cooling step was designed to re-solutionize the Al sheet so that after cold forming, the paint-bake (20 minutes at 180°C) heat-treatment response could be maximized. The cold-forming step was designed to input a minimum of 5 percent cold deformation in the majority of the formed component, as some level of RT deformation is important in promoting higher strengths in the final component after the paint-bake cycle. Table 3 shows tensile test results for the trays formed at the different hot-forming temperatures, followed by the RT final forming step. The results are the average of four tensile tests, with the American Society for Testing and Materials (ASTM) sub-sized sheet specimens being sectioned from the flat bottom of the formed tray.

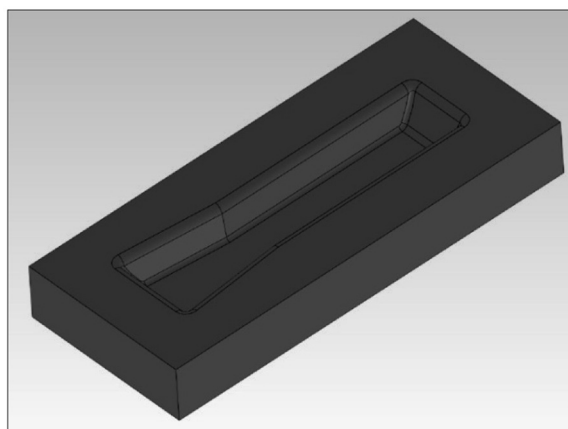


Figure 6. Three-dimensional prototype tray component die design

Table 3. Tensile test results for hot/RT-formed tray materials

Forming Conditions	0.2% Yield Strength (MPa)	Ultimate Tensile Strength (MPa)	Elongation (%)
HF 500 C/AC + CF + PB	119.7	210.3	22.9
HF 500 C/WQ + CF + PB	121.4	211.2	22.8
HF 540 C/AC + CF + PB	140.8	241.8	22.9
HF 540 C/WQ + CF + PB	144.8	245.0	22.8

HF = Hot Form; CF = Cold Form; AC = Air Cool; WQ = Water Quench; PB = Paint Bake (180°C for 20 min.)

As the results indicate, both trays formed at 540°C (i.e., air-cooled and water-quenched) approached the goal of 150 MPa yield stress while retaining excellent tensile ductility (>22 percent elongation). The forming of the tray geometry was achieved primarily by draw-in of the sheet, due to the lack of binder control available with the prototype tools. A bottom view of the hot-preformed tray and final RT-formed tray is shown in Figure 7, and both figures show significant draw-in of the sheet along the length. The resulting plastic deformation, as determined from thickness measurement, was found to be in the 5 to 15 percent range depending on location in the tray. In commercial practice, the tooling design would incorporate some

level of binder control to reduce wrinkling in more complex part geometries, and to generate higher elongations during the hot-forming step. However, regardless of the amount of plastic deformation that results from forming, the deformation that occurs during the hot-forming step is essentially annealed out of the material at the elevated forming temperature. With sufficient cooling, the material comes out of the hot-forming step in the solutionized condition, similar to the as-received (T4) condition. During the final RT-forming step, the objective is to 1) cold form sufficiently to achieve final part shape and dimensions, and 2) impart sufficient RT deformation (5 percent) to enhance the paint-bake heat-treatment response.



Figure 7. Bottom view of hot-preformed (left) and final-formed (right) Al tray showing sheet draw-in around the perimeter.

In conjunction with the demonstration of the hot/RT-forming process, PNNL prepared sheet samples for PACCAR coating and adhesive strength evaluations. A key concern of the project team is that thermal cycling of the Al sheet to the hot-forming temperatures (500 to 540°C) can result in the formation of a thicker Al oxide layer or an oxide layer with lower adherence strength. Sample material of the 6000-series sheet alloy was heated to both 500 and 540°C, and then subjected to fan-cooling or water-quench. PACCAR prepared test panels by sending them through standard production pre-treatment steps and the production E-coating process. Next, the test panels were tested for dry-film thickness, and dry and wet paint adhesion based on ASTM D3359 test method. Test results showed that all test panels passed the adhesion test and results were comparable to baseline test panels.

Conclusions

The second phase of this project has demonstrated combinations of hot- and cold-forming steps for the 6000 series Al sheet alloy using a prototypical “A-pillar” tray. The design of the tray is such that the part cannot be formed at RT from the 6000-series Al alloy using conventional stamping technologies. During FY 2012, multiple trays were hot preformed, followed by RT final forming and heat-treatment using a simulated paint-bake cycle. Tensile test specimens sectioned from the Al trays demonstrated tensile yield strengths approaching 150 MPa, with excellent residual ductility. Adhesive bonding strength evaluations conducted by PACCAR demonstrated that the elevated-temperature forming step and post-forming cooling do not result in any degradation of adhesive bond strength using established surface-preparation steps and bonding procedures.

Non-Rare Earth High-Performance Wrought Magnesium Alloys

Principal Investigator: Curtis A. Lavender, PNNL
(509) 372-6770; e-mail: curt.lavender@pnnl.gov

Tim Skszek, Magna Cosma International
(248) 689-5512; e-mail: tim.skszek@cosmaeng.com

Accomplishments

- A series of magnesium alloys were synthesized and extruded to produce high-performance Mg alloys with fine-grain size dispersions. (FY 2012)
 - Grain sizes appear to be <5 μm .
 - Dispersions ~15 nm interact with dislocations.
- A test article was developed to compare energy absorption of Al to Mg. (FY 2012)
 - 7-mm outside diameter (OD), 0.5-mm wall tube, 15 mm in length.
 - A high-rate compression test was developed to understand strain-rate sensitivity given that the predominant deformation mechanism changes in compression.
 - Strain-rate sensitivity has not been observed to date.
- A non-rare earth (RE) containing Mg alloy processed for fine-grain size and dispersion can absorb energy similar to 6061 aluminum. (FY 2012)
 - This is a 20 percent mass savings over 6061.
 - The mode of failure is different.
- Microstructural modeling has been initiated to help understand behavior and predict energy absorption. (FY 2012)
 - Grain size, as it impacts stress strain, has been added.
 - Strengthening with hard second phase has been added.
 - This work will now leverage fracture and ductility project.

Future Directions

- Produce at least three additional alloys based on the microstructural modeling to demonstrate the predictability of the performance and microstructure relationship.

Technology Assessment

- Target: Develop high-energy absorption Mg alloys that do not contain RE elements that can replace Al extrusions at a mass savings of 20 percent (based on density).
- Target: Use inverse process modeling to develop a low-cost process to produce microstructures required for high performance at a low cost, making Mg extrusion viable for automotive applications.
- Gap: Currently produced Mg alloys that possess high strength and ductility (energy absorption) use RE elements that increase cost and are of limited supply, resulting in a reluctance of the automotive industry to use Mg extrusions.
- Gap: The cost to produce high-performance Mg extrusion has prevented use in automotive applications.

Introduction

The use of Mg in automotive applications where extrusions would be preferred has been limited by the cost and energy absorption capacity of Mg. If applications like bumper beams, crush tips, intrusion beams, and shotgun tubes could be fabricated from Mg, significant vehicle mass savings could be realized. In past projects, Mg has been processed for use in applications requiring energy absorption like that of Al. This was primarily accomplished using very slow extrusion rates (raising cost) or a powder metallurgy processes requiring rapid solidification and RE-alloying additions.

The purpose of this project is to develop and demonstrate low-cost wrought Mg alloys that do not rely on RE-alloying elements for their strength, ductility, and energy absorption properties. A novel low-cost processing method, in conjunction with Mg alloys containing RE substitutes, will be developed to produce the microstructure and properties needed for the automotive applications in a cost-effective manner.

Technical Approach

The project will be performed in three phases. In the first phase, the project team will produce high-performance alloys using RE additions to develop high-energy absorbing microstructures for use as model systems for non-RE alloys. In the second phase, the team will develop the microstructure found in phase 1 into high-performance alloys without RE additions. During the second phase, at least one alloy will be selected and processed for evaluation by Magna Cosma International for use in automotive applications that require additional formability (e.g., bending or hydroforming). In the third phase of the project, an inverse process-modeling method will be used to develop a cost-effective processing approach for producing the alloy with the energy-absorbing properties.

The following technical steps are planned:

- Produce RE-Mg alloy extrusions and perform mechanical tests comparing quasi-static tension and compression results to the Al alloy 6061 and the conventional Mg alloy AZ31.
- Evaluate the energy absorption capability of the RE-Mg via impact tests and compare to 6061 and AZ31.
- Evaluate, experimentally, the deformation mechanisms of the RE alloys using interrupted strain tests in tension and compression at room temperature.
- Develop a continuum level model to predict microstructure evolution and mechanical deformation behavior of Mg alloys during processing. Validate using experimental data.
- Downselect up to three alloys from the previous task, consolidate the materials by extrusion and evaluate the non-RE alloys for strength and energy absorption characterization at both quasi-static and elevated strain-rate tension tests.
- Produce sufficient material to provide partner Magna Cosma International with tubular extrusions that can be formed into shapes (e.g., crush tips, roof structural support beams) for testing and comparison to conventional materials.
- Develop the “Model Alloy” by implementing statistical continuum mechanics model embedded with crystal plasticity. Use the model to predict grain size, dispersion, and textural effects.
- Use experimental data, crystal plasticity, inverse process path modeling, and laboratory demonstrations to develop the necessary process that will create the desired microstructure using an optimum low-cost, high-shear, liquid-to-shape processing route.
- Prototype and demonstrate a small system to produce extruded shapes from direct liquid-to-solid processing. Although the system design will be driven by modeling, it is anticipated the system will use pressurized liquid metal to fill a cavity that houses a series of high-shear mixers. The liquid will be solidified during the mixing process, fracturing the coarse intermetallics, and producing the strain needed for the fine-grain size (as predicted by the inverse modeling), and provide the driving force for the subsequent extrusion.
- Magna Cosma International will evaluate extrusions produced by the system for formability. Billets produced by the process will be rolled at PNNL and subjected to formability tests using limited dome height and warm gas-pressure forming.
- The prototypic system and design methodology will be provided to Magnesium Elektron North America (MENA), who will perform cost analysis and scale the process for production of large quantities of material.

Results and Discussion

The initial phase of this effort was to determine the microstructural characteristics of a rapidly solidified high-performance, RE-containing Mg alloy and compare them to those of conventional alloys with similar processing. High-performance Mg alloys exhibit yield strengths in excess of 500 MPa in both tension and compression, unlike conventional alloys where the compressive yield strength is 0.6 to 0.7 of the tensile yield strength. This behavior has been attributed to the fine-grain size and the contribution of twinning relative to the strengthening associated with grain boundaries; where the reduction in strength associated with twinning is offset by the strengthening associated with the increased grain boundary volume.

During this reporting period, the effort was focused on evaluating the energy absorption capability of the high-performance RE-containing alloys, energy absorption of highly processed non-RE element containing alloys, and modeling to predict the desired microstructure in support of low-cost thermomechanical process development. The results from this period's activity will be used to demonstrate that low-cost high-strain processing can be used to develop microstructures that result in high-performance Mg alloys in extruded forms. High performance for this project is defined as high strength and ductility and compressive yield strength equal to or greater than tensile yield strength. It is the combination of the three properties that will allow the Mg to exhibit high-energy absorption and performance. The non-RE alloy used for this portion of the project was the alloy ZK60A, subjected to non-commercial processing to produce a very fine-grain size extrusion. For the purposes of this report, the alloy will be called FGZK60. The commercial alloys AA6061 in the T6 condition (6061) and magnesium AZ31 in the T5 condition (AZ31) were used for comparison.

Figure 8 shows the microstructure of FGZK60 as characterized by Georgia Tech University. Figure 8(a) shows the 3- μm grain size and Figure 8(b) shows the Mg-zinc (Zn) precipitate phase (approximately 15 nm) interacting with dislocations.

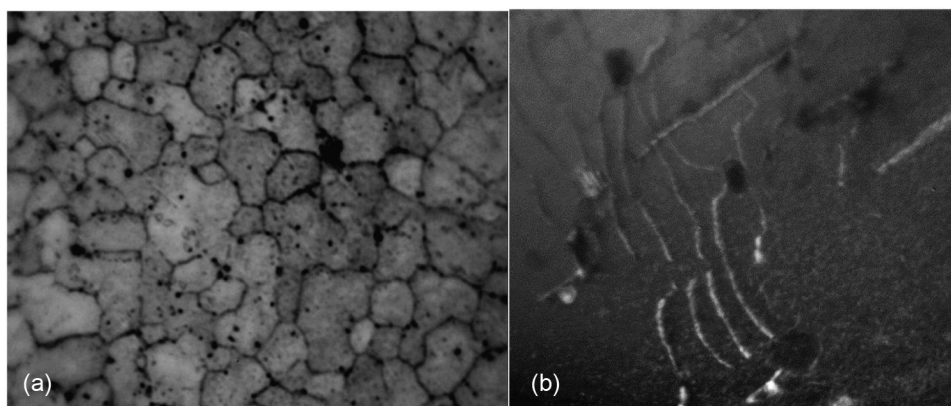


Figure 8. (a) Optical micrograph and (b) dark field transmission electron micrograph of FGZK60. The grain was approximately 3 μm and the precipitates shown interacting with the dislocations are approximately 15 nm.

The sample used for the energy absorption test (Figure 9) was a tube with a 7-mm OD, 0.5-mm wall thickness, and a 15-mm overall length. Additional samples were tested in compression at ambient temperature and varying strain rate to determine strain-rate sensitivity. For tests performed in excess of 30 m/s, a second system was used equipped with high speed cameras and speckle imaging to capture velocity and strain rate as shown in Figure 10. To date, no samples have exhibited significant strain-rate sensitivity and all future tests will be performed using the simpler quasi-static test methods. An example of the compressive stress strain curves is shown in Figure 11 for the AZ31 alloy.

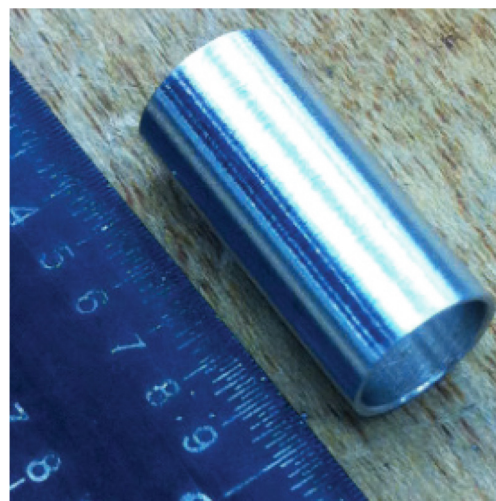


Figure 9. Tubular sample used to evaluate energy absorption in high-performance Mg alloys

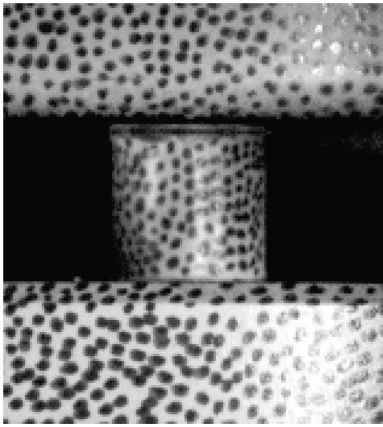


Figure 10. Crush tube sample used for compression testing where the crosshead velocity was in excess of 30 m/s. Speckle strain imaging was to determine actual crosshead velocity and strain rate.

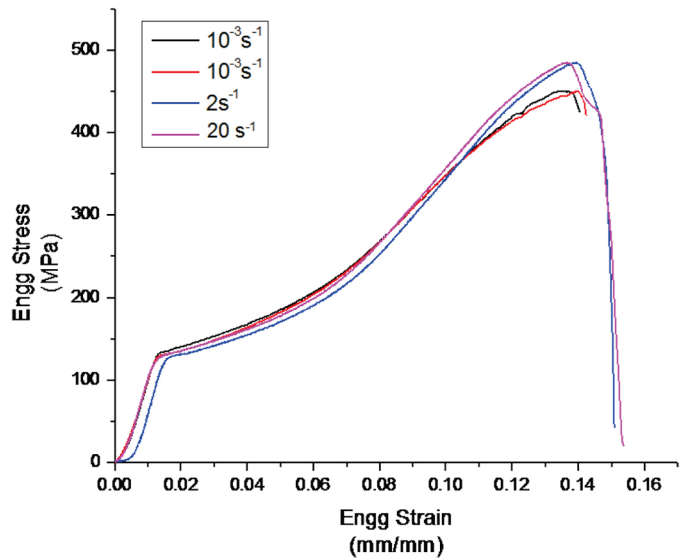


Figure 11. Compressive stress-strain curves for the AZ31 alloy at strain rates ranging from 10^{-2} to 20 s^{-1} indicating little or no strain-rate sensitivity.

Using experimentally determined constitutive relations, the tubular compression test (crush) was simulated by finite element (FE) modeling to assure that the crush sample could be used to compare the Al to Mg. The results of this test are shown in Figure 12, where the Al alloy 6061 was compared to the FGZK60 and the commercial AZ31 alloy (extruded at PNNL). The compression simulation showed that most energy (as determined from the area under the respective curve) was absorbed by the 6061 followed by the FGZK60 and AZ31 in decreasing order. When the simulation results were normalized for mass, the FGZK60 had the highest energy absorption followed by the 6061 and AZ31 alloys. This “specific” absorption difference would result in a more than 22 percent mass savings for the FGZK60 over the 6061. The simulation demonstrated that the tubular sample selected would provide relatively constant energy absorption over the test range and therefore was used for experimental testing of actual tube samples.

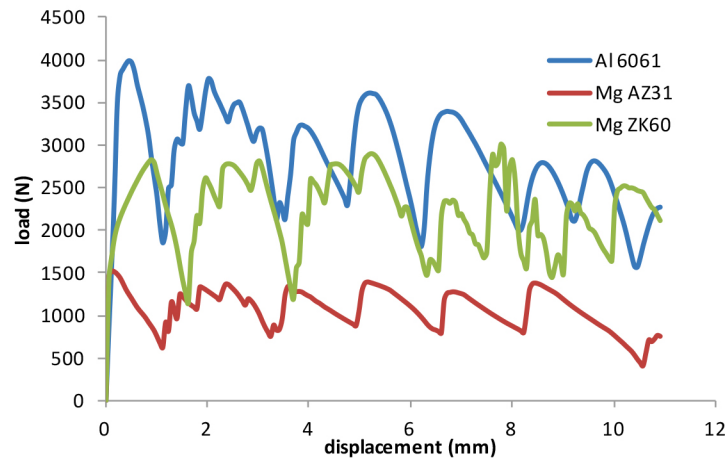


Figure 12. Simulated energy absorption for the crush test of 7-mm OD \times 0.5-mm wall thickness tubes of 6061 Al alloy and FGZK60 and AZ31 Mg alloys using constitutive models derived from compression tests

The tube samples from 6061, AZ31, and FGZK60 were tested at quasi-static rates using the fixture shown in Figure 13. Energy absorption was measured over an \sim 8 to 11 mm displacement and plotted in Figure 14. The area under the curve, determined for each test, indicated that the energy absorption was slightly higher (5 percent) for 6061. When results were normalized for mass, the FGZK60 samples exhibited 20 percent more energy absorption than the 6061 alloy. However, the mode of deformation for the FGZK60 was different than that of the 6061. The FGZK60 alloy absorbed energy by wall thickening and some splitting, whereas the 6061 folded. The actual energy absorption values were lower than the simulated

values, likely due to the difficulty FE modeling has dealing with high tri-axial strains associated with folding and buckling. More detailed FE modeling would be needed to understand this effect and is beyond the scope of this project, which requires only relative results.

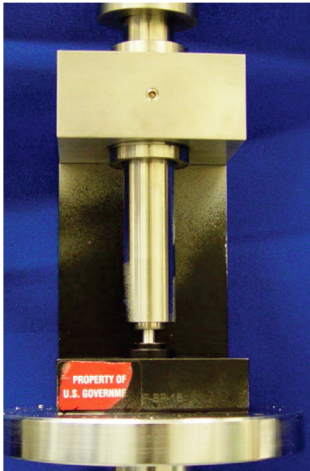


Figure 13. Test fixture used for quasi-static energy absorption testing of 7-mm OD x 0.5-mm wall thickness tubes of 6061 Al and FGZK60 Mg alloys

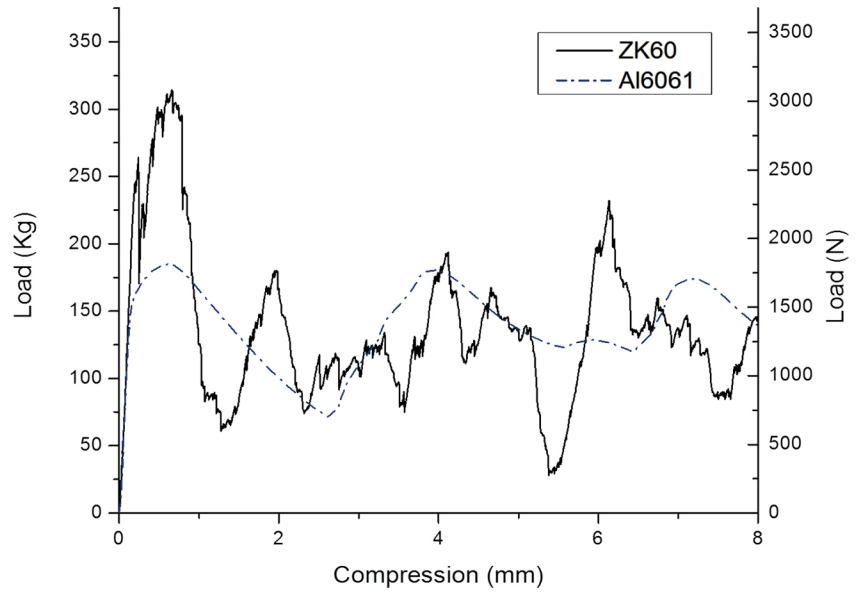


Figure 14. Energy absorption for the crush test of a 7-mm OD x 0.5-mm wall thickness tube of 6061 Al and FGZK60 (labeled as ZK60 in this figure) Mg alloys.

The results of the tube crush test indicate that a Mg alloy subjected to non-commercial processing without RE elements can absorb energy in excess of the 6061 Al alloy. Therefore, the next technical steps of the project were initiated to determine the required microstructure to achieve the FGZK60 properties with commercially viable processing. The primary objective is to develop a fine-grained alloy with a sufficient aging response to produce fine precipitates. The precipitates will likely be Al or Zn and can be formed by a T6-type heat treatment. However, developing dispersions that can act as nuclei and grain pinning provide a greater challenge for Mg alloys. Typically in Al alloys, Mn is added to form nuclei and grain pinning dispersions. For Mg, the options are more limited; however, silicon (Si) is an intermetallic former, and, conveniently, nearly identical to Mg in the galvanic series in 5% sodium chloride. Therefore, an MgSi intermetallic will not degrade the corrosion resistance of the alloy like other intermetallic formers (e.g., Fe, RE, and Al). The next series of activities will focus on the Si addition to Mg to develop fine-grain sizes.

The principal of the fine-grain size is described in Figure 15, where symmetry in the compressive yield and tensile yield strengths are achieved by decreasing grain size. As the grain size is decreased, the twinning in Mg is suppressed and compressive yield strengths are increased. Conventionally processed Mg alloys have a compressive strength normally 70 percent that of the tensile strength, resulting in buckling during bending and compression. In addition, a significant increase in ductility can be expected when the grain size decreases. Therefore the fine-grained alloy should be expected to absorb more energy.

The fine-grained alloy will be designed to target a 2 μm grain size or finer and will be developed by introducing dispersoids of a size and volume fraction per the synthetic microstructure that predicts the relationship used to develop the curves in Figure 16. By using more than 8% volume fraction of dispersion less than 1.5 μm in diameter (a dimension in Figure 16) the grain size will be less than 2 μm in diameter. This approach will be the basis for the alloy thermochemical process. Sufficient second phase forming alloying constituent (likely to be Si) will be added to the alloy and fractured and redistributed by strain to achieve the 2 μm grain size.

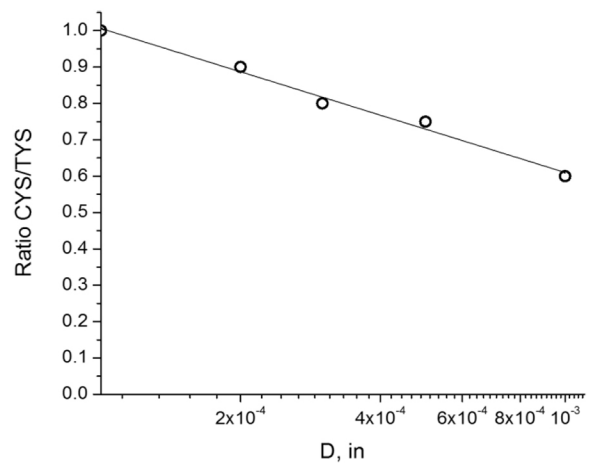


Figure 15. Effect of grain size on compressive-to-tensile yield ratio for Mg (Busk and Leontis, 1950).

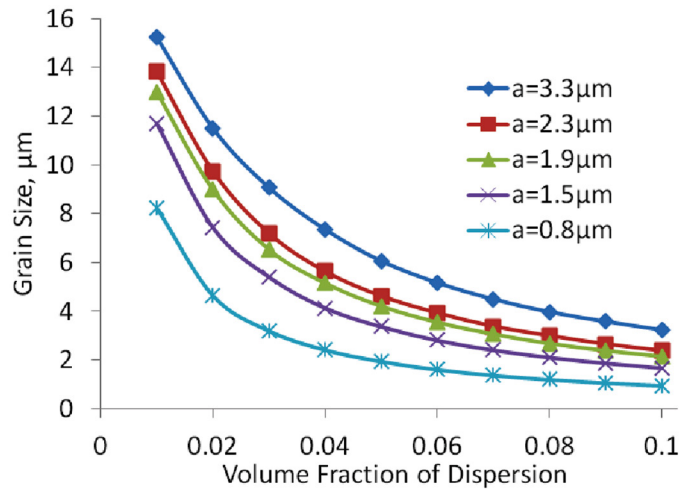


Figure 16. Synthetic microstructure prediction of grain size versus volume fraction of second phase dispersion size to be used for inverse process modeling.

Technology Transfer Path

The technology transfer for this project will occur late in phase 2 and during phase 3. The initial phase will be focused on laboratory development and understanding the Mg alloys from a mechanistic standpoint. After the alloy is understood, the technology transfer will occur in two ways: 1) produce and deliver tubes to Magna Cosma for evaluation and 2) transfer process knowledge to Transmet Inc. and MENA. In addition, MENA has contributed alloy feedstock for the early rapid-solidification processing and has played an active role in alloy selection.

Magna Cosma and MENA are cost sharing partners in the project and the Georgia Institute of Technology and Transmet are subcontractors and are, or will be, engaged in the project at the appropriate phases.

Conclusions

- A fine-grained Mg alloy was shown to absorb energy similar to 6061 Al at a mass savings of more than 20 percent.
- A test sample was designed to demonstrate energy absorption in Al and Mg. The sample was a 7-mm OD × 0.5-mm wall thickness tube with a 15-mm overall length tested in axial compression.
- The fine-grain size expected to produce high-energy absorbing Mg alloys is largely controlled by the presence of fine dispersions acting as nuclei and grain boundary pinners.

Publications

Pan, W.; Li, D.S.; Tartakovsky, A.M.; Ahzi, S.; Khraisheh, M.; Khaleel, M. A new smoothed particle hydrodynamics non-Newtonian model for friction stir welding: Process modeling and simulation of microstructure evolution in a magnesium alloy, accepted for publication in *International Journal of Plasticity*, 2012.

Li, D.S.; Ahzi, S.; M'Guil, S.; Wen, W.; Lavender, C.; and Khaleel, M.A. Modeling of Deformation Behavior and Texture Evolution in Magnesium Alloy using the intermediate ϕ -model, submitted for publication in *International Journal of Plasticity*, 2012.

Li, D.S.; Lavender, C.; Choi, K.S.; Sun, X.; and Khaleel, M.A. Inverse Materials Design in Wrought Magnesium Alloys to Increase Crashworthiness. Presented at the Society of Engineering Science 49th Annual Technical Meeting, Atlanta, GA, October 12, 2012. PNNL-SA-91285.

Li, D.S.; Choi, K.S.; Lavender, C.A.; Nyberg, E.A.; Sun, X.; and Khaleel, M.A. Modeling of Crashworthiness of Wrought Magnesium. Presented at 2012 TMS Conference, Orlando, FL, March 13, 2012. PNNL-SA-86511.

Joshi, V.V.; Nyberg, E.A.; Soulami, A.; Edwards, D.J.; Chua, A.Z.; and Lavender, C.A. 2012. In-Plane Compression and Tensile Testing of AZ31B Sheet and their Deformation Mechanisms. Presented at the 9th International Conference on Magnesium Alloys and Their Applications, Vancouver, Canada, July 8-12, 2012. PNNL-SA-85705.

Reference

Busk, R.S. and Leontis, T.E. The Pellet Metallurgy of Magnesium, *Trans AIME*, **1950**, 188, 297.

Enhanced Room-Temperature Formability in High-Strength Aluminum Alloys Through Pulse-Pressure Forming (PPF)

Principal Investigator: Richard W. Davies, Pacific Northwest National Laboratory
(509) 375-6474; fax: (509) 375-6844; e-mail: rich.davies@pnnl.gov

Principal Investigator: Aashish Rohatgi, Pacific Northwest National Laboratory
(509) 372-6047; fax: (509) 375-6448; e-mail: aashish.rohatgi@pnnl.gov

Accomplishments

- AA6022-T4E32 and AA7075-T6 were identified as the high-strength Al alloys of commercial interest. A literature survey of their formability, constitutive equations, and flow curves was performed to ascertain their amenability for formability enhancements via high-strain-rate forming. (FY 2012)
- Demonstrated greater than 70 percent increase in room-temperature formability of AA6022-T4E32 alloy through pulse-pressure forming (PPF) under conditions close to plane-strain deformation. (FY 2012)

Future Directions

- Determine the formability of AA7075 high-strength Al alloys under pulse-pressure and quasi-static forming.
- Quantify the deformation history of AA6022 and AA7075 high-strength Al alloys under PPF at room temperature and identify deformation parameters that lead to enhanced formability.
- Conduct a finite element model analysis to quantify the mass savings with the use of AA6022 and AA7075 in a candidate automotive part.
- Develop constitutive equations to describe the deformation behavior and formability of AA6022 and AA7075 under high strain-rates.

Technology Assessment

- Target: Achieve 70 percent improvement in the room-temperature formability (near plane-strain) in 6xxx and 7xxx Al alloys.
- Gap: The room-temperature formability of Al alloys (e.g. 5xxx and 6xxx) in plane strain typically does not exceed 25 percent while the high-strength 7xxx alloys have almost no formability. An improvement of 70 percent or more can help make the formability of some Al alloys be comparable to that of deep drawing quality steel that possess plane strain formability of ~45 percent. However, such formability enhancements in Al alloys are not possible without elevated temperatures due to their low strain-rate sensitivity at quasi-static rates during conventional room-temperature stamping.
- Target: Determine the strain, strain-rate, velocity, and strain-path of AA6022 and AA7075 as a function of time during PPF.

- Gap: The strain-rates during PPF of sheet metals typically exceed 1000 /s and the constitutive behavior of Al alloys can be quite different at strain-rates exceeding 1000/s, relative to their behavior at quasi-static rates. Further, PPF strain-rates can vary significantly during the course of deformation as a function of time and location on the workpiece. However, the knowledge of strain-rates and strain-path during high-rate forming is generally lacking in the literature which has hindered development of accurate and validated numerical models of high-rate forming processes.

Introduction

The goal of this project is to extend the room-temperature formability of high-strength aluminum alloys (e.g., 6xxx and 7xxx) to enable their use in structural automotive components conventionally made of steel. Such structural members are not typically fabricated in 6xxx and 7xxx Al alloys owing to the limited formability of these alloys under conventional room-temperature stamping conditions. In a prior project (Davies, 2012), PNNL has demonstrated that high-strain-rate forming (without a die) of AA5182-O Al alloy at room temperature can achieve safe strains that are ~2 times greater than those achievable under room-temperature quasi-static forming. Further, the enhancement in safe strains can be as high as ~6 times when the forming process is performed inside a die. Similar formability enhancements were envisioned in heat-treatable, high-strength 6xxx and 7xxx alloys, enabling lightweight alternatives to steel structural members in automotive applications. However, further understanding is needed of the practical forming limits in PPF processes and their dependence upon process parameters and design. This project will quantify the deformation behavior of 6xxx and 7xxx Al alloys under PPF and develop validated constitutive relations to enhance understanding of high-rate forming processes and the resulting sheet metal formability.

Approach

The work scope of this project was developed in conjunction with General Motors (GM) and Alcoa. Two Alcoa Al alloys, AA6022-T4E32 (1.2 mm) AA7075-T6 (1 mm), were identified as representative high-strength, heat-treatable Al sheet alloys that, if sufficiently formable at room temperature, are attractive candidates for automotive structural applications. The literature survey of these alloys focused on formability, constitutive equations, and flow curves. Electro-hydraulic forming (EHF) and electromagnetic forming (EMF) techniques were considered as the two candidate PPF techniques to perform high-rate forming experiments. PNNL's existing equipment configuration, previously used for AA5182-O alloy, was evaluated with respect to the use of the (relatively) higher strength AA6022 and AA7075 alloys. High-rate and quasi-static forming experiments were performed on AA6022. Post-forming safe strains were measured using the conventional strain-grid technique and the effect of strain-rate on room-temperature formability evaluated.

Results and Discussion

An initial survey of open literature found no results for high-rate forming limit diagrams of AA6022 or AA7075. Some high-rate deformation data for AA7075-T6 was reported with evidence of slight positive strain-rate sensitivity (Davis, 1993). A slight increase in plastic elongation at fracture at strain-rates >1000/s has also been reported for AA7075, although in T7351 condition (El-Magd and Abouridouane, 2006). High-rate deformation data was not found for AA6022.

PNNL's existing equipment and capabilities were leveraged and the EHF technique with a 6-in.-diameter test sheet was selected as the experimental approach to determine the high-rate forming conditions that could enhance the room-temperature formability in AA6022 and AA7075. Test specimens were designed and fabricated to achieve a state near plane strain. **Figure 17** shows an image of a typical test specimen where the elliptical cutouts were designed to create a state of near plane strain in the region between the cutouts. AA6022 specimens were tested using EHF technique (Rohatgi et al., 2012). A driver sheet made of AA5182-O was used under the test specimens to prevent the water from escaping through the elliptical holes. Boron nitride was applied as a lubricant on the contacting surfaces to minimize friction between the driver and the test sheet. **Figure 18a and b** show images of the test specimens deformed at high-rate (via EHF) and at quasi-static rate, respectively. Unlike a quasi-static

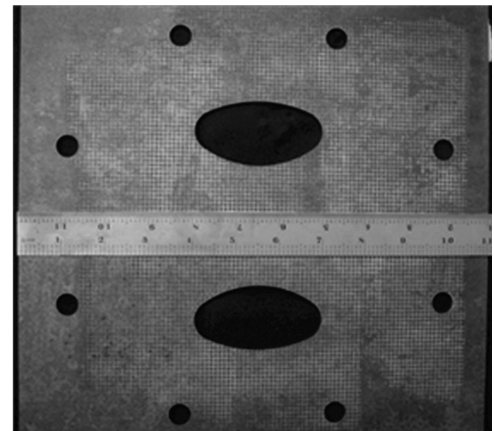


Figure 17. Image of a test specimen, designed to achieve a state near plane strain during PPF and quasi-static forming.

test that can be stopped immediately upon specimen failure, the same is not feasible in an EHF test. Hence, the two halves of the failed EHF specimen (Figure 18a) are pushed apart to a greater extent than in the quasi-statically failed specimen (Figure 18b). The post-forming safe strains around the failure region of the EHF and quasi-statically tested specimens were measured using the conventional strain-grid technique and are shown in Figure 19. These safe strains are plotted in the forming limit diagram in Figure 20. The influence of high-rate forming (open symbols) and quasi-static forming (filled symbols) on formability can be determined by comparing their respective maximum value of major strain (y-axis) at a given minor strain (x-axis). For example, at $\sim 5\%$ minor strain, the safe major strain for AA6022 increases from $\sim 23\%$ at quasi-static rate to $\sim 41\%$ at high-rate, i.e. $\sim 78\%$ increase. Such increase in formability at high strain-rates has been attributed in the literature to increased strain-rate sensitivity at these rates.

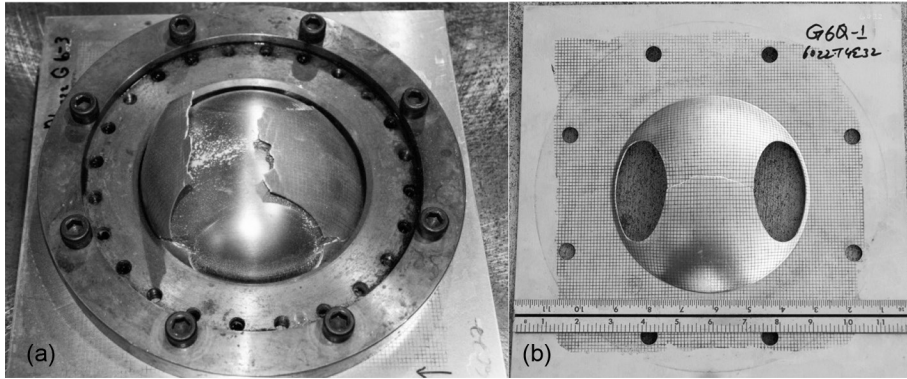


Figure 18. Images of tested AA6022 specimens. (a) EHF tested specimen showing the fractured AA6022 sheet with an underlying, intact driver sheet. (b) Quasi-statically tested specimen with failure across the specimen apex (driver sheet is not shown).

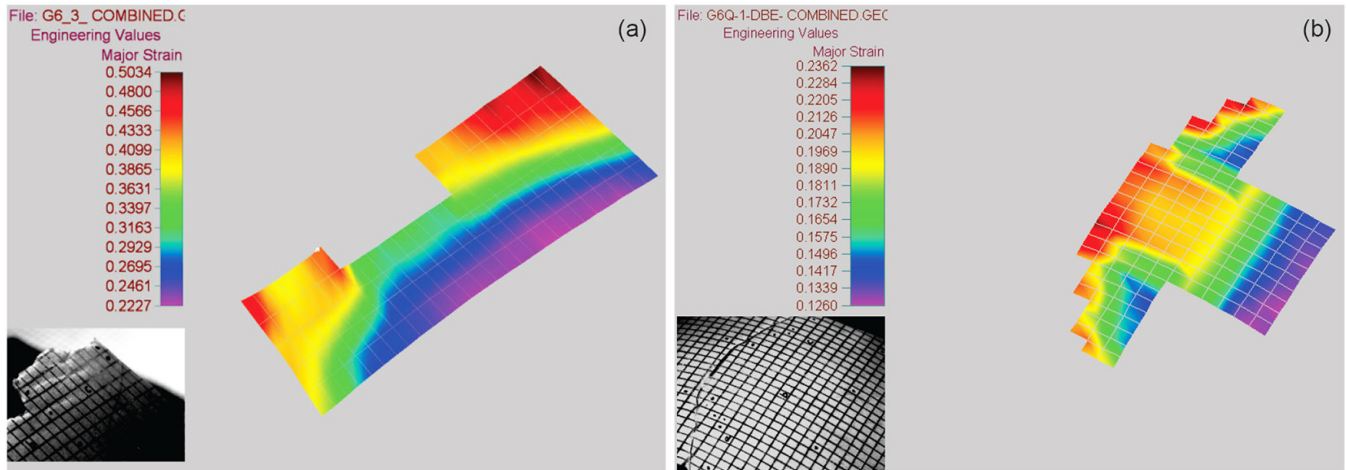


Figure 19. Strain contours of post-forming strains on (a) high-rate tested and (b) quasi-statically tested AA6022.

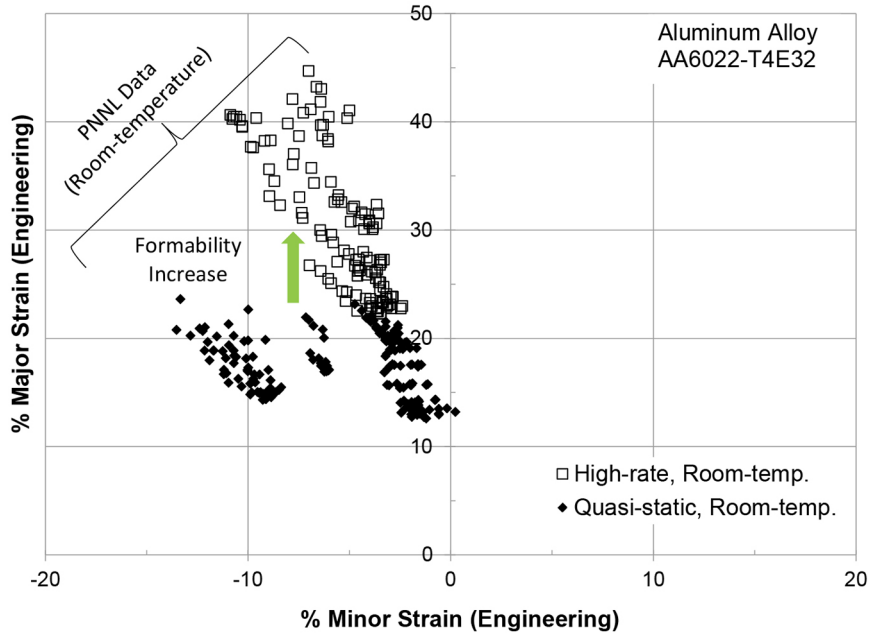


Figure 20. Quasi-static forming limit curve of AA6022-T4E32 superimposed with the safe strains (filled square symbols) obtained at high strain-rates using the EHF technique.

In FY 2013, AA7075 will be tested under PPF and quasi-static conditions to determine if it, too, leads to formability enhancements during high-rate forming. High-rate forming experiments on AA6022 and AA7075 will be performed in conjunction with PNNL's novel technique of combining high-speed imaging with digital image correlation (DIC). This testing approach will help quantify the strain, strain-rate, velocity and strain path during PPF. Finally, specimens will be formed inside a die to determine if die-forming will result in greater formability enhancement than observed in the absence of die, similar to the trend previously observed in AA5182-O.

The work in this project is significantly different from other published research on high-rate forming in that this project will provide the quantitative strain-rates and strain path that can lead to formability enhancement. Therefore, while other on-going high-rate forming research may focus on aspects such as tooling design and development etc., this research is focused on quantifying the underlying deformation conditions (strain-rate, strain path etc.) that are independent of any particular system design but whose knowledge is critical in order to achieve enhanced formability.

Technology Transfer Path

PNNL will provide the results of the formability investigation and the constitutive equations for AA6022 and AA7075 to industry to enable automakers to identify which structural component features, currently not formable via stamping, would be best candidates for high strain-rate forming. The team will also evaluate ways to deploy high-rate forming techniques for cost-effective industrial implementation.

Conclusions

While heat-treatable 6xxx and 7xxx Al alloys can be precipitation strengthened to the design strength requirements of structural members in automotive applications, their weight-saving potential has not yet been fully realized owing to their poor room-temperature formability. This project was developed to leverage the previously demonstrated success in enhancing the room-temperature formability of Al alloys through EHF technique and investigate if similar success could be obtained in 6xxx and 7xxx alloys.

Building upon the prior results from a non-heat-treatable Al alloy (AA5182), this work extends the scope of high-rate forming research to heat-treatable high-strength 6xxx and 7xxx Al alloys. 6022-T4E32 and 7075-T6 were selected as the candidate Al alloys and the EHF technique was selected to demonstrate enhanced room-temperature formability.

EHF experiments on AA6022 were conducted and preliminary results have shown enhanced formability relative to the strains achievable by quasi-static forming. These results mirror formability enhancements previously obtained in non-heat-treatable AA5182 alloy and suggest that further formability enhancements may be possible by forming AA6022 inside the die (as observed in the case of AA5182).

Presentations/Publications/Patents

Davies, R.W., Rohatgi, A., Stephens, E.V., Soulami, A., Smith, M.T. and Vanarsdale, G. Constitutive relations and formability of aluminum AA5182 alloy during pulse pressure forming at high strain rates. Presented at the International Symposium on Plasticity and its Current Applications (Plasticity 2012), January 3-8, 2012, San Juan, Puerto Rico, USA.

Rohatgi, A., Stephens, E.V., Edwards, D.J., Smith, M.T., Davies, R.W., Soulami, A. and Vanarsdale, G. Pulse-pressure forming (PPF) of light-weight metals. Presented at the ASME-MSEC 2012, June 4-8, 2012, Notre Dame, IN, USA.

Davies, R.W. Pulse-Pressure Forming (PPF) of Lightweight Materials. Presented at the 2012 U.S. Department of Energy Vehicle Technologies Program Annual Merit Review and Peer Evaluation Meeting, May 13-17, Arlington, VA, USA.

Rohatgi, A., Stephens, E.V., Davies, R.W., Smith, M.T. and Soulami, A. Electro-hydraulic forming of sheet metals: Free-forming vs. conical-die forming. *J. Mater. Process. Technol.* **2012**, 212, 1070-1079.

Rohatgi, A., Stephens, E.V., Edwards, D.J., Smith, M.T. and Davies, R.W. Electro-hydraulic forming of advanced high-strength steels: Deformation and microstructural characterization. In *Proc. ASME-MSEC 2012*, Paper no. 7322, June 4-8, 2012, Notre Dame, IN, USA.

References

Davies, R. W. Pulse Pressure Forming of Lightweight Materials, In *2011 Annual Progress Report: Lightweighting Materials*. U.S. Department of Energy: Washington, D.C., 2012, pp. 2-24–2-27.

Davis, J. R. *ASM Specialty Handbook-Aluminum and Aluminum Alloys*, Davis, J. R., Ed., ASM International: Ohio, USA, **1993**, p. 697.

El-Magd, E.; Abouridouane, M. Characterization, modelling and simulation of deformation and fracture behaviour of the light-weight wrought alloys under high strain rate loading. *International Journal of Impact Engineering*, **2006**, 32, 741-758.

Rohatgi, A., Stephens, E.V., Davies, R.W., Smith, M.T. and Soulami, A. Electro-hydraulic forming of sheet metals: Free-forming vs. conical-die forming. *J. Mater. Process. Technol.* **2012**, 212, 1070-1079.

Aluminum Formability Extension Through Superior Blanking Process

Principal Investigators: Xin Sun and Richard W. Davies, Pacific Northwest National Laboratory
(509) 372-6489; fax: (509) 372-6099; e-mail: xin.sun@pnnl.gov
(509) 375-6474; fax: (509) 375-4448; e-mail: rich.davies@pnnl.gov

Principal Investigator: Sergey Golovashchenko, Ford Motor Company
(313) 337-3738; fax: (313)390-0514; e-mail: sgolovas@ford.com

Accomplishments

- Performed new blanking experiments of AA6111-T4 aluminum sheets with different clearances. The influences of tool stiffness were studied.
- Performed uniaxial tension stretchability experiments with sheared samples.

- Performed two-dimensional (2D) plane strain simulations for traditional and superior blanking techniques on aluminum AA6111-T4 sheet alloys. The simulations showed similar results with experimental measurements in burr geometry, burr height evolution, and mechanism of sliver formation.
- Performed preliminary stretching simulations based on three-dimension (3D) models with both schematic and actual predicted shearing-edge geometry and initial plastic strain (IPS) distribution to investigate the separate and combined effects of shearing-edge geometry and IPS on ductility.

Future Directions

- Base material testing to measure effects of pressure on failure strain for model inputs.
- Further controlled experiments of traditional and superior blanking processes with quantitative cross section measurements for model validation.
- Accurate determination of the damage parameters for more quantitative blanking and subsequent stretchability simulations.
- Accurate determination of the plastic behavior at large strains by DIC for more precise blanking and stretchability simulations.
- Blanking simulations incorporating machine characteristics (i.e., support stiffness, damping, and cutting rate).
- More controlled stretchability experiments with various edge conditions for model validation.
- Stretchability simulations with sheared edge damage parameters predicted from the validated blanking simulations at large strains.
- Hole punching and hole expansion tests with various clearance.
- Simulations of hole expansions with different punched hole edge conditions.

Technology Assessment

- Target: Achieve 90 percent accuracy of the blanking simulations with experiments in terms of cut edge geometry.
- Gap: The simulations results of cut edge geometry are very close to experimental observations. For more precise prediction, more accurate damage parameters and plastic model at large strains are necessary.
- Target: Achieve 90 percent accuracy of the stretchability simulations with experiments in terms of the elongation to fracture.
- Gap: The current preliminary uniaxial tension stretchability study show similar trend with experiments on the influence of cutting clearance on stretchability. Again, quantitative comparison necessitates the use of accurate damage parameters and plastic model at large strains.

Introduction

The automotive OEMs and their Tier 1 suppliers have an extraordinarily high capital investment in sheet metal forming facilities, equipment, and associated infrastructure. The ability to redirect these capital-intensive facilities from steel to aluminum component manufacturing would dramatically increase the wide-spread commercialization of aluminum sheet in vehicles. This project aims to enhance the overall formability of aluminum using the existing OEM capital infrastructure by developing enhanced processes for the blanking, piercing, and trimming operations to extend aluminum formability in the subsequent forming operations. The formability of the aluminum sheet in conventional automotive stamping is typically limited by the processes that prepare the blank for the stamping operation (i.e., blanking, piercing, and trimming). The overall formability and subsequent quality of a part is often limited by the height of burrs on a sheared surface, the microstructural damage imparted on the sheet, and the dimensional accuracy and absence of splitting (Golovashchenko, 2006; Golovashchenko, 2008).

Approach

This project will further develop and mature a superior blanking process to enhance the room-temperature formability of aluminum sheets with improvements on existing trimming infrastructures. The proposed approach is based on a new trimming method (Golovashchenko, 2006; Golovashchenko, 2008; Ilinich and Golovashchenko, 2011) with various mechanisms of scrap/offal support and extensions of the technology using other new and unique techniques. The goal of this work is to use a combined experimental and numerical approach to develop processing windows and parameters for preparation of stamping blanks that achieve robust, extended ductility compared to conventionally trimmed blanks. Our activities in FY 2012 focused on developing the experimental validated modeling framework for accelerating the development and subsequent implementation of the superior blanking process.

Results and Discussion

First, experimental studies were carried out to determine the influence of trimming parameters on the quality of sheared surface and its ability to stretch during the subsequent flanging, hemming operations, and drawing of sheet metal work pieces. The influence of blanking clearance and blanking tool stiffness on trimming quality of production panels made by AA6111-T4 sheet alloys were examined. After the blanking experiments, half dog-bone samples were machined from the blanked sheet for tensile stretchability experiments. The dog-bone side of the sample was machined to avoid fracture and the straight side was designated to bear the properties of the different sheared edges.

On the modeling side, blanking process simulations were first performed with 2D plane strain FE models (with ABAQUS/Explicit) on AA6111-T4 sheet alloys to examine the effects of various blanking parameters on the sheared edge geometry and the resulting damage parameters (see Figure 21). Three-section Swift/Holoman fitting of an experimental uniaxial tension stress-strain curve was used to extrapolate the material plastic behavior at large strains, while the blanking tools (i.e., upper and lower trimming tools, clamping pad and the scrap support) are assumed to be rigid. The Rice-Tracy damage model was used for the simulation with damage parameters estimated from experimental measurements of grain aspect ratio near the fracture surface. Fine meshes were used at the sheared zone (Figure 21c) with adaptive meshing and adaptive contact technique implemented between the sharp corners of the trimming tools and the blank to avoid interpenetration in the later stage of the shearing process.

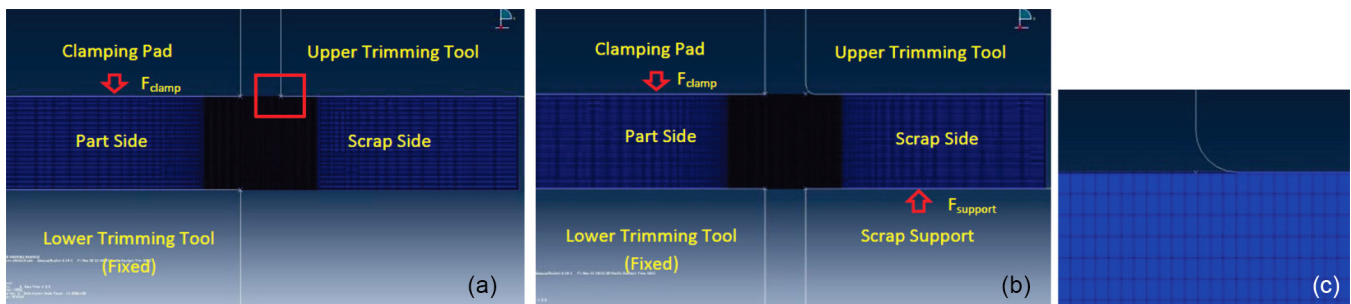


Figure 21. FE models for the traditional (a) and advanced (b) trimming processes where the middle section of the blank has much finer meshes (c).

Figure 22 compares the predicted sheared edge geometry with different clearance (top row) to experimental measurements for traditional trimming processes (bottom row). The comparison between simulation and experimental results shows that the general trends are the same in that the burr sizes increase with the blanking clearances. The burr size and shapes correspond well with experimental observations for clearances of 32 and 43 percent, while the results of 21 and 10 percent clearances correspond better to the experimental results of 10 and 2 percent. Note that tool stiffness can play an important role at small clearances where the preset clearance can vary and fluctuate during the blanking process.

Next, the advanced blanking process was simulated with different clearance. Figure 23 compares the predicted (top row) and measured (bottom row) part and scrap geometry. As observed by Golovashchenko et al. (2006), the deformation is symmetric if the upper and lower trimming tools have similar corner fillet radius and there are equal chances of separation of the scrap and part sides from the corner near the bottom trimming tool or from the corner near the top trimming tool. With the introduction of a dull upper trimming tool, the local strain at the corner of lower trimming tool is much higher. The high

strain localization leads to fracture initiation from this location and effectively transfers the burr region from the part side to the scrap side. Predicted results show that this experimental observation has been well captured by the FE simulations. Both the experiments and simulations have shown that the fracture surface becomes more tilted from the vertical direction with increasing clearance up to 32 percent and then become smaller after the clearance is 43 percent. The tilt angle is similar for the clearances of 43 and 60 percent.

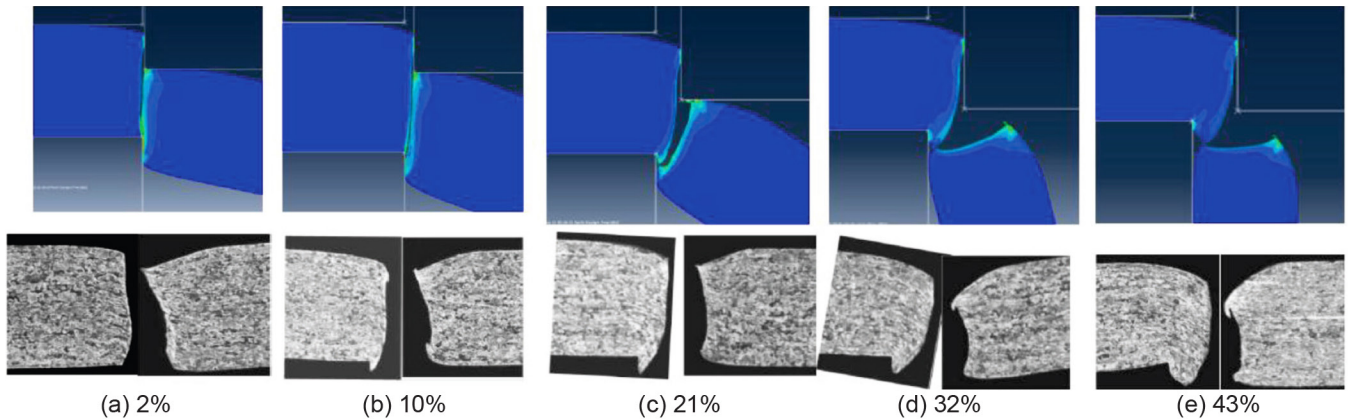


Figure 22. The sheared edges on the part and scrap side predicted by FE simulations (top row) and the corresponding experimental observations (bottom row) under various cutting clearances for traditional trimming process.

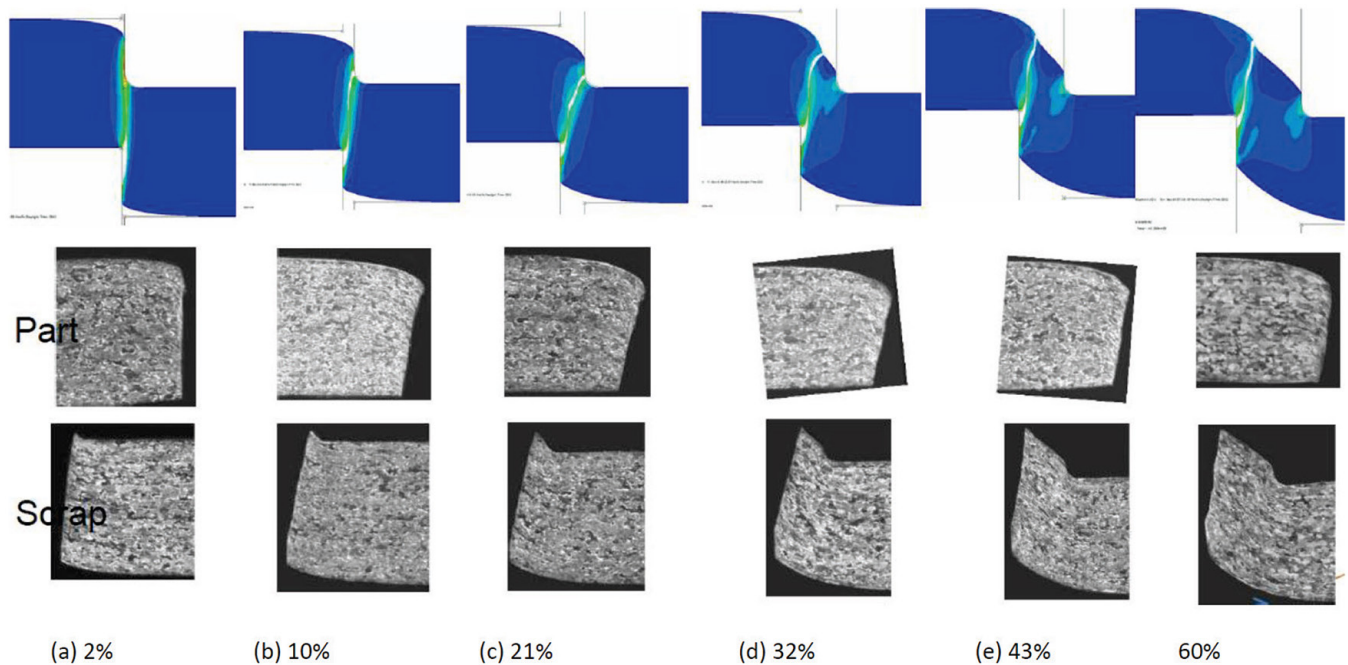


Figure 23. The sheared edges on the part and scrap side predicted by FE simulations (top row) and the corresponding experimental observations (bottom row) under various cutting clearances and scrap support.

In summary, the current FE simulations for both traditional and advanced trimming simulations have well captured the mechanisms of crack initiation, burr and sliver formation, and fracture surface shapes and their evolution.

The results of recent uniaxial tension stretchability experiments with sheared samples are consistent with those reported by Golovaschenko et al. (2008). Three major failure modes were observed depending upon the trimming conditions. For samples with no cutting damage or small clearance blanking, the sample tended to fail along a localized necking band slanted relative to the loading direction (Figure 24a). For samples with large blanking clearance, cracking started at the cut edge and propagated across the sample width (Figure 24b). For samples with intermediate clearances, the failure modes were a mixed mode between the two (Figure 24c).

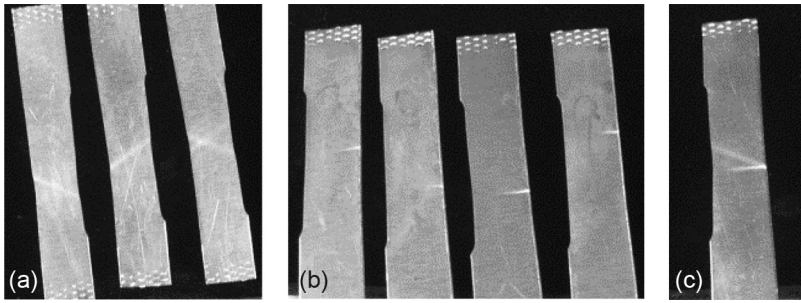


Figure 24. Tensile samples of sheared aluminum sheet 6111-T4 and typical failure modes: (a) Mode 1 – small cutting clearance, (b) Mode 2 – large cutting clearance, (c) Mixed mode 1-2 – intermediate cutting clearance.

Preliminary stretching simulations with 3D FE models have been performed with different sheared edge geometries and initial damage levels to investigate the effects of edge geometry and IPS on the overall predicted sample ductility. The various 3D models were generated by simply shearing different number of layers of elements near the edge, which schematically represent different shearing-edge geometries induced by different shearing gaps between die and punch. IPS was also considered in the sheared-layers of elements such that the magnitude of IPS linearly decreases from a high value (for example, 0.6) down to zero as the distance from the edge increases. 3D uniaxial tension models of the blanked sample have also been developed with the actual predicted edge geometry and equivalent strain field mapped. For example, the 3D FE models for the half dog-bone tensile samples with and without cutting-induced burr geometry are illustrated in Figure 25a and b.

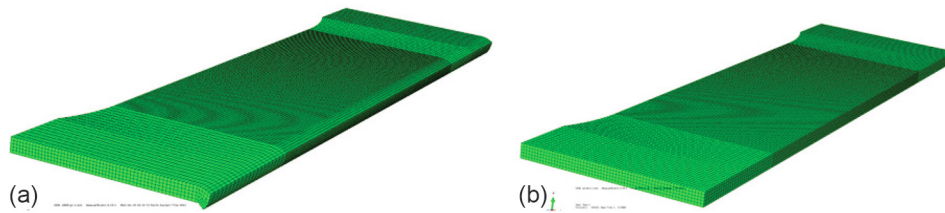


Figure 25. 3D half dog-bone models with (a) initial burr geometry and (b) perfect edge.

Figure 26 shows the predicted stress-strain curves from the preliminary stretching simulations for different edge geometries with the considerations of IPS. Note that the curves in this figure are calculated based on the force-displacement curve of the sample obtained from ABAQUS/Explicit simulation. As shown in Figure 6, different levels of IPS near the shearing edge, combined with edge geometry, result in different ductility and predicted failure modes for different sheared edge conditions. This is consistent with the experimental observations presented in Figure 24. Separate effects from the edge geometry and IPS are slated for examination using simulations and experimental methods to determine a dominant factor on the ductility of sheared samples.

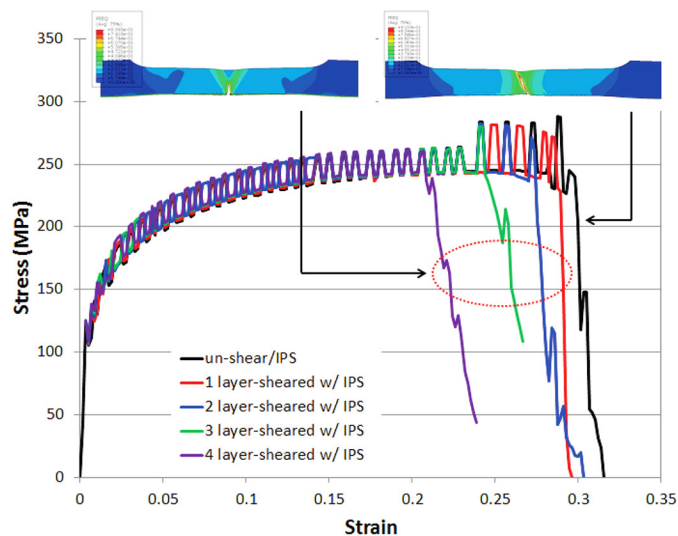


Figure 26. Predicted stress-strain curves and failure modes for different sheared edge conditions.

Technology Transfer Path

The technology transfer of this project will be directly through Ford Motor Company and its Tier 1 suppliers. The broader commercialization of the technology through the Tier 1 suppliers will reach the entire automotive OEM industry.

Conclusions

In FY 2012, this project focused on the development of the validated modeling framework for shearing and the subsequent stretching operations. The 2D plane strain simulations for the traditional blanking process indicated that cracking initiates at the blank near the corner of upper trimming tool at a location outside the fillet radius where the blank tends to lose contact with the tool and experiences positive triaxiality. The predicted burr sizes increase with increased blanking clearances. The simulations for the advanced blanking process with scrap support and dull upper trimming tool have shown that the crack initiation location shifts to the sharp corner of the lower trimming tool. This leads to the formation of burrs on the scrap side and therefore results in much better edge quality on the part side. All simulation conclusions are consistent with experimental cutting observations.

Preliminary stretching simulations were also performed. IPS (i.e., damage, near the shearing edge of the sample) may have a dominant effect on the resulting ductility. The results of the new blanking experiments and tensile stretchability are similar to those reported by Golovashchenko et al. (2006) in terms of influences of cutting clearances on cutting edge geometry and the failure model and elongation in the tension tests.

Future activities include additional experimental characterizations on modeling parameters and model validation. In addition, hole punching with various clearances and subsequent hole expansion experiments and simulations are planned for FY 2013.

References

1. Golovashchenko, S. F. Quality of Trimming and Its Effect on Stretch Flanging of Automotive Panels. *Journal of Materials Engineering and Performance*, **2008**, 17(3), 316–325.
2. Golovashchenko, S. F. A Study on Trimming of Aluminum Autobody Sheet and Development of a New Robust Process Eliminating Burrs and Slivers. *International Journal of Mechanical Sciences*, **2006**, 48, 1384–1400.
3. Ilinich A.; Golovashchenko, S.F.; Smith L.M. *Journal of Materials Processing Technology*, **2011**, 211, 441–449.

C. Industrial Scale-Up Of Low-Cost Zero-Emissions Magnesium By Electrolysis: Metal Oxygen Separation Technologies (MOxST)

Principle Investigator: Adam C. Powell, IV
Metal Oxygen Separation Technologies (MOxST)
11 Michigan Dr., Natick, MA 01760
(781) 395-3190; fax (617) 963-7207; e-mail: apowell@moxst.com

Technology Area Development Manager: William Joost
U.S. Department of Energy
1000 Independence Ave., S.W., Washington, DC 20585
(202) 287-6020; fax: (202) 856-2476; e-mail: william.joost@ee.doe.gov

Contractor: Metal Oxygen Separation Technologies (MOxST)
Contract #: DE-EE0005547

Executive Summary

Direct electrolysis of magnesium oxide (MgO) has been a dream of the magnesium industry for decades. It is straightforward to make MgO from brines or sea water by reaction of dissolved MgCl_2 with NaOH producing NaCl and insoluble $\text{Mg}(\text{OH})_2$ which is removable by filtration. Heating the hydroxide then drives off its water to produce MgO. Today's chloride electrolysis plants must then use carbochlorination or chloride dehydration to produce pure MgCl_2 , and electrolyze that to produce Mg metal and Cl_2 gas. Direct MgO electrolysis would save this carbochlorination step, which is energy and capital intensive and can produce harmful dioxin and furan emissions. MgO electrolysis would also eliminate the need to carefully contain chlorine which often escapes as a pollutant, and would potentially use less energy due to the lower enthalpy of formation of MgO vs. MgCl_2 .

The MOxST MagGen™ system performs this direct MgO electrolysis. This process dissolves MgO in a molten salt, then applies a direct current potential across the salt, producing magnesium vapor at the cathode and oxygen gas at the zirconia-sheathed anode. The zirconia acts as a solid electrolyte which separates the magnesium and oxygen products, preventing back-reaction between them. It also protects the anode from the harsh molten salt environment, enabling the use of a variety of inert anode materials. And zirconia is very selective, such that the oxygen by-product is much more pure than that produced by conventional inert anodes without zirconia protection, such as nickel ferrite.

The overarching objective of this project is to bring MOxST's MagGen™ primary magnesium production system from large laboratory demonstration today to the threshold of plant construction. This efficient zero-emissions process makes high-purity magnesium directly from abundant domestically-produced industrial magnesia in a single step, with a high-purity oxygen by-product, and with condenser heat available for other uses.

Success of this project will prepare the technology for industrial implementation of this process, reducing the costs, energy use, and emissions associated with magnesium production, and helping vehicle manufacturers to realize their goals of reduced weight and increased vehicle efficiency. It may also improve vehicle recyclability by increasing the value of post-consumer automotive scrap metal.

Toward those ends, this project's tasks during this period were as follows:

1. Project Management and Reporting
2. Design, Build and Test Alpha Prototype This is a fully-featured prototype designed to demonstrate all aspects of the process with a focus on maximum possible run time

3. Anode Optimization Optimize zirconia tube composition and structure for this novel application, and develop other components including low-cost charge transfer material and current collector.
4. Electrolysis Cell Cost, Energy, and Emissions Modeling Characterize these aspects of the process relative to current practices in automotive materials and magnesium competitors
5. Test Magnesium Product Composition Understand the source and disposition of impurities in the system to meet the requirements of automotive components
6. Full Production Scale Magnesium Plant Preliminary Design Scope out requirements and begin site review for a potential magnesium production plant using this technology

Accomplishments

- Designed, built, and tested full alpha prototype; focused on uptime metrics. Integrated components from raw material feeding, electrolysis, condensing, and product ingot casting. (FY2012)
- Ran the longest electrolysis experiment to date, 140 hours, with sustained tube integrity; set benchmark for increasing tube life. (FY2012)
- Modeled and measured impurity gases from argon exiting the electrolysis cell and determined excellent feasibility for future argon recycling. (FY2012)
- Conducted first demonstration of the continuous liquid-phase magnesium condenser. (FY2012)
- Fabricated first in-house ceramic anode tubes, which achieved over 99% theoretical zirconia density, a marked improvement over off-the-shelf tubes. (FY2012)
- Performed extensive multi-physics modeling on system components including the anode current collector assembly, molten salts in the electrolysis cell, and condenser system components. (FY2012)
- Modeled and calculated annual energy savings from magnesium production at 84-340 TBTU, reducing industrial emissions by 4.3-45 MMT CO₂e, depending on elasticity of magnesium demand. (FY2012)
- Designed and fabricated an oxygen-generating current collector with very low resistance at target temperature with no measurable increase in resistance for duration of experiment. (FY2012)
- Fabricated 11 small-scale electrolysis cells for anode testing. (FY2012)
- Produced magnesium by electrolysis with 99.97% product purity; identified methods to reduce purities even more by regulating current density. (FY2012)
- Submitted one provisional and three full patent applications. (FY2012)
- Visited four potential brown field sites for a magnesium plant, two of which have sufficient power allocation, and three of which have rail lines. (FY2012)

Future Directions

- Continue safety tests of the alpha prototype and make magnesium metal for tensile testing and part fabrication.
- Design and build an energy-efficient beta prototype with much larger capacity than the alpha and all required process features for a full-scale unit.
- Build a salt recycler capable of meeting prototype testing needs.
- Finalize the design of anode assemblies and prepare to manufacture sufficient numbers to meet prototype testing needs.
- Prepare an economic model of a full plant including transportation and utilities; select candidate plant sites and develop a site plan.

Technology Assessment

- Target: Alpha prototype to achieve 50% of industry standard uptime.
- Gap: Traditional material handling is not suited for raw material feed in this application.
- Gap: Novel application requires new online maintenance procedures.
- Target: Beta prototype to achieve 20% increase in uptime over the FY2012 performance of the alpha prototype.
- Gap: Systems integration poses compatibility and scale-up challenges.
- Target: Choose and test final salt recycling unit operations.
- Gap: Application may not produce sufficient waste material to recycle.
- Target: Down-select final methods for producing anode assembly components.
- Gap: Testing anode assemblies requires significant alpha/beta prototype access.

Introduction

The objective of this project is to bring MOxST's MagGen™ (Figure 1) primary magnesium production system from large laboratory demonstration to the threshold of plant construction. This zero-emissions, energy-efficient process makes high-purity magnesium from domestic industrial magnesia in a single step. By-products include high-purity oxygen and condenser heat, both available for other uses.

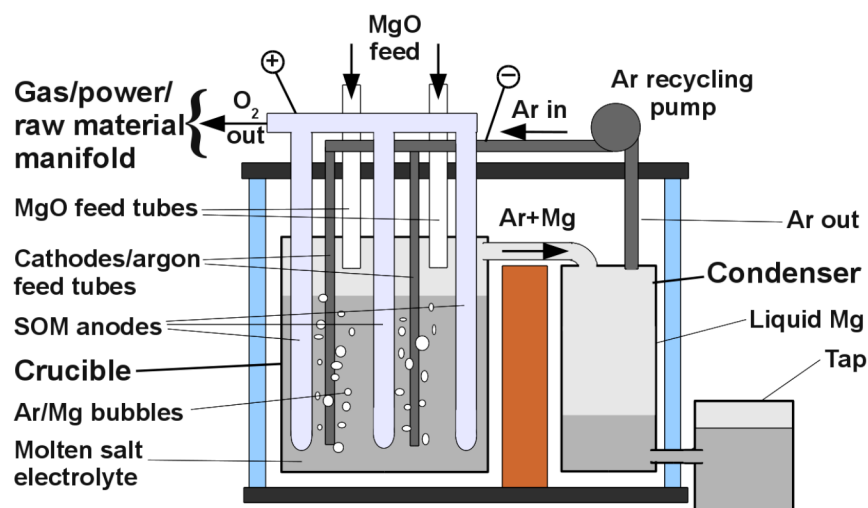


Figure 1. MOxST's Primary Magnesium Production System, MagGen™

Approach

The alpha prototype is designed to run for as long as possible. The goal is to identify and ameliorate as many failure modes as possible at a small scale, then apply those lessons to future prototypes in order to maximize uptime at full production scale. The main system components to refine include the raw material feeder, current collector assembly, crucible, condenser, and ingot caster. The alpha will produce magnesium metal for tensile testing and part die-casting. The beta prototype will have three to six times the capacity of the alpha, with all required process features for a full-scale unit.

Results and Discussion

The full alpha prototype is focused on maximizing uptime by improving component design. MOxST has made significant improvements to the magnesia feeder, current collector assembly, and condenser.

The MOxST raw material feeder delivers MgO into the crucible at a controlled rate. We have demonstrated that the feeder in use can operate at rates suitable for the beta prototype at very high current, and have run it intermittently to meet the needs of the alpha prototype.

At the start of this project, there was no clear path to a current collector capable of carrying the very high 100-500 A current of each anode at high temperature in oxygen for longer than a few hours. MOxST now has a patent-pending low-resistance current collector assembly proven in experiments to have no discernible degradation or resistance change. We will soon conduct long-term testing of this assembly.

MOxST has developed and demonstrated a new patent-pending two-stage magnesium condenser which produces liquid magnesium from the argon-diluted magnesium vapor coming from the crucible. This is a challenge because of the limitation on magnesium partial pressure in the crucible imposed by chemical compatibility with the zirconia tubes, and the 3 torr vapor pressure at its melting point – one of the highest melting point vapor pressures of all metals.

Additionally, MOxST has begun making high-quality zirconia tubes for the current collector assembly in order to increase tube lifetime and ultimately magnesium manufacturing uptime. MOxST quickly succeeded in producing tubes with better density and fewer defects than the best off-the-shelf tubes. Making our own tubes allows us the flexibility to change compositions and processing methods and measure their effects on long-term robustness with complete understanding of all stages of the process.

We have also gained tremendous new insights on interactions between molten salts, reactive metals, and zirconia ceramics. This led to achievement of highest current efficiency to date, with the best zirconia robustness ever observed in an electrolysis experiment.

The alpha prototype has produced magnesium with 99.97% product purity, and current controls are predicted to produce even higher purity levels. Furthermore, modeling and experimentation has demonstrated excellent feasibility for recycling argon gases exiting the electrolysis cell.

Finally, our modeling results indicate that the annual energy savings from magnesium production using the MOxST MagGen process range 84-340 TBTU when compared to conventional production techniques, reducing industrial emissions by 4.3-45 MMT CO₂e, depending on elasticity of magnesium demand. We calculated industrial energy/emissions based on:

- 735 kJ/mol MgO (8.41 kWh/kg) reduction enthalpy to Mg vapor and oxygen gas
- 1.84 kWh/kg heat and electrical losses through leads (Total heat and resistance loss based on Wiedmann-Franz law)
- 2.75 kWh/kg thermal loss through gases and vessel walls (conservative estimate approximately double the 1.86 in the figure of our report to DOE)
- Assuming no recovery of condenser waste heat, total is $8.41 + 1.84 + 3.75 = 14$ kWh/kg for MOxST
- 70% Mg is recycled at 3.3 kWh/kg (MOxST, 2012)
- 155 kg/vehicle new magnesium (plus 5 kg/vehicle existing magnesium) replacing 59 kg/vehicle Al and 227 kg/vehicle steel, 131 kg/vehicle weight reduction (U.S. Automotive Materials Partnership, 2006)
- 64 kWh/kg magnesium production energy use today [50% chloride electrolysis 43.6 kWh/kg, 50% Pidgeon 102 kWh/kg (Das, 2011)]
- 24 kWh/kg aluminum production energy use (BCS, 2007)
- 9.5 kWh/kg steel production energy use (Stubbles, 2000)
- 12 million vehicle sales/year in North America

- 0.688 kg CO₂ emissions per kWh electricity (U.S. electric power average [10])
- Low elasticity compares today's magnesium production with that of MOxST
- High elasticity compares MOxST magnesium production energy with that of the steel and aluminum it replaces.

Technology Transfer Path

During the course of this project, the technology will move from laboratory scale to prototype production systems. These prototype systems will be located at plants and/or customer sites to log sufficient uptime to demonstrate financially viable commercial production.

Additionally, we will continue to collaborate with program partners to discuss implementing our technology and other advances, such as new sheet rolling and other technologies. Working with die casters and other parts suppliers, we will define future expectations and have deals in place when metal production ramps up.

Conclusions

MOxST has met targets on all tasks and has overcome significant technical hurdles. Component design of the alpha prototype has steadily improved, resulting in longer system uptime, higher current efficiency, and much lower zirconia degradation in this process than before. We have solved or are solving some of the biggest challenges at the alpha prototype scale, and are preparing to implement those solutions in our much larger beta prototype. And we are making great strides toward production of zirconia tubes optimized for this application, which will likely lead to even longer tube life and system uptime.

Though scale-up challenges remain, MOxST is well on its way to realizing the project's goal of scaling up the MagGen™ magnesium primary production system, and the vision of low-cost zero-emissions magnesium production.

Presentations/Publications/Patents

Soobhankar, P. Scaling Up Solid Oxide Membrane Electrolysis Technology for Magnesium Production. *TMS Annual Meeting*, March 12, 2012.

Powell, A. C. Multi-Physics Modeling of Molten Salt Transport in Solid Oxide Membrane (SOM) Electrolysis and Recycling of Magnesium. *TMS Annual Meeting*, March 12, 2012.

Powell, A. C. Zirconia Solid Electrolyte Application to Metal Production and Recycling: Theory and Practice. *Seventh Annual MIT-University of Tokyo Reactive Metal Workshop*, March 16, 2012.

Powell, A. C.; Strauss, J. P. Primary Production and Molten Salt-Assisted Recycling of Metals with Inert Gas Purification. U.S. Provisional Patent Application 61/646,343 filed May 13, 2012.

Powell, A. C. SBIR Phase II: Low-Cost Low-Impact Magnesium Production by Solid Oxide Membrane Electrolysis. Poster presented at *NSF SBIR Grantees Workshop*, May 6-9, 2012.

Derezinski, S. J.; Spiridigliozzi, L. Scale-Up of Magnesium Production by Fully Stabilized Zirconia Electrolysis. *DOE Annual Merit Review*, May 17, 2012.

Powell, A. C. Zero-Emissions Energy-Efficient Magnesium Primary Production and Recycling Technologies at MOxST. International Magnesium Association: *Proc. 69th Annual World Magnesium Conference*, May 22, 2012.

Powell, A. C.; Soobhankar, P.; Derezinski, S. J.; Lau, G.; Pal, U.; Guan, X.; Gopalan, S. Conductor of High Electrical Current at High Temperature in Oxygen and Liquid Metal Environment. U.S. Non-Provisional Patent Application 11/600,761 filed August 31, 2012.

References

BCS. *U.S. Energy Requirements for Aluminum Production: Historical Perspective, Theoretical Limits and Current Practices*. BCS: Washington, DC, 2007.

Das, S. Technical Cost Modeling: Life Cycle Analysis Basis for Program Focus. Presented at the 2011 DOE/EE Vehicle Technologies Program Annual Merit Review, **2011**.

http://www1.eere.energy.gov/vehiclesandfuels/pdfs/merit_review_2011/lightweight_materials/lm001_das_2011_o.pdf

MOxST. *Efficient One-Step Electrolytic Recycling of Low-Grade and Post-Consumer Magnesium Scrap*. DOE DE-EE0003454 Final Report. **2012**. <http://www.osti.gov/bridge/purl.cover.jsp?purl=/1046980/1046980.pdf>

Stubbles, J. *Energy Use in the U.S. Steel Industry: An Historical Perspective and Future Opportunities*. Energetics: Washington, DC, 2000.

U.S. Automotive Materials Partnership. *Magnesium Vision 2020: A North American Automotive Strategic Vision for Magnesium*. **2006**. http://www.uscar.org/commands/files_download.php?files_id=240.

D. Modeling and Computational Materials Science — Oak Ridge National Laboratory

Field Technical Monitor: C. David Warren
Oak Ridge National Laboratory
1 Bethel Valley Road, Oak Ridge, TN 37831
(865) 574-9693; fax: (865)574-6098; e-mail: warrencd@ornl.gov

Principal Investigator: Nagraj Kulkarni
Oak Ridge National Laboratory
1 Bethel Valley Road, Oak Ridge, TN 37831
(865) 576-0592; fax: (865) 576-2813; e-mail: kulkarnins@ornl.gov

Industrial Partner: U.S. Automotive Materials Partnership Integrated Computational Materials Engineering Team, Magnesium Electron North America

Collaborators: Bruce Warmack, Balasubramaniam Radhakrishnan, ORNL; Jerry Hunter, Virginia Tech; Yongho Sohn, Kevin Coffey, University of Central Florida; Graeme Murch, Irina Belova, University of Newcastle, Australia

Technology Area Development Manager: William Joost
U.S. Department of Energy
1000 Independence Ave., S.W.; Washington, DC 20585
(202) 287-6020; fax: (202) 856-2476; e-mail: william.joost@ee.doe.gov

Contractor: Oak Ridge National Laboratory
Contract No.: DE-AC05-00OR22725

Executive Summary

Typical Mg alloys are brittle during vehicle crash events and difficult to form without elevated-temperature processing. While several current efforts are aimed at understanding the crashworthiness and formability of current alloys, the long-term solution is to develop new, more ductile alloys. A key component to new alloy development is to have a comprehensive understanding of the diffusion of elements within the alloy. This project is aimed at developing that understanding.

Accomplishments

- Obtained Mg tracer diffusivities in polycrystalline Mg-Al-Zn (MAZ, Mg-aluminum-zinc) alloy samples over a broad temperature range using our secondary ion mass spectrometry (SIMS) –based thin-film stable-isotope technique, thus extending previous Mg self-diffusion measurements to Mg tracer diffusion measurements in alloys.
- Established a technique for Zn tracer diffusion studies in Mg alloys and verified Zn impurity diffusion in pure Mg using the SIMS-based thin-film stable isotope technique.
- Modeled effective diffusion in polycrystalline magnesium using a Monte Carlo technique to include orientation-dependent volume diffusivities and grain boundary (GB) diffusivities.
- Obtained interdiffusion coefficients using incremental diffusion couples in the Mg-Al-Zn system.
- Developed a new theoretical approach for isotopic interdiffusion analysis involving diffusion couples with end-members having varying isotopic abundances.

- Modeled GB diffusion analytically and designed GB diffusion experiments using the SIMS-based stable isotope technique for experiments using small-grained (<1 μm) Mg thin films.
- Established a diffusion website to facilitate interaction and data sharing/analysis among our collaborators, and another website to share results with the general public.

Future Directions

- This project is expected to end in FY 2012, although more diffusion experiments and analysis in Mg-alloy systems remain to be done.

Technology Assessment

- Target: Enable rapid development of new Mg alloys using an integrated computational materials engineering (ICME) approach by providing critical diffusion data.
- Gap: Little diffusion data for Mg alloys exists that can be used to construct a diffusion database. It is essential to have tracer diffusion data as the foundation of robust diffusion databases because such data are based on accurate diffusion measurements in homogeneous alloys and are independent of thermodynamics.
- Gap: Elements such as Al that are important constituents of Mg alloys are monoisotopic. Hence there are no enriched stable isotopes of these elements that can be used in our approach. Additionally, the radioactive isotope for Al is not available at the present time. Diffusion couple studies in Mg alloys containing Al can fill this gap. Additionally, analysis of thin-film diffusion couple experiments involving varying abundances of enriched isotopes in the initial end-member compositions can provide tracer diffusion data using a new formalism developed during the course of this project.
- Gap: There exists very little information on GB diffusion in Mg alloys. The team is developing a SIMS technique for such studies using Mg alloy thin films of controlled grain sizes.

Introduction

The objective of this project is to experimentally determine the fundamental isotopic (tracer) diffusion coefficients in Mg alloys in order to create a diffusion database, and provide this database to participants involved in various tasks in the Mg ICME program.

Approach

The approach for measuring the tracer diffusion coefficient is based on the thin-film method (Shewmon, 1989). The procedure requires the preparation of homogeneous single-phase alloy samples followed by deposition of stable isotopes or radioisotopes of these elements in the form of thin films on the sample surfaces. After diffusion annealing at various temperatures below the melting temperatures of these alloy samples, the isotopic diffusion depth profiles in these samples are measured using SIMS. Analysis of the diffusion depth profile data using the thin-film solution (Shewmon et al., 1954) provides the tracer diffusivity for the selected sample composition at the annealing temperature. By repeating such measurements at different compositions and temperatures, tracer diffusion data for elements such as Mg and Zn in single phase MAZ alloys are obtained. In the case of monoisotopic alloying elements such as Al, tracer diffusivities will be computed indirectly using diffusion theory (Darken–Manning relations) that connects interdiffusion coefficients (obtained from diffusion couples) with tracer diffusion coefficients and thermodynamics. The collection of tracer diffusion data for all the components in the MAZ system will then be fitted using suitable functions to generate the tracer diffusion database. At higher temperatures, the tracer diffusion in polycrystalline alloy samples is likely to be dominated by volume diffusion, whereas at lower temperatures there will likely be an additional contribution from GB diffusion. Although most of our measurements in this fiscal year are focused on volume diffusion measurements in large-grained samples, we have developed appropriate techniques whereby SIMS can be used in future studies for GB diffusion measurements in Mg thin films at low temperatures ($\sim 1/3$ of melting point or $0.3 \cdot$ melting temperature).

Results and Discussion

In the previous fiscal year, we demonstrated that the Mg self-diffusion coefficients determined using the SIMS-based thin film stable isotope technique compared very well with those based on historic radiotracer measurements, and we extended measurements to low temperatures not accessible by classical methods. Our objectives in this fiscal year were to

- extend our approach for Mg tracer diffusion studies in MAZ and Mg-RE alloys
- establish a technique for Zn tracer diffusion studies and determine Zn tracer diffusivities in MAZ alloys
- develop an effective diffusion model to include microstructure effects (anisotropy and GB diffusion) in polycrystalline microstructures
- conduct interdiffusion couple studies in MAZ to extract the Al tracer coefficient using diffusion theory
- develop a new formalism suitable for analyzing interdiffusion experiments when different isotopes of the interdiffusing elements are present in the end-members of a diffusion couple
- initiate GB diffusion studies in Mg
- establish a diffusion website for dissemination of diffusion data and analysis to our collaborators and the general public

We were successful in measuring the Mg tracer diffusivities in three MAZ alloys and expect to work on more MAZ and Mg-RE alloys. Tracer diffusion measurements of Zn in Mg and MAZ alloys proved to be quite challenging because of the high Zn vapor pressure. This required us to develop a tailored Zn tracer diffusion procedure, which we demonstrated by measuring the Zn impurity diffusion coefficient in pure Mg. Additional difficulties in sputter deposition of Zn isotopic films caused us to postpone several Zn tracer experiments in MAZ alloys. For modeling effective diffusion in polycrystalline Mg microstructure, we developed a Monte Carlo model to include GB and bulk diffusion contributions. Most of the diffusion couple experiments in incremental MAZ alloys, as well as electron microprobe analysis (EPMA) to determine the concentration profiles in these couples, have been completed. The analysis of the EPMA data to determine the interdiffusion coefficients along the binary Mg–Al (~8 at. % Al) was completed. The complete analysis for all the couples is expected to be finished by October. Our collaborators from Newcastle proposed a new formalism for the analysis of diffusion couple data with the couple end-members consisting of varying isotopic abundances of the elements of the alloys. This technique requires the availability of larger quantities of enriched stable isotopes if conventional bulk diffusion couple experiments are used; however, if thin-film diffusion couple experiments are conducted, it is likely that the approach would be more cost-effective and practical. We explored some preliminary GB diffusion models using analytical approaches and applied these to analyze Mg self-diffusion and impurity GB diffusion SIMS profiles in Mg thin films of controlled grain sizes. Finally, we created a diffusion website that served as a repository of our diffusion data and facilitated interactions among collaborators. A subset of this was used to create a diffusion website for the general public.

A. Mg Tracer Diffusion Studies in Mg-Al-Zn Alloys

Mg tracer diffusion experiments were carried out in four sample compositions, including pure Mg, MA6, MZ3, and MA3Z1, where M=Mg, A=Al, Z=Zn and the number indicates the nominal weight percentages of the minority elements. Prior to the tracer diffusion anneals, the samples were pre-annealed at temperatures below the solidus to homogenize the compositions and obtain large grain sizes (hundreds of microns), and then conditioned for sufficient time at the diffusion annealing temperatures. Sputter deposition of the Mg isotopic thin films on this initial set of samples was completed using an arrangement shown in [Figure 1](#). A total of 11 Mg-alloy samples, and some witness silicon samples for thickness calibration, were used for deposition of isotopic Mg thin films. The conditions used for Mg isotopic deposition were similar to those previously established in order: (a) RF pre-clean (126 W, 20 sccm argon at 5 mTorr for 60 s); (b) Mg deposition at 50 W dc, 20 sccm argon at 5 mTorr for 50 s. Suitable diffusion annealing temperatures and times for the Mg-alloy samples were selected based on calculations using Mg self-diffusion diffusion parameters as input. The Mg tracer diffusion coefficients were obtained at various temperatures for the compositions selected; they are illustrated together on a master Arrhenius plot ([Figure 2](#)).

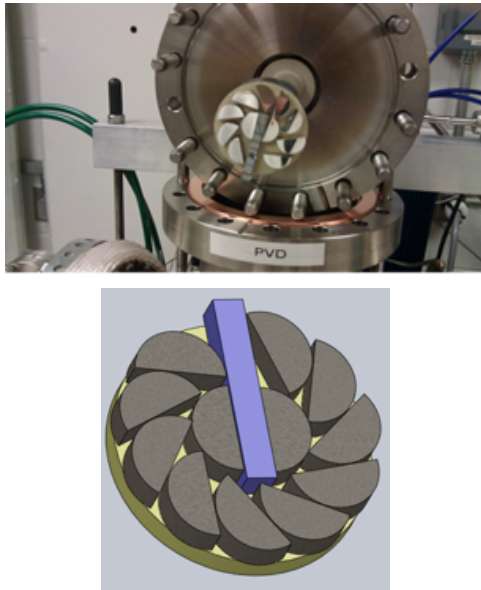


Figure 1. Setup for thin film sputter deposition on Mg alloy samples.

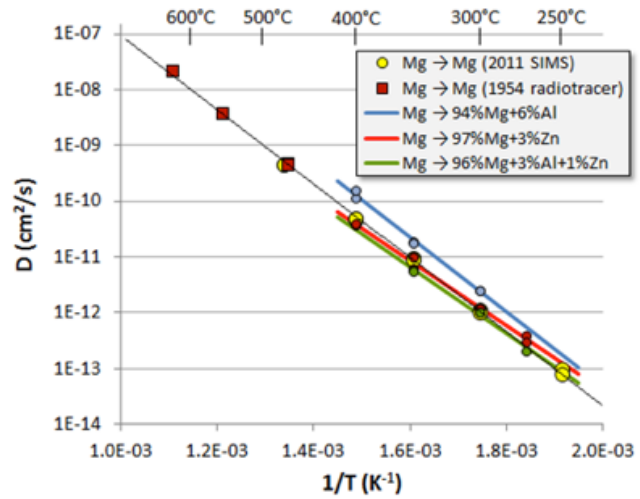


Figure 2. Arrhenius plot for the Mg tracer diffusivities in pure Mg and the three Mg alloys.

B. Zn Tracer Diffusion Studies

Tracer diffusion studies in Mg using isotopic zinc ($Zn-68$) thin films present some unique challenges because of the high Zn vapor pressure at desired diffusion temperatures. Calculations reveal that even at the lowest diffusion temperature of $270^{\circ}C$, the Zn evaporates at a rate of 448 nm/min . In other words, little of the isotopic Zn film will be available for tracer diffusion. However, the evaporation rate is only about 5 nm/min at $200^{\circ}C$, so a pre-annealing treatment of approximately $6-7\text{ min}$ was used to allow the Zn to diffuse into the sample to a depth roughly equal to its deposited thickness. Following this step, the Mg samples were raised to the intended diffusion temperatures. The idea is that the evaporation or out-diffusion is greatly impeded once the Zn is alloyed. As expected, the Zn diffused in $\sim 100\text{ nm}$ into the magnesium, as shown in Figure 3. Another issue is the low production of Zn ions produced by SIMS. Even so, optimization of conditions allowed a dynamic range of ~ 15 , sufficient for analysis. Finally, as expected, high Zn concentrations produce multiple Mg-Zn compound phases that have low effective diffusivities. This is very apparent in Figure 4 at depths of less than $1\mu\text{m}$. Consequently, the nonlinear fitting of the SIMS data was performed on the dilute region between 2 and $6\mu\text{m}$. An important issue is whether the holdup region with low-diffusivity Mg-Zn compound phases affects the measured diffusivity in the dilute region. Monte Carlo modeling was applied to fit the entire depth profile. By using three step diffusivities ranging over four orders of magnitude with depth, we determined that the diffusivity determined by simple nonlinear fitting was consistent with the dilute region of the Monte Carlo model. This conclusion has important consequences for tracer diffusion studies using the SIMS-based stable isotope technique, and it enables the determination of dilute-region tracer diffusivities in spite of multiple phases in high-concentration regions near the surface.

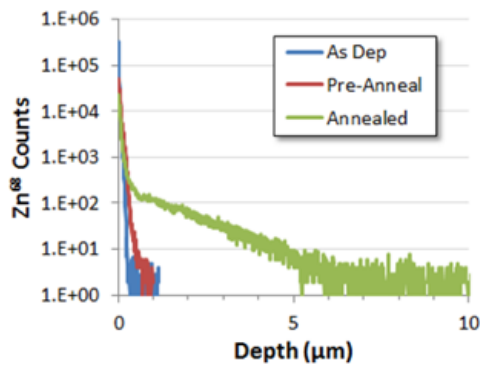


Figure 3. SIMS analysis of three $68Zn$ -coated pure Mg samples: as deposited, pre-annealed for 7 min at $200^{\circ}C$, and diffused at $300^{\circ}C$ for 1 h . Pre-annealing was needed to minimize evaporation of Zn during tracer diffusion annealing.

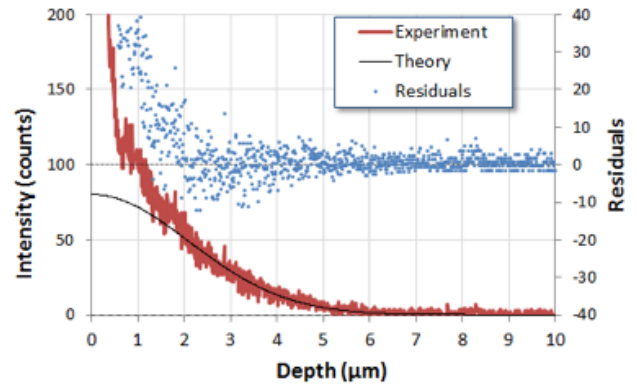


Figure 4. SIMS intensity of $68Zn$ ions with sputter depth. Nonlinear fitting was done in the dilute region between 2 and $6\mu\text{m}$, resulting in a tracer diffusivity of $6.19 \times 10^{-2}\text{ cm}^2/\text{s}$. The region $< 1\mu\text{m}$ is consistent with low-diffusivity multiple Mg-Zn compound phases.

Analysis of Zn tracer diffusion in the Mg alloy samples, MA6 (6 wt % Al), MZ3 (3 wt % Zn) and MA3Z1 (3 wt % Al and 3 wt % Zn), were discontinued because of roughness and grain size issues (the Mg-Zn alloy samples had grain sizes of <100 nm, whereas the Mg-Al alloy samples had much larger grain sizes of hundreds of nm). We believe that these problems originated with the lack of control over the Zn sputter deposition process and because of oxidation of the Zn-68 isotopic target foil. Second, grain sizes in the alloys (especially Mg-Zn alloys) were much smaller than the pure Mg samples, leading to questions about grain-boundary diffusion and differential orientation-induced roughening. These samples should be repeated after changing the Zn isotopic deposition technique (thermal evaporation) and further annealing the Mg-Zn alloy samples to ensure larger grain sizes prior to the tracer diffusion anneals.

Analysis of the SIMS diffusion profile for Zn-68 in pure Mg provided a Zn impurity diffusion coefficient that is ~ 30% larger than the one obtained using extrapolated radiotracer diffusivity data from Lal (1967; Lal and Levy, 1966) and about 75% larger than that by Čermák (2006) (Table 1).

Table 1. Impurity diffusion coefficient of Zn in pure Mg using the SIMS technique compared with extrapolated radiotracer data from Lal and Čermák.

Author	Tracer element	D0 (m ² /s)	Q (kJ/mol)	T (°C)	T (°K)	D (m ² /s)	Time (h)	1/e length (μm)
K. Lal, CEA	Zn*	4.10E-05	120	299.8	572.8	4.67E-16	1.002	2.60
Čermák	Zn*	1.05E-04	125.8	299.8	572.8	3.54E-16	1.002	2.26
This work (SIMS)	Zn-68 (stable)	-	-	299.8	572.8	6.19E-16	1.002	2.99

C. Effective Diffusion Modeling in Polycrystalline Magnesium

The objective of the diffusion modeling is to use a multiscale modeling approach to compute the effective diffusion coefficient within a microstructure as a function of the grain size, grain orientation, and grain misorientation distribution that depend on prior processing of the alloy. Ultimately, these models can be combined with our current mesoscale processing–microstructure models so that the diffusion-controlled microstructure evolution in which solute diffusion and microstructure evolution occur concurrently can be predicted. Thus far, we have used two different simulation techniques to capture the diffusion at two length scales—molecular dynamics (MD) simulations to capture the diffusion at the length scale of individual GBs, and a Monte Carlo–based simulation technique that will ultimately use the computed GB and bulk diffusion coefficients as inputs to effective diffusion computations at a length scale of a statistically representative microstructure. The effective diffusion computations will also use experimentally measured bulk/GB diffusivities in multicomponent alloys where the availability of a reliable interatomic potential for MD is questionable. Current capabilities also exist for mapping experimentally quantified target microstructures into three-dimensional computational domains so that the target grain size, grain orientation, and grain misorientation distribution are captured accurately in the simulation domain.

So far, MD simulations have focused on {10-10} tilt boundaries in Mg because of their prevalence in wrought alloys. An important feature of the GBs is the formation of facets during the diffusion anneals, and the localized diffusion within the GB plane with no clear indication of a throughput along the entire GB plane. These findings are very significant when one applies the usual approach of calculating effective diffusion by assuming a fully percolating diffusion path along all GBs within a microstructure. The effective diffusion calculations (Figures 5 and 6) use a large number of independent random walkers through a microstructure, and the diffusion coefficient is calculated by averaging the mean square displacement of these walkers. The parallel code allows the simulation of large, statistically significant microstructures with a large number of grains with periodic boundary conditions. The simulations capture the transition in the Arrhenius slope from volume to GB diffusion as the temperature is decreased, and the increase in effective diffusion as the grain size is decreased.

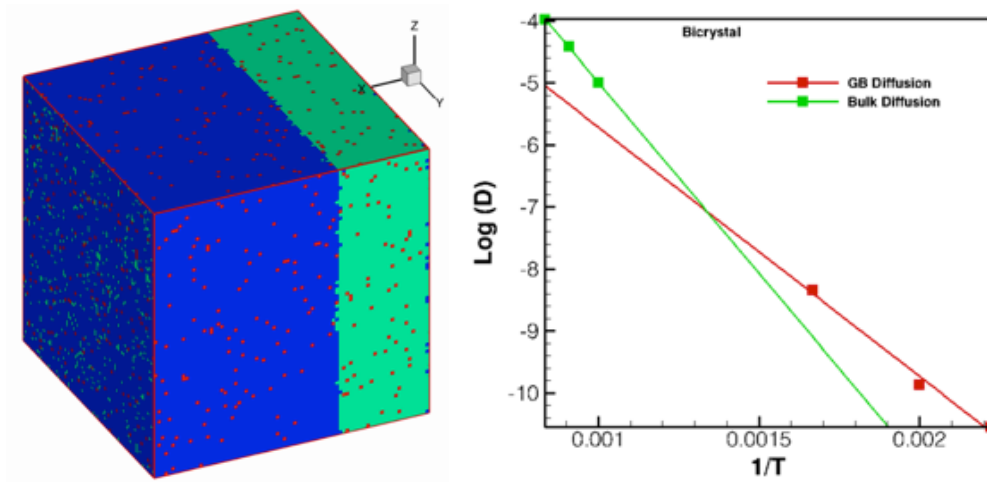


Figure 5. Effective diffusion in a bicrystal demonstrating bulk diffusion dominating at high temperatures and grain-boundary diffusion dominating at low temperatures.

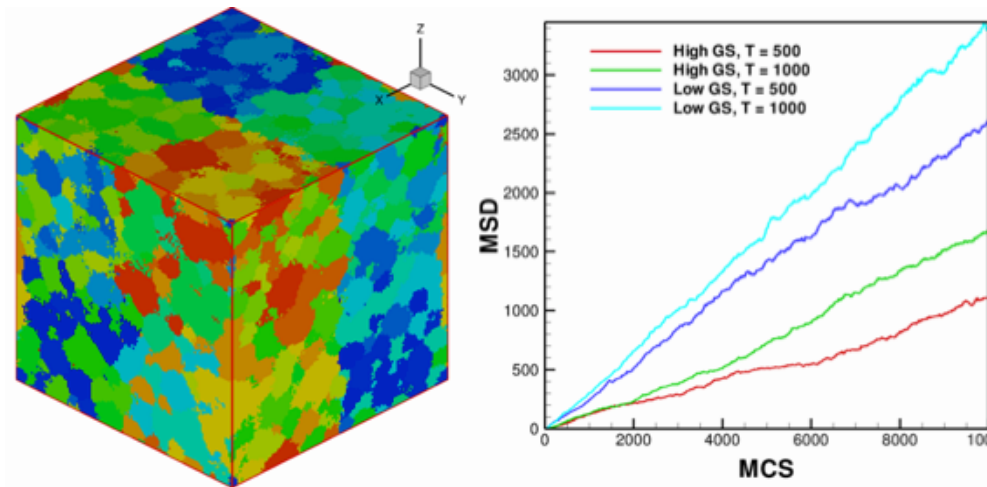


Figure 6. Effective diffusion in a bicrystal demonstrating bulk diffusion dominating at high temperatures and grain-boundary diffusion dominating at low temperatures.

D. Interdiffusion Studies in Mg-Al-Zn Alloys

Two of the most common alloying elements in Mg alloys are Al and Zn. Both Zn and Al are common alloying elements in commercial Mg alloys, typically added for solid solution and precipitation strengthening, castability, and grain refinement. During FYs 2010 and 2011, diffusion controlled intermetallic phase formation and growth studies in the full-range Mg-Al and Mg-Zn diffusion couples were reported. In FY 2012, interdiffusion studies at various temperatures and times were carried out using incremental diffusion couples (Figure 7, left side) in the Mg solid-solution regime of the MAZ system.

At compositional extremes, the Boltzmann-Matano (B-M) graphical method (Shewmon, 1989) may fail to provide adequate resolution to ascertain a reliable interdiffusion coefficient and subsequent extrapolation of impurity diffusion coefficients. The Hall (1953) method puts the concentration gradient in terms of a probability distribution, thus permitting the determination of the interdiffusion coefficient at impurity levels. Through solid-to-solid diffusion couples of Mg and Mg solid-solutions, the concentration gradient of the solute can be measured more accurately in the regime approaching infinite dilution; this allows explicit determination of interdiffusion, impurity, intrinsic, and tracer diffusion coefficients. Mg solid solutions of varying compositions (MA9, MZ6, MA3Z1, and MA1Z3) were bonded to pure Mg (Figure 7, left side). Additionally, binary solid-solutions were bonded together (MA9-MZ6, MA3-MZ3). The concentration profiles have been measured for several couples using EPMA; however, the interdiffusion analyses from these profiles are still to be completed. Interdiffusion coefficients using the B-M and Hall methods for binary Mg-MA9 diffusion couples are shown in Figure 7 (right side).

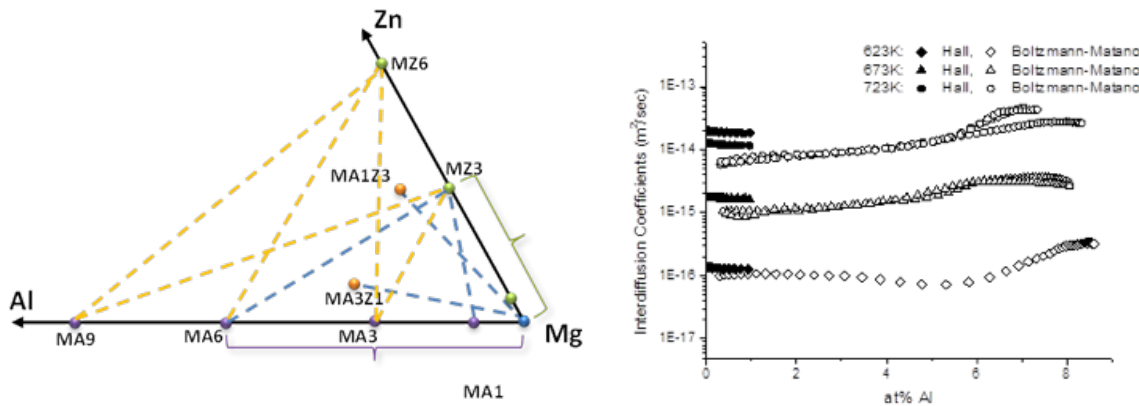


Figure 7. (Left) Illustration of selected couples for interdiffusion studies. Mg is shown being bonded to MA6, MA9, MZ3 and MZ6. Other couples are joined by dashed lines. (Right) Interdiffusion coefficients using the Boltzmann-Matano and Hall methods for the binary Mg-MA9 diffusion couple.

The interdiffusion coefficient can be related to the tracer diffusion coefficients by the Darken-Manning relation, which factors in the thermodynamic factor and vacancy-wind factor. Using the Manning formalism, when the concentration of the solute goes to zero, both the thermodynamic and vacancy-wind factors go to unity. Thus the interdiffusion coefficient can be equivocated to the tracer diffusion coefficient of an infinitely dilute solute. For concentrated Mg alloys, knowledge of the Mg tracer coefficient, the thermodynamics, and the interdiffusion coefficient can be used to compute the Al tracer coefficient, which cannot be experimentally determined using stable isotopes because Al is monoisotopic. This analysis will be completed following the interdiffusion analysis that is currently under way.

E. New Theoretical Formalism for Isotopic Interdiffusion Analysis

The widespread availability of precise SIMS measurement of different isotopes of the same element has generated the need for a new formalism suitable for analyzing interdiffusion when different isotopes of the interdiffusing elements are present. Such a general theory of interdiffusion involves the consideration of the atomic components and their available isotopes. The main condition for the successful experimental application of this analysis is an alteration of the abundance(s) of the isotopes at one end of a diffusion couple. The resulting profiles, when measured, can provide a significant amount of new information. Using the derived equations, the self-diffusion coefficients of the corresponding isotopes can be obtained as a function of the composition covered in an interdiffusion experiment. Taken together with an appropriate diffusion kinetics theory for concentrated regions and the five-frequency model for dilute compositions, this information provides significant additional assistance in solving the interdiffusion equations. In the case of a ternary, especially, the only way to analyze the ternary interdiffusion profiles using existing approaches was to design two appropriate diffusion couple experiments with intersecting diffusion composition paths. With this traditional approach, the only available diffusion data would have been at the composition where the diffusion paths intersected. The newly developed formalism provides a methodology to calculate all the four interdiffusion coefficients and the three self-diffusion coefficients as functions of composition along a single diffusion path. More details will be provided in future publications on this topic.

The practical realization of such diffusion couple experiments using conventional bulk diffusion couples is limited by the cost and availability of large quantities of enriched isotopes. However, it is felt that the use of thin-film diffusion couples, prepared using co-sputter deposition from isotopic targets, provides a possible means of proving the use of this new formalism. Such experiments have not been conducted at the present time.

F. Grain Boundary Diffusion

GB diffusion has important roles in grain growth, creep, and deformation behavior and is the dominant diffusion process in fine-grained materials. A quantitative description of GB diffusion is required for accurate computational modeling of evolving microstructures. Traditional GB diffusion experiments are carried out using bicrystals and radioactive tracers, which are very expensive and time consuming and provide data only for a single, specific GB orientation. The SIMS-based, thin film technique is much more representative of GB diffusion in polycrystalline materials. The main drawback to this method is that the SIMS probe size (typically several microns) is far larger than the GB region (~0.5 nm), meaning that a single SIMS measurement must sample over multiple GBs in order to obtain an appreciable signal. This type of diffusion study needs to be carried out using extremely fine-grained materials to ensure a relatively large volume-fraction of GBs and thus a substantial

SIMS signal of the tracer diffusant. It is difficult to obtain and maintain these necessary small grain sizes using bulk samples because of the possibility of GB diffusion-activated grain growth during the diffusion anneal. Thin films provide the ideal geometry for this condition mainly because small grain sizes can be maintained over the course of diffusion experiments, since grain growth and boundary migration are constrained by the film thickness. As a general rule, average grain sizes in thin films are roughly equal to the film thickness.

We suggest the use of both a top-down experiment with an analysis based on Gilmer and Farrell's (1976) solutions and a lateral diffusion experiment with the typical Suzuoka (1964) analysis. Both of these methods are approaches to overcoming the problem that the diffusant would quickly penetrate the entire thickness of the film through the GB under appropriate GB diffusion conditions. The Gilmer-Farrell solution accounts for buildup of diffusant in the GB tail region due to a reflecting boundary condition at the back end of the film. The lateral method provides ample, uninhibited diffusion length to which the "semi-infinite" solutions (Suzuoka) can be applied. The GB diffusion experiments are carried out under conditions consistent with Harrison's B (1961) kinetics regime, as this will provide an appreciable diffusant signal for SIMS measurements and can be accomplished with reasonable Mg film thicknesses. Future work will begin with Al diffusion studies into pure Mg films, sputtered on thermally oxidized Si substrates (~50 nm SiO₂). The thermal oxide is intended to act as a diffusion barrier to satisfy the reflecting boundary condition for the Gilmer-Farrell analysis and eliminate surface/interface diffusion effects with the lateral diffusion experiments. Once the proper methodology to extract D_{gb} from the experiments is confirmed, studies involving ²⁵Mg as a tracer into (~99.9%) pure ²⁴Mg films can be done. This is necessary because of the ~10% background signal of ²⁵Mg in commercially pure Mg. If the ²⁴Mg level in the film is increased from ~80 to 99.9%, the SIMS signal measuring the ²⁵Mg diffusant increases by a factor of 200, allowing detectable concentrations in the GB tail region. Further studies with Al, Mg, and Zn diffusion into co-sputtered Mg-rich alloy films are planned. Using analytical GB diffusion models (Suzuoka, 1964), tracer diffusion profiles in Mg thin films consisting of parallel GBs were obtained as shown in Figure 8.

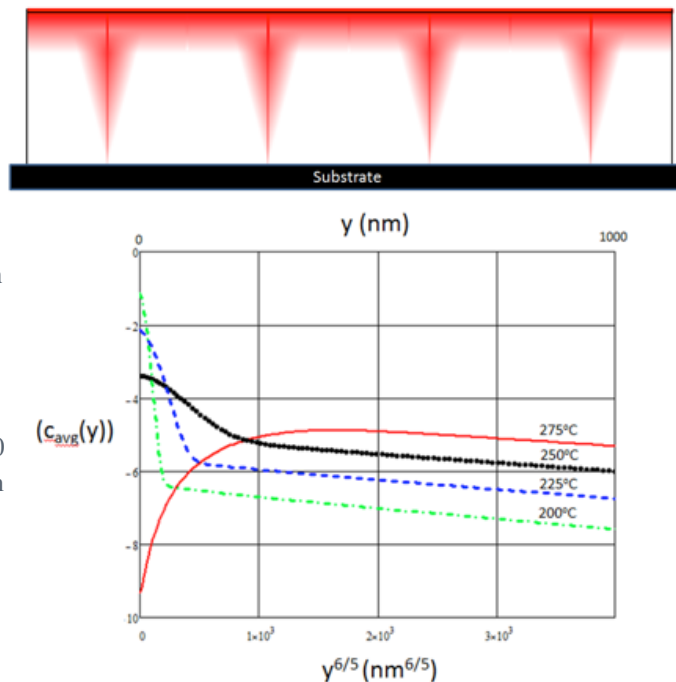


Figure 8. (Top) Schematic representation of tracer (in red) diffusion through multiple parallel grain boundaries in a thin film according to Harrison regime B kinetics. (Bottom) Variation of averaged tracer concentration as a function of penetration distance $y^{6/5}$, based on the averaged Suzuoka solution applied to the case of Mg grain boundary self-diffusion. Y-range is 0–1000 nm, finite tracer thickness is 10 nm, grain size is 500 nm, and diffusion conditions are 10 minutes at 200, 225, 250, and 275°C; $D_{vol} = 0.396, 2.004, 8.683, \text{ and } 32.911 \text{ nm}^2/\text{s}$, based on Mg self-diffusivities (this work), respectively; $D_{gb} = 5.9 \times 10^4, 1.6 \times 10^5, 4 \times 10^5, \text{ and } 9.2 \times 10^5 \text{ nm}^2/\text{s}$, respectively, based on an empirical grain boundary diffusion model by Gjostein (1973).

Technology Transfer Path

To facilitate the transfer of the diffusion data for the computational materials design of Mg-based automotive components, we have begun the process of creating a *public diffusion website* as a type of database containing diffusivity measurements and analyses. This website includes a concise tabulation of results, combining historical and our recent results of the self-diffusion in Mg. We also provide details of our methods, experimental conditions, and data recorded during various measurements. The database will be augmented with additional diffusivity results (after publication), including the diffusion of Mg, Zn, Al and other materials into Mg alloys. The public diffusion website is essentially a subset of a private diffusion website that is used by our team of collaborators. The url is <http://www.ornl.gov/sci/diffusion>.

Conclusions

This work establishes a unique and critical capability in the United States for tracer diffusion studies in alloys using the SIMS-based stable isotope technique. We have measured the Mg tracer diffusion coefficients in several MAZ alloys as a function of temperature. We established a new technique for Zn tracer diffusion studies in Mg alloys to account for the high Zn vapor pressure and applied it for Zn impurity diffusion studies in Mg. An effective diffusion model for polycrystalline Mg was developed based on a Monte Carlo technique. Interdiffusion studies in incremental MAZ diffusion couples were conducted at various temperatures and times, and the analysis of the concentration profiles to compute the interdiffusivities was completed for a binary Mg-MA9 couple. A new diffusion formalism was developed that is suitable for analyzing interdiffusion behavior when different isotopes of the interdiffusing elements are present in order to provide fundamental tracer diffusion data from diffusion couple experiments. A procedure for GB tracer diffusion experiments and analysis applicable for SIMS studies in Mg thin films was developed with the aid of analytical models.

Presentations / Publications/ Patents

Invited Presentations

Warmack, R.J.; Kulkarni, N.S.; Radhakrishnan, B.; Hunter, J.; Tuggle, J.; Sohn, Y.H.; Coffey, K.R.; Dein, E.; Murch, G.E.; Belova, I.V.; and Mundy, J. Diffusion Studies in Mg-Al-Zn. *10th NIST Diffusion Workshop*, Gaithersburg, MD, 2012, May 3–4.

Contributing Presentations

Kulkarni, N.S.; Hunter, J.; Warmack, R.; Radhakrishnan, B.; Sohn, Y.H.; Coffey, K.R.; Murch, G.E.; Belova, I. Tracer and Interdiffusion Studies in Mg-Al-Zn Alloys. *9th International Conference on Magnesium Alloys and Their Applications (Mg-2012)*, Vancouver, BC, Canada, 2012, July 8–12.

Brennan, S.; Bermudez, K.; Sohn, Y.H. Intermetallic Growth and Interdiffusion in the Mg-Nd System. *9th International Conference on Magnesium Alloys and Their Applications (Mg-2012)*, Vancouver, BC, Canada, 2012, July 8–12.

Kulkarni, N.S.; Warmack, R.J.; Hunter, J.L.; Tuggle, J.; Kammerer, C.; Sohn, Y.H.; Coffey, K.R.; Murch, G.E.; Belova, I.V. Diffusion in Mg-Al-Zn alloys. *8th International Conference on Diffusion in Solids & Liquids (DSL 2012), Symposium on Diffusion Processes & Reactions in Engineering Solids*, Istanbul, Turkey, 2012, June 25–29.

Kulkarni, N.S.; Todd, P.; Radhakrishnan, B.; Warmack, R.; Sohn, Y.H.; Hunter, J.; Murch, G.E. Tracer Diffusion Database: Benefits and Techniques. *2012 TMS Annual Meeting and Exposition: Symposium on Computational Thermodynamics and Kinetics*, Orlando, FL, 2012, March 11–15.

Radhakrishnan, B.; Kulkarni, N.S.; Sohn, Y.H.; Hunter, J. Computation and Validation of Effective Diffusion Coefficient in a Magnesium Polycrystal. *2012 TMS Annual Meeting and Exposition: Symposium on Computational Thermodynamics and Kinetics*, Orlando, FL, 2012, March 11–15.

Belova, I.V.; Murch, G.E.; and Fiedler, T. Lattice Monte Carlo Determination of Harrison Kinetics Regimes for Grain Boundary Diffusion in Materials with Inhomogeneous Grain Structures. *2012 TMS Annual Meeting & Exhibition*, Orlando, Florida, 2012, March 11–15.

Bermudez, K.A.; Brennan, S.T.; Sohn, Y.H. Interdiffusion and Phase Formation in the Mg-Y System. *2012 TMS Annual Meeting and Exposition: Symposium on Magnesium Technology 2012*, Orlando, FL, 2012, March 11–15.

Brennan, S.; Bermudez, K.; Kulkarni, N.S.; Sohn, Y.H. Diffusion Couple Investigation of the Mg-Zn System. *2012 TMS Annual Meeting and Exposition: Symposium on Phase Transformations and Deformation in Magnesium Alloys*, Orlando, FL, 2012, March 11–15.

Tuggle, J.; Hunter, J.; Kulkarni, N.S.; Sohn, Y.H. Secondary Ion Mass Spectrometry for Mg Tracer Diffusion: Issues and Solutions. *The 2012 TMS Annual Meeting and Exposition: Symposium on Magnesium Technology 2012*, Orlando, FL, 2012, March 11–15.

Tuggle, J.; Hunter, J.; Seay, J.; Giordani, A.; Kulkarni, N.S.; Warmack, R.; Sohn, Y.H.; Brennan, S.; Coffey, K.R.; Radhakrishnan, B.; Todd, P. Secondary Ion Mass Spectrometry for Mg Tracer Diffusion: Issues and Solutions. *Appalachian Regional Microscopy Society Meeting*, Boone, NC, 2011, October 20–21.

Giordani, A.; Hunter, J.; Tuggle, J.; Seay, J.; Kulkarni, N.S.; Warmack, R.; Sohn, Y.H.; Brennan, S.; Coffey, K. R.; Radhakrishnan, B.; Todd, P. Measurement of Long (>10 μm) Magnesium Self-Diffusion Length Using Secondary Ion Mass Spectroscopy. *Appalachian Regional Microscopy Society Meeting*, Boone, NC, 2011, October 20–21.

Kulkarni, N.S.; Hunter, J.; Sohn, Y.H.; Brennan, S.; Coffey, K.R.; Radhakrishnan, B.; Todd, P.; Murch, G.E.; Belova, I.V. Tracer Diffusion Studies in Mg-Al-Zn. *Symposium on Phase Stability, Diffusion, Kinetics and their Applications (PSDK-VI), Materials Science & Technology 2011 (MS&T 2011)*, Columbus, OH, 2011, October 16–20.

Journal Publications

Belova, I.V.; Fiedler, T.; Kulkarni, N.; Murch, G.E. The Harrison Diffusion Kinetics Regimes in Solute Grain Boundary Diffusion. *Philosophical Magazine* **2012**, 92, pp 1748–1763.

Brennan, S.; Bermudez, K.; Kulkarni, N.S.; Sohn, Y. Interdiffusion in the Mg-Al System and Intrinsic Diffusion in $\beta\text{-Mg}_2\text{Al}_3$. *Metallurgical and Materials Transactions A* **2012**, 43A, pp 4043–4052.

Brennan, S.; Warren, A.P.; Coffey, K.R.; Kulkarni, N.; Todd, P.; Kilmov, M.; Sohn, Y. Aluminum Impurity Diffusion in Magnesium. *Journal of Phase Equilibria and Diffusion* **2012**, 33, pp 121–125.

Conference Proceedings

Bermudez, K.; Brennan, S.; Sohn, Y. H. Intermetallic Phase Formation and Growth in the Mg-Y System. In *Proceedings of the 9th International Conference on Magnesium Alloys and Their Applications, Mg Technology 2012*; Mathaudhu, S.N., Hort, N., Sillekens, W.H., Neelameggham, N.R., Eds.; TMS, Warrendale, PA; pp 145–148, 2012.

Brennan, S.; Bermudez, K.; Kulkarni, N. S.; Sohn Y. H. Diffusion Couple Investigation of the Mg-Zn System. In *Proceedings of the 9th International Conference on Magnesium Alloys and Their Applications, Magnesium Technology 2012*; Mathaudhu, S.N., Hort, N., Sillekens, W.H., Neelameggham, N.R., Eds.; TMS, Warrendale, PA: pp 323–327, 2012.

Brennan, S.; Bermudez, K.; Sohn, Y. H. Intermetallic Growth and Interdiffusion in the Mg-Nd System. In *Proceedings of the 9th International Conference on Magnesium Alloys and Their Applications, Magnesium Technology 2012*; Poole, W.J., Kainer, K.U., Eds.; TMS, Warrendale, PA: pp 417–421, 2012.

References

Čermák, J.; Stloukal, I. Diffusion of Zn-65 in Mg and in Mg-xAl Solid Solutions. *Physica Status Solidi (a)—Applications and Materials Science* **2006**, 203(10), pp 2386–2392.

Gilmer, G.H.; Farrell, H.H. Grain-Boundary Diffusion in Thin-Films.1. Isolated Grain-Boundary. *Journal of Applied Physics* **1976**, 47(9), pp 3792–3798.; Grain-Boundary Diffusion in Thin-Films. 2. Multiple Grain-Boundaries and Surface-Diffusion. *Journal of Applied Physics* **1976**, 47(10), pp 4373–4380.

Gjostein, N.A. Short Circuit Diffusion, p. 241. In *Diffusion: Papers Presented at a Seminar of The American Society for Metals, 1972*; American Society for Metals, 1973.

Hall, L.D. An Analytical Method of Calculating Variable Diffusion Coefficients. *Journal of Chemical Physics* **1953**, 21(1), pp 87–89.

Harrison, L.G. Influence of Dislocations on Diffusion Kinetics in Solids with Particular Reference to Alkali Halides. *Transactions of the Faraday Society* **1961**, 57(8), pp 1191.

Lal, K., Ph.D. Thesis., 1966a. Diffusion of Various Elements in Magnesium. (English translation of French title). In CEA Report R3136, 1967.

Lal, K.; Levy, V. Etude de la Diffusion du Cerium et du Lanthane dans le Magnesium. *Comptes Rendus Hebdomadaires Des Seances De L Academie Des Sciences Serie C* **1966b**, 262(1), pp 107.

Shewmon, P. *Diffusion in Solids*, 2nd ed.; The Minerals, Metals & Materials Society: Warrendale, Pennsylvania, 1989; pp. 15–19.

Shewmon, P. G.; Rhines, F. N. Rate of Self-diffusion in Polycrystalline Magnesium. *Transactions of the American Institute of Mining and Metallurgical Engineers* **1954**, 200(9), pp 1021–1025.

Suzuoka, T. Exact Solutions of 2 Ideal Cases in Grain Boundary Diffusion Problem + Application to Sectioning Method. *Journal of the Physical Society of Japan* **1964**, 19(6), pp 839.

E. Modeling And Computational Materials Science – Pacific Northwest National Laboratory

Mechanistic – Based Ductility Prediction For Complex Mg Castings

Principal Investigator: Xin Sun
Pacific Northwest National Laboratory
902 Battelle Boulevard, P.O. Box 999, Richland, WA 99352
(509)372-6489; e-mail: xin.sun@pnl.gov

Industry Partners: Mei Li
Ford Motor Company
(313) 206-4219; e-mail: mli9@ford.com

John Allison
University of Michigan
(734) 615-5150; fax: (734) 763-4788; e-mail: johnea@umich.edu

Field Technical Monitor: Dean Paxton
Pacific Northwest National Laboratory
(509)375-2620; e-mail: dean.paxton@pnl.gov

Technology Area Development Manager: William Joost
U.S. Department of Energy
1000 Independence Ave., S.W., Washington, DC 20585
(202) 287-6020; fax: (202) 856-2476; e-mail: william.joost@ee.doe.gov

Contractor: Pacific Northwest National Laboratory (PNNL)
Contract No.: DE-AC05-00OR22725 & DE-AC06-76RLO1830

Executive Summary

An integrated experimental and multi-physics modeling approach was adopted to develop the ductility prediction capability for complex Mg castings. The FY 2012 focus included 1) casting preparation with the subsequent location-dependent microstructure and ductility characterization, 2) the quality mapping approach for mean ductility prediction using casting process simulations and 3) microstructure-based finite element modeling considering both intrinsic and extrinsic ductility limiting factors.

Accomplishments

- Cast Mg alloy plates of different thicknesses with various Al contents under eight different conditions and characterized their porosity and microstructures. (FY 2012)
- Developed initial tensile testing standard and completed initial tensile property characterization. (FY 2012)
- Established quality mapping for mean ductility using MAGMAsoft simulations for a generic closure panel casting, and validated quality mapping using a Ford production liftgate casting. (FY 2012)
- Performed x-ray tomography on selected samples and developed an image-processing tool for visualization of three-dimensional (3D) pore distribution within the sample from the x-ray tomography data. (FY 2012)

- Performed synthetic microstructure-based 3D/two-dimensional (2D) finite element analyses to investigate the effects of various intrinsic and extrinsic factors on the ductility of Mg castings. (FY 2012)

Future Directions

- Refine the quality mapping approach for predicting the mean and statistical variation in ductility.
- Complete tensile testing, and correlate the fracture surface microstructures with x-ray tomography and scanning electron microscopy (SEM) and quantify the influence of Al content and thickness.
- Complete microstructure mapping for all conditions to be used for micro-mechanical model development.
- Evaluate the effects of large size pores and their locations on the ductility of Mg castings using synthetic-microstructure-based 3D/2D simulations.
- Determine the material parameters from experiment for the intrinsic ductility prediction model.

Technology Assessment

- Target: Develop a ductility prediction method for high-pressure die casting with potential for less than 5 percent error.
- Gap: Conventional computational techniques and most phenomenological approaches have little or no capability for predicting ductility.

Introduction

Mg castings have found increasing applications in lightweight vehicles because Mg and its alloys are the lightest metallic structural material. However, a critical technical hurdle hindering wider application of Mg castings in vehicle applications is its limited ductility. It is well established that microstructure features (e.g., properties and distributions of porosity, brittle eutectic phases, and grain size) can significantly influence the ductility of Mg castings. However, these microstructure features vary from alloy to alloy, with different casting processes, and in different locations on a single casting (Chadha et al., 2007; Song et al., 2009). Although some commercial casting software and material models are available for research of Mg castings, their predictive capabilities typically stop short of predicting the location-dependent stress versus strain behavior, particularly ductility. The purpose of this project is to develop an empirical casting process simulation tool and a mechanistic-based ductility predictive capability to provide a modeling framework applicable to future alloy design and casting process optimizations.

Approach

Plates were cast under eight different conditions and characterized through metallographic preparation. Tensile testing was conducted on samples cut from the plates. The data from the initial characterization will be used to map the microstructure for all conditions and develop a weak link analytical model for ductility and strength in the aluminum-manganese (AM) bearing alloy series. Results will be extended to real-world structures by using plate bulge testing to eliminate any edge effects and to validate the models developed in this project.

To provide a modeling framework, a mechanical properties quality mapping approach was considered, which includes both the mean value and the statistic variation of ductility. **Figure 1** shows the proposed flowchart for the establishment of quality mapping. Experimental values for the ductility in different locations of the GCIP (Generic Closure Inner Panel) casting under different processing conditions were determined through tensile testing. Simulations of each set of processing conditions were conducted using Magmasoft and the simulation outputs (i.e., criteria functions) were collected for the corresponding locations. A linear regression methodology was used to develop the quality mapping equation and the equation was subsequently validated on a prototype Lincoln MKT door inner casting.

For the tasks on the effects of extrinsic factors (i.e., porosity), a high resolution x-ray technique was adopted onto AM casting samples (cut from 2-mm-thick plate) to visualize the 3D pore distributions within samples and to characterize their distribution features. A special image-processing tool was also developed for this purpose. Synthetic microstructure-based

3D/2D simulations investigated the effects of the skin regions on ductility and feasible correlations between 3D and 2D simulation results. For the tasks on intrinsic ductility prediction of Mg castings, a series of microstructure samples were generated independently with varying grain material properties and the area fraction of β phase (fully connected, 20 percent, and 10 percent), as shown in Figure 2. The α grains were modeled using von Mises plasticity and β using linear elasticity. Analyses were conducted using the open source finite element package Finite Element All-Wheel Drive.

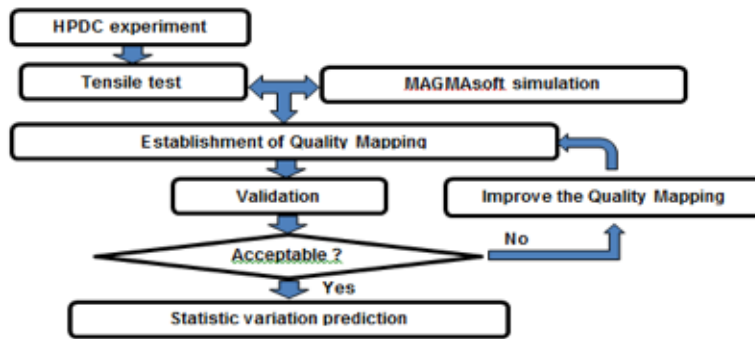


Figure 1. Flowchart of establishment of quality mapping.

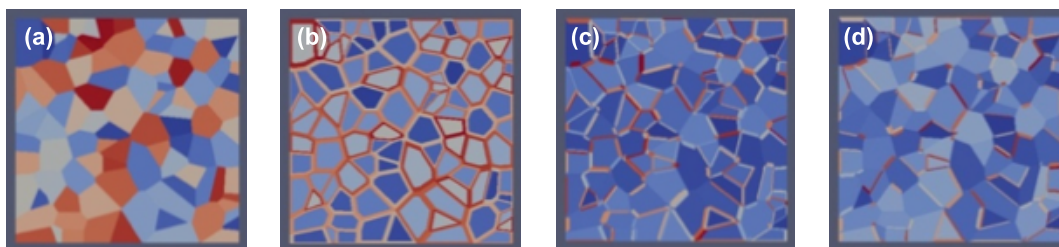


Figure 2. Example microstructure geometries (150- μ m square). (a) Initial Voronoi tessellation, (b) with β phase along all grain boundaries, i.e. fully connected β phase, (c) with β phase along randomly selected grain boundaries (20% β), (d) randomly placed β (10% β).

Results and Discussion

Plates were cast in two thicknesses (i.e., 2.5 and 5 mm) and four compositions (i.e., 4, 5, 6, and 7 wt% Al) for a total of eight unique conditions. These plates were sectioned and imaged to create a microstructure map and the major microstructural features were indexed. These samples were polished to show pore size and distribution, and etched to reveal β phase fraction. For example, Figure 3 shows the microstructures of AM70 castings. Tensile testing was conducted in accordance with ASTM E8/B557. Tensile results exhibited modulus and yield-strength values that had modest variations. Large variations in ductility and ultimate tensile strength were observed. Initial analytical modeling approaches were evaluated and an initial strength model was developed using grain size and solid-solution strengthening (Yasi et al., 2010). Ductility models evaluated include a modified Brown Embury model and an analytical model from Weiler and Wood (2012).

For quality mapping, all of the values for the different criteria functions were collected and normalized. It was determined that the most critical criteria functions were air entrapment (AE), air contact (AC), flow length (FL), liquidus to solidus (LS), and temperature at 100% fill (T). The quality mapping was established to generate the correlation between the criteria functions and ductility.

$$\text{Strain} = C_0 - C_1 * \text{LS}^C_2 - C_3 * \text{FL}^C_4 - C_5 * \text{AE}^C_6 - C_7 * \text{AC}^C_8 + C_9 * \text{T}^C_{10} \dots \dots \dots (1)$$

The quality mapping was then used to predict the mean ductility. Figure 4(a) shows an example of result.

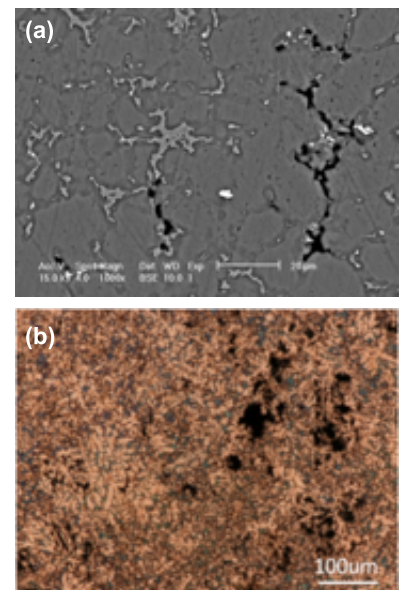


Figure 3. (a) AM70, 5-mm thick, back-scatter image (BSE) image: white are β phase, black are pores, (b) AM70, 5-mm thick: blue are β phase, black are pores.

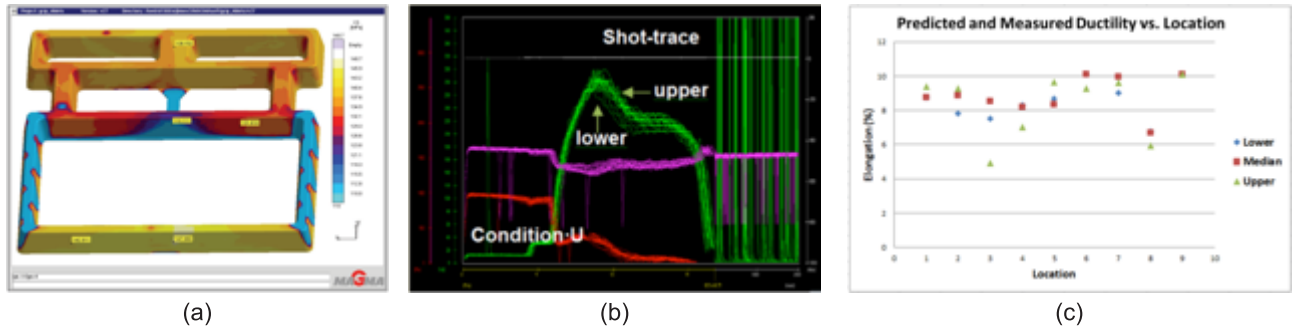


Figure 4. (a) Quality map for elongation to failure of AM60 GCIP casting, (b) shot-traces and (c) comparison of the test and predicted statistic variation of ductility in the castings produced under condition U.

In all cases, the filling profile, which could significantly influence the ductility in the casting, was defined based on the shot-trace of each casting, as shown in Figure 4(b). According to the upper-, median-, and lower-bound conditions, the statistic variation of ductility was predicted (see Figure 4(c)). The test and predicted data demonstrate a qualitatively accurate comparison. The quality mapping was successfully validated using another vehicle component casting.

Figure 5 shows an example of visualization of pore distribution within an AM60 sample after processing the x-ray tomography data. Pore distribution features indicate that larger pores are generally in the center region. The pore volume fraction for this region was calculated to be 1.3 percent, which is similar to the experimental measurement. Figure 6(a) shows a predicted failure mode of a 3D model where the damage models in ABAQUS were employed. Figure 6(b) shows the stress-strain curves of 3D models with the same overall pore volume fraction, but with different thicknesses of skin region. For the same overall pore volume fractions, the skin regions appear to have negligible effect on ductility. Figure 6(c) shows the effects of pore volume fraction on ductility based on different modeling methods. In the figure, two types of 2D modeling methods show similar trends to those predicted by 3D modeling, indicating that 2D modeling methods can predict the ductility of 3D model based on a 2D/3D correlation curve.

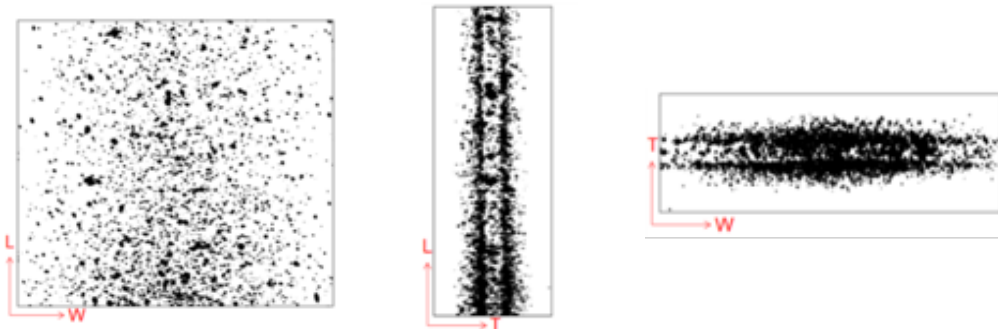


Figure 5. Visualization of pore distribution within an AM60 sample from x-ray tomography.

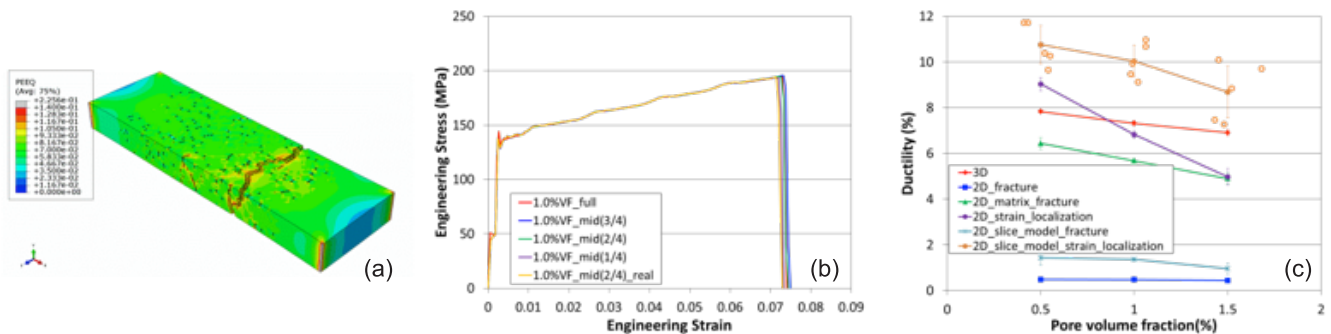


Figure 6. (a) Failure mode of a 3D model, (b) stress-strain curves for different thicknesses of skin region, and (c) effect of pore volume fraction on the ductility based on different modeling methods.

For intrinsic ductility prediction tasks, the resulting stress-strain responses for various conditions showed little to no variation, indicating that the sample size can be used as a representative volume element. Figure 7 demonstrates an increase in strength due to increased β . The β phase dominated the local stress/strain response in all samples with fully connected β . More local variation in stress/strain was seen with decreasing β . Analyses were also conducted with cohesive zone models (CZMs) along all material interfaces to allow for debonding within the sample. Initial results demonstrated a softening behavior compared to those of the same sample without CZMs.

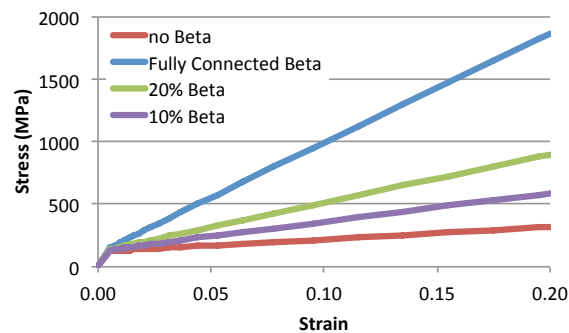


Figure 7. Stress-strain curves from the microstructure samples shown in Figure 2 containing varying area fractions of β .

Technology Transfer Path

The deliverables of this project will be transferred through Ford to the original equipment manufacturer participants and casting producers. Industry can use the modeling methodology and results to improve performance and reduce the number of prototypes needed to validate a design, saving time and cost.

Conclusions

First, metallographic procedures were detailed, major microstructural features were indexed, and tensile results analyzed. Initial approaches to modeling the ductility analytically were evaluated and will continue to be developed into an analytical model. By cataloging the major features, results can be integrated into the intrinsic and extrinsic ductility models and quality mapping.

MagmaSoft simulations were conducted for various processing conditions and the criteria functions collected to establish quality mapping for mean ductility. Quality mapping was validated on a prototype door inner casting and the predicted ductility found to be in reasonable agreement with measured data from similar locations. In addition, the predicted statistic variation of ductility based on the quality mapping is encouraging.

For extrinsic factor tasks, an image-processing tool for x-ray tomography data was developed to visualize the 3D pore distribution features. Synthetic microstructure-based 3D/2D modeling indicated that the skin regions do not significantly affect ductility and that possible correlations may exist between the 3D and 2D predictions. For intrinsic ductility task, bulk stress-strain responses for various intrinsic microstructural features showed little to no variation, indicating that adopted sample size is representative. Initial simulations were conducted to demonstrate the use of cohesive zones to allow debonding and failure within the sample. Various experiments are being planned to obtain the material parameters needed to investigate the intrinsic ductility.

Presentations/Publications/Patents

Sun, X., Choi, K.S., Li, D.S., Li, M. and Allison, J. Ductility Prediction for Magnesium Casting using Microstructure-based Finite Element Method. In 9th International Conference on Magnesium Alloys and their Applications, July 8-12, 2012, Vancouver, British Columbia, Canada.

Sun, X., Choi, K.S. and Li, D.S. Predicting the Influence of Pore Characteristics on Ductility of Thin-Walled High Pressure Die Casting Magnesium. Submitted for *Materials Science and Engineering A*, 2012.

References

Chadha, G., Allison, J.E. and Jones, J.W. The Role of Microstructure on Ductility of Die-Cast AM50 and AM60 Magnesium Alloys. *Metallurgical and Materials Transactions A*, **2007**, 38, pp. 286–297.

Song, J., Xiong, S.M., Li, M. and Allison, J.E. The correlation between microstructure and mechanical properties of high-pressure die-cast AM50 alloy. *Journal of Alloys and Compounds*, **2009**, 447, pp. 863-869.

Weiler, J.P. and Wood, J.T. Modeling the tensile failure of cast magnesium alloys. *Journal of Alloys and Compounds*, **2012**, 537, pp. 133–140.

Yasi, J.A., Hector, L.G. and Trinkle, D.R. First-principles data for solid-solution strengthening of magnesium: From geometry and chemistry to properties. *Acta Materialia*, **2010**, 58, pp. 5704–5713.

F. Multi-Material Enabling – Oak Ridge National Laboratory

Field Technical Monitor: C. David Warren
Oak Ridge National Laboratory
1 Bethel Valley Road; Oak Ridge, TN 37831
(865) 574-9693; fax: (865) 574-6098; e-mail: warrencd@ornl.gov

Technology Area Development Manager: William Joost
U.S. Department of Energy
1000 Independence Ave., S.W.; Washington, DC 20585
(202) 287-6020; fax: (202) 856-2476; e-mail: william.joost@ee.doe.gov

Contractor: Oak Ridge National Laboratory (ORNL)
Contract No.: DE-AC05-00OR22725

Executive Summary

Significant weight reduction in future vehicle structures will likely occur through the adoption of a variety of materials including light metals. The obstacles to incorporating these materials include material cost and manufacturability. In addition to these obstacles, critical technologies are needed to enable the cost-effective performance necessary for application of these materials. Those technologies include multi-material joining, corrosion prevention, and nondestructive evaluation (NDE).

This project consists of seven tasks critical for the welding, inspection, development, and implementation of lightweight metal structures: dynamic characterization of spot welds in advanced high-strength steels (AHSSs); friction stir spot welding (FSSW) of AHSS; improving fatigue performance of AHSS welds; online weld quality monitoring and control with infrared (IR) thermography; IR heat treatment of cast bimetallic joints and residual stress characterization; understanding protective film formation by magnesium (Mg) alloys in automotive applications; and high strength, lightweight engines for heavy-duty diesel trucks.

Activities And Developments

Dynamic Characterization of Spot Welds in Advanced High Strength Steels

Principal Investigator: Zhili Feng, ORNL
(865) 576-3797; fax: (865)574-4928; e-mail: fengz@ornl.gov

Principal Investigator: Srdjan Simunovic, ORNL
(865) 241-3863; fax: 241-0381; e-mail: simunovics@ornl.gov

Contributors: Lili Zheng, Yanli Wang, Laura Riester, ORNL

Accomplishments

- Completed detailed microstructure characterization and microhardness mapping of the welds produced earlier in the project covering 17 combinations of steel grades, coatings, thicknesses, and two layer (2T)/three layer (3T) stacks.
- Determined the local stress-strain properties in the weld region and heat affected zone (HAZ) of selected welds by means

of miniature tensile and digital image correlation (DIC) method for use in the dynamic model of spot welds.

- Obtained full field deformation information during lap shear testing by the DIC method.
- Incorporated the damage mechanics based approach necessary to simulate the failure of spot welds of different grades of AHSS.

Future Directions

- Incorporate damage mechanics based failure criterion into the spot weld element (SWE) formulation.
- Validate a SWE formulation for different AHSS thickness combinations of 2T stacks and different 3T thickness configurations.
- Complete impact testing of selected spot welds under different loading conditions.

Technology Assessment

- Target: A spot weld modeling tool capable of incorporating the behavior of spot welds (strength, failure mode, and deformation rate effects) that is practical to use in advanced auto body structure crashworthiness computer aided engineering (CAE) for more efficient design of structures of AHSS for lightweighting while meeting crash requirement and cost-effectiveness goals.
- Gap: The prediction of spot weld failure of AHSS in finite element modeling (FEM) crash analysis is unsatisfactory, which greatly affects the overall accuracy of crash analysis of welded structure components.
- Gap: The lack of accurate crash analysis of welded structures impedes the rapid and optimum insertion of AHSS and other lightweight materials in auto body structures.

Introduction

The primary driver for increased use of AHSSs in auto body structures is the drastic improvements in performance while reducing the total vehicle weight. Resistance spot welding is by far the most common joining process used in automotive manufacturing. Typically, there are several thousand spot welds in a vehicle. Because the separation of spot welds can affect the crash response of welded structural components, the static and dynamic behavior of the spot welds has been one of the critically important considerations in vehicle design and manufacturing.

The CAE-based simulation of the crash behavior of auto body structures is an indispensable tool that enables rapid and cost-effective design and engineering of crashworthy automotive body structures. The prediction of spot weld failure in crashworthiness CAE simulation has been unsatisfactory for AHSSs and other lightweight metals such as aluminum (Al) and Mg alloys. The lack of fundamental understanding of and predictive capability for spot weld behavior is a critical barrier that hinders rapid and optimum insertion of lightweight materials in automotive body structures. Weld failures, detected in later stages of the new model car development cycle, have frequently resulted in design compromises that can adversely affect the weight savings available by using AHSS. Further lightweighting opportunities from optimized use of AHSS and other lightweighting materials are not possible without an improved understanding of the phenomena and the development of spot weld CAE tools.

Approach

This project is developing a new and robust approach to reliably predict the deformation and failure of spot welds in advanced crashworthiness CAE. These developments will provide solutions to the barriers for the design and engineering of crashworthiness for welding-intensive automotive body structures. The project covers multiple grades of AHSSs, weld configurations, welding conditions, and loading modes required for industry CAE implementation. The outcome is an optimized model that can be implemented in crash simulation finite element analysis codes used by automotive crash modelers.

A three-pronged approach, supported by experimental data, was used to develop the new spot weld modeling method.

- A SWE formulation and associated constitutive models, optimized for robustness in CAE simulation and practical to use by automotive crash modelers, with the complexity to incorporate weld geometry and microstructure effects are being developed.
- A physics based, integrated, electrical-thermal-mechanical-metallurgical spot weld process model is being developed which includes the weld geometry, microstructure, and residual stress results needed by SWE.
- A companion weld characterization and impact test database for development and validation of the new spot weld modeling approach is being developed.

Results and Discussion

In FY 2012 we completed detailed cataloging and characterizing of the resistance spot welds and their testing results generated in FY 2012. The testing matrix covered more than 220 unique combinations of materials and welding and mechanical testing conditions. Multiple duplicates of welds were produced for each combination. The specific information in the data in the welding and testing matrix comprises the following:

- four different grades of steels [dual phase (DP) 600, DP 980, transformation-induced plasticity (TRIP) 780, boron];
- four different surface coatings (hot dipped galvanized, hot dipped galvanized, hot dipped aluminized, and uncoated);
- three different thicknesses (1.0, 1.2, and 2.0 mm);
- 2T and 3T stackups;
- dissimilar steel welding (DP 600/DP 980, DP 600/TRIP 780, TRIP 780/boron);
- three different weld nugget sizes [minimum per American Welding Society (AWS) specification, maximum attainable without expulsion, and medium] for each combination of steel grade, coating, and thickness; and
- static testing under lap shear, cross tension, coach peel, and specially designed in-plane torsion conditions.

Cross-sectioning was performed on all spot weld combinations to determine the size and the shape of the weld nugget and the macroscopic voids or defects that can influence the strength of the welds. [Table 1](#) presents a collage of cross-sectional macros of 2T stackup welds between different steels. The collage of 3T stackup welds is shown in [Table 2](#). Compared to the 2T stackup welds, it is more difficult to produce defect-free welds in 3T stackup configuration. For example, solidification shrinkage voids were observed in boron steels for both the medium and maximum nugget sizes. The effects of such voids on the failure of spot welds under various loading conditions are being investigated.

Experimental microhardness mapping shows that boron steel exhibits considerable HAZ softening under all welding nugget sizes and welding conditions. The HAZ softening is less pronounced for DP 980, and TRIP 780 and DP 600 show minimal HAZ softening. Examples of the microhardness mapping are given in [Figure 1](#) for two dissimilar steel welds, boron/TRIP 70 and TRIP 780/DP 600. The microhardness mapping results (including the HAZ softening) were used in assisting the development of the spot weld model.

Table 1. Cross-sectional macros of 2T welds made between different steels.

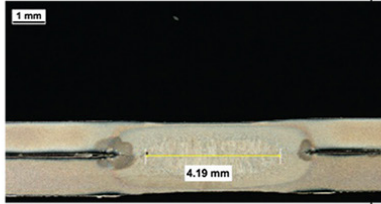
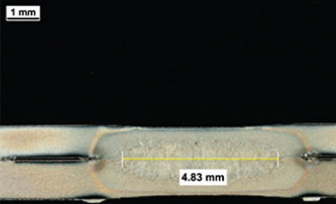
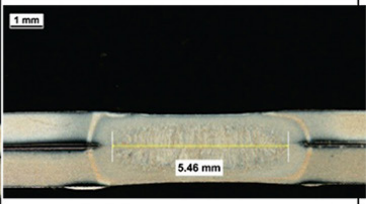
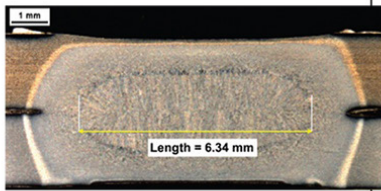
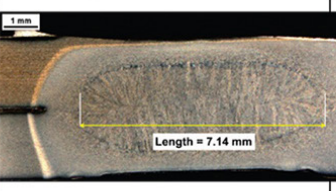
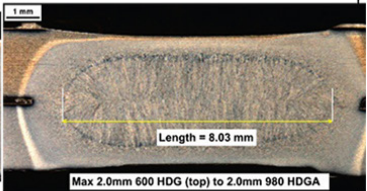
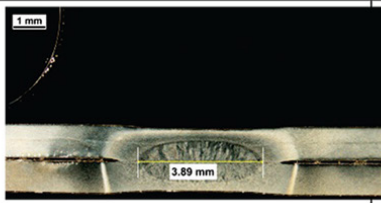
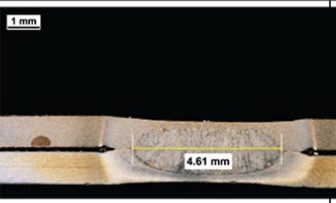
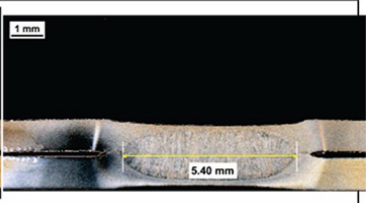
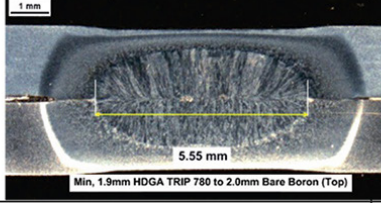
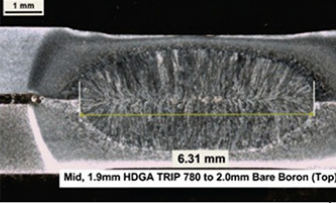
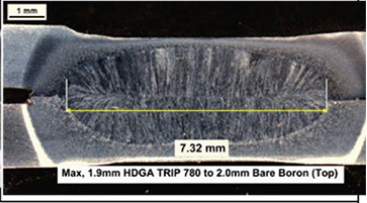
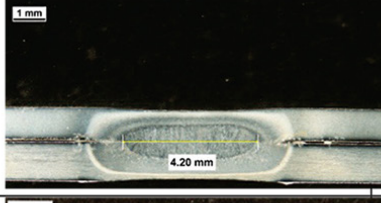
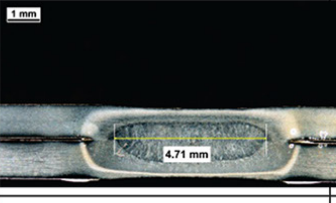
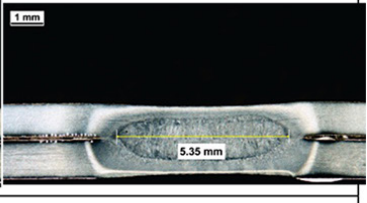
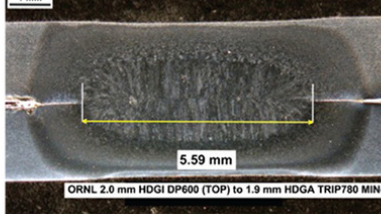
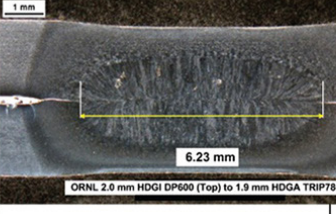
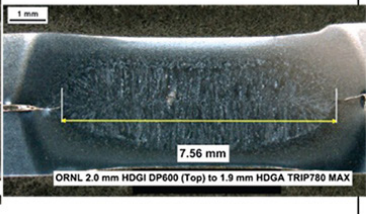
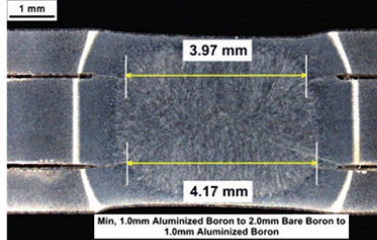
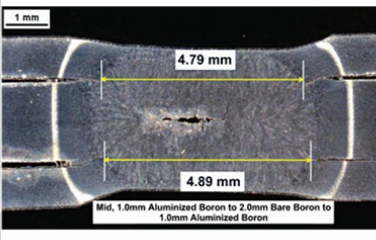
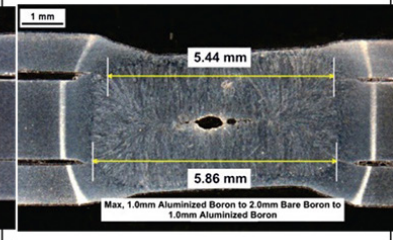
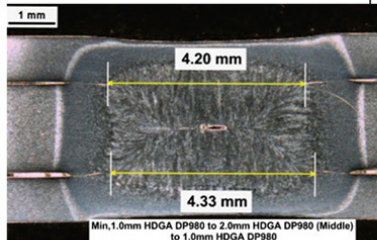
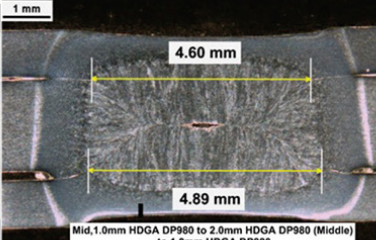
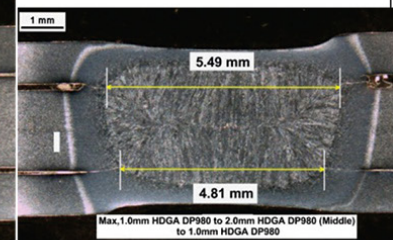
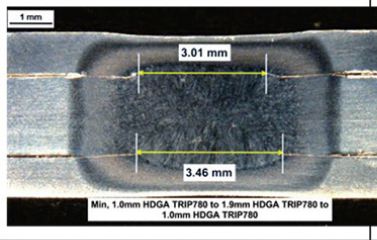
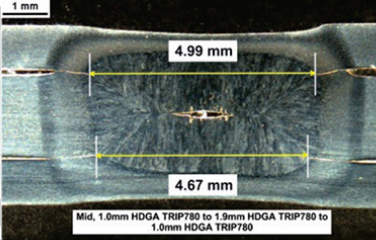
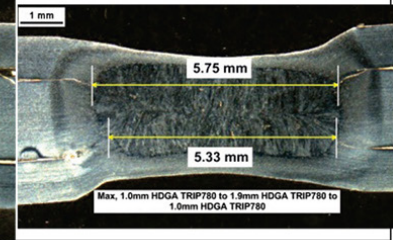
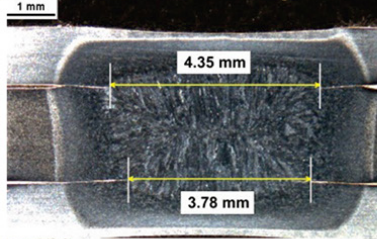
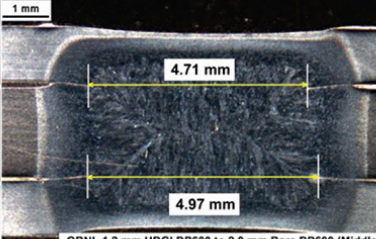
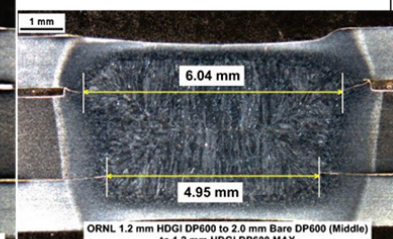
Material	Button size		
	minimum	medium	maximum
DP 980/DP 600 (1 mm/1 mm)			
DP 980/DP 600 (2 mm/2 mm)			
Boron/TRIP 780 (1 mm/1 mm)			
Boron/TRIP 780 (2 mm/1.9 mm)			
TRIP 780/DP 600 (1 mm/1.2 mm)			
TRIP 780/DP 600 (2 mm/2 mm)			

Table 2. Cross-sectional macros of 3T welds.

Material	Button size		
	minimum	medium	maximum
Boron			
DP 980			
TRIP 780			
DP 600			

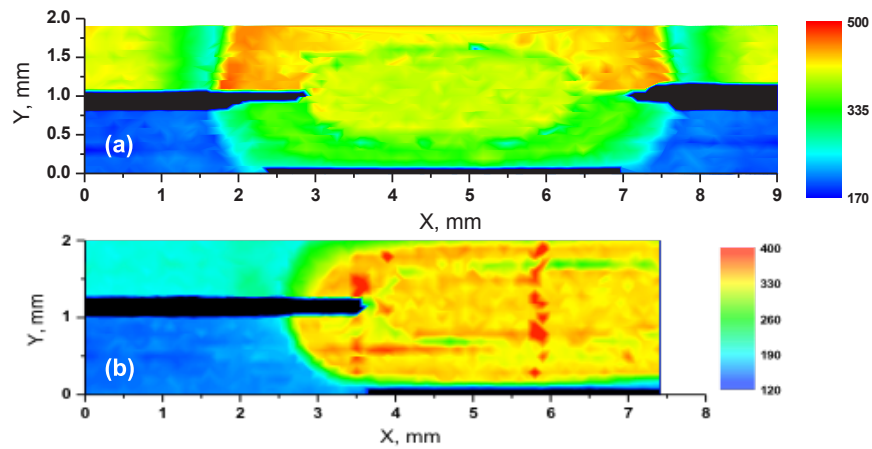


Figure 1. Microhardness mapping results: (a) 1 mm boron/TRIP 780 2T spot welds and (b) 2 mm TRIP 780/DP 600 2T spot welds. Both are shown for the minimum nugget size.

The local mechanical properties (stress-strain curves) in the weld region were characterized by means of small tensile specimens and miniature tensile specimens with the assistance of DIC methods. Figure 2 shows the dimensions of the tensile specimen in relationship to the spot weld configuration. The miniature tensile specimen was used to determine the stress-strain curves inside the weld nugget, whereas the small tensile specimen was for the composite behavior of both the weld nugget and the HAZ, especially the softening effect of the HAZ. For both test configurations, the testing material was electric discharge machined from the 3T stackup welds, with specimens being taken from the top, middle, and bottom sheet as shown in Fig. 2(c). Figure 3 shows the examples of the local stress-strain curves in boron steel welds. The small specimen results clearly illustrate the effects of the HAZ softening and the solidification voids. The miniature specimen measures the mechanical properties inside the weld nugget and the effect of solidification voids. The measured localized mechanical properties were used in the FEM model.

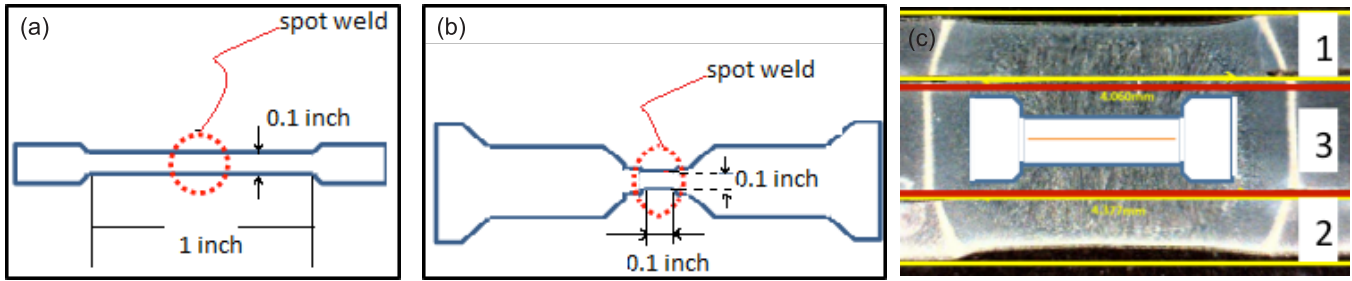


Figure 2. Schematics of (a) the small tensile specimen and (b) the miniature tensile specimen; (c) the miniature specimen in relation to the spot weld.

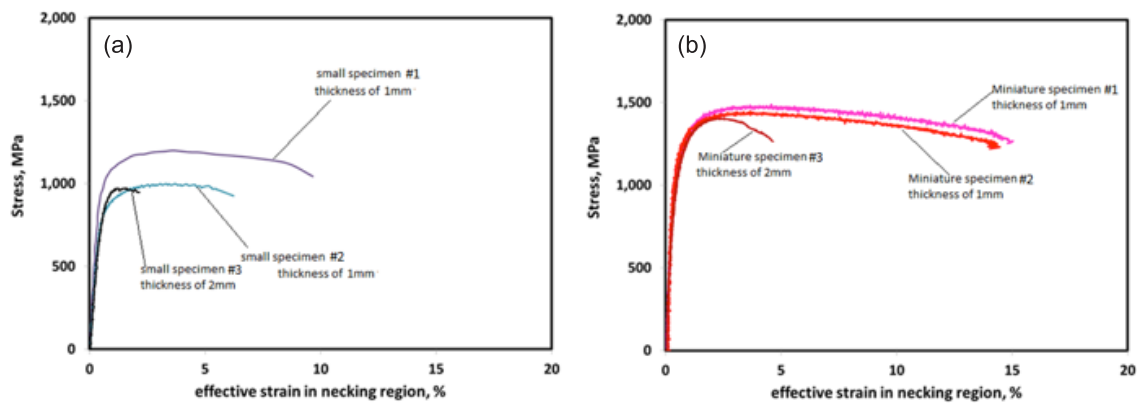
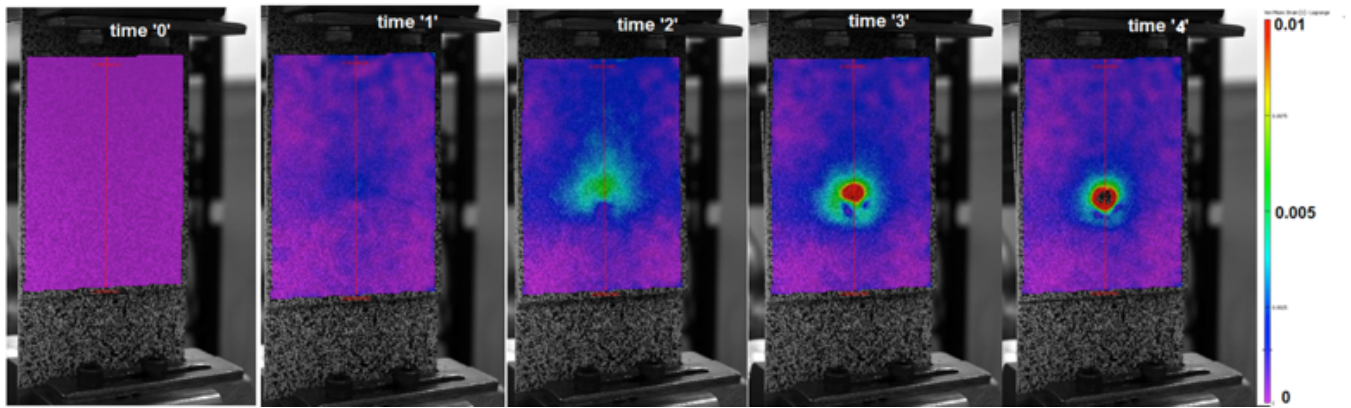


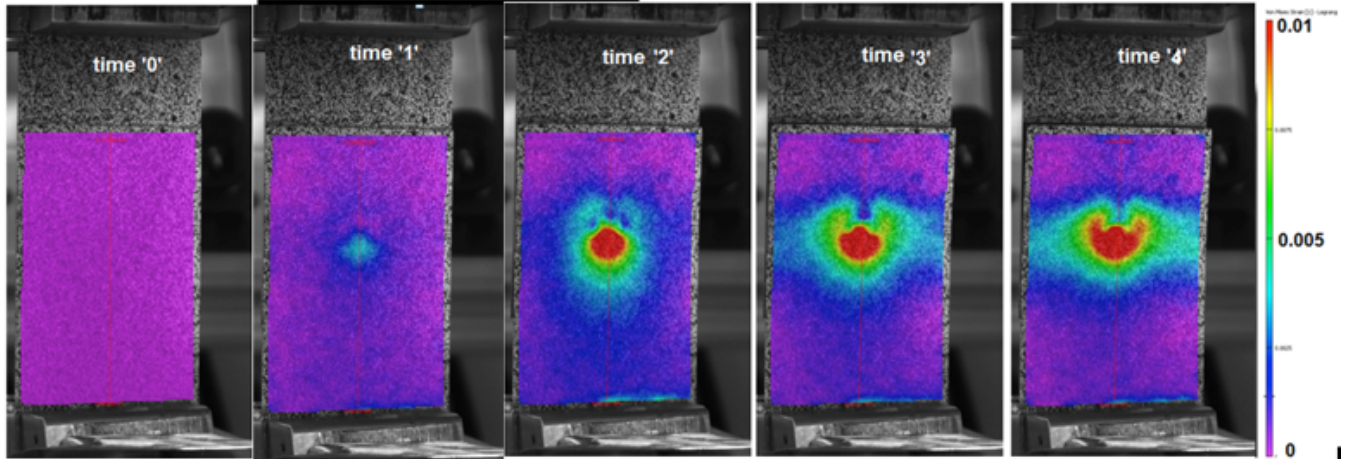
Figure 3. Stress-strain curves of (a) the small tensile specimens and (b) the miniature tensile specimens.

Full field DIC measurements were performed to study the surface strain development during lap shear tensile testing, correlate the local deformation behavior near the weld nugget region with the change in the failure mode (i.e., interfacial versus button pullout), and study the differences in deformation of dissimilar steel welds. Figure 4 presents the surface strain evolution of boron/TRIP 780 spot weld. There was considerably more localized deformation on the TRIP 780 side, although the button pullout failure occurred on the boron steel side. The measurement results were used to assist and validate the FEM spot weld model simulations.

The modeling development effort in FY 2012 focused on systematic full-scale three-dimensional (3D) solid element modeling of the spot weld to gain fundamental understanding of the deformation and failure of the AHSS spot weld and build the basis for the development of the computationally robust SWE model. To this end, a damage mechanics based failure criterion was developed and incorporated in the 3D solid element model. This new development, in concert with the use of local mechanical properties, made it possible to correctly predict the spot weld deformation and failure behavior of several different steel grades.



(a)



(b)

Figure 4. Strain evolution during lap shear tensile test for the 1 mm boron/TRIP 780 2T specimen with a minimum nugget size: (a) strain maps of the boron sheet and (b) strain maps of the TRIP 780 sheet.

Figure 5 shows the predicted failure mode for four different lap shear tensile testing cases of different steels, thicknesses, and stackup conditions. The model was capable of correctly predicting all the failure conditions experimentally observed. The model was also capable of consistently predicting the force-displacement as shown in Figure 6.

Based on the results of the detailed full-scale 3D solid element modeling, we began to develop a SWE formulation using the cohesive element. We expect to complete the development of the SWE model in FY 2013.

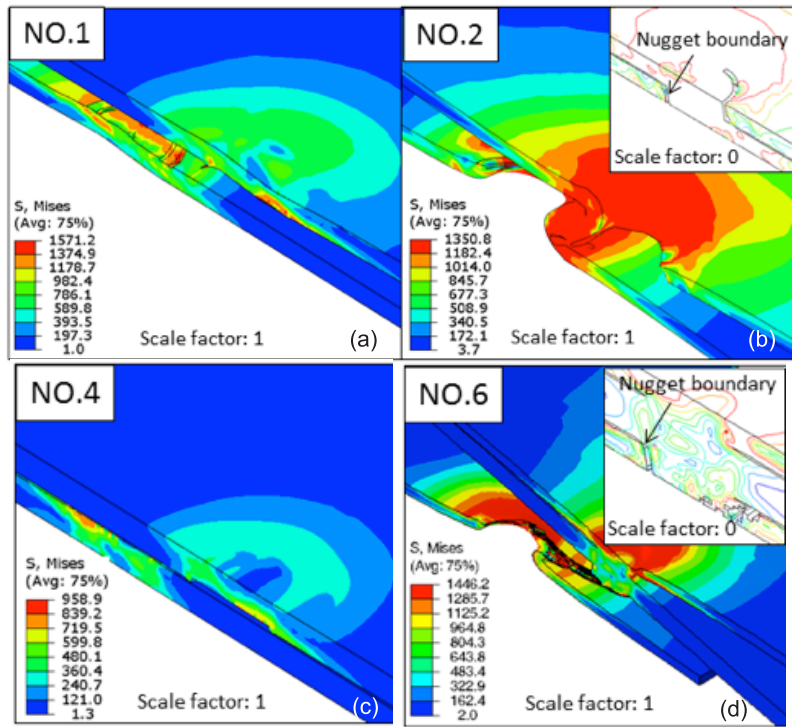


Figure 5. Von Mises stress contours and predicted failure modes for (a) 1 mm thick boron steel with 4 mm weld nugget exhibiting interfacial failure, (b) 1 mm thick boron steel with 4.8 mm weld nugget exhibiting button pullout failure, (c) 2 mm thick DP 980 with interfacial failure, and (d) 3T boron steel with button pullout failure at the nugget boundary.

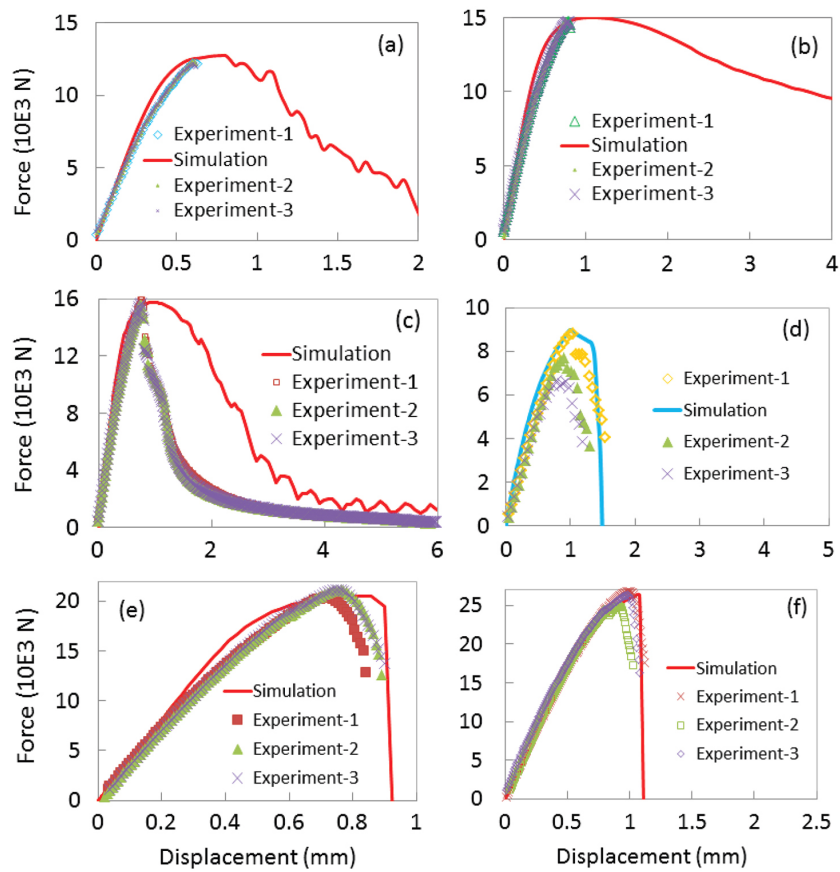


Figure 6. Comparison of lap shear load versus displacement curves between the model prediction and experimental measurements for (a) 1 mm thick boron steel with interfacial failure (2T, 4 mm weld nugget), (b) 1 mm thick boron steel with button pullout failure (2T, 4.8 mm weld nugget), (c) 1 mm thick boron steel with button pullout failure (2T, 5.5 mm weld nugget), (d) 2 mm thick DP 980 steel with interfacial failure (2T, 5.7 mm weld nugget), (e) 2 mm thick DP 980 steel with interfacial failure (2T, 6.8 mm weld nugget), and (f) 3T boron steel with button pullout failure (4 mm weld nugget).

Technology Transfer Path

An initial version of the integrated weld process model has been licensed and transferred to selected industry partners. An experimental database has been developed for use by original equipment manufacturers (OEMs) and suppliers. Beta testing of the spot weld model is planned with selected automotive OEMs. Finally, technology transfer of the SWE model is expected through licensing the code and through publication of the basic theories and mathematical formulations of the model.

Conclusions

In FY 2012, considerable progress was made on both comprehensive analysis and characterization of the spot weld and testing data produced in FY 2011 and use of the detailed full-scale 3D solid-element FEM model to gain fundamental understanding of the deformation and failure of spot welds to build a sound basis for the development of the computationally robust SWE model. The local materials properties in the weld nugget and HAZ were determined through a combination of microhardness mapping and small and miniature specimen tensile testing. Full field deformation evolution during lap shear tensile testing was obtained for model validation. A ductile failure initiation and evolution damage mechanics based failure model was developed successfully to catch the deformation and failure behavior for spot welds of AHSSs. The model was tested among various materials and geometric configurations. The failure mode prediction capability was verified by the experimental observations. The predicted force-displacement curves agreed well with the tested results.

Friction Stir Spot Welding of Advanced High Strength Steel II

Principal Investigator: Zhili Feng, ORNL
(865) 576-3797; fax: (865) 574-4928; e-mail: fengz@ornl.gov

Contributors: Tsung-Yu Pan, Mike Santella, ORNL

Industry Contributors: Ford Motor Company, General Motors Company (GM), Chrysler Corporation, MegaStir, Ceradyne, Inc., Kawasaki

Accomplishments

- For weld times of 4 s, the maximum lap shear tensile strengths measured were 17 kN for DP 780, 22 kN for galvanized DP 780, and 16 kN for hot-stamped boron steel (HSBS). All of these values exceeded the minimum specified in the AWS specification for resistance spot welds.
- For otherwise identical welding conditions, increasing tool rotation speed from 800 to 1,600 rpm increased strength values for spot welds made with DP 780 and galvanized DP 780 (DP 780GA). Using a two-step process rather than a one-step process had a similar effect. Metallographic examinations indicated this is at least partly related to increased bonded area.
- Stir tools made of six different tool materials were evaluated. The materials included a tungsten 25% rhenium alloy, polycrystalline cubic boron nitride (PCBN), silicon nitride (Si_3N_4), titanium diboride, tungsten carbide-cobalt, and a cermet made of complex carbides bonded by a refractory metal alloy.
- PCBN demonstrated the most promise as a stir tool. Wear rates in PCBN tools appeared to be very low, although quantitative evaluation of tool wear was beyond the project scope. Potential disadvantages of PCBN are that the overall durability, availability, and cost may prove prohibitive for widespread commercial applicability.

Future Direction

- The primary future plan is to transfer the results to an industrial FSSW machine maker such as Kawasaki for potential implementation at automotive OEMs.

Technology Assessment

- Target: Determine the technical and economic feasibility of FSSW to join AHSSs in terms of joint strength, processing time, and cost benefits. This will be done relative to AWS specifications and resistance spot weld methods.
- Gap: Joining of AHSS by conventional joining processes such as resistance spot welding can be challenging because of weld quality issues related to the degradation of weld microstructures and the resulting degradation of properties.

Introduction

An initial project on FSSW of AHSSs showed that friction stir spot welds made in high strength steels could develop acceptable tensile lap shear strengths. Efforts were also made to improve joint strength through systematic investigations into weld process parameters and tool design. This was accomplished primarily by using redesigned tools and refined operating parameters, the selection of which was guided by analysis of process output data, microstructure analysis, and strength testing. Two important conclusions of the initial project relate to process cycle time and tooling costs. In FY 2011, friction stir spot welds of various combinations of HSBS, DP 780, DP 980, TRIP 590, and TRIP 780 were demonstrated to be capable of exceeding minimum values required for resistance spot welds. However, it is unlikely that this process will ever have spot welding times competitive with those of resistance spot welding. It was also determined that tools made of PCBN would not be able to meet the process cost target to compete effectively with resistance spot welding electrodes. To address this, low cost Si_3N_4 stir tools, which cost about 30 times less than PCBN tools, were studied. In FY 2011, a concave shoulder Si_3N_4 stir tool was tested with results of weld strength and durability comparable to the PCBN tool of a similar geometry. Comparing the results with various PCBN tool geometries, a convex shoulder tool was shown to have better weld strength than the concave shoulder tool.

Approach

This project is a collaborative effort between ORNL and Pacific Northwest National Laboratory. A panel of consultants, including representatives from Chrysler, Ford, and GM, has been active in guiding technical activities. Guidance on specific technical issues has also been solicited from MegaStir (PCBN friction stir tool manufacturer), Ceradyne (Si_3N_4 manufacturer) and Kawasaki (robot manufacturer).

The project team manufactured convex shoulder tools out of Si_3N_4 and tested their process performance and weld quality (quasi-static and fatigue strengths) in FY 2012. FSSW was used to join AHSSs: DP 780GA, TRIP 780 MPa steel (TRIP 780), and HSBS. FSSW tools were made of EKasin direct injection molded Si_3N_4 from Ceradyne. Welds were made by a two-step displacement control process with weld times of 4, 6, and 10 s. Quasi-static joint strength was tested at ORNL. Fatigue testing was subcontracted to Professor Jwo Pan at the University of Michigan.

The concave (DIM97) and convex (SN11) shoulder tools are shown in [Figures 7 and 8](#). Both had shoulder diameters of 10 mm. The tips were 5 mm in diameter and 2 mm in length. Three equally spaced flat features were cut on the end of the pins to aid with stirring action. The SN11 tool had the additional feature of spirals on the shoulder surface.

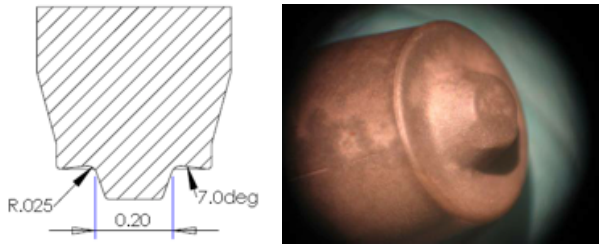


Figure 7. FSSW tool geometry of concave shoulder tool (DIM97).

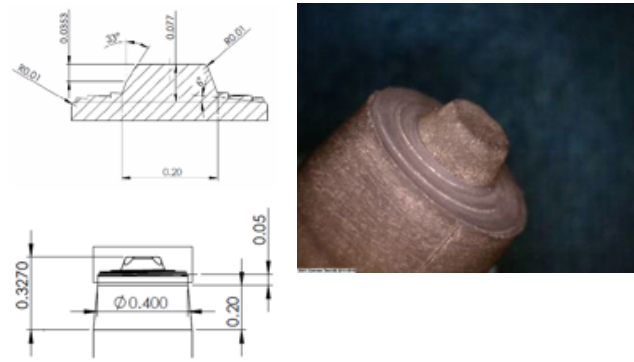


Figure 8. FSSW tool geometry of convex shoulder tool (SN11).

Results and Discussion

Figures 9 and 10 show the failure load from lap shear tests of DP 780GA-HSBS and TRIP 780-HSBS combinations by tools DIM97 (concave) and SN11 (convex). For each of the material combinations and FSSW times, welds made with the convex tool always gave higher load to failure than those made with the concave tool and exceeded minimum values required of resistance spot welds.

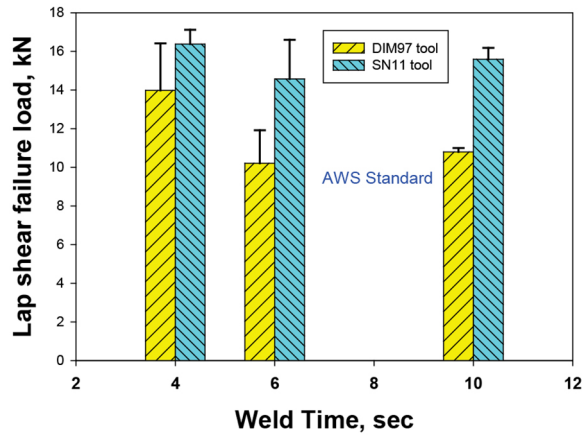


Figure 9. Lap shear failure load of FSSW welds made of DP 780GA-HSBS.

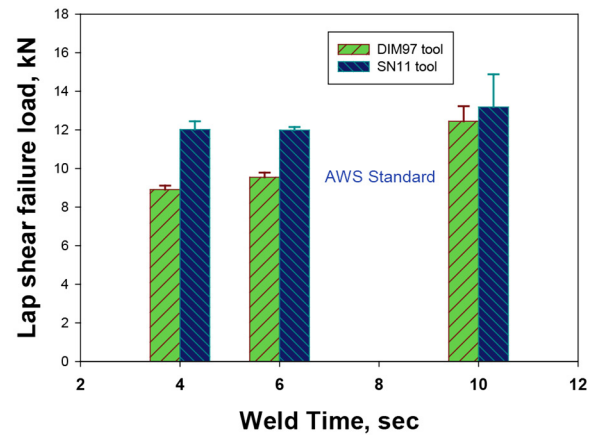


Figure 10. Lap shear failure load of FSSW welds made of TRIP 780-HSBS.

There was no apparent wear on tools throughout the study within the number of welds made. A more systematic study of tool wear is a part of the ongoing study.

Due to a material shortage, only DP 780GA-HSBS welds (not TRIP-HSBS) in lap shear specimens were made to examine whether fatigue performance is also better for welds made with the convex tool. Lap shear specimens with DP 780GA-HSBS welds were tested under cyclic loading conditions. The load ratios were set at 0.1 and 0.2, and the effect of the load ratio on fatigue life appears to be minimal. Figure 11 shows the experimental results for DP 780GA-HSBS welds in lap shear specimens made with the concave and convex tools. The welds made by the convex tool also gave a higher fatigue life for a given load range under low-cycle loading conditions. This is quite consistent with the higher strength for the welds made with the convex tool under quasi-static loading conditions. The apparent drop at the low life cycle end (between 100-1000 cycles) for the convex tool was likely the test data scattering common in fatigue testing.

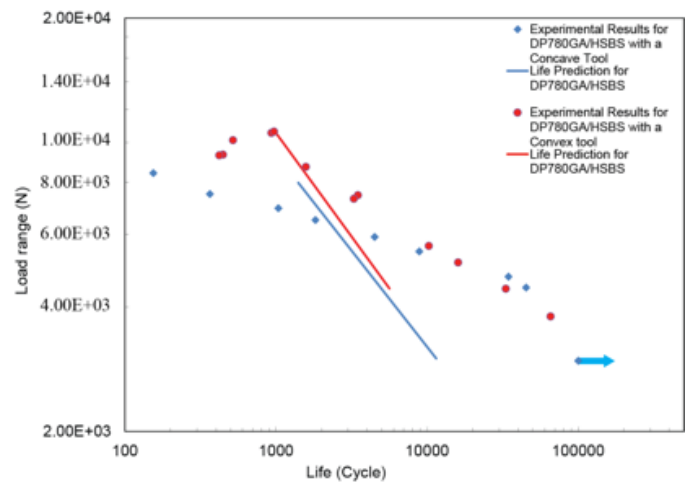


Figure 11. A comparison of the experimental results and fatigue life estimations for DP780GA-HSBS welds made with (a) a concave tool and (b) a convex tool.

Based on the observed failure modes, a kinked fatigue crack growth model was adopted to estimate fatigue life. As an initial development of the model, the stress intensity factor solutions for life estimations are based on the closed-form solutions for idealized spot welds in lap shear specimens of equal sheet thickness. The fatigue life estimations based on the kinked fatigue crack growth model are also shown in the figure. Although the model prediction is promising under low-cycle loading conditions improvement is necessary, especially for the high-cycle loading conditions. For example, computational stress intensity factor solutions for the welds with the actual profiles with the reduced thicknesses near the crack fronts would be considered for an estimation of fatigue lives. Further research should be carried out to improve the fatigue estimation method.

Technology Transfer Path

We are working with a major automotive tier one supplier, Kawasaki Robotics, USA in Wixom, Michigan, to conduct trials on their robotic equipment based on the tools and process parameters developed at ORNL since FY 2012. Robotic equipment will be better received and more adaptable to the automotive manufacturing environment than the gentry-type MTS machine used during the development phase at ORNL. The joint strength, tool durability, and process parameters will be verified during the trials at Kawasaki and transferred to potential OEM customers.

Conclusions

Lap shear testing indicated that friction stir spot welds of various combinations of HSBS, DP 780, and TRIP 780, made with convex Si_3N_4 stir tools, have higher quasi-static and fatigue strength than those made with concave tools. The quasi-static strengths exceed the minimum values required of resistance spot welds.

Improving Fatigue Performance of AHSS Welds (ORNL–ArcelorMittal Cooperative Research and Development Agreement)

Principal Investigator: Zhili Feng, ORNL
(865) 576-3797; fax: (865) 574-4928; e-mail: fengz@ornl.gov

Principal Investigator: Benda Yan, ArcelorMittal USA
(219) 399-6922; e-mail: benda.yan@arcelormittal.com

Contributors: Wei Zhang, Dongxiao Qiao, Stan David, ORNL; Wenkao Hou, ArcelorMittal; Wesley Wang, Esab; Stephen Liu, Sindu Thomas, Colorado School of Mines

Accomplishments

- Developed a new weld fatigue testing specimen configuration that is essential to maintain the weld residual stress field representative of actual welded automotive body structures.
- Completed a comprehensive survey of open literature to collect the published chemistry of low transformation temperature (LTT) filler wires. Downselected and produced three different types of baseline LTT filler wires.
- Completed the initial fatigue testing of baseline welds fabricated with both conventional filler wire and the LTT filler wires to generate the applied stress magnitude against cycles to failure (S-N) curves.
- Completed the initial development of a weld thermal-metallurgical-mechanical model to gain understanding on the effect of low temperature phase transformation on the formation of compressive weld residual stress at the fatigue cracking initiation region.

Future Directions

- Measure the near surface weld residual stress distribution in the baseline welds using techniques such as ASTM hole-drilling, x-ray diffraction, and/or neutron diffraction.
- Study the phase transformation kinetics and associated lattice/volume change for LTT filler metals using thermomechanical testing in Gleeble system and a novel in situ neutron diffraction experiment developed in a synergetic activity.
- Complete the development of a 3D weld residual stress model to determine the phase transformation effect at the weld start and stop regions where fatigue cracking initiation is typically observed in fatigue testing. Validate the 3D weld model using the experimental residual stress data.
- Develop the next generation of LTT filler metals with balanced properties of compressive surface stress, weld toe geometry, and resistance to fatigue cracking.

Technology Assessment

- Target: Develop robust, in-process weld fatigue life improvement technologies that can be used to join AHSS auto-body structural components with cost penalties acceptable to the auto industry.
- Gap: The weld fatigue strength in the as-welded condition does not increase in proportion to the yield/tensile strength of AHSS. The insensitivity of weld fatigue strength to steel static strength is a major barrier for lightweighting through down-gauging for chassis and other load-bearing components.
- Gap: Today's weld fatigue improvement techniques are mostly post-weld based. The added steps are cost prohibitive in the high volume mass production automotive environment, and there is great variability in the fatigue life achieved by the post-weld based techniques.

Introduction

Under a cooperative research and development agreement (CRADA), ORNL and ArcelorMittal USA are working together to develop the technical basis and demonstrate the viability of innovative technologies that can substantially improve the weld fatigue strength and durability of automotive body structures. Durability is one of the primary metrics in designing and engineering automotive body structures. Fatigue performance of welded joints is critical to the durability of a body structure because the likeliest locations for fatigue failure are often at welds. Recent studies by the Auto/Steel Partnership Sheet Metal Fatigue Committee, DOE's Lightweighting Materials Program, and others (Bonnen, 2006; Yan, 2005; Iyenger, 2008; Feng, 2008; Feng 2009) have clearly revealed that, unlike the base metal fatigue strength, the weld fatigue strength of AHSS is largely insensitive to the base metal composition, microstructure, and strength under typical welding conditions used in body-in-white (BIW) manufacturing. The lack of an inherent weld fatigue strength advantage of AHSSs over conventional steels is a major barrier for vehicle weight reduction through down-gauging. Down-gauging leads to increases in material stresses, thereby reducing durability under the same dynamic loading conditions. A recent comparative study (Feng, 2011) reveals that other lightweight alloys such as Al and Mg alloys may not offer improved weld fatigue strengths on a specific weight (strength divided by density) basis. Therefore, solutions to improve the fatigue strength of welds are critical to BIW lightweighting for all light metals.

Approach

Instead of using post-welding techniques to improve the weld fatigue strength, this project focuses on developing in-process weld technology as part of the welding operation. The overall goal of the project is developing effective ways to control and mitigate the key factors governing the fatigue life of AHSS welds, including weld residual stress, weld profile, and weld microstructure/chemistry. This joint research effort also fully utilizes state-of-the-art integrated computational weld engineering (ICWE), neutron/synchrotron and other advanced residual stress measurement techniques, and fatigue testing and microstructure analysis capabilities at ORNL and ArcelorMittal Global R&D to perform the research and development.

The project is investigating effective means to control and mitigate the key factors governing the fatigue life of AHSS welds, including weld profile, weld residual stress, and weld microstructure/chemistry. Two specific in-process approaches will be further developed in this project. Technical and economic issues unique to the automotive body structural welding environment have been identified and will be addressed.

Results and Discussion

In FY 2012 the specific focus of the project was the establishment of welding and fatigue testing equipment and a computational weld mechanics model for studying the effect of volumetric change due to low temperature phase transformation on the formation of surface compressive stress. Major automotive OEMs were surveyed to identify weld patterns representative of those in vehicle AHSS structures. Based on the survey findings, a new weld fatigue testing specimen configuration was developed with the assistance of finite element structural analysis.

Figure 12(a) shows the typical chassis and engine motor mount structures assembled using stitches of gas metal arc seam welds. Considering the representative weld pattern, a special weld fatigue specimen configuration was designed, as shown in Figure 12(b). This specimen was fabricated by placing a 50 mm long seam weld on a lap joint of two steel sheets. This is the most commonly used weld type in automotive structures. Moreover, the specimen contains both weld start and stop, which are the critical locations for fatigue crack initiation. The special weld fatigue specimen configuration not only maintains the weld residual stress field representative of actual seam welds but also produces the stress-strain conditions representative of those endured by vehicle structural welds.

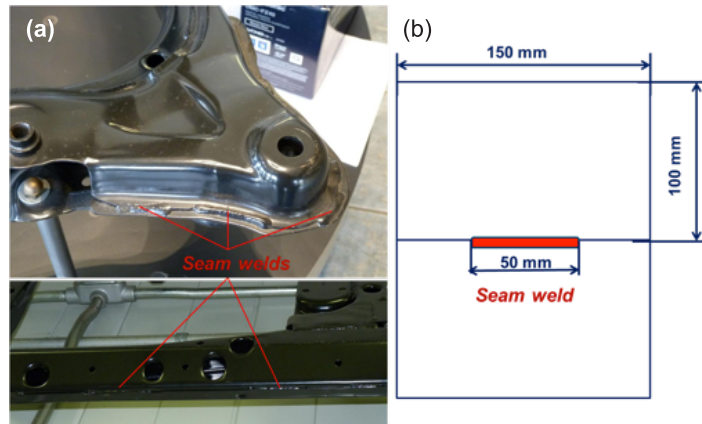


Figure 12. (a) Representative welding pattern used for assembling automotive body structures and (b) special weld fatigue specimen configuration.

An ArcelorMittal robotic gas metal arc welding (GMAW) system with cold metal transfer function available at ArcelorMittal, shown in Figure 13(a), was used to fabricate baseline welds. The fatigue testing system at ArcelorMittal, shown in Fig. 13(b), was modified for testing the specific weld specimen configuration to generate the S-N curves of various welds.

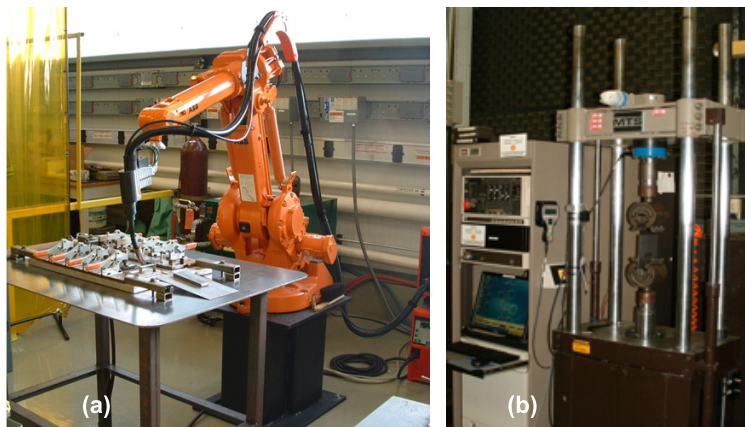


Figure 13. (a) Welding and (b) fatigue testing systems at ArcelorMittal.

A comprehensive open literature survey was carried out on the low temperature phase transformation research. Four different types of baseline LTT filler wires were downselected and produced in FY 2012 for welding and fatigue testing.

ORNL's ICWE model was used to analyze the effect of low temperature phase transformation and other relevant welding and geometric factors on the weld residual stress distribution. The ICWE model first calculates the transient temperature distribution during welding. The temperature history is then input to a martensitic phase transformation submodel to obtain the volume change (or transformation plasticity) upon weld cooling. Finally, the temperature profile and the transformation plasticity are used in the mechanical model to predict the resulting residual stress distribution in the welded sheets. The representative lap joint testing coupon shown in Figure 12 was modeled. Figure 14 shows the finite element geometry and mesh of the seam weld of the lap joint. The predicted temperature distributions at different times during welding are plotted in Figure 15. The interaction between the heat source and workpiece results in rapid heating and formation of the weld pool, indicated by the red region in Figure 15(a) to 15(c). As the heat source travels, an elongated weld pool shape is formed. As soon as the welding is completed (at time = 5 s), the entire weld cools down rapidly. The spatial distribution of temperature is highly nonuniform, which is a major driving force for the formation of residual stresses.

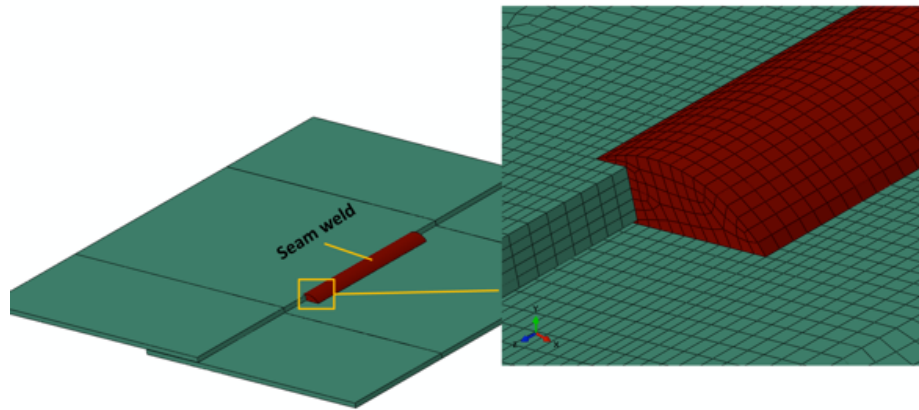


Figure 14. Finite element geometry and mesh of the seam weld of a lap joint.

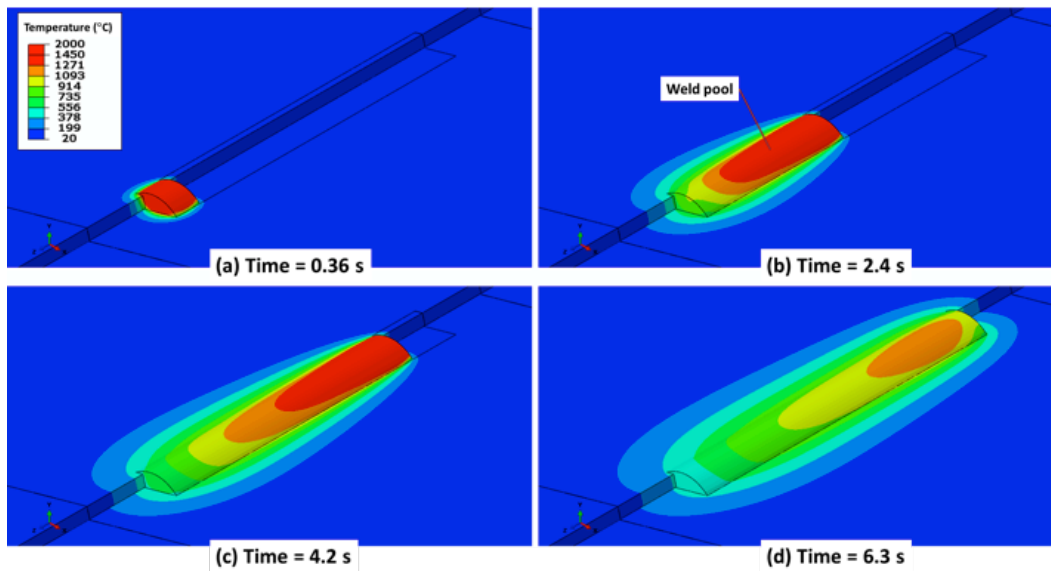


Figure 15. Temperature distribution at different times during seam welding.

With knowledge of weld temperature distribution, the formation of residual stresses can be calculated taking into account the plasticity associated with low temperature martensitic transformation. The metallurgical submodel for describing the martensitic transformation as a function of chemistry and cooling rate is under development. Figure 16 shows an example of the 3D weld residual stress distribution. The stress concentration near the weld start location is apparent. The 3D model will be validated using the experimental residual stress data in FY 2013. The validated model will then be used to determine the LTT effect at the weld start and stop regions, where fatigue crack initiation is typically observed.

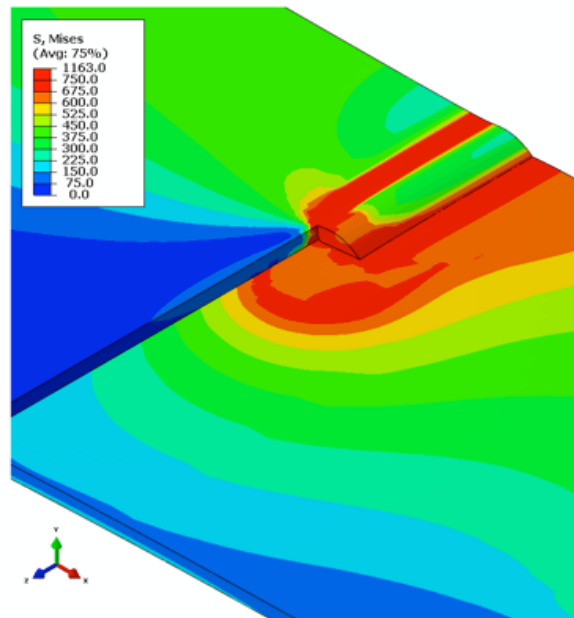


Figure 16. Contour plot of von Mises residual stress concentration near the weld start location (weld made with conventional weld filler metal).

Four different types of LTT wires were produced in FY 2012. They were used to make weld testing coupons and subjected to fatigue testing to develop a baseline knowledge of the performance of the LTT wire in terms of weld fatigue, residual stress, etc., to assist in refinement and optimization of the LTT wire and welding practices scheduled in FY 2013 and beyond. The conventional ER70S-3 filler wire was also used for comparison. The fatigue testing is resource intensive and time consuming. First round fatigue testing of the LTT wire is still in progress. Nevertheless, we have identified one LTT file wire that shows promising improvement in weld fatigue life under the high cycle and low stress conditions that are mostly relevant to the durability of the auto body structures.

In addition, a new welding procedure was investigated in FY 2012. Initial fatigue testing in FY 2012 suggested that this new welding procedure could also improve the weld fatigue life. This new welding procedure will be further studied and refined in FY 2013.

Technology Transfer Path

The primary technology transfer path is to work closely with the project industrial partners, a major steel supplier and a major welding consumables manufacturer, that have the business interests and the marketing capability to quickly commercialize the technology developed in this project. In addition, we plan to disseminate the findings and results from the project to automotive OEMs and other interested parties through the extensive communication channels that we have established over the years.

Conclusions

Weld fatigue life has been identified as one of the key technology barriers to widespread use of lightweight materials (AHSS and Al and Mg alloys) for auto body structure lightweighting. The technology developed in this project is expected to provide cost-effective and practical solutions to the automotive industry to address this critical issue.

The specific focus in FY 2012 was the establishment of welding and fatigue testing equipment and a computational weld mechanics model for studying the effect of volumetric change due to low temperature phase transformation on the formation of surface compressive stress. The initial fatigue testing of baseline welds fabricated using four types of LTT wires has been completed. Factors governing the weld fatigue life (e.g., residuals stress state, weld macro profile, and microstructure) are being characterized. Significant activities are planned in FY 2013 to develop the technical and scientific bases for tailored design of next generation LTT filler metal with balanced properties of compressive surface stress, weld toe geometry, and resistance to fatigue cracking.

Online Weld Quality Monitor and Control with Infrared Thermography

Principal Investigator: Zhili Feng, ORNL
(865) 576-3797; fax: (865) 574-4928, e-mail: fengz@ornl.gov

Project Team: Jian Chen, Ralph B. Dinwiddie, Wei Zhang, ORNL
Partner: Benda Yan, ArcelorMittal
(219) 399-6922; fax: (219) 399-6562; e-mail: benda.yan@arcelormittal.com

Partner: Martin Jones, Ford Motor Company
(313) 805-9184; fax: (734) 458-0495; e-mail: mjone147@ford.com

Partner: Blair Carlson, GM
(586) 864-7698; fax: (413) 702-2091; email: blair.carlson@gm.com

Accomplishments

- Developed the first prototype of a fully automated online real-time IR inspection system that meets the inspection requirements of the mass production environment and can be readily integrated into existing production lines.
- Identified new IR signatures and refined IR data analysis algorithms with improved accuracy and reliability for both real-time and postmortem applications.
- Generated a reference weld quality database consisting of nugget size, weld thickness (indentation depth), weld shape, and stuck welds and porosity for a wide range of steels, coatings, thicknesses, and stackup configurations.
- Demonstrated the overall satisfactory system performance for both real-time and postmortem inspection for a wide range of spot weld conditions under laboratory testing conditions.

Future Directions

- Complete the postmortem prototype IR inspection system (hardware and software integration).
- Conduct beta testing of both the real-time and postmortem prototype systems with additional welds.
- Perform field demonstration of the IR inspection expert system to confirm the feasibility and robustness of the system to OEMs and other stakeholders.

Technology Assessment

- Target: A spot weld quality inspection system based on IR thermography that can detect the stuck weld, weld nugget size (up to 0.2 mm resolution), and surface indentation (up to 0.1 mm resolution) in both the two layer (2T) and three layer (3T) stackup configurations.
- Target: An inspection system that can meet or exceed the inspection cycle time requirements dictated by the mass production assembly line environment, including (1) collection time less than 2–3 s for online inspection, (2) collection time less than 5–10 s for offline inspection, and (3) data analysis and decision making time less than 1–2 s.
- Gap: Automated, robust, and efficient IR image acquisition and analysis algorithms and hardware systems to determine weld quality within the targeted time period and with the necessary quality and weld attribute resolution currently do not exist.

Introduction

Resistance spot welding is the most widely used technology for assembling auto body structures. Variations in welding conditions, part “fit-up,” and other production conditions inevitably occur in the complex, high volume BIW assembly process. These variations can result in out-of-tolerance joints that impair the quality and performance of the vehicles. The

increased use of AHSSs and other lightweight metals is expected to pose even more stringent requirements on joint quality. Despite the extensive research and development efforts over the years, nondestructive weld quality inspection still remains a critical issue for the auto industry, largely due to the unique technological and economical constraints of the auto production environment: any weld quality inspection technique must be fast, low cost, and low in false rejection rate and not interfere with the highly automated welding fabrication process. Inspection systems that meet these requirements do not currently exist.

This project aims at developing a field-deployable, online weld quality monitoring method based on IR thermography. A distinct advantage of IR thermography as an NDE tool is its nonintrusive, noncontact nature. This makes the IR based tool especially attractive for the highly automated BIW assembly lines.

Approach

The project consists of the following major tasks to achieve the project goal.

- Refine and optimize the field-deployable IR measurement techniques that can reliably detect the characteristic thermal signature patterns of various weld quality attributes both in real time and in postmortem online inspection.
- Develop the robust IR image analysis software that, in real-time, can analyze the IR thermal image for the characteristic signature of various weld defects and weld joint configurations to provide quantitative measure of the quality.
- Develop a prototype IR weld quality monitoring expert system (hardware and software) that is cost effective and suitable for field demonstration.
- Validate and demonstrate the effectiveness and robustness of the technology for a wide range of spot welds made with different steel grades, coatings, thicknesses, and stackup configurations with varying quality attributes (nugget size and indentation depth, etc.) commonly encountered in BIW production.
- Identify and work with potential industry entities for technology transfer and eventual commercialization.

A unique prerequisite for the IR thermography based NDE technology in automotive applications is that the surface of the materials and welds cannot receive any special treatments. All the development and testing in this project is on the as-welded or as-received surfaces.

Results and Discussion

In FY 2012, significant progress has made in three major areas: (1) identification of new weld quality IR thermal signatures and the associated data analysis algorithms that greatly improved the sensitivity and accuracy of weld quality determination; (2) a data acquisition system for automated IR image acquisition, hardware control, system triggering, and synchronization; and (3) a fully automated prototype inspection system that integrates the IR signature analysis expert system and the inspection hardware for both postmortem and real-time application. In addition, a new IR signature and data analysis method has been developed to positively quantify noncircular weld shapes produced in nonideal welding conditions. Moreover, the expert system software has been refined so it can complete the intensive data analysis within 3 s on a moderate performance personal computer.

Extensive testing and development of both the real-time and postmortem approaches were conducted against a variety of AHSSs with different grades, thickness gauges, coatings, and stackup configurations. **Table 3** presents the testing matrix completed to date on both 2T and 3T stackups. Each combination includes a set of spot welds carefully produced with a range of weld quality attributes (such as different nugget sizes, indentations, and defects).

To establish the reference weld quality data necessary, a select number of welds was evaluated destructively to measure the weld nugget size, existence of surface cracking and/or porosity defects, and weld hardness and microstructure. (The destructive measurement technique and examples of destructive measurement were summarized in the FY 2011 report.) That data are used to correlate the IR thermal signals to the weld quality. The destructive measurements were highly labor intensive and time consuming (4–8 h/sample). To effectively evaluate several hundred weld coupons, the computerized

ultrasonic C-scan method was also used this year. In the ultrasonic C-scan method, the weld sample and ultrasonic transducers are submerged in a water tank to use water as the couplant. C-scan measurement of a weld typically took several minutes to complete. Because of this, the underwater C-scan is not suitable for the automotive assembly line although it yielded high fidelity results on weld nugget size, porosity defects, and weld shape (Figure 17).

Table 3. Testing matrix completed to date.

2T stack			3T stack		
Steel Grades, Coating, Thickness	Post-mortem	Real-time	Steel Grades, Coating, Thickness	Post-mortem	Real-time
• DP590 Galvanized 1.2mm • DP590 Galvanized 1.2mm	X	X	• Boron Aluminized 1.0mm • Boron 2.0mm • Boron Aluminized 1.0mm	X	X
• DP590 Galvanized 1.8mm • DP590 Galvanized 1.8mm	X	X	• DP600 HDGI 1.0mm • DP600 2.0mm • DP600 HDGI 1.0mm	X	X
• DP980 Cold rolled 1.2mm • DP980 Cold rolled 1.2mm	X	X	• DP980 HDGA 1.0mm • DP980 HDGA 2.0mm • DP980 HDGA 1.0mm	X	X
• DP980 Cold rolled 1.2mm • DP980 Cold rolled 2.0mm	X	X	• TRIP780 HDGA 1.0mm • TRIP780 HDGA 2.0mm • TRIP780 HDGA 1.0mm	X	X
• DP980 Cold rolled 2.0mm • DP980 Cold rolled 2.0mm	X	X			
• Boron Aluminized 1.0mm • Boron Aluminized 1.0mm	X				
• Boron Aluminized 1.0mm • Trip780 HDGA 1.0mm	X				
• DP980 HDGA 1.0mm • DP980 HDGA 1.0mm	X				
• Boron 2.0mm • Boron 2.0mm	X	X			
• DP600 HDGI 2.0mm • Trip780 HDGA 2.0mm	X	X			
• Boron 2.0mm • Trip780 HDGA 2.0mm	X	X			

- *Each combination including spot welds with varying attributes (i.e., nugget size, indentation & defects)*
- *X corresponding to those which data has been collected*

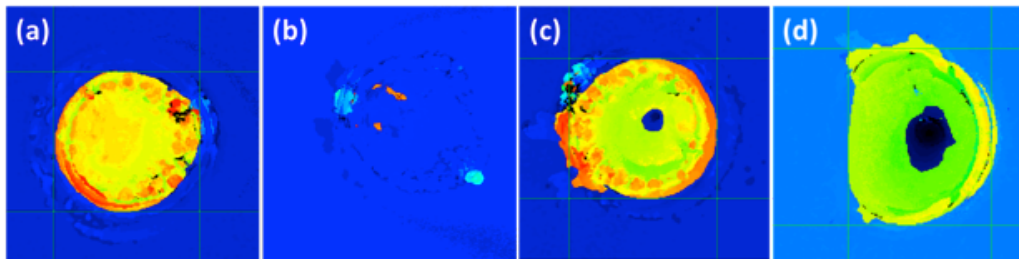


Figure 17. Weld quality attributes as determined by the underwater C-scan ultrasonic method: (a) a good weld, (b) a stuck weld, (c) a weld with center porosity, and (d) a noncircular weld with porosity defect.

A prototype hardware system was integrated with the prototype expert software for IR image acquisition and data analysis. The system is schematically shown in Figure 18. The hardware mainly consists of (1) a computer with specially designed software for system control, data acquisition, and IR image analysis; (2) a low cost IR camera; (3) an induction heating device (for postmortem inspection only); and (4) auxiliary input/output interface instruments for signal communications among the computer, external heating device, and the other electrical accessories. The entire inspection is fully automated from IR image acquisition and analysis to decision making on the weld quality. The system is synchronized with the spot welding machine for real-time monitoring, whereas for the postmortem case, it can be triggered by an external signal to meet the synchronization requirement for online automated inspection.

The prototype IR inspection system for real-time application is shown in Figure 19. Once the IR expert software receives the triggering signal from the spot welding machine (a manual push button for now for demonstration purpose), it starts to collect IR images from the camera, analyzes the image data, compares the processed data with the weld quality information in its database, and finally makes a decision to accept/reject the weld.



Figure 18. Schematic of the IR thermography based resistance spot welding quality inspection system.

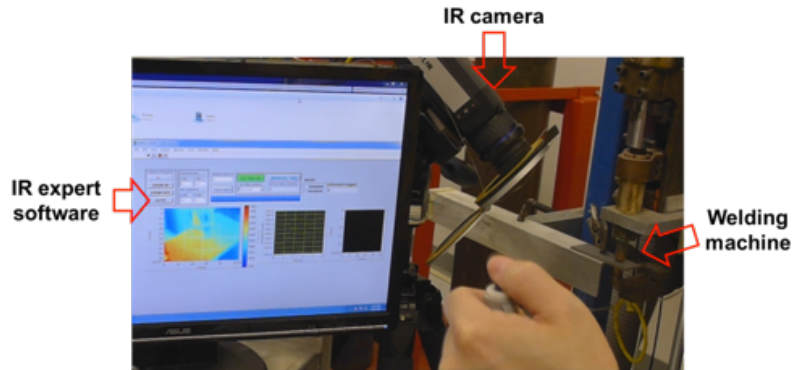


Figure 19. Prototype IR thermography based system for real-time inspection.

The IR image analysis algorithms have been vastly improved since last year. For postmortem inspection, the entire image collection and data analysis can be done in 3 s. A new ability to examine the weld shape was added. Weld shape, nugget size, and indentation depth can be accurately quantified by the new algorithms. Figure 20 shows the IR thermal signature for two different welds: (a) a good weld and (b) a weld with noncircular shape and void defect. The algorithm to quantify the void defect is more challenging and under further development.

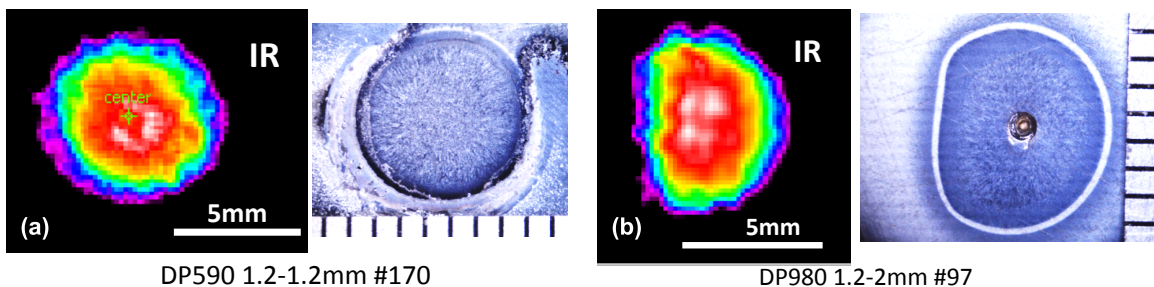


Figure 20. Comparison of the processed postmortem IR thermal signature: (a) good weld; (b) weld with irregular shape and void defect.

Figure 21 shows more examples of postmortem IR thermal signatures with respect to measured nugget size for welds made of different steels, coatings, and thicknesses. A good correlation is obtained between the weld nugget size and the IR signature. In particular, the stuck weld, one of the most critical defect types, can be accurately detected. Testing is ongoing to cover even more weld types and materials.

Figure 22 shows another postmortem IR signature to determine the weld indentation or weld thickness. Such IR signatures can be used to quantitatively estimate the indentation depth and the defect of stuck weld.

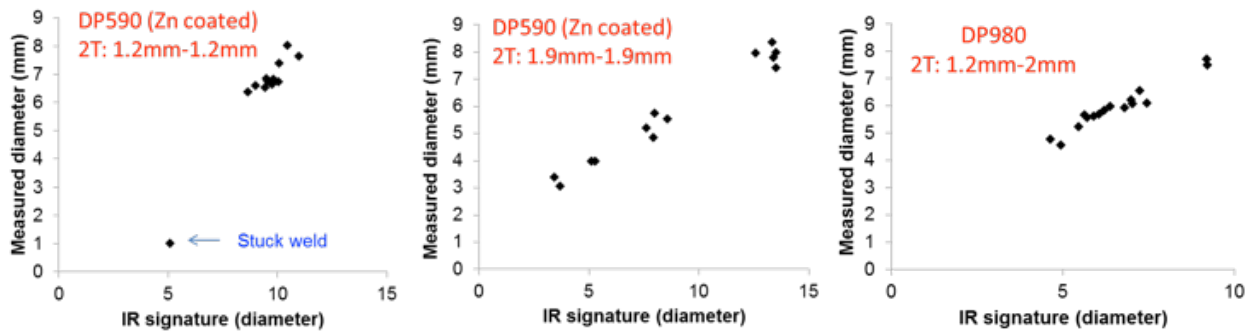


Figure 21. Postmortem IR thermal signature with respect to measured weld nugget size for welds made of different steels, coatings, and thicknesses.

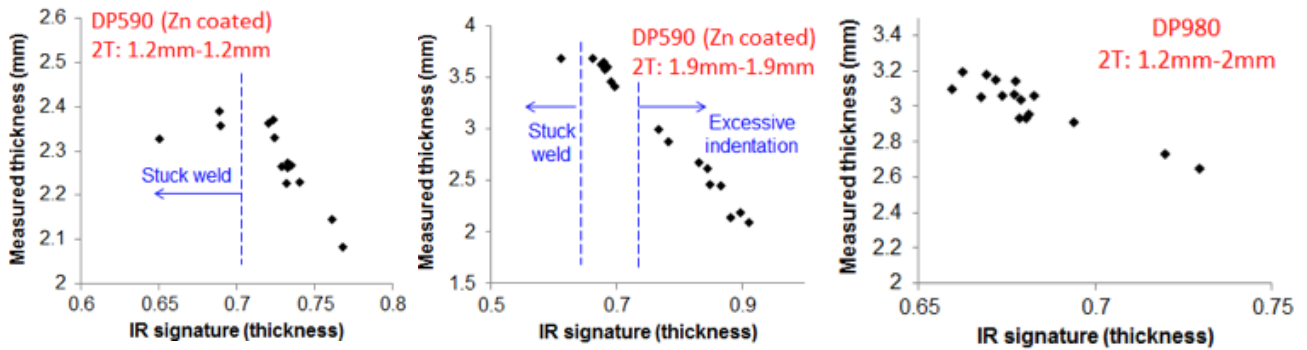


Figure 22. Postmortem IR thermal signature with respect to measured weld thickness (indentation depth) for welds made of different steels, coatings, and thicknesses.

Figure 23 shows examples of the real-time inspection. A new IR signature has been identified that positively correlates to the weld nugget size. An efficient data analysis algorithm was implemented to automatically analyze the collected IR images pixel by pixel and frame by frame to obtain the characteristic 3D isosurface shown in the figure. Such isosurfaces are quantitatively correlated with weld nugget size for both 2T and 3T stackup configurations.

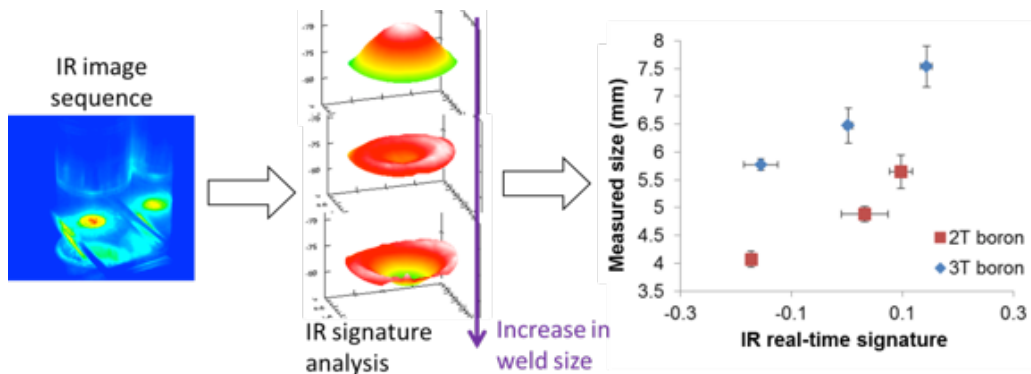


Figure 23. Real-time IR inspection providing reliable weld nugget size detection. 2T: two 1 mm thick hot dip coated boron steels; 3T: a 2 mm thick boron steel without coating sandwiched between two 1 mm thick hot dip coated boron steels.

Technology Transfer Path

We plan to conduct beta testing of the prototype IR NDE system at two or three selected OEM sites in FY 2013 to introduce the technology to the end users. Potential technology transfer and commercialization partners are being identified. As part of the system prototyping and commercialization effort, we plan to work with IR camera manufacturers, IR system integrators, and auto assembly line system integrators to make effective use of the technical expertise and capabilities in both the IR sensor technology and welding operation/assembly fields.

Conclusions

Significant work was accomplished in FY 2012 toward the development of a cost-effective, robust, and accurate IR thermography based system to inspect spot weld quality. Destructive sectioning and the underwater C-scan ultrasonic scanning methods were applied to obtain the reference weld nugget size, weld shape, and defects such as porosity for the IR NDE system development. New image analysis algorithms for both real-time and postmortem applications have been developed with improved inspection accuracy and robustness. A prototype fully automated, efficient, and robust IR inspection system was developed. The inspection time for both real-time and postmortem applications is reduced to 3 s, which can readily meet the online and offline inspection cycle time requirements. The ability to reliably detect the stuck weld, one of the most critical defect types, was successfully demonstrated.

Infrared Heat Treatment of Cast Bimetallic Joints and Residual Stress Characterization

Principal Investigator: Thomas R. Watkins, ORNL
(865) 387-6472; fax: (865) 574-3940; e-mail: watkinstr@ornl.gov

Principal Investigator: Timothy W. Skszek, Cosma Engineering
(248) 786-2584; e-mail: tim.skszek@vehmaintl.com

Investigators: Donald Erdman III, Pooron Joshi, Gerald M. Ludtka, Adrian Sabau, Hebi Yin, Wei Zhang, ORNL; Xiaoping Niu, Promatek Research Centre

Accomplishments

- Successfully completed a gateway milestone/“Go/No-Go” decision point on February 3, 2013, by delivering a modified T6 heat treatment for flat castings. After this modified T6 heat treatment, the minimum performance requirements were met. Samples exhibited a yield strength > 250 MPa, ultimate tensile strength (UTS) > 310 MPa, and elongation > 8%.
- Delivered a modified T6 heat treatment of flat castings. After this modified T6 heat treatment, the minimum performance requirements were met. Samples exhibited a yield strength > 250 MPa, UTS > 310 MPa, and elongation > 8%.
- Delivered a T5 heat treatment of flat castings. After this T5 heat treatment, the minimum performance requirements were met. Samples exhibited a yield strength > 172 MPa, UTS > 243 MPa, and elongation > 6%.
- Completed 85% of the neutron residual stress data collection for a series of conventionally heat treated joints.
- Initiated thermomechanical modeling and torsional joint testing.

Future Direction

- Future work will be aimed toward developing and documenting Al T5 and modified Al T6 IR heat treating methods for the bimetallic joints; determining the minimum duration of time at temperature with IR heating to achieve yield strength, UTS, and elongation of conventional T5 and T6 tempers as validated using similarly IR processed flat samples (see below); completing the modeling effort; and completing the prototype assembly.

Technology Assessment

- Target: Complete and document both a modified T6 and a T5 heat treatment schedule for a bimetallic joint. Manufacture demonstration joints and validate that flat casting samples treated per this schedule meet minimum performance requirements: modified T6: Yield strength > 250 MPa, UTS > 310 MPa, elongation > 8%; and T5: Yield strength > 172 MPa, UTS > 243 MPa, and elongation > 7%.
- Gap: Current heat treatments are either too time consuming or degrade the beneficial residual stresses.

Introduction

This project addresses the DOE Vehicle Technologies Program Lightweighting Materials technology barrier of “Joining and Assembly” by facilitating the use of lightweight, high performance materials that will contribute to the development of vehicles that provide better fuel economy yet are comparable in size, comfort, and safety to today’s vehicles. The project is focused on a specific application on a high volume vehicle platform; however, the joining technologies and methods developed will be applicable to multiple joints throughout other vehicle architectures.

The technical objective of the project is to develop and model a heat treatment process based on IR heating of an Al casting and a bimetallic joint to produce a T5 temper in a shorter period of time than is currently achievable and, separately, a modified T6 temper for improved mechanical properties without loss of joint integrity. IR heat treatments have been demonstrated to provide reduced processing time, reduced energy requirements, and improved material properties of Al components including strength and elongation relative to convection thermal heat treatment methods. The bimetallic joints (Buchholz, 2011) under consideration are part of the automotive front and rear cross-car structure, wherein a steel tube is enveloped by molten Al to form a joint. It is believed that a novel IR heat treatment approach may be able to tailor the temperature profile, after casting, to strengthen the Al, better manage the residual stresses, and achieve a superior joint. Fabrication and thermal processing of a bimetallic structure comprising two dissimilar materials presents processing challenges to mitigate, reduce, and optimize many materials issues such as residual stresses, interfacial reactions, and varying properties.

Approach

The project has been organized into three research areas: IR processing experiments and prototype assembly, model development and validation, and characterization of castings and joints. Two distinct sets of samples are being examined: flat casting samples and sectioned bimetallic “joint only” samples. Cosma supplies both flat castings and joint-only samples under standard processing conditions (T5 and modified T6) and untempered, non-heat-treated flat casting and joint-only samples.

During phase II of this project T5 and modified T6 IR heat treating methods for flat Al-Si-Mg castings (i.e., not bimetallic joints) are being applied, modified, and developed for bimetallic joints. The minimum time at temperature with IR heating to achieve yield strengths, UTSs, and elongation of conventional T5 and T6 tempers is being determined. Residual stresses are being measured as necessary using neutron diffraction. A thermomechanical model will be completed.

Results and Discussion

IR processing experiments and prototype assembly. An electric IR heating furnace at ORNL was used to test novel IR heat treatments. The batch-type furnace consists of an array of quartz lamps, which heat the sample from beneath. To understand the IR system better, flat casting samples of A356 were instrumented with three thermocouples that were placed on the top, bottom, and in a side hole of the flat casting sample as shown in [Figure 24](#). The sample holder was designed to minimize heat transfer losses by conduction. Temperature control and furnace operation were optimized using this setup. The following were considered: temperature-controller output power feedback, ramp rate, temperature set point overshoot, and location of controlling thermocouple. A series of flat castings were processed with this furnace using T5 and modified T6 heat treatments and then tested mechanically. In a T6 heat treatment, the sample is taken up to the solutionizing temperature to dissolve any precipitates and homogenize the alloy. The sample is then quenched to room temperature to retain the solute-rich chemistry of the homogeneous matrix, which was formed at high temperature. The sample is then reheated to a lower aging temperature to generate controlled dispersions of very small strengthening precipitates within the matrix of Al grains. In a T5 heat treatment, the as-cast sample is simply heated to a lower temperature and aged.

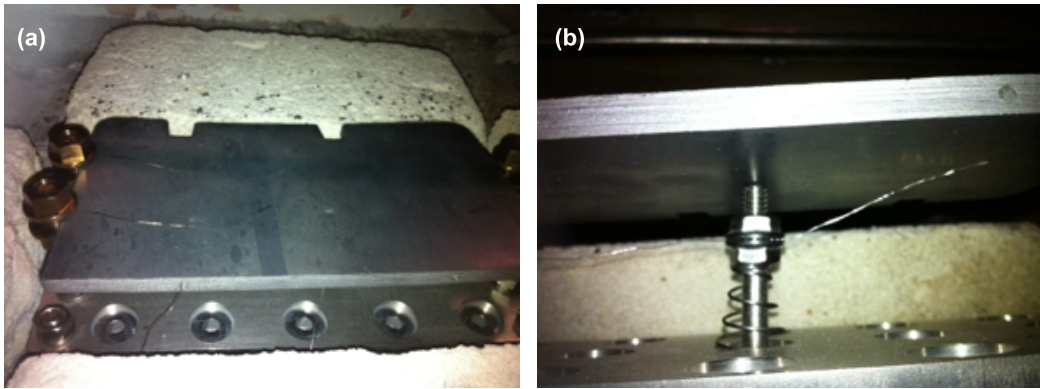


Figure 24. A flat casting showing thermocouple placement: (a) sample placed in a fixture with the fine top and bottom thermocouple wires visible; (b) bottom thermocouple placement with drilled side hole for a thermocouple.

As part of the IR processing experimental program, the heat flux incident to the surface of the flat casting sample was measured to assist the thermal modeling. The heat flux sensor was placed into a fixture [Fig. 25(a)] such that the sensor surface was located at the same offset distance from the top panel as the flat casting samples. Preliminary measurements of the incident heat flux were conducted at several power levels of the IR furnace with each measurement lasting about 15 to 20 s. This short time duration was desired to minimize the heat conduction away from/to the sensing area. As shown in Figure 25(b), the discrete points are the measure values, and the lines are the curve fit. Lastly, a prototype furnace is being assembled to heat treat the joints. This work is in its preliminary stages and will be reported on next year.

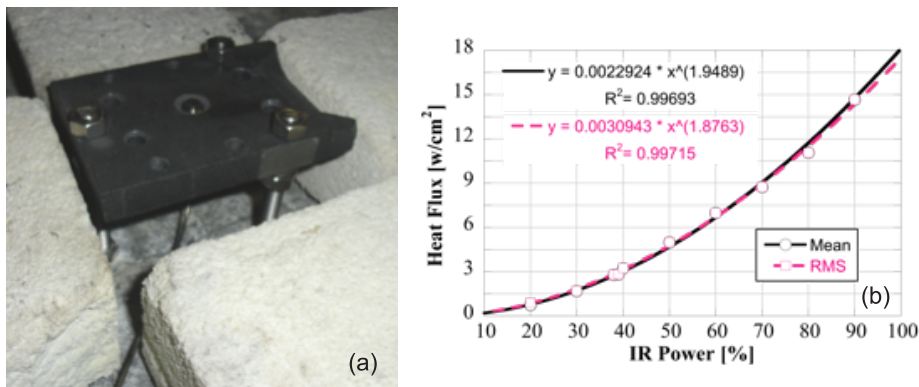


Figure 25. Heat flux measurements: (a) fixture showing heat flux sensor embedded in the center of the graphite plate and (b) measured incident heat fluxes at various fractional IR power levels.

Characterization of castings and joints. The series of flat casting samples that were heat treated to either T5 or a modified T6 temper were subsequently mechanically tested, and the yield strength, UTS, and elongation were determined. Many of the modified T6 heat treatment trials produced samples which exceeded the minimum performance requirements (see “Target”), indicating the robustness of the approach. For each heat treatment, two tensile samples were machined and tensile tested (e.g., Figure 26). While the T5 heat treatment did not quite meet the elongation performance requirement (see “Target”), new T5 heat treatment trials are pending.

Residual stresses play an important role in these joints. A series of conventionally heat treated joints are being examined using neutron diffraction to measure and map the residual stresses in the joint region. The measurements were conducted at the High Flux Isotope Reactor at ORNL. The HB-2B beam line was used. The positions of the (211) steel reflection and (311) Al reflection were measured in the radial, hoop, and axial directions. The experimental details are similar those

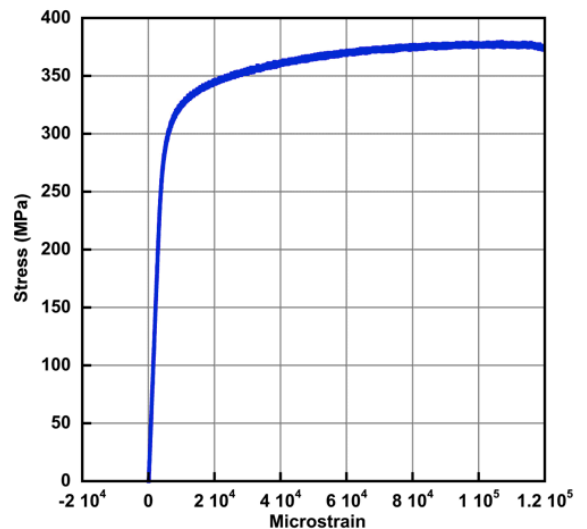


Figure 26. Stress as a function of microstrain for one of the flat castings. (e.g., note 1.2×10^5 microstrain = 0.12 strain).

described in Johnson et al. (2012). Figure 27 shows the experimental setup. Table 4 lists preliminary residual stresses for two samples showing that the 538°C heat treatment reduces the magnitude of the residual stresses in each material in almost every direction. More residual stress analysis work will be done on other joints heat treated at lower temperatures. These results will then be compared to mechanical testing results.

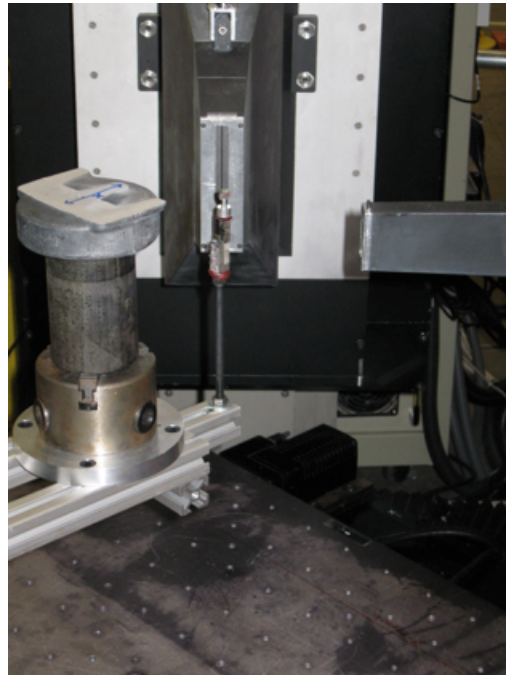


Figure 27. Steel-aluminum joint mounted on the goniometer and positioned for radial measurements. The incident snout is to the right, and the receiving snout is center. The strain free reference cubes are shown lined up in the gauge volume (i.e., the projected intersection of the incident and receiving slits).

Table 4. The residual stresses (in megapascals) in the as-cast and 538°C/1,000°F heat treated sample. The values in parentheses are standard deviations based on replicate strain measurements.

Sample	Aluminum Radial	Hoop	Axial	Steel Radial	Hoop	Axial
As-Cast	-40 (10)	+14 (10)	-41 (10)	+52 (35)	+167 (35)	+43 (35)
538°C/1,000°F	+9 (10)	+53 (10)	+6 (10)	-30 (26)	-31 (26)	-65 (26)

This same series of heat treated joints is also undergoing torsion testing to see what effect the heat treatment has on the interfacial strength. Torsional testing of the bimetallic joint was carried out using an axial-torsional servohydraulic test machine to evaluate the strength of the joint between the steel cylinder and cast Al “knuckle.” The steel tube was gripped with a custom clamping fixture, while the Al portion of the joint was constrained inside a square, U-shaped fixture that eliminated rotation (see Figure 28). At the full capacity of the test machine, 20,000 in.-lb, the joint remained intact. Subsequently, cyclic fatigue was carried out on the structure at 0.5 Hz with amplitude from 0 to 20,000 in.-lb. All tests were very similar with respect to damage evolution.

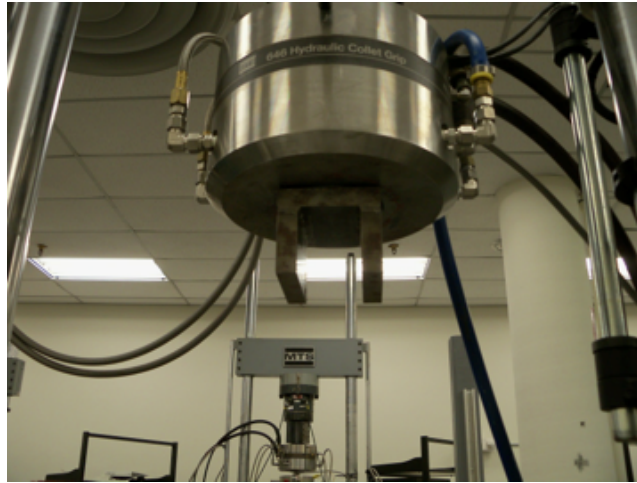


Figure 28. Steel-aluminum joint torsion testing setup showing the square, U-shaped fixture that holds the Al portion of the joint.

Model development and validation. Several models were developed in this project to efficiently assist in the development of new heat treating schedules. A semiempirical model for the age hardening was developed and successfully applied to optimize the aging treatment. Also, a semiempirical model for the solutionizing part of the heat treatment was developed. The solution heat treatment model will help in devising solution heat treatment schedules at lower temperatures than those traditionally considered for the T6 heat treatment. A heat transfer model of the bimetallic part was completed, and a residual stress analysis model is being developed.

Technology Transfer

This project is a CRADA with Cosma Engineering to develop specific heat treatments aimed at both current and future vehicle platforms.

Conclusions

The purpose of this project is to investigate an IR heat treatment to increase yield strength and elongation of the cast Al portion of an Al–steel bimetallic joint to achieve a superior joint. The project has been organized into three research areas: IR processing experiments and prototype assembly, model development and validation, and characterization of castings and joints. Flat casting samples were heat treated with an IR lamp. The mechanical properties of these samples exceeded the minimum performance requirements given in the “Technology Assessment” subsection, achieving gateway milestones. Residual stress and torsion strength characterization have begun. The thermal modeling is almost complete and the stress modeling has begun. Preparations are under way to assemble a prototype IR furnace to heat treat bimetallic joints.

Understanding Protective Film Formation by Magnesium Alloys in Automotive Applications

Principal Investigator: Mike P. Brady, ORNL
(865) 574-4805; fax: (865) 576-5413; e-mail: bradymp@ornl.gov

Principal Investigator: Kinga A. Unocic, ORNL
(865) 574-0996; fax: (865) 576-5413; e-mail: unocicka@ornl.gov

Partners: Bruce Davis, Magnesium Elektron North America (MENA)
(618) 709-502; e-mail: Bruce.Davis@Magnesium-ElektronUSA.com

Accomplishments

- Demonstrated successful transmission electron microscopy (TEM) cross-sectional imaging of Mg alloy surface films formed under aqueous and thermal oxidation conditions.
- Initiated experiments to downselect aqueous and thermal water vapor oxidation conditions to yield Mg alloy surface films potentially amenable to isotopic tracer studies to provide new insight into film growth mechanisms.

Future Directions

- Conduct isotopic tracer studies using H_2^{18}O and D_2^{16}O for model ultrahigh purity Mg relative to baseline AZ31B (nominal Mg-3Al-1Zn-0.4Mn wt % base) and rare earth- (RE-) modified Elektron 717 (ZEK 100 RE addition type based on Mg-1Zn wt % + Nd, Zr) alloys to provide new insight into film growth mechanisms as a function of alloy content and exposure conditions.
- Correlate TEM cross-sectional imaging of surface films formed under aqueous and thermal oxidation conditions with alloying additions in ultrahigh purity Mg relative to AZ31B and Elektron 717 alloys to provide new insight into film structure as a function of alloy content and exposure conditions.
- Conduct electrochemical studies of ultrahigh purity Mg and commercial AZ31B and Elektron 717 alloys relative to model single-phase Mg + Al, Mg + Al + Zn, and Mg + RE alloys under aqueous conditions with and without salt species.

Technology Assessments

- Target: Gain improved understanding of protective film formation by Mg alloys and conversion coatings as a function of alloy chemistry and impurities, microstructure, and exposure conditions.
- Target: Provide a fundamental basis to design and optimize new Mg alloys and/or conversion coating processes to improve corrosion resistance under automotive relevant conditions.
- Gap: The lack of corrosion prevention strategies is a key limiting factor to more widespread use of Mg alloys in automotive applications.
- Gap: Alloying has been shown to modify surface film performance; however, a detailed understanding of how and why is currently lacking. Such an understanding is needed to develop improved alloys and surface treatments/coatings to permit more widespread adoption of Mg alloys.

Introduction

The purpose of this project is to develop an improved understanding of how alloy composition, microstructure, and exposure conditions effect the establishment, continuity, nature, and growth of protective films on Mg alloys. The study of both bare, untreated Mg alloy surfaces and conversion coated surfaces is being pursued. The corrosion of Mg alloys has been the subject of intense research activity, with significant gains in mechanistic understanding in recent years for both pure Mg and Mg alloys. These studies have identified the inability of Mg alloys to establish a continuous and fully protective surface

film under many exposure conditions as a key factor underlying their susceptibility to corrosive attack. Alloying has been shown to modify surface film performance; however, a detailed understanding of how and why is currently lacking. Such understanding is needed to provide a fundamental basis to develop improved alloys and improved surface treatments and coatings to permit more widespread adoption of Mg alloys in automotive applications. Deliverables on this project are related to application, development, and suitability assessment of advanced characterization techniques to provide new insights into Mg alloy corrosion.

Approach

The ambient corrosion of Mg differs from many corrosion-resistant structural alloy classes in that the protective surface films can become quite thick, on the order of tens to hundreds of nanometers, rather than the few nanometers typically encountered in stainless steels. As a result, corrosion resistance is influenced not only by classical thin film electrochemical passivity considerations but also by thermodynamic and kinetic considerations typically encountered in thick film, high temperature alloy oxidation phenomena.

The proposed experimental approach will seek to merge ambient and high temperature corrosion study approaches, leveraging extensive and unique expertise in these areas at MENA and ORNL. It will also take advantage of the world-class characterization capabilities available at ORNL to more fully probe and understand the chemical, morphological, and structural features of the surface films formed on Mg alloys and conversion coatings as a function of alloy composition, microstructure, and exposure condition.

A major early project goal will be to complete an assessment of which advanced characterization techniques are most amenable to providing new insights into film formation on Mg alloys. This is a key activity as Mg alloys are notoriously difficult to work with. Sample procedure techniques will need to be developed, and not all proposed characterization approaches will prove effective. Advanced characterization approaches to be investigated include (1) secondary ion mass spectrometry (SIMS) $D_2^{16}O$ and $H_2^{18}O$ tracer studies of Mg alloys/coatings under immersion aqueous and gaseous vapor exposure conditions to gain insight into the growth aspects of the surface films, (2) development of ex situ focused ion beam (FiB) sample preparation and TEM of film/surface layer cross sections, (3) ex situ neutron scattering techniques (small angle, inelastic, etc.) to characterize Mg alloy surface film nanoporosity and hydrogen species incorporation as a function of alloy composition and exposure condition, and (4) atom probe tomography techniques to provide 3D quantification of chemistry at the atomic scale in the bulk Mg alloy and the alloy in the vicinity of the alloy-surface layer interface to characterize corrosion-driven alloy clustering or precipitation phenomena.

Results and Discussion

Per input from industrial partners, the project is initially focused on AZ31B as a baseline commercial alloy and the RE-modified alloy Elektron 717. Model alloys based on pure Mg and the matrix phase compositions of commercial AZ31B and Elektron 717 alloys [Mg-2Al and Mg-2Al-1Zn for AZ31B and Mg-X (X = Ce, Eu, Gd, La, Nd, Y, Zr) for Elektron 717] are being manufactured by MENA for electrochemical and corrosion studies, both bare substrate and after conversion coating.

Because successful application of advanced characterization techniques to fully elucidate the structure and chemistry of films formed on Mg is a major component of this project, initial efforts were devoted to development of FiB cross section sample preparation protocols for TEM analysis. Test samples of AZ31B were selected for initial characterization and development of sample preparation protocols under two exposure conditions: thick film (> 100 nm) formation after 24 h aqueous immersion in 5 wt % sodium chloride solutions and thin film (< 50 nm) formation after polishing and air drying at 370°C for 40 min.

The film formed on the salt-exposed AZ31B was irregular, with regions ranging from a few microns thickness, suitable for cross-sectional TEM imaging as shown in [Figure 29](#), to tens of microns thickness. Bulk x-ray diffraction and TEM imaging indicated a complex mixture of MgO and Mg(OH)₂. The FiB technique was successful in producing a high quality cross-sectional image which revealed that the film was duplex, with an inner continuous and uniform ~100 nm thick MgO layer underlying a thick mixed MgO + Mg(OH)₂ region with nanoscale porosity. At the alloy-film interface, there was evidence in the image and maps of local enrichment of Zn. Although not as definitive as the Zn enrichment, the maps also suggested possible enrichment of Al in the continuous MgO region near the interface with the nanoporous MgO + Mg(OH)₂ outer layer. The combination of the FiB-TEM imaging with x-ray photoelectron spectroscopy (XPS), which has previously been

widely applied to characterization of Mg surface films, and the planned SIMS $D_2^{16}O$ and $H_2^{18}O$ isotopic tracer studies are anticipated to be able to provide the capability to track film structure and chemistry evolution as a function of alloy content and exposure conditions.

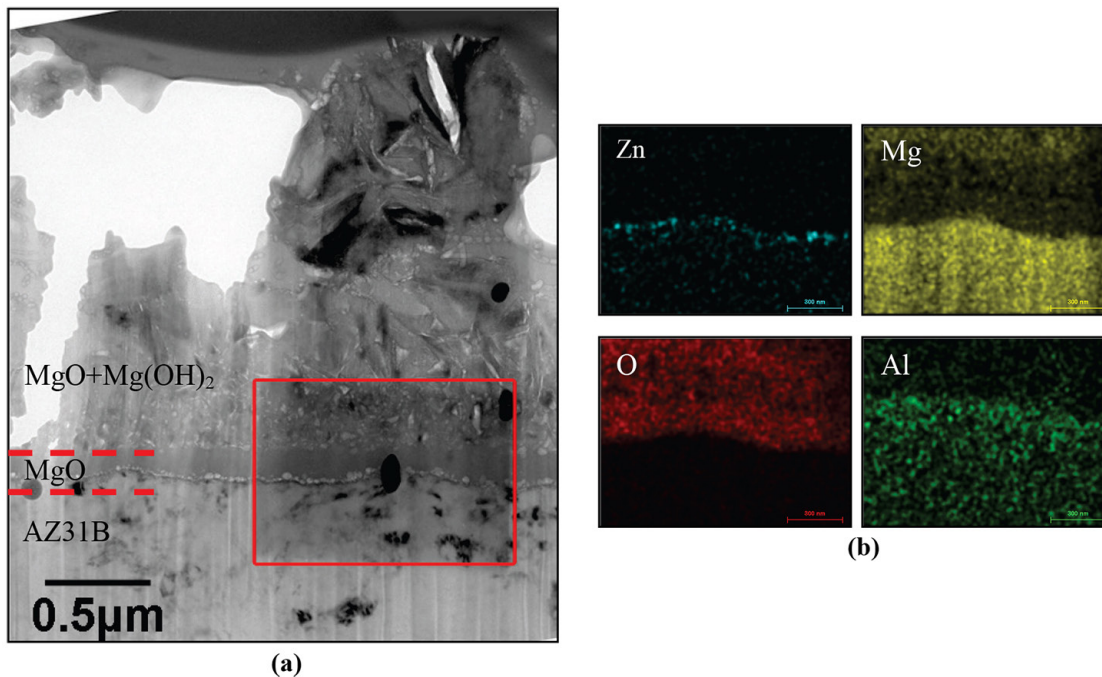


Figure 29. Cross-sectional TEM image of the film formed on AZ31B after exposure in 5% sodium chloride for 24 h (a), with corresponding x-ray maps (b) for Zn, Mg, O, and Al elements generated from the area enclosed by the red rectangle in the cross-sectional image.

Experimental protocols for FiB preparation of thin Mg surface films were developed using 370°C/40 min air oxidized AZ31B [Figure 30(a)]. The film consisted of a roughly 20 nm thick and dense MgO layer identified via fast Fourier transform. High resolution TEM revealed that the MgO was formed of nanocrystals [Fig. 30(b)]. Such high resolution TEM imaging will be applied to study the alloy-film interface structure and possibly assess the segregation of alloying additions and impurities in this region. It is anticipated that this capability will be particularly useful for studying films formed on model Mg + RE and Elektron 717 alloys in planned work to more fully elucidate the mechanistic basis for improvement of corrosion resistance with RE additions.

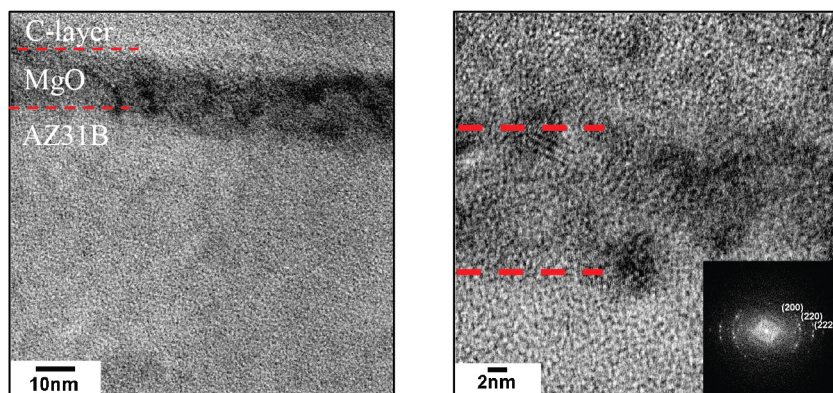


Figure 30. TEM image of the MgO cross section formed on AZ31B after exposure for 40 minutes at 370°C (a) and higher magnification image of the oxide scale with fast Fourier transform generated from the MgO layer (b). Note that the carbon layer (C-layer) was deposited for sample preparation purposes.

Technology Transfer Path

Basic understanding of the film formation on Mg alloys and its behavior in different environments will provide insight into how improvements can be made to design and optimize new Mg alloys and conversion coatings to improve corrosion resistance under automotive relevant conditions. The current gap in basic understanding of the film formation mechanics and kinetics and correlation with alloy chemistry and microstructure is a key factor limiting achievement of improved corrosion resistance to permit more widespread use of Mg alloys in automotive applications. Teaming with MENA, a leading Mg alloy producer, on this project will provide a direct path for incorporating insights from this effort into practice.

Conclusions

A key to understanding the corrosion response of Mg alloys is a complete characterization of the micro/nanoscale location of key alloying elements and impurities in the surface film and the near-surface alloy regions. The capability to successfully cross-sectionally image both thick and thin film formation by FiB/TEM techniques was demonstrated on salt exposed and thermally oxidized AZ31B. This characterization method provided detailed structure and elemental distribution information for the oxide/hydroxide films formed. Such imaging will be the basis for understanding film formation for planned corrosion, oxidation, and electrochemical studies of AZ31B and Elektron 717 relative to ultrahigh purity Mg and model single-phase Mg alloys in FY 2013. It will also provide an improved basis for interpretation of XPS and SIMS studies.

High Strength, Lightweight Engines for Heavy-Duty Diesel Trucks

Principal Investigator: G. Muralidharan, ORNL
(865) 574-4281; fax: (865) 574-4357; e-mail: muralidhargn@ornl.gov

Principal Investigator: Amit Shyam, ORNL
(865)241-4841; fax: (865) 574-6098; e-mail: shyama@ornl.gov

Other ORNL Team Members: Michael P Brady, Allen Haynes

Principal Investigator: Roger England, Cummins
(812) 377-3135; e-mail: roger.d.england@cummins.com

Accomplishments

- Downselected two components, exhaust manifolds and pistons, for materials evaluation and improvement.
- Developed constrained thermal fatigue (CTF) testing capability at ORNL.
- Identified several potential alternate exhaust manifold materials, and compiled a subset of available literature data on them.
- Completed CTF testing on several materials under one selected temperature cycling condition.
- Initiated oxidation tests on several alternate exhaust manifold materials over a range of temperatures and in varying atmospheres, and determined that several new alloys perform better than the baseline alloys.

Future Directions

- Downselect potential manifold materials for FEM to predict stresses in exhaust manifolds.
- Complete materials property measurements for downselected materials to provide input for FEM.
- Identify potential alloy modification paths using computational modeling for austenitic nodular cast iron (D5S) and cast austenitic stainless steels, if required based on FEM results.

- Identify material property requirements for next generation piston materials.
- Identify potential next generation monolithic materials for higher temperature operation of pistons.
- Identify potential coating materials and manufacturing techniques for required thermal insulation of piston combustion faces.

Technology Assessment

- Target: Achieve targeted improvements in engine efficiency through modifications of engine operating conditions including increased pressures and temperatures.
- Gap: New materials are required to meet the new operating requirements, which impose more demanding temperatures, pressures (hence stresses), and environments.

Introduction

This Lightweight Materials project with Cummins is in the first year and supports the goals of improving the efficiency of heavy duty vehicles and targets the achievement of a 50% brake thermal efficiency in heavy-duty diesel engines. The fuel efficiency roadmap for the 50% brake thermal efficiency engine considers six main areas for efficiency improvement in the baseline engine, several of which involve making more efficient use of thermal energy (heat) in the engine. Increased operating temperatures and improved thermal management are expected to enable significant increases in power density, thus resulting in greater power output for the same sized engine or engine downsizing (lightweighting) for the same power output. One of the approaches for improving the thermal efficiency is the use of thermal insulation to decrease heat loss in certain components, which results in increased temperatures in the selected components within the engine. It is becoming apparent that several key components will be exposed to temperatures beyond the capabilities of current engine and exhaust materials, requiring the availability of the next generation of high temperature materials to allow the engine to reach the efficiency, durability, and emission targets. Because of different combinations of property requirements, new materials technologies specific to the targeted engine components are needed to enable operation in the higher temperature environment.

Approach

The overall approach used in this project involves the following major tasks.

Task 1. Component Design, Materials, and Manufacturing Process Evaluation.

As part of the initial component evaluation study, candidate components, materials, designs, and manufacturing processes will be assessed and an initial evaluation of the critical improvements needed to meet the engine efficiency goals of the current heavy duty diesel engines will be completed. FEM of component stress and temperature will be conducted to identify the critical stresses and temperatures expected and specify the material characteristics that would enable the team to achieve the required stresses and temperatures in these components. Based upon the results of that evaluation, an initial set of materials, materials microstructure and property requirements, and materials characterization matrix will be identified. Key component manufacturing routes and potential implications for materials microstructure and properties will be identified to enable follow-on evaluation.

Task 2. Materials Testing and Component Design Modification.

Materials microstructure and properties are crucial to successful design and reliable operation of engine components. Expected combustion system changes in the high efficiency engines will result in changes to cylinder pressure and temperature from that of current engines, which will influence the materials requirements for this effort. New, advanced materials and associated manufacturing processes have to be assessed to evaluate the functionality, ease of fabrication, and reliability of key components. Based upon the finite element analyses of components, an initial test matrix considering the materials and properties to be evaluated will be defined. Test specimens will be fabricated or acquired and tested over the range of conditions identified in the test matrix. ASTM standard test methods will be used. A statistically significant body of data will be generated to facilitate component design.

Task 3. Prototype Component Fabrication and Testing.

Based upon component design, materials property, and manufacturing process evaluations, prototype components will be fabricated using advanced materials. Once prototype components become available, component-level tests will be performed to determine their durability. The results of component performance and durability evaluations will be used to decide on areas that need to be improved to achieve the desirable performance, weight, or fabricability characteristics suitable for use in heavy duty diesel engines.

Results and Discussion

A detailed analysis of the development of the next generation high efficiency, heavy duty engine being envisioned by Cummins showed that exhaust manifolds and pistons are two components where improvements in high temperature capabilities would have a positive impact on the thermal efficiency of the future heavy duty engines. Increased combustion efficiency requires the pistons and exhaust manifolds to accommodate increased temperatures. Current materials physical limits define the allowable combustion operating temperatures and pressures. Creating components with a higher temperature capability in the piston and exhaust system will also allow increased waste heat recovery from exhaust gases aiding in the overall thermal efficiency. Increasing the high temperature strength of the exhaust manifold material allows a reduction in the wall thickness of the component thus reducing the overall weight of the exhaust manifold while allowing higher operating temperatures in the exhaust gas. This enables a reduction in weight of the engine and associated components while providing more energy for the turbocharger to convert to work through a decrease in thermal mass, thus reducing the fuel penalty associated with after-treatment catalyst heat-up/light-off with a significant positive impact on fuel economy and emissions.

An increase in the temperature capability of piston materials will also have a positive impact on the efficiency of the next generation diesel engines. Pistons are carefully engineered to withstand the harsh environment during the combustion process and to possess sufficient strength to efficiently translate energy from the combustion process to mechanical work. A significant penalty is incurred in engine efficiency due to the necessity to cool the backside of the piston combustion bowl with a jet of engine oil to prevent the large thermal excursions that would otherwise occur during the combustion process. Improving the high temperature capability of the piston material would allow a reduction in the flow of cooling oil and would enable better utilization of the energy produced during the combustion process, thus improving overall engine efficiency. Materials with an appropriate thermal conductivity will ensure that heat is effectively retained during the combustion phase of the engine cycle thus enabling maximum heat recovery from the exhaust gases. Replacement of current materials with materials with a higher strength at higher temperatures would also allow redesign of components with a lower weight for the same stress levels, thus facilitating lightweighting and increased power density and resulting in increased efficiency due to the decrease in rotating mass.

Because the current materials (high silicon-molybdenum (SiMo) cast irons in exhaust manifolds and 4140 steel in pistons) are already operating near the limits of their temperature and strength capabilities, new materials with the right combination of properties are required for these components. It is anticipated that critical technologies such as waste heat recovery will not only necessitate the availability of improved materials to achieve the efficiency targets in the next generation high efficiency engines, but will also drive the development of advanced materials that would enable the manufacture of a durable, commercially viable, improved thermal efficiency engines in the future.

Table 5 shows the key properties that were initially identified by the team to be of interest for the two components. These properties will be used for initial screening of new materials for this application and to define the initial test matrix.

Table 5. Components downselected and the critical materials properties of interest.

Component	Critical material properties of interest
Exhaust Manifold	CTF strength, elevated temperature strength, high temperature fatigue strength, creep strength, oxidation resistance, thermal expansion coefficient, specific heat, density, elastic modulus, thermal conductivity, microstructural stability at high temperatures, and the ability to be cast into complex shapes.
Piston	CTF strength, high temperature strength, high temperature fatigue strength, thermal conductivity, density, specific heat, oxidation resistance

Based upon the preliminary evaluation, CTF was identified as a key test capability and was developed as part of this project.

Constrained thermal fatigue testing capability.

Many essential diesel engine components develop substantial cyclic thermal stresses due to repetitive thermal cycling from low temperatures during shutdown to elevated temperatures during operation and short-term temperature excursions due to load variations during operation. The development of thermal stresses is exacerbated in components such as exhaust manifolds, pistons, and cylinder heads, which are rigidly constrained. Such CTF damage, although common in service conditions, is difficult to simulate experimentally in laboratory specimens (Figure 31). A CTF laboratory test has been developed at ORNL to support the material development needs of this CRADA. The test specimens are rigidly constrained in this testing method, and cyclic stresses are generated by temperature cycling the gage section of the specimen between specified temperatures at a specified heating rate. In addition, a hold time at the maximum temperature in the cycle is introduced to generate a trapezoidal temperature versus time control signal (Figure 32). Heating/cooling rates of 1°C/s have been used in current testing with a feedback loop temperature controller, although other rates are achievable. Precise temperature control was achieved with a program using LabVIEW software written at ORNL specifically for this purpose. A high temperature extensometer is placed in the gage section of the specimen and the evolution of the stress and strain signals with thermal cycling is continuously recorded. The magnitude of the stress developed during thermal cycling is a function of the material; mechanical and thermal properties such as yield strength, Young's modulus, and coefficient of thermal expansion; and experimental variables such as the temperature range of the thermal cycle. Overall, the material's resistance to CTF is determined by the yield strength of the material in the temperature cycle range, creep strength, oxidation resistance, and low cycle fatigue strength.

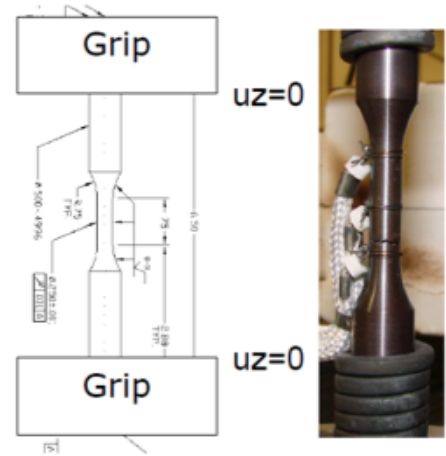


Figure 31. Schematic and image of a setup for CTF.

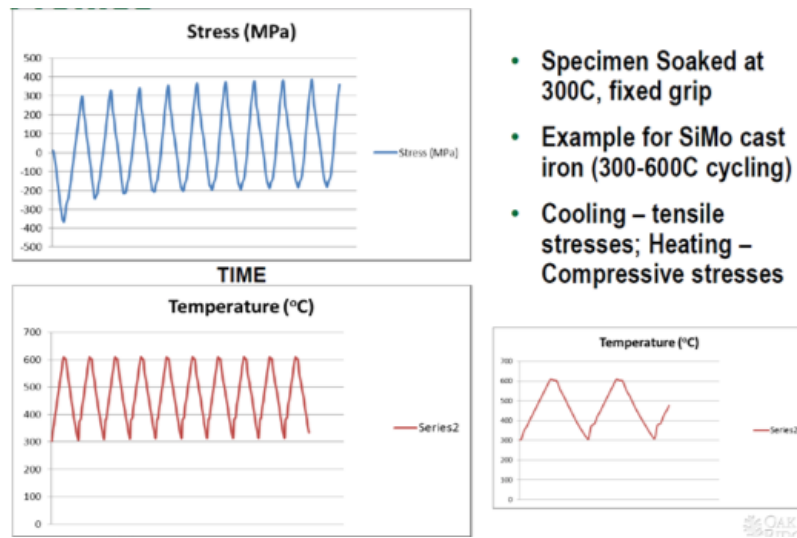


Figure 32. Examples of stress vs time and temperature vs time profiles.

Initial set of new materials for exhaust manifolds has been identified.

Several new classes of materials have been identified as alternatives to the high SiMo cast irons currently used in exhaust manifolds. The following are the three major classes of materials.

- D5S-austenitic nodular cast iron
- Cast austenitic stainless steels (chromia-forming)
- Alumina-forming, cast austenitic stainless steels

Table 6 shows some example candidates of cast austenitic stainless steels being considered for this application. The “ORNL” in parenthesis denotes alloys developed at ORNL. It is anticipated that the properties of these alloys will be evaluated against the requirements predicted from finite element models. Alloys that meet the requirements will be downselected for more extensive evaluation.

Table 6. Compositions of cast austenitic stainless steels being evaluated for application in exhaust manifolds, in weight percent.

Alloy	Type of Alloy	Fe	Cr	Ni	Mn	Mo	Nb	W	Si	C	Remarks
High SiMo Cast Iron	Nodular ferritic cast iron	Bal.			0.3	0.6			4.0	3.45	Baseline alloys
D5S	Nodular austenitic cast iron	Bal.	2	35	0.5				5	1.9	High performance cast iron
Cast CF8C	Cast austenitic	Bal.	19	10	<1	0.3	0.8	0	1	0.07	
Cast CF8C+	Cast austenitic	Bal.	19	12.5	4.0	0.3	0.8	0	0.5	0.1	0.25N
CF8C+CuW	Cast austenitic	Bal.	19	12.5	4.0	0.3	0.8	1	0.5	0.1	3Cu,0.3N
TMA 4705 (ORNL) Typical	Cast austenitic	Bal.	26	23.5	0.6	0.47	0.35	0.28	1.33	0.6	Centrifugal casting data only
TMA 6301 (ORNL) Typical	Cast austenitic	Bal.	24	34.2	1.0	0.02	0.41	0.35	1.22	0.43	Centrifugal casting data only
HK30	Cast austenitic	Bal.	25	20						0.3	Standard grade
Hercunete-S A3N	Cast austenitic	Bal.	20	10	1		2	3	0.6	0.45	Hitachi’s cast austenitic
Cast AFA (ORNL) Typical	Alumina-forming cast austenitic	Bal.	14	25	2	2	1	1	1	0.45	Vacuum casting data only, Al 3.5 C:0.2–0.5

Initial test matrix has been defined and data collection for materials downselection and FEM has been initiated. To aid in the downselection process, relationships between the compositions of the alloys, processing (casting), microstructure, and thermomechanical properties are being developed. Initial focus has been on developing property data on the oxidation behavior and CTF behavior of the initial set of candidate alloys. Table 7 is a summary of the materials being evaluated for their oxidation resistance, testing conditions, and status of the tests. Table 8 is a summary of the materials being evaluated for CTF resistance, testing conditions, and status of the tests.

Table 7. Summary of oxidation testing conditions, materials being tested, and status of tests.

Condition	SiMoA	SiMoB	SiMoC	D5S	HP	HK	TMA 6301	TMA 4705	CF8C plus	CAFA 4	CAFA 6
800°C air + 10% H ₂ O (100 h cycles)	1,000 h section; 3,000 h ongoing	1,000 h section; 3,000 h ongoing	1,000 h section; 3,000 h ongoing	700 h section at 1,000 h; 700 h ongoing	1,000 h section; 3,000 h ongoing	1,000 h section; 3,000 h ongoing	1,000 h section; 3,000 h ongoing	1,000 h section; 3,000 h ongoing	1,000 h section; 2,000 h-stop (fail)	1,000 h section; 5,000 h-stop	2,600 h ongoing
750°C air + 10% H ₂ O (100 h cycles)	1,000 h section; 2,500 h ongoing	1,000 h section; 2,500 h ongoing	1,000 h section; 2,500 h ongoing	900 h section at 1,000 h; 900 h ongoing	1,000 h section; 2,500 h ongoing	1,000 h section; 2,500 h ongoing	1,000 h section; 2,500 h ongoing	1,000 h section; 2,500 h ongoing	1,000 h section; 2,500 h ongoing	1,000 h section; 5,000 h-stop	1,000 h section; 2,300 h ongoing
700°C air + 10% H ₂ O (100 h cycles)	1,000 h section; 3,300 h ongoing	1,000 h section; 3,300 h ongoing	1,000 h section; 3,300 h ongoing	1,000 h section; 1,100 h ongoing	1,000 h section; 3,300 h ongoing	1,000 h section; 3,300 h ongoing	1,000 h section; 3,300 h ongoing	1,000 h section; 3,300 h ongoing	1,000 h section; 3,300 h ongoing	1,000 h section; 5,000 h-stop	2,800 h ongoing
650°C air + 10% H ₂ O (100 h cycles)	1,000 h section; 1,200 h ongoing	1,000 h section; 1,200 h ongoing	1,000 h section; 1,200 h ongoing	1,000 h section; 1,100 h ongoing	1,000 h section	1,000 h section	1,000 h section	1,000 h section			
700°C air (no added H ₂ O), 500 h cycles	500 h ongoing (stop at 1,000 h, section)			500 h ongoing (stop at 1,000 h, section)							
650°C air (no added H ₂ O), 500 h cycles	500 h ongoing (stop at 1,000 h, section)			500 h ongoing (stop at 1,000 h, section)							

Table 8. Summary of CTF testing conditions, materials being tested, and status of tests.

Thermal fatigue testing condition			SiMo cast iron	D5S	H-series cast austenitic stainless steel	CF8C plus
Tmin	Tmax	ΔT				
300°C	800°C	500°C	Complete	Planned	Complete	Complete
400°C	800°C	400°C			Complete	
450°C	800°C	350°C				
500°C	800°C	300°C	Complete	Planned	Complete	Complete
550°C	800°C	250°C			Complete	
600°C	800°C	150°C	Complete	Planned	Complete	Complete
650°C	800°C	150°C	Complete			
700°C	800°C	100°C	Complete	Planned	Ongoing	
300°C	500°C	200°C	Stopped			
300°C	600°C	300°C	Complete			
300°C	700°C	400°C	Complete			

Technology Transfer

As this is a CRADA with Cummins, new technologies will be readily implemented through the engines manufactured by Cummins. Publications and presentations will also disseminate the scientific knowledge acquired through this project.

Conclusions

A detailed analysis of the development of the high efficiency, heavy duty engine being developed by Cummins showed that an increase in the temperature capabilities of exhaust manifolds and piston materials would have a significant positive impact on achieving improved engine efficiencies. Because the current materials (high SiMo cast irons in exhaust manifolds and 4140 steel in pistons) are already operating at the limits of their temperature and strength capabilities, new materials with the appropriate combination of improved properties are required for these components in future heavy duty diesel engines with

targeted improvement in thermal efficiency. Several alternate materials, as well as strategies for improving the best current materials, have been identified as candidates for the next generation exhaust manifolds. Oxidation testing and CTF tests have been initiated to enable downselection and for further data collection to enable FEM of exhaust manifolds. Material property requirements (monolithic materials and coatings) for advanced pistons and potential strategies for their improvement are being evaluated and will be defined during the next project year.

Conclusions

This project comprises seven tasks aimed at developing the computational tools, process methods, and inspection methods for joining lightweighting metals. It also encompasses the development of higher strength materials for improving engine efficiency and development of an understanding of corrosion mechanisms for Mg alloys. In FY 2012, a ductile failure initiation and evolution damage mechanics based failure model was developed to catch the deformation and failure behavior for spot welds of AHSSs and successfully validated against test coupons using multiple materials and test geometries. FSSW methods for joining AHSSs were developed with quasi-static strengths exceeding the minimum values required for resistance spot welds using the same materials. A CRADA was initiated with ArcelorMittal to address the weld fatigue life of AHSSs, which is one of the key technology barriers to industrial applications for AHSS. Weld production equipment, experimental analysis equipment, and weld fatigue models have been put in place to address this issue. Significant work was accomplished toward the development of a cost-effective, robust, and accurate IR thermography based system to inspect spot weld quality. The inspection time for both real-time and postmortem applications was reduced to 3 s, and the ability to reliably detect the stuck weld, one of the most critical defect types, was successfully demonstrated. Work continued on a CRADA with Cosma for developing an IR heat treatment to increase yield strength and elongation of the cast Al portion of an Al-steel bimetallic joint to achieve a superior joint. Residual stress and torsion strength characterization have begun. The thermal modeling is almost complete, and the stress modeling has begun. A key effort was initiated to develop an understanding of the corrosion response of Mg alloys by performing a complete characterization of the micro/nanoscale location of key alloying elements and impurities in the surface film and the near-surface alloy regions. Materials were selected for study in support of an advanced diesel engine program goal to improve engine efficiencies through increasing the high temperature capabilities of exhaust manifolds and pistons.

Presentations/Publications/Patents

Chen, J.; Feng, Z.; Wang, H.; Zhang, W. Non-destructive Inspections of Welds and Joints Using Infrared Imaging and Post-Weld Heating, U.S. patent application, May 2011.

Chen, J.; Feng, Z.; Zhang, W. A Non-destructive and Real-time Inspection System for Monitoring Resistance Spot Welding Using Infrared Thermography, U.S. patent application, August 2012.

Chen, J.; Zhang, W.; Yu, Z.; Feng, Z. Automated Spot Weld Inspection Using Infrared Thermography. In *Proceedings of the 9th International Conference on Trends in Welding Research* (in press).

Hong, S.H.; Sripichai, K.; Yu, C.S.; Avery, K.; Pan, J.; Pan, T.Y.; Santella, M. *Failure Modes of Friction Stir Spot Welds in Lap-Shear Specimens of Dissimilar Advanced High Strength Steels under Quasi-Static and Cyclic Loading Conditions*; SAE Technical Paper 2012-01-0479, 2012 SAE Congress, Detroit, April 16, 2012; SAE International: Warrendale, PA.

Qiao, D. et al. The Effect of Martensitic Phase Transformation on Weld Residual Stress Distribution in Steel Sheet Lap Joint—A Computational Study. In *Proceedings of the 9th International Conference on Trends in Welding Research* (in press).

Santella, M.; Hovanski, Y.; Pan, T.Y. *Friction Stir Spot Welding (FSSW) of Advanced High Strength Steel (AHSS)*; SAE Technical Paper 2012-01-0480, 2012 SAE World Congress, Detroit, MI, April 16, 2012; SAE International: Warrendale, PA.

References

- Bonnen, J.; Iyengar, R.M. Fatigue of Spot Welds in Low-Carbon, High-Strength Low-Alloy, and Advanced High-Strength Steels and Fatigue of Fusion Welds in Advanced High-Strength Steels. In *2006 International Automotive Body Congress, 2006*; 19–30.
- Buchholz, K. Two-Metal Cradle from Cosma is Production-Ready. *Automot. Eng.* [Online] **2011**, 15. <http://www.sae.org/mags/AEI/9505> (accessed September 2011).
- Feng, Z.; Chiang, J.; Kuo, M.; Jiang C.; Sang, Y. A New Perspective on Fatigue Performance of Advanced High-Strength Steel GMAW Joints. In *Sheet Metal Welding Conference XIII*, **2008**.
- Feng, Z.; Sang, Y.; Jiang, C.; Chiang, J.; Kuo, M. Fatigue Performance of Advanced High-Strength Steels (AHSS) GMAW Joints. SAE technical paper 09M-0256, 2009 World Congress, Detroit, MI, April 20-23, 2009; SAE International, Warrendale, PA.
- Iyengar R.M. et al, Fatigue of Spot-Welded Sheet Steel Joints: Physics, Mechanics and Process Variability. Presented at the 2008 Great Designs in Steel Seminar, April 9, 2008, <http://www.autosteel.org/sitecore/Content/Internal/Listers/NewsLister.aspx?targetItem=45b2e452-b956-46ee-8c0f-f73412249fc6&siteLocation=02daea4d-8e63-45fb-bd5f-df17e7c30e6e&contentSource=Primary> (accessed November 14, 2012).
- Johnson, E.M.; Watkins, T.R.; Schmidlin, J.E.; Dutler, S.A. A Benchmark Study on Casting Residual Stress. *Metall. Mater. Trans. A*, **2012**, 43A(5), 1487–96.
- Yan, B.; Lalam S.H.; Zhu, H. *Performance Evaluation of GMAW Welds for Four Advanced High-Strength Steels*; SAE International Paper No. 2005-01-0904; SAE International: Warrendale, PA, 2005.

G. Multi-Material Enabling – Pacific Northwest National Laboratory

Field Technical Monitor: Dean Paxton
Pacific Northwest National Laboratory
902 Battelle Boulevard, P.O. Box 999, Richland, WA 99352
(509)375-2620; fax: (509)375-2186; e-mail: dean.paxton@pnnl.gov

Technology Area Development Manager: William Joost
U.S. Department of Energy
1000 Independence Ave., S.W., Washington, DC 20585
(202) 287-6020; fax: (202) 856-2476; e-mail: william.joost@ee.doe.gov

Contractor: Pacific Northwest National Laboratory
Contract No.: DE-AC05-00OR22725 & DE-AC06-76RL01830

Executive Summary

The Multi-Materials Enabling project consists of two tasks focused on research and development that can lead to greater implementation and manufacturing of multi-material lightweight components/systems in automotive applications. The tasks include the following: 1) Self-Pierce Riveting (SPR) Process Simulation, Analyses, and Development for Magnesium Joints, and 2) High-Speed Joining of Dissimilar Alloy Aluminum Tailor-Welded Blanks.

More energy efficient and environmentally friendly highway transportation is critical to reducing both the environmental impacts and energy consumption associated with transportation mobility. While transformational propulsion technologies and hybrid architectures show great promise in meeting such goals, these and other forthcoming solutions depend upon significant weight savings in passenger and commercial vehicles to fully capitalize on their potential to provide freedom of mobility without harmful emissions and dependence on foreign petroleum. Significant weight savings in the automotive fleet is likely to occur through the use of various advanced materials. While improvements in the properties, manufacturability, and cost of advanced materials are critical in achieving vehicle weight reduction, technologies that support the use of these materials in a multi-material system are equally important. Unlike a single material system, structures composed of different metals and polymer composites present significant challenges in areas such as joining, corrosion, recycling, and nondestructive evaluation. Work conducted in this agreement seeks to overcome these challenges by developing new techniques, establishing standards, and preparing advanced technologies for a production environment.

The following sections outline specific task work conducted at PNNL in the area of multi-material enabling technologies. Each task supports one or more goals within the Multi-Material Enabling Agreement.

Activity And Developments

Self-Pierce Riveting (SPR) Process Simulation, Analyses, and Development for Magnesium Joints

Principal Investigator: Elizabeth Stephens, PNNL
(509) 375-6836; e-mail: elizabeth.stephens@pnnl.gov

Co-Principal Investigator: Xin Sun, PNNL
(509) 372-6489; e-mail: xin.sun@pnnl.gov

Co-Principal Investigator: Eric Nyberg, PNNL
(509) 375-2103; e-mail: eric.nyberg@pnnl.gov

Accomplishments

- Developed a numerical tool for SPR simulation. A finite element method (FEM) SPR model was developed in LS-Dyna using explicit analysis and sheet material constitutive behavior from thermo-mechanical experimental test data. (FY2012)
- Completed thermo-mechanical experimental tests to implement into the model. Tensile stress-strain responses were investigated at quasi-static and intermediate strain rates and temperature profile and cooling rate tests were performed on AZ31B-O magnesium (Mg) sheets. (FY2012)
- Conducted a parametric study on rivet length, rivet material, sheet temperature, and cooling rate. (FY2012)
- Demonstrated that medium carbon steel rivets yield the best results in terms of the shape of the locked rivet, distance between the tip of the rivet and the tail free surface, and filling of the die. (FY2012)

Future Directions

- Perform a friction coefficient parametric study and complete finite element analysis process optimization.
- Numerically identify a heating mechanism that will provide the necessary temperature profile for SPR joining.
- Disseminate modeling results via publications in peer-reviewed journals and conference presentations.

Technology Assessment

- Target: Create Mg SPR joints of similar and dissimilar materials under the guidance of SPR modeling tools established by PNNL with no tail side cracking.
- Target: Produce Mg SPR joints with a minimum target joint strength of $1.5 \text{ kN} * t$ (substrate thickness).
- Gap: Mg alloys have low ductility at room temperature and when conventional SPR processing is used with Mg, it typically causes rivet tail end cracking.
- Gap: Cracks in the SPR joint can be detrimental to the joint performance in terms of static and fatigue strength, as well as corrosion performance.

Introduction

Increased pressure from government agencies and consumer advocate groups to produce safer, more durable, fuel-efficient vehicles, has led automotive original equipment manufacturers (OEMs) to investigate Mg for use in the major structural sections of vehicles. Mg components offer a potential weight reduction of approximately 50 percent when substituted for the higher density or lower strength steel materials conventionally deployed in vehicles. Historically, inadequate joining methods for Mg components have limited their applications in vehicles. Over the years, a variety of joining technologies have been introduced into the automotive industry to achieve lightweight vehicle goals. SPR is potentially a viable method for joining similar and dissimilar metals involving Mg. SPR is a low energy consumption joining process with relatively low initial capital equipment cost. Because SPR is a mechanical joining process, the joint formation process involves large plastic deformation at the rivet tail end to ensure a mechanical interlock between the rivet material and the bottom sheet material. However, Mg alloys have low ductility at room temperature; thus, conventional SPR processing typically causes rivet tail end cracking. These cracks can be detrimental to the joint performance in terms of static and fatigue strength, as well as corrosion performance.

The purpose of this project is to provide a reliable mechanical joining technology for Mg joint applications and to enable the success of mechanical fastening of Mg by assisting the Mg SPR process development and cycle time through rivet process simulation and experimentation. This will be achieved by providing actual SPR joint performance data of Mg/Mg and Mg/dissimilar metal joints so that more accurate data is applied to the overall structural design and by developing process windows to provide design recommendations/guidelines for effective Mg SPR joining.

Approach

This project is focused on developing and enabling the SPR process for joining Mg components in new vehicle applications to reduce vehicle weight. This project aims to eliminate or substantially address key technical barriers in using self-piercing rivets in Mg-joining applications by using an integrated modeling and experimental approach. Barriers include tail side cracking of Mg sheet or castings due to the lack of ductility at room temperature; lack of desired joint properties including corrosion at the joint; and lack of acceptable processing parameter windows. Furthermore, the project will explore alternate/non-conventional rivet metals that are similar to the materials being joined to minimize the galvanic potential in the joint and an alternative joining method (e.g., clinching) that may further promote joining of Mg. Initial work focuses on the development of a numerical tool that will be used to develop reliable Mg riveting process parameters through modeling and provide guidance in the development of joining process windows. The temperature profile and the heating mechanism that will provide the steady state or transient heating profile needed to achieve the desired ductility will be identified numerically.

The project is divided into two phases. Phase 1 will focus on validating, experimentally, the modeling tool previously developed for Mg SPR joining using conventional rivet materials and geometries. In addition, this phase will validate, experimentally, predicted results from the modeling tool to provide actual joint performance data (e.g., joint strength, fatigue strength, and corrosion performance) for the joint combinations evaluated. Phase 2 will focus on optimizing Mg SPR joints using the established modeling tool to investigate alternate rivet materials, including coatings or interlayers (e.g., adhesives). This will include addressing potential joint corrosion issues and optimizing rivet geometry (i.e., shape and length) and die design to ensure joint integrity and joint performance. In addition, clinch joining, an alternate joining method that may be used singly or in conjunction with SPR, will be explored for its potential to advance joining of Mg.

Technology Transfer Path

Technology transfer will occur throughout the project via close collaboration between PNNL and an industrial partner. The technology transfer approach includes establishing a CRADA between Emhart Teknologies, an SPR equipment supplier, and PNNL that will include the development of process equipment and processing parameters necessary to achieve successful Mg SPR joints.

Results and Discussion

In FY 2012, efforts focused on developing an SPR numerical tool and performing necessary tests to provide material property input for the model. Numerical simulations of the self-piercing riveting process have been carried out using the commercial finite element (FE) code LS-Dyna. A two-dimensional axisymmetric model was developed (see [Figure 1](#)) that included two Mg sheets to be joined, rivet, and tools (i.e., die and blank holder). A rigid vertical displacement was applied to the top part of the rivet. The rivet comes in contact with the upper sheet, deforms it, and pierces through until it locks the bottom sheet to the corners of the die. A failure criterion with elements deletion technique has been implemented in the model to simulate the piercing. The rivet material considered was low carbon steel, medium carbon steel, or high carbon steel. The behavior of the rivet material was modeled using an elastic-plastic constitutive model with kinematic and isotropic hardening. Parameters of the model were obtained from the open literature.

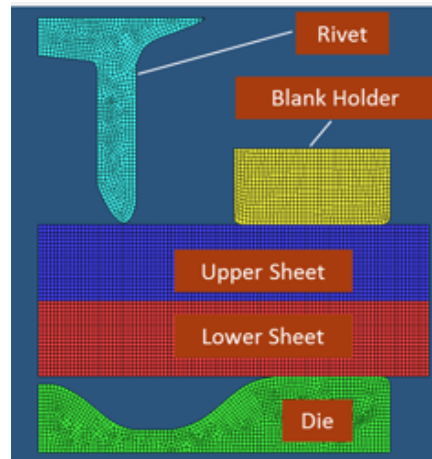


Figure 1. Representation of the FEM model.

The Johnson-Cook equation was used to describe constitutive behavior to account for the strain rate and temperature sensitivity of AZ31B-O Mg sheets. The equation is expressed as follows:

$$\sigma = (A + B\varepsilon_p^n) \left(1 + C \ln \dot{\varepsilon}_p^* \right) \left(1 - T_*^m \right) \quad (1)$$

where ε_p is the equivalent plastic strain, $\dot{\varepsilon}_p^* = \dot{\varepsilon}_p / \dot{\varepsilon}_0$ is the dimensionless plastic strain rate, and $T_*^m = (T - T_{room}) / (T_{melt} - T_{room})$ is the homologous temperature. T_{melt} is melting point, T_{room} is the room temperature and T is the temperature of a material element (all temperatures in Kelvin). Model parameters were calibrated using the experimental data obtained from tensile tests carried out at different temperatures and strain rates, and temperature profile/cooling rate tests carried out on AZ31B-O Mg sheets (2 mm thick).

[Figure 2](#) shows the tensile stress-strain behavior of the Mg sheet material tested in the rolling direction. Four temperatures ranging from 200 to 350°C were adopted at strain rates of 0.005 and 5/s. The results show that the flow stress of AZ31B-O has positive strain-rate sensitivity at a given temperature. On the other hand, a significant drop in the strain to failure was observed when the strain rate increased. Temperature increase results in a softening of the material and a significant improvement in ductility. Therefore, high temperatures (300 to 350°C) appear to be more suitable for the joining of the Mg sheets via the SPR process.

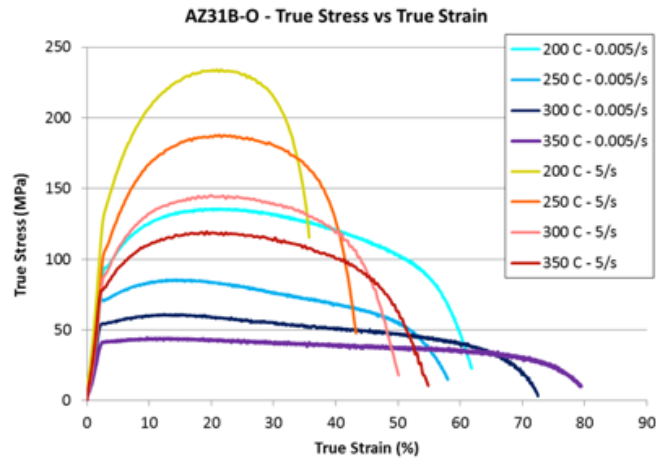


Figure 2. Tensile stress-strain curves for AZ31B-O Mg at quasi-static and intermediate strain rates and different temperatures.

The FEM model was able to successfully simulate the SPR process. The upper sheet was split into two parts and the rivet tail and bottom sheet locked into the corner of the die. Figure 3 shows the different stages of the SPR process. The small void between the top and bottom sheet is an artifact of the element removal in the FEM model. In the real process, material is deformed into this region during piercing.

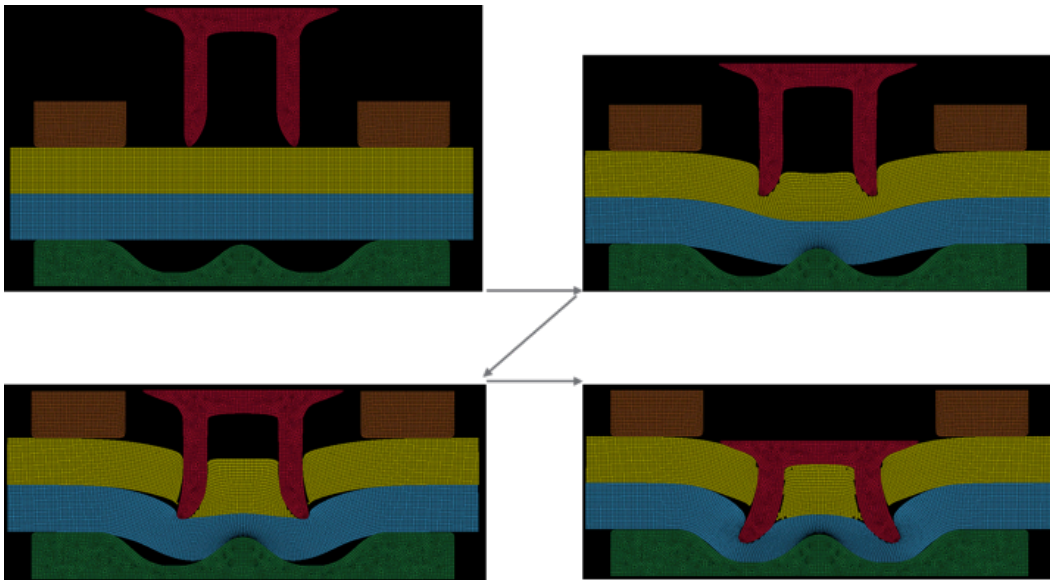


Figure 3. Different stages of the SPR process predicted by the FEM model.

Parametric studies were conducted using rivet and die geometry, rivet material, Mg sheet temperature, and cooling rate (i.e., incorporating temperature gradients in simulations). As was already shown in the tensile test data, a temperature above 300°C is necessary to obtain satisfactory SPR joints. This temperature represents a good combination between softness of the sheet and ductility. The cooling rate was demonstrated to be a crucial factor for a good SPR joint. Several factors can be responsible for the sheet cooling: (i) heat sinks (holder, die), (ii) duration between the moment the heat source is removed, and (iii) start of the piercing process. Figure 4 represents the model prediction for different cooling rates at $T = 300^{\circ}\text{C}$ for a medium carbon steel rivet material. A better rivet lock was observed at the medium cooling rate (center image).

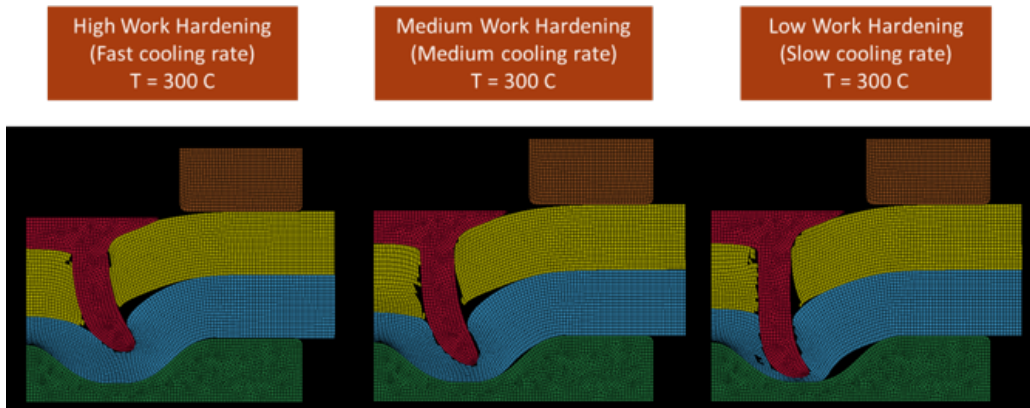


Figure 4. Parametric study on the cooling rate at $T = 300^{\circ}\text{C}$ and medium carbon steel rivet.

Observations drawn from several simulation combinations include the following.

- Low carbon steel rivets work better at $T > 300^{\circ}\text{C}$ with slow cooling rates.
- Medium carbon steel rivets work at most temperatures with a large range of cooling rates.
- High carbon steel rivets work for lower temperatures with a fast cooling rate.

Table 1 qualitatively represents the model predictions for the different combinations at $T = 300^{\circ}\text{C}$ and the effect of cooling rates.

Table 1. Summary of the joining behavior at different cooling rates and rivet material.

Cooling rate	Fast						Slow
Low Carbon	Red	Red	Red	Red	Green	Green	Green
Med Carbon	Red	Green	Green	Green	Green	Green	Red
High Carbon	Green	Green	Green	Green	Red	Red	Red

Conclusion

In this reporting period, a numerical tool was developed for SPR simulation. Sheet material constitutive behavior was implemented into the model using thermo-mechanical experimental data. Parametric studies on rivet length, rivet material, sheet temperature, and cooling rate were conducted. The modeling tool identified a temperature range of 325 to 350°C for SPR of Mg/Mg sheet using conventional rivet materials and geometries. In addition, the SPR modeling tool demonstrated that medium carbon steel rivets yield the best results in terms of shape of the locked rivet, distance between the tip of the rivet and the tail free surface, and filling the die.

High-Speed Joining of Dissimilar Alloy Aluminum Tailor-Welded Blanks

Principal Investigator: Yuri Hovanski, PNNL
(509) 375-3940; e-mail: Yuri.Hovanski@pnl.gov

Industry Partners:

Blair Carlson, General Motors, e-mail: blair.carlson@gm.com
Mark Eisenmenger, TWB LLC, e-mail: mark.eisenmenger@twbcompany.com
Brandon Landino, Alcoa, e-mail: Brandon.landino@alcoa.com

Accomplishments

- Down-selected the alloys and gauges for this study; received, sized, and disseminated to each of the partners hundreds of sheets in each alloy/gauge combination totaling more than 2000 lb of aluminum sheet metal provided by Alcoa. (FY 2012)
- Completed the pre-study evaluating feasibility of laser-based technologies—including single- and double-spot laser and laser hybrid in comparison to friction stir welding in AA5182. (FY 2012)
- Determined the General Motors (GM) component to be used for final evaluation and scheduled die modifications to fit a tailor-welded blank scheduled for initial testing during next year. (FY 2012)
- Initiated full design of experiment to quantify the measurable effects of tooling on formability and weld quality in high-speed friction stir welded tailor-welded blanks made in dissimilar thicknesses and alloy combinations. (FY 2012)

Future Directions

- Weld parameter development for both dissimilar alloy and dissimilar thickness tailor-welded combinations that combine statistical design of experiment approaches with formability screenings to quantify the influence of tooling and parameters on post-weld properties.
- Coupon production and evaluation that ultimately supports full-size component production and testing.
- Support technology transfer of welding and formability analysis to automotive supply chain.
- Probabilistic evaluation of alloy/thickness combinations that support component-forming models.
- Component production, stamping validation, and production durability testing of aluminum tailor-welded blanks.
- Development of weld parameters for 5XXX to 7XXX series sections.

Technology Assessment

- Target: Achieve friction stir weld speeds for aluminum tailor-welded blanks in excess of 4 m/min with repeatable quality and surface finish.
- Gap: While conventional laser techniques are capable of welding at speeds from 4 to 10 m/min, linear speeds for friction stir welding have traditionally been below the 3 m/min range.
- Target: Develop capability for high-speed friction stir welding within the automotive supply chain by transferring high-speed friction stir welding techniques to at least one supplier that is capable of producing high-volume quantities of welded blanks.
- Gap: Friction stir welding is currently performed by only a few niche companies, none of which with the capability to support high-volume production.
- Target: Probabilistic analysis that supports formability modeling of tailor-welded components as a direct input, avoiding the complexity of direct phenomenological relations that currently do not exist.

- Gap: Modeling efforts of as-welded blanks lack the constitutive relationships needed to correctly predict the post-weld formability; however, probabilistic analysis inserted as an input may allow the modeling efforts to move forward based on statistically derived boundaries.
- Target: Full-size welded components that demonstrate modeled performance.
- Gap: Currently modeling efforts to not accurately represent as-welded components; thus, a modeling effort needs to be fully verified with full-size component testing.

Introduction

Strategic research and development investments over the last few decades have moved tailor-welded products from concept to reality. Several companies now produce dissimilar thickness panels, tailor-welded coils, and tailor-welded tube sections in a variety of steel alloys for use in many applications (e.g., door inners, shock towers, floor pans). Use of the tailor-welded technology is increasing with greater demand for lightweight structures that reduce part count and lower cost. While automotive OEMs would like to expand the usage of tailor-welded technologies into aluminum alloys, current joining technologies significantly reduce the formability of the as-welded materials. Aluminum alloys have great potential for usage in tailor-welded structures, and preliminary assessments show that the weight of numerous high-volume automotive components could be reduced by more than 40 percent.

While preliminary assessments demonstrate that tailor-welding technologies have the potential to reduce part count, cost, and weight, the joining technology needed to provide adequate formability of the as-welded blank is not sufficiently developed to transfer the technology to any supplier. While several groups have shown the preliminary potential for FSW 5083 aluminum blanks of similar thickness, no weld schedules exist that can be modified or adapted for very dissimilar thicknesses (2:1 thickness ratios and greater) in dissimilar aluminum alloy combinations (e.g., 5000 series to 6000 or 7000 series aluminum alloys). To achieve weight savings in excess of 40 percent, weld parameters must be developed that enable multiple alloys to be joined in very dissimilar thickness sheet combinations while maintaining the majority of their original formability.

While the majority of data related to friction stir welding of Al tailor-welded blanks (TWB) is based around non-precipitation strengthened alloys, a material set that is very amenable to producing as-welded blanks with formability similar to the parent sheet, very little data has been produced relating the functional relationships between tool design, process parameters, fixturing, and alloy combinations. As joining of dissimilar Al alloys has proved much more problematic when considering the as-welded formability of TWBs, successful implementation will depend upon a much greater understanding of the influence of each of these factors on the formability of the tailor-welded component. Thus, further development of the friction stir welding process in these form factors will be necessary to provide a side-by-side comparison with other welding techniques.

Furthermore, previous pitfalls have hindered the progress of Al TWBs, as several groups have moved directly from welding to stamping without understanding the formability limits of the TWBs. This weld and stamp approach has proven problematic, as very little information on the usability of the as-welded component comes from the stamped part. Whether the part forms or fails provides little data as to whether the blanks will ultimately work in another application, and as such does not lead to a successful deployment path. Predictive formability analysis has previously been developed and used at PNNL to determine the probabilistic forming limit for a weld blank. This approach, in conjunction with stamping models, has the potential to determine the overall probabilistic formability limits and provide an understanding of how they can be applied to numerous part geometries while avoiding the expense of the weld and stamp methodology.

This project proposes to develop the functional relationships of factors driving the weld formability of both dissimilar thickness AA5182 as well as dissimilar alloy combinations. Furthermore, the best in class parameter set for each will then be analyzed to determine the probable forming limit, which will be used to model the overall stamping process. The process will be validated as the technology is transferred for actual part production, providing the tools needed to be able to further implement the process on other parts, geometries, and materials.

Approach

To develop the joining technology needed to enable aluminum TWBs for high-volume automotive components, the work scope is divided into four main task areas. The first focuses on the initial weld development for formability, including quantifying the effects of tool design and process parameters on formability. The second is designed to provide a comparison of the formability of aluminum welds produced via friction stir, laser, and laser-plasma welding. This task will ultimately lead to a decision gate that provides the information necessary to justify capital investments and product design using aluminum TWBs. The third task is divided into several areas that will emphasize preparing the process for commercialization. This includes push the process to higher linear weld speeds, tying probabilistic formability data into the component-forming models, and assisting the transfer of the weld process into a supplier’s facility. This task will lead to the concluding task of producing actual production-ready coupons that will be stamped and tested by GM as a conclusion to the project efforts.

Results and Discussion

When the project began in the second quarter of FY 2012, the first order of business was to coordinate the team and timeline such that each participant would be able to provide their contributions in a timely and effective manner to allow successful completion. A set of aluminum alloys and thickness were selected to accommodate the eventual production of a full-size door-inner, with combinations of dissimilar thickness AA5182, and a dissimilar alloy combination of AA5182 and AA6022. [Table 2](#) shows the alloys selections, thicknesses, and tempers selected, based on their availability and ability to meet current OEM specifications for strength and ductility.

Table 2. Material selection matrix for high-speed joining of aluminum tailor-welded blanks.

Alloy Designation	Temper	Thickness (mm)
6022	T4	2.0
6022	T4E32	1.0
5182	O	1.2
5182	O	2.0

Because both sets of 6022 were age-sensitive, storage locations were setup to reduce the effects of natural aging at temperatures well below freezing. Because welding and testing are to be performed at several locations, material handling was crucial to the overall quality controls for the welding, testing, and analysis to be performed over the life of the project (3 years).

A preliminary effort in evaluating dissimilar thickness AA5182 was performed using 0.9-mm and 2.1-mm thicknesses. Welding was performed using friction stir welding, laser welding with single and double spot, and laser hybrid welding. [Table 3](#) summarizes the results from these welding techniques, and shows that with measuring limited dome height alone, several of the specimens welded using laser techniques compared well with the friction stir welded specimens. Nevertheless, only friction stir welding passed all the qualification measures (i.e., shape, formability, and lack of defects). Laser-based processes struggled most significantly with the overall shape along the weld, demonstrating difficulty to avoid sheet position mismatch, undercut, and unacceptable levels of both concavity and convexity depending on the specific process and setup.

Table 3. Comparative limited dome height data for welding of dissimilar thickness AA5182.

Method	Welding Speed (m/min)	Dome Height (mm)
Laser, single spot	8	11.7 ± 0.3
Laser, twin spot (across weld)	6	15.1 ± 0.4
Laser, twin spot (along weld)	6	14.3 ± 1.0
Laser-plasma hybrid	8	11.9 ± 4.0
Laser-plasma hybrid 2	6	14.3 ± 3.0
Friction Stir Welding	3	15.4 ± 0.5

Dome height was determined using a standardized limited dome height test. The operation was modeled using ABAQUS/Explicit with the punch and die treated as rigid analytical surfaces as shown in [Figure 5](#). The aluminum sheet in a 2:1 thickness matchup was modeled to the maximum strain found in tensile testing each of the sheet materials. The model

predicted a dome height of approximately 16.0 mm for a 2:1 thickness ratio in the pre-study for the AA5182 materials. As this alloy was not very susceptible to degradation in the heat affected zone, the simplified model represents the measured results fairly well.

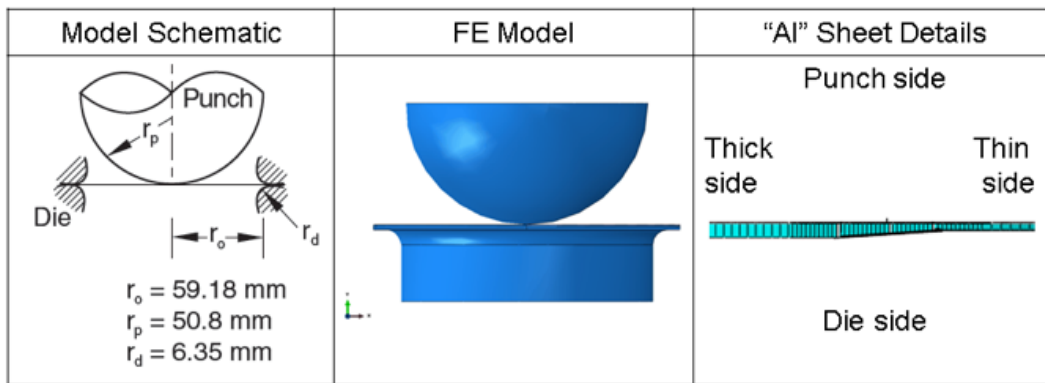


Figure 5. Schematic representation of the FEM for a limited dome height test with a 2:1 thickness ratio.

Technology Transfer Path

Technology transfer into the high-volume automotive supply chain was a key task critical to the planning of the entire effort. The project was designed to provide technological expertise from the researchers at the PNNL who engage the entire supply chain, including: the material provider, Alcoa; the high-volume automotive supplier, TWB LLC.; and the OEM, GM. With this team engaged from start to finish in the project, the technology will be developed and transferred using alloys and gauges already set for production quantities and quality sufficient to meet the demands of high-volume automotive production. A production line will be set up within the high-volume supplier's facility with quality and production standards in place, allowing full-size production components to be produced for testing by the automotive OEM.

At the conclusion of the project, the entire supply chain should be staged and able to supply aluminum tailor-welded blanks for high-volume production components. This path should effectively bridge the gap between the development and utilization by supporting the industrial implementation as part of the project.

Conclusions

Initiation of this work on high-speed joining of dissimilar aluminums provided a broad ability for the entire supply chain to become involved in moving aluminum joining of dissimilar thickness aluminum sheet towards high-volume production. The project team was involved in outlining the specific materials of interest and putting in place the proper material handling rules to ensure data over the life of the project is relevant and consistent. Each of the industrial partners contributed significant in-kind efforts in FY 2012, including materials and expertise provided by the Alcoa team, weld studies and material analysis provided by GM, and business/cost modeling and capital equipment investment by TWB LLC.

With the results from the pre-study covering 2:1 thickness ratio AA5182, friction stir welding was able to rise above the laser processes evaluated by GM. While all laser processes were able to run at significantly higher linear speeds, only the twin laser configured with the lasers across the weld line were able to produce post-weld formability similar to the friction stir welded specimens as indicated by the dome heights shown in Table 2. The twin spot laser welds produced a much more uniform cross-section, but failed to remain consistent in shape along the length of the weld.

Friction stir welds in the same material joined at approximately 3 m/min were able to maintain consistent shape, density, and performance along the length of the welds analyzed for the pre-study. A more detailed analysis of the effects of process parameters and tool design is underway for combination of the materials shown in Table 1, and results will be available as progress continues.

Presentations/Publications/Patents

Carsley, J.; Hovanski, Y.; Pilli, S.; Verma, R.; Hartfield-Wunsch, S.; Carlson, B.; Eisenmenger, M. High Speed Joining of Aluminum Tailor-Welded Blanks for Automotive Applications. Presented at Material Science and Technology 2012, Pittsburgh, PA, Oct. 2012.

3. Carbon Fiber and Polymer Composites

A. Predictive Tools For Carbon Fiber Composites – Pacific Northwest National Laboratory

Implementation of Property Prediction Models into Autodesk® Moldflow® Packages

Principal Investigator: Ba Nghiep Nguyen
Pacific Northwest National Laboratory
P.O. Box 999 – MSIN J4-55, Richland, WA 99352
(509) 375-3634; e-mail: Ba.Nguyen@pnnl.gov

Field Technical Monitor: Dean Paxton
Pacific Northwest National Laboratory
(509)375-2620; e-mail: dean.paxton@pnl.gov

Technology Area Development Manager: Carol Schutte
U.S. Department of Energy
1000 Independence Ave., S.W., Washington, DC 20585
(202) 287-5371; fax: (202) 856-2476; e-mail: carol.schutte@ee.doe.gov

Contractor: Pacific Northwest National Laboratory (PNNL)
Contract No.: DE-AC05-00OR22725 & DE-AC06-76RLO1830

EXECUTIVE SUMMARY

Recently, long-fiber thermoplastic (LFT) composites have attracted great interest within the automotive industry because these materials offer much better structural performance (e.g., higher elastic moduli, strength, and durability) than their short-fiber analogues and can be processed through injection molding with some specific tool design. However, to compute and tailor the mechanical properties of LFTs for automotive applications, process and property prediction models as well as computational tools must be developed to predict the microstructure and resulting mechanical properties of these composites. Under Phase II of the Predictive Engineering project funded by the Lightweight Materials program in the U.S. Department of Energy (DOE) Office of Vehicle Technologies, PNNL developed the property prediction (constitutive) models for injection-molded LFTs that describe the linear and nonlinear behaviors of these materials (e.g., Nguyen et al., 2008, Nguyen et al., 2009, Nguyen et al., 2010). PNNL then built the computational tools named EMTA (Eshelby-Mori-Tanaka Approach) (Nguyen, 2010a) and EMTA-NLA (Eshelby-Mori-Tanaka Approach to Non-Linear Analysis) (Nguyen, 2010b) to implement the developed constitutive models for LFTs. The models explore the standard and improved Eshelby-Mori-

Tanaka approaches that consider elastic fibers distributed in a thermoplastic matrix whose behavior can be linear or nonlinear dependent on the loading prescribed to the composite.

In an effort to transfer the technologies developed under the Predictive Engineering project to the American automotive and plastics industries, PNNL obtained the approval of the DOE Office of Vehicle Technologies to provide Autodesk, Inc. with the technical support for the implementation of the basic property prediction models of EMTA and EMTA-NLA in the Autodesk® Moldflow® packages. These models are the elastic stiffness model (accounting for fiber length and orientation distributions), the fiber/matrix interface debonding model, and the elastic-plastic models. PNNL's technical support to Autodesk included (i) providing the theoretical property prediction models as described in published journal articles and reports, (ii) providing explanations of these models and computational procedures, (iii) providing the necessary LFT data for process simulations and property predictions, and (iv) performing EMTA-NLA/ABAQUS® analyses to further assess and validate the elastic-plastic damage models for select LFT materials.

Accomplishments

- Autodesk's staff implemented the EMTA elastic model, accounting for fiber length and orientation distributions in LFTs (Nguyen et al., 2008), in Autodesk Simulation Moldflow Insight (ASMI, an injection molding simulation and warpage analysis software) (FY 2012)
- Autodesk's staff implemented the EMTA fiber/matrix debonding model, accounting for fiber length and orientation distributions in LFTs (Nguyen et al., 2010, Nguyen, 2010a), in ASMI (FY 2012)
- Provided Autodesk staff with technical support and LFT data for model implementation and validation (FY 2012)
- Performed EMTA-NLA/ABAQUS® analyses of selected LFT structures for further model validation (FY 2012)

Future Directions

Implement the EMTA-NLA elastic-plastic damage models in Autodesk Moldflow Structural Alliance (AMSA, a software package that interfaces ASMI to the structural analysis codes, ABAQUS®, ALGOR®, and ANSYS®)

Technology Assessment

- Target: Implement the basic property prediction models of EMTA and EMTA-NLA in Autodesk® Moldflow® packages for LFT structures
- Gap: Autodesk's staff need to implement EMTA-NLA elastic-plastic damage models for nonlinear analyses using AMSA and a structural analysis code

Introduction

Under the previous Predictive Engineering effort, PNNL developed linear and nonlinear property prediction models for LFTs. These models were implemented in PNNL's EMTA and EMTA-NLA codes. While EMTA is standalone software for the computation of a composite's thermoelastic properties, EMTA-NLA includes a series of nonlinear models implemented in ABAQUS® via user subroutines for structural analyses. In these models, fibers are assumed to be linear elastic while the matrix material can exhibit a linear or typical nonlinear behavior, depending on the loading prescribed to the composite. The key idea is to model the constitutive behavior of the matrix material and then to use an Eshelby-Mori-Tanaka approach, combined with numerical techniques for fiber length and orientation distributions, to determine the behavior of the as-formed composite.

The basic property prediction models of EMTA and EMTA-NLA have been subject for implementation in the Autodesk Moldflow software packages. These models are the elastic stiffness model accounting for fiber length and orientation distributions, the fiber/matrix interface debonding model, and the elastic-plastic models. The PNNL elastic-plastic models for LFTs describes the composite nonlinear stress-strain response up to failure by an elastic-plastic formulation associated with either a micromechanical criterion to predict failure or a continuum damage mechanics formulation coupling damage to plasticity. All models account for fiber length and orientation distributions and fiber/matrix debonding that can occur at any

stage of loading. This report summarizes the recent results from ASMI analyses using the EMTA models and EMTA-NLA/ ABAQUS® analyses for further assessment of the EMTA-NLA models to support their implementation in AMSA.

Approach

After mold filling simulation and fiber length and orientation predictions by ASMI for the final composite part or component, it is necessary to predict the elastic properties of the as-formed LFT composite and the extent of warpage caused by thermal stresses during processing. The EMTA models and their implementation in ASMI help solve these problems. Next, nonlinear analyses of LFT structures under loading are achieved by AMSA that is interfaced with a structural analysis package using EMTA-NLA elastic-plastic models.

Results and Discussion

The first application illustrates ASMI analysis of a large 50wt% long-glass-fiber/polyamide 6,6 (PA6,6) plaque (12 in. × 12 in. × 0.11 in.) from injection molding simulation to elastic properties prediction using the EMTA elastic model accounting for fiber length and orientation distribution (Nguyen et al., 2008). **Figure 1** shows the ASMI model for the injection molding simulation of this plaque. Before any property predictions, it was necessary to check fiber orientation and length predictions as the predicted fiber orientation and length are used in subsequent property predictions. **Figure 2(a)** provides the predicted and experimental through-thickness distributions of the orientation tensor components A_{11} and A_{22} in the flow and cross-flow directions in the center of the plaque. **Figure 2(b)** shows the predicted and measured fiber length distributions for the same region. These predictions are within 15 percent of experimental results. Next, predicted fiber orientation and length distributions were used to compute the elastic properties for the plaque. **Figure 3** shows the contours of the elastic moduli expressed in the principal orientation axes. The predicted flow (18030 MPa) and cross-flow (13071 MPa) moduli at the center of the plaque are within 15 percent of the experimental results (16100 and 11400 MPa).

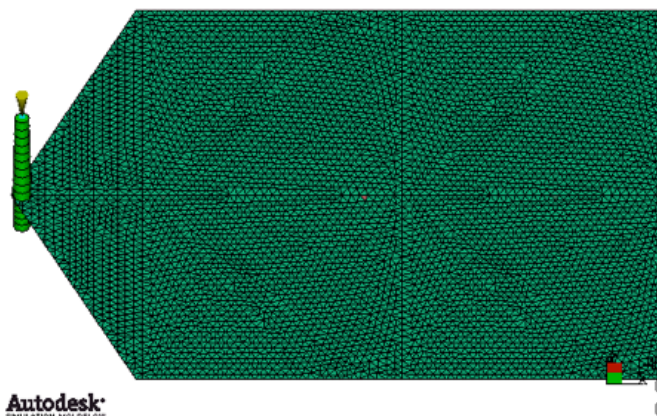


Figure 1. ASMI model for analyzing of the large long-glass-fiber/PA6,6 plaque.

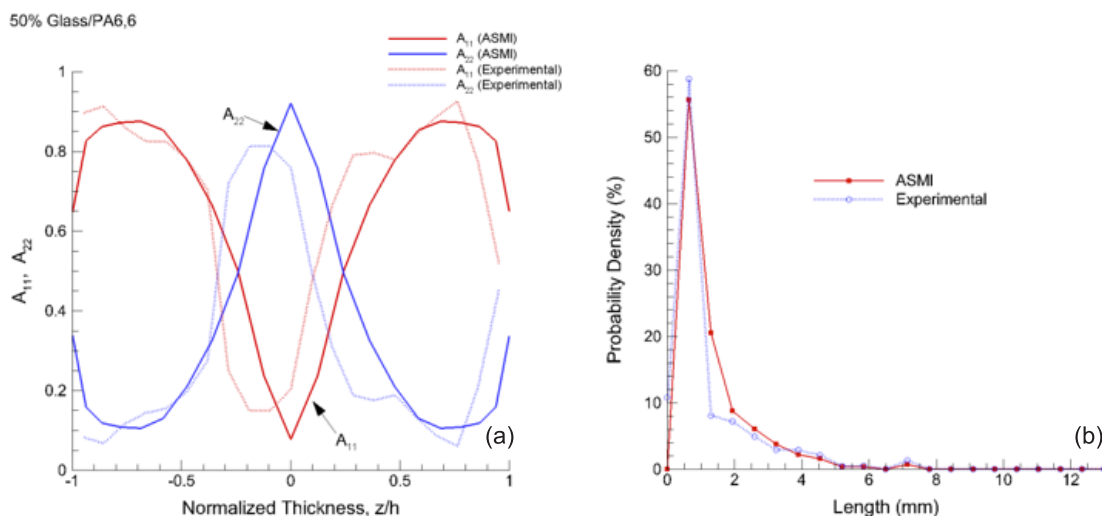


Figure 2. (a) Predicted and measured fiber orientation distribution and (b) predicted and measured fiber length distribution for the center of the long-glass-fiber/PA6,6 plaque.

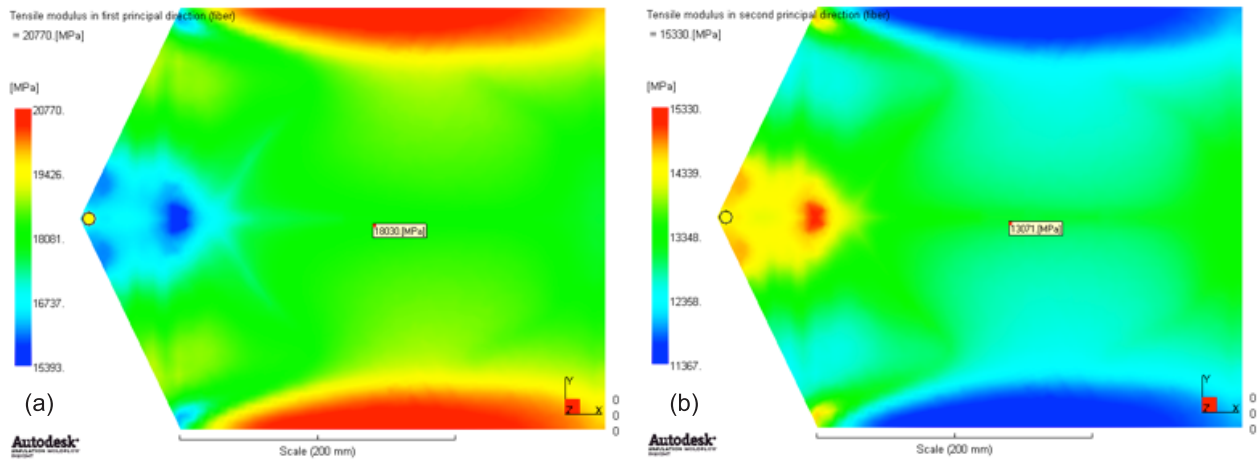


Figure 3. (a) Predicted distribution of the first principal elastic modulus, and (b) predicted distribution of the second principal elastic modulus for the long-glass-fiber/PA6,6 plaque.

Fiber/matrix debonding can occur in the final composite after processing or in use. The extent of debonding depends on processing condition and the quality of fiber/matrix adhesion. Fiber/matrix interface imperfections and partial debonding after processing reduce the mechanical properties of the as-formed composite. Fiber/matrix debonding in EMTA was modeled by a modified Eshelby-Mori-Tanaka approach based on Qu (1993). The debonding model uses a damage parameter controlling the fiber/matrix interface compliance. Figures 4(a) and (b) illustrate the first principal elastic modulus computed for a 40wt%-long-glass/polypropylene (PP) center-gated disk without and with incorporation of debonding, respectively. These results show that partial fiber/matrix debonding after processing causes a significant reduction of elastic moduli in the injection-molded composite. The predicted first principal elastic moduli without and with debonding are 7815 MPa (Figure 4(a)) and 6891 MPa (Figure 4(b)) at 35 mm from the center, respectively.

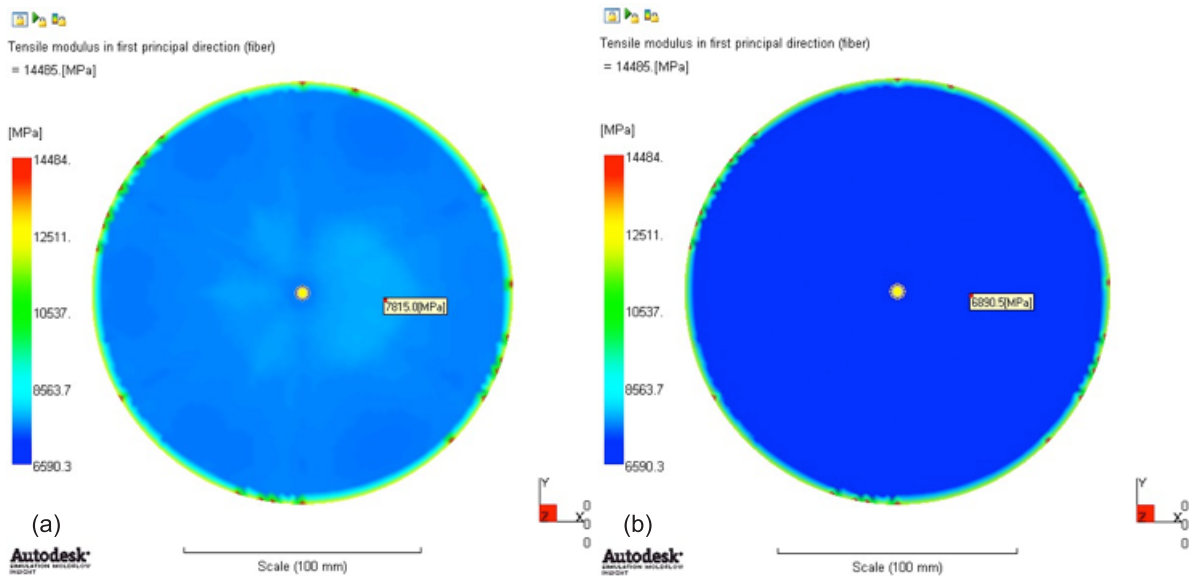


Figure 4. Predicted first principal elastic modulus in a glass/PP disk without (a) and with debonding (b).

EMTA-NLA/ABAQUS® analyses were performed that include layered shell modeling and three-dimensional (3-D) modeling of selected LFT specimens using the elastic-plastic damage models of EMTA-NLA to further validate these models for supporting their implementation in AMSA. Figure 5(a) shows the damage development in a core layer of a tensile specimen cut from the glass/PA6,6 plaque (illustrated in Figure 1) along the flow direction on the plaque centerline. Total failure occurs when the damage variable attains the critical value ($SDV3 = 0.3$ for this material). More damage accumulations occurred in the specimen end region near the gate due to perturbed flow, which affects local fiber orientation. In addition, to assess the stress/strain response captured at the specimen center, layered shell and 3-D models of the specimen center were built and analyzed. Figure 5(b) shows the detailed damage distribution in the specimen center predicted by the 3-D model using 3-D solid elements of ABAQUS. As the fibers in the core layers are rather aligned with the cross-flow direction, tensile loading applied in the flow-direction has caused more damage in these layers as well captured by the 3-D model.

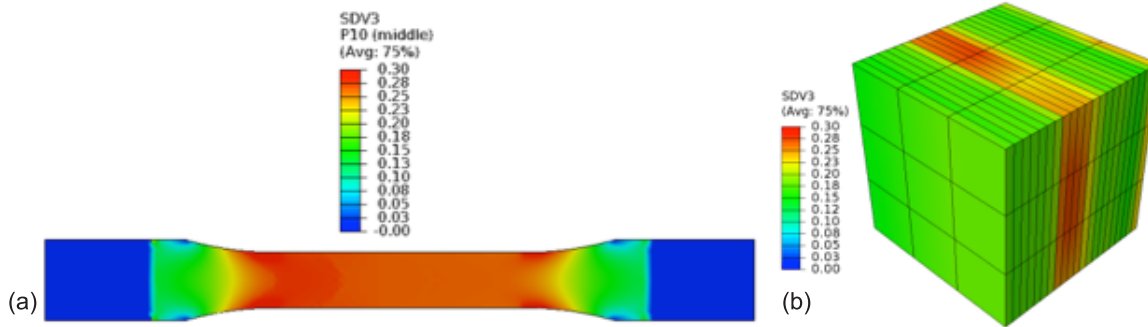


Figure 5. EMTA-NLA/ABAQUS analysis of a tensile specimen cut from the glass/PA6,6 plaque: (a) Predicted damage distribution in the specimen at the onset of failure, and (b) 3-D damage analysis of the specimen center. The red areas indicate the damage variable SDV3 has attained the critical value at failure for this material.

Figure 6 presents the predicted stress/strain responses compared to the experimental results obtained from four different tensile tests (labeled “Experiments 1-4”) performed at Oak Ridge National Laboratory (ORNL) under the previous Predictive Engineering PNNL/ORNL effort. ORNL cut the ASTM D638 Type 1 standards specimens from the glass/PA6,6 plaques along the flow direction on the plaque centerline and loaded them to failure. Table 1 gathers the predicted strengths based on different models and experimental strength averaged over all four measured values. The relative errors are also given in Table 1. All predicted strengths agree with the average measured strength within 15 percent. It is notable that accounting for fiber/matrix debonding in addition to matrix damage has improved the stress/strain prediction during the final phase of loading.

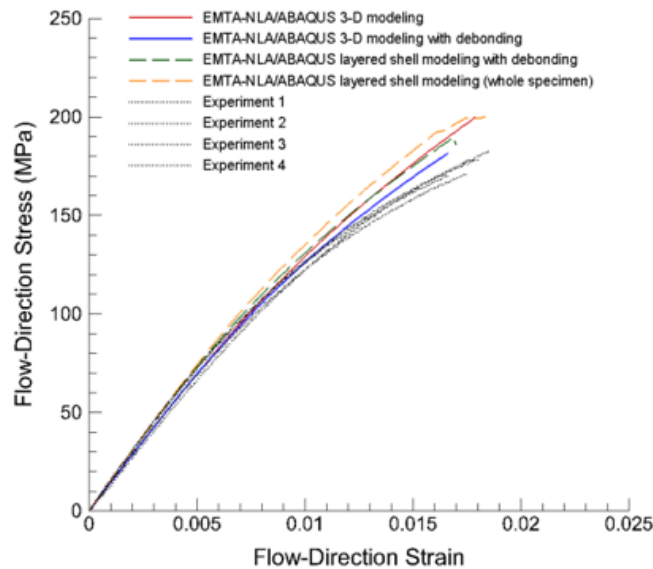


Figure 6. Predicted and experimental stress-strain responses of the flow-direction specimens cut from the glass/PA6,6 plaque

Table 1. Predicted flow-direction strengths for the glass/PA6,6 based on different EMTA-NLA/ABAQUS models and experimental strength averaged over four measured values (Figure 6).

	3-D Model	3-D Model (Debonding)	Layered-shell Model (Debonding)	Layered-shell Model (whole specimen)	Experimental
Flow-direction strength (MPa)	200.2 (13.9%)	182.1 (3.6%)	189.5 (7.8%)	199.3 (13.4%)	175.8

Technology Transfer Path

The implementation of the EMTA models in Autodesk® Moldflow® is a sound technology transfer path that will allow the automotive and plastics industry to have a predictive tool to design LFT composites.

Conclusions

The implementation of EMTA elastic and debonding models in ASMI allows for predicting elastic properties of LFT composite structures related to semi-structural and structural applications. Fiber/matrix debonding significantly affects mechanical properties (e.g., stiffness, stress-strain response, strength). Good fiber/matrix adhesion is crucial in minimizing this defect. Future work includes Autodesk's implementation of the EMTA-NLA elastic-plastic models in AMSA for nonlinear analyses of LFT structures using AMSA and a structural finite element analysis code.

Presentations/Publications/Patents

Nguyen, B.N.; Kunc, V. Engineering Property Prediction Tools for Tailored Polymer Composite Structures. Presented at the 2012 DOE Vehicle Technologies Office Annual Merit Review (http://www1.eere.energy.gov/vehiclesandfuels/pdfs/merit_review_2012/lightweight_materials/lm068_nguyen_2012_o.pdf).

References

- Nguyen, B.N.; Bapanapalli, S.K.; Holbery, J.D.; Smith, M.T.; Kunc, V.; Frame, B.J.; Phelps, J.H.; and Tucker III, C.L. Fiber Length and Orientation Distributions in Long-Fiber Injection-Molded Thermoplastics – Part I: Modeling of Microstructure and Elastic Properties. *J. Compos. Mater.* **2008**, *42*:1003-1029.
- Nguyen, B.N.; Bapanapalli, S.K.; Kunc, V., Phelps J.H., and Tucker III, C.L. Prediction of the Elastic-Plastic Stress/Strain Response for Injection-Molded Long-Fiber Thermoplastics.” *J. Compos. Mater.* **2009**, *43*: 217-246.
- Nguyen, B.N. and Kunc V. An Elastic-Plastic Damage Model for Long-Fiber Thermoplastics. *Intl J. of Damage Mech.* **2010**, *19*(6):691-725.
- Nguyen, B.N. *EMTA User's Guide*. PNNL-20013, Pacific Northwest National Laboratory, Richland, Washington, 2010.
- Nguyen, B.N. *EMTA-NLA User's Guide*. PNNL-19997, Pacific Northwest National Laboratory, Richland, Washington, 2010.
- Qu, J. The Effect of Slightly Weakened Interfaces on the Overall Elastic Properties of Composite Materials. *Mech. Mater.* **1993**, *14*: 269-281.

B. Low Cost Carbon Fiber Development – Oak Ridge National Laboratory

Field Technical Monitor: C. David Warren
 Oak Ridge National Laboratory
 1 Bethel Valley Road; Oak Ridge, TN 37831
 (865) 574-9693; fax: (865) 574-6098; e-mail: warrencd@ornl.gov

Technology Area Development Manager: Carol Schutte
 U.S. Department of Energy
 1000 Independence Ave., S.W.; Washington, DC 20585
 (202) 287-5371; fax: (202) 856-2476; e-mail: carol.schutte@ee.doe.gov

Contractor: Oak Ridge National Laboratory (ORNL)
 Contract No.: DE-AC05-00OR22725

Executive Summary

The cost of producing carbon fiber (CF) is the single largest obstacle to its incorporation in future automotive systems. According to a cost study performed by the program, 51% of the cost of producing CF is attributable to the cost of the precursor, 43% of the cost of carbon fiber is attributable to the conversion of the precursor into carbon fiber and activating the surface for resin compatibility, and the remaining 6% of the cost is for spooling and handling. Significant effort is being expended on developing lower cost, higher rate production technologies. Conversion work includes development of a higher speed, lower cost oxidative stabilization process and development of a microwave assisted plasma (MAP) process carbonization method.

The first task is aimed at developing an atmospheric plasma processing technique to rapidly and inexpensively oxidize polyacrylonitrile (PAN) precursor fibers. Conventional oxidation is a slow thermal process that typically consumes more than 80% of the processing time in a conventional CF conversion line. A rapid oxidation process could dramatically increase the conversion line throughput and appreciably lower the fiber cost. The second project has already demonstrated the potential for significantly accelerating carbonization while simultaneously reducing the after treatment cost of effluent mitigation. To supply developmental quantities of fiber, a significant upgrade to the ORNL CF pilot line has been completed as the third project. **Figure 1** shows a breakdown of CF production costs and the range that each of these tasks affects in the production process.

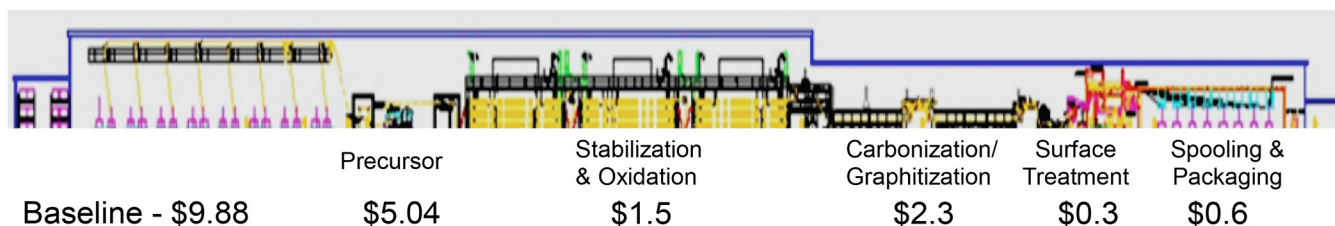


Figure 1. Role of low cost carbon fiber program tasks in the CF production process. (Base diagram courtesy of Harper International.)

The strategy for transitioning each of these technologies to industry is to involve industry as early in the development process as is practical to reduce investment risk. The advanced oxidation task is nearing a maturity stage to start involving oxidation oven manufacturers within the next 18 months. The advanced carbonization project already has an industrial partner involved.

Activities And Developments

Advanced Oxidative Stabilization of Carbon Fiber Precursors

Principal Investigator: Felix Paulauskas, ORNL
(865) 576-3785; fax: (865) 574-8257; e-mail: paulauskasfl@ornl.gov

Other Participants:

Truman Bonds, Jeremy Jackson, ReMaxCo Technologies, LLC; Robert Norris, Amit K. Naskar, Soydan Ozcan, and Kenneth D. Yarborough, ORNL; Professor Joseph Spruiell and Professor Robert Benson, University of Tennessee

Accomplishments

- Began refinement and optimization of the close proximity indirect exposure (CPIE) plasma process using textile grade PAN in a laboratory-scale reactor.
- Confirmed that the localized damage that was seen in the previous equipment generations is no longer a problem with the CPIE method.
- Successfully processed textile grade PAN (26,000 filament tow) with new advanced oxidation technique to required density levels in under 35 min. Achieved 361.9 ksi strength, 23.3 Msi modulus, and 1.44% strain-to-failure, exceeding program strength and strain requirements of 250 Ksi and 1.0%, respectively, and within 10% of modulus requirement of 25 Msi.
- Completed design and began construction of the scaled CPIE reactor, Multiple Tow Reactor 2 (MTR2), which is the next scale-up step in the plasma oxidation process.
- Conducted chemical characterization using Fourier transform infrared (FTIR) spectroscopy techniques. FTIR characterization provides a correlation between chemical properties and resultant mechanical properties which allows for the development of an understanding of the relationship between process parameters and final carbonized fiber properties.
- Applied for one new patent and awarded another patent based on advanced plasma processing techniques.
- Plasma oxidized 3 × 3,000 aerospace grade filament tows simultaneously in less than 35 min and produced, after carbonization, samples exceeding the minimum program goals of 250 Ksi tensile strength, 25 Msi modulus, and 1% strain.

Future Directions

- Finalize design and construction of the scaled-up CPIE reactor (MTR2).
- Install program control and data acquisition equipment and fiber stretching equipment for MTR2.
- Continue refining and scaling up the reactor design and processing protocols to achieve high speed, multiple large tow, semicontinuous (multiple pass) plasma oxidation process.
- Conduct rate-effect studies.
- Scale up the process and equipment to ORNL small pilot line scale.
- Develop pre-industrial-scale oxidation oven technical specifications for integration into the ORNL Carbon Fiber Technology Facility (CFTF).

Technology Assessment

- Target: Develop higher rate, lower cost methods for oxidation of CF precursors.
- Gap: Conventional oxidation methods require 80–120 min thus limiting CF production rates.
- Gap: Conventional oxidation methods contribute \$1.54/lb to the cost of carbon fiber and, more importantly, are the rate limiting and mass throughput limiting steps due to the 80–120 min residence times required for oxidative stabilization. These times must be reduced to increase the mass throughput of the entire conversion system.

Introduction

The purpose of this project is to develop a plasma processing technique to rapidly and inexpensively oxidize PAN precursor fibers. Conventional oxidation is a slow thermal process that typically consumes more than 80% of the processing time in a conventional CF conversion line. A rapid oxidation process could dramatically increase the conversion line throughput and appreciably lower the fiber cost. Atmospheric pressure plasma is a new and relatively inexpensive technology to implement in industrial processes (Roth, 2001). A related advanced carbonization project has already demonstrated the potential for significantly accelerating carbonization. The oxidation residence time must be greatly reduced to effect fast conversion and match the speed of the advanced carbonization technology. This project is developing an atmospheric plasma oxidation technology to integrate with other advanced fiber conversion processes to produce low cost CF with properties suitable for use by the automotive industry. Critical technical criteria include:

- Mechanical properties of ≥ 25 Msi tensile modulus, ≥ 250 Ksi tensile strength, and $\geq 1.0\%$ ultimate elongation in the finished fiber (DOE programmatic goals);
- Uniform mechanical and morphological properties along the length of the fiber tow and from filament to filament;
- Repeatable and controllable processing input conditions; and
- Significant unit cost reduction compared with conventional processing.

This effort is aimed at further developing those technologies to be able to continuously process 12K–50K tows of fiber and achieve properties meeting program minimum mechanical property requirements with variations less than 15% from tow to tow and along the length of the tow. These goals are to be met while significantly reducing the time required for oxidative stabilization from 90–120 minutes, down to less than 30 minutes. Reducing the oxidative stabilization time will permit greater fiber production rates and a corresponding decrease in carbon fiber production costs.

Approach

We are developing a nonthermal, atmospheric plasma process for rapidly oxidizing PAN precursor fiber which can be subsequently converted to carbon fiber. As illustrated in [Figure 2](#), conventional oxidative stabilization produces a “core-shell” geometry with a distinct interphase between the slowly growing, fully oxidized shell and the shrinking, stabilized inner core. Plasma processing enhances oxygen diffusion and produces different chemistries in the PAN oxidation process. This results in an acceleration of the oxidized layer growth rate and oxidation of the fiber more uniformly, with a considerably less pronounced interface between the two regions. Previous work has shown this approach can reduce the required residence time for complete oxidation.

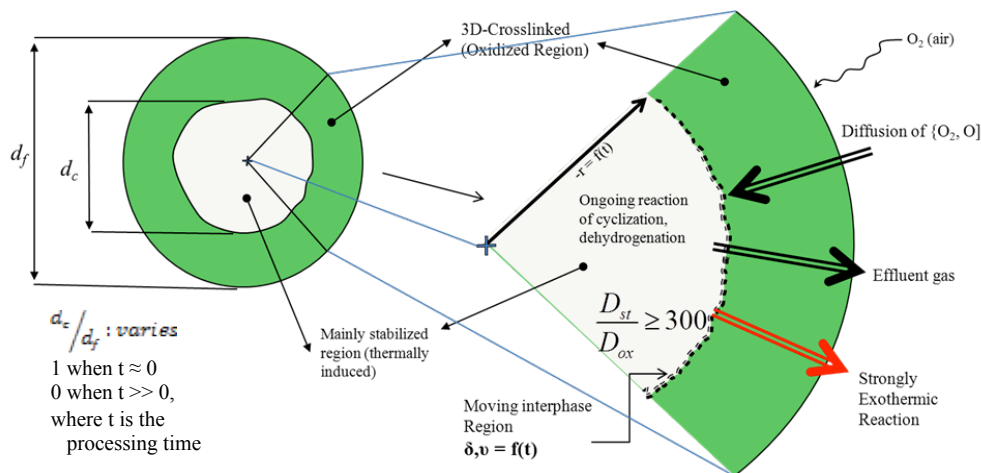


Figure 2. Single filament cross section during conventional oxidative stabilization process (Paulauskas, 2010; Paulauskas, 2004).

Results and Discussion

With the completion of work performed in FY 2011, the research team had a rapid, reliable advanced process for oxidation of PAN precursors and had overcome the technical obstacles to be able to develop a scaled reactor for the ORNL Small Pilot Line (1 ton/year). The transition from Phase I to Phase II took place in November 2011 (FY 2012), where the focus transitioned from technology development to technology scaling, verification, and demonstration.

Until late FY 2011, 3,000-filament aerospace grade PAN was primarily used in this research in order to eliminate the uncertainties that are associated with using a less well characterized precursor. However, the research has now reached a point where less expensive, 26,000 filament textile grade PAN can be coupled with this advanced conversion process to facilitate further cost reductions in the overall CF production cost. Using textile grade PAN introduces new challenges, which have been a portion of the focus of the experimental work conducted in FY 2012 along with further refining the processing parameters for aerospace grade carbon fiber precursors.

Mechanical Analysis

Precursors were oxidized using the CPIE plasma process at ReMaxCo using the reactor designed at ORNL. All oxidized PAN fibers (OPFs) of sufficient density from the CPIE process were mechanically, chemically and morphologically evaluated at ORNL. ORNL performed single filament tests on a portion of the OPF samples and conventionally carbonized the remaining OPFs followed by single filament testing of the carbonized samples. Table 1 contains the mechanical properties of the various types of PAN-based precursors used in this research. The two textile fibers have the same chemical composition. The difference lies in the stretching during the generation process, which affects the final mechanical properties.

Table 1. Mechanical properties of various grades of PAN precursor (oxidized but not carbonized fiber).

Type	Fiber Dia. (μm)	Peak Stress (Ksi)	Modulus (Msi)	Strain @ Break (%)
Aerospace	12.3	76.9	1.8	9.93
Commodity (range)	11.7–13.5	36.5–73.5	1.5–1.5	11.2–24.0
Textile (Stretched)	13.0*	65.6	1.0	12.17
Textile (Relaxed)	15.6*	36.7	0.6	14.02

*The wet spinning filament generation process of textile grade PAN results in a precursor with a kidney shaped cross section. The resulting diameter is dependent on the measurement technique used.

Three significant differences exist between aerospace grade PAN and textile grade PAN. The first is in the size of the tow. The typical aerospace grade PAN used in the research is a tow consisting of 3,000 filaments, while textile PAN tows typically are comprised of 24,000–26,000 filaments. The second difference lies in the chemical purity. While aerospace grade PAN is typically more than 99% pure, textile grade PAN purity is much lower. The third difference lies in the physical structure, with textile PAN having a higher percentage of morphological defects than aerospace PAN. These differences introduced additional challenges in the oxidation of textile PAN that required significant effort to overcome.

In previous work, reported last year, significant damage to the fibers had been noted due to the application of the plasma process. Those issues have been resolved during the past year with a redesign of the process equipment. Below are two microscopic images of oxidized textile PAN fiber samples (Figure 3). No damage is present as a result of the oxidation processing using the newest equipment configuration.

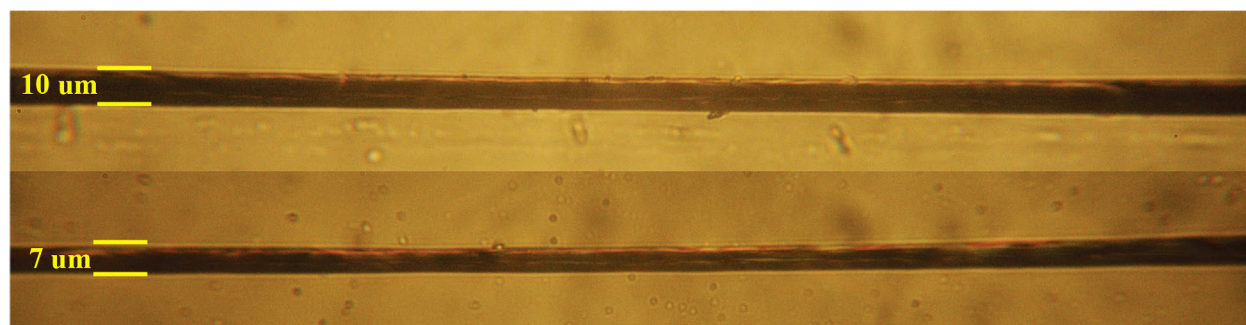


Figure 3. Sample 1 is the larger diameter (10 μm) and was processed under lower tension. Sample 2 is the smaller diameter (7 μm) and was processed under higher tension. Higher levels of tensioning during oxidative stabilization yield more fiber stretching and are necessary for increasing the resultant carbonized fiber mechanical strength.

Table 2 contains recent mechanical properties for both the oxidized and carbonized versions of the fibers. Typically, 16 filaments were measured per reported result. The ultimate strength of several samples exceeded the program minimum requirement of 250 ksi and the strain at break minimum requirement of 1.0%. The requirement for a minimum modulus of 25 Msi was approached but has not yet been met. That milestone is expected to be met in early FY 2012.

Table 2. Mechanical properties of select samples of 24K–26K textile grade PAN.*

Test Num.	Oxidized Fibers					Carbonized Fibers			
	Res. Time (min)	Fiber Dia. (μm)	Peak Stress (ksi)	Modulus (Msi)	Strain @ Break (%)	Fiber Dia. (μm)	Peak Stress (ksi)	Modulus (Msi)	Strain @ Break (%)
ORNL Aero.	75–120	13.1	42.7	1.0	14.7	7.9	359.8	29.6	1.17
Aero.	75–120	11.8	43.7	1.4	13.0	7.4	427.2	25.9	1.58
Com.	75–120	12.6	37.8	1.2	20.4	7.2	543.9	30.7	1.60
589	32	10.8	28.0	0.9	18.8	7.0	246.6	16.4	1.4
590	32	11.9	21.7	0.8	18.0	6.8	228.0	17.6	1.2
591	32	9.6	25.5	0.8	13.0	6.2	318.4	20.0	1.5
600	33.6	9.4	30.2	1.1	14.1	6.0	361.9	23.3	1.4
601	32	9.7	31.3	1.0	25.7	6.3	294.6	21.5	1.3
604-2	33.6	8.5	27.7	0.9	15.8	5.2	244.3	23.8	1.0
605	33.6	8.5	28.1	0.9	19.2	6.7	174.5	15.6	1.1

*Note: Bright yellow blocks in the table highlight properties exceeding program requirements. Aerospace grade represents a high quality fiber. Commodity grade is accepted as a medium grade fiber. Textile grade represents the range of low cost fibers. Blocks highlighted in brown contain data from conventionally processed fibers, displayed for comparison. It is important to remember that the textile grade results presented here should only be compared to conventional textile grade fiber, not higher grades of PAN. All results are from single tow processing.

Chemical Analysis

In mid FY 2011, a spectroscopic study was conducted to determine the correlation between the chemical, physical, and mechanical properties of OPF. A review of the literature confirmed the ability to directly relate FTIR measurements to the tensile strength, modulus, and density of OPF. The challenge of this technique lies in the capture of properties through the full cross section of the OPF filaments and not just the outer skin. Preliminary relationships between various chemical bonds in the OPF and density, tensile strength, and modulus were established. Due to the export control nature of this work the findings cannot be publically disclosed. This work was continued through FY 2012, which resulted in some previous findings being disregarded and others further pursued. A variety of measurement techniques were investigated, including attenuated total reflectance, specular reflectance, and diffuse reflectance methods. So far, diffuse reflectance is showing the most promise since it can capture more energy reflected from the fiber.

In an effort to establish a reliable in situ fiber property diagnostic technique, it was deduced that the oxidized fiber would be a good candidate for dielectric spectroscopy. An existing relationship between ORNL and the University of Tennessee-Knoxville provided access to the necessary equipment; however, the research team still has to determine the best way to cast the fiber into a sample coupon for proper measurement. Work in this area is ongoing.

MTR2 Design and Construction

As requested by the DOE manager, during the final stages of the design of MTR2, possible candidate reviewers were approached for review of this design, both inside ORNL and outside in industry (U.S. citizens only). Initial responses were positive, but once process and equipment details were discussed, these individuals were unable to perform the review due to their lack of knowledge in atmospheric plasma technology. Most industrial processing experts have backgrounds in vacuum plasma equipment and/or conventional CF conversion but not in both of these areas which are crucial to evaluating the equipment design. A final design was selected by the research team and construction initiated.

Current Status

The research team continues to focus on optimizing the new CPIE technique for PAN fibers. In addition, construction and fabrication work is currently being performed on the next generation MTR2 advanced oxidation unit. This device will represent a significant scale-up from the current level of CPIE processing and will involve a minimum capability of processing $4 \times 26,000$ filament tows. Four serial modules will make up MTR2. The fiber stretching system has already been designed and is being procured. This system consists of three independent winders with encoders for constant line speed capabilities.

Technology Transfer Path

During the latter portion of this work, ORNL will evaluate potential partners and partnership arrangements for scaling the technology to the preproduction demonstration scale comparable with the 25-tonne-per-year scale currently being implemented at the ORNL CFTF. A deliverable of this project is technology documentation adequate for specifying the equipment in the 25 tonne per year size range. Equipment and process details will be demonstrated and discussed with potential partners allowing for development of collaborative proposals for moving to the next size scale and eventually to commercialization.

Conclusions

The Phase II work of scaling, verifying, and demonstrating the advanced plasma oxidation process began this fiscal year. Fibers have been processed exceeding the program mechanical property goals of 250 ksi strength, 25 Msi modulus and 1% elongation at break using aerospace precursors. Fibers have been processed from textile grade precursors meeting all program requirements except for the modulus. FTIR analysis has been conducted and as a result strong correlations between process input parameters and resultant fiber mechanical properties have been developed. Design of the next generation advanced oxidation processing equipment has been completed and procurement is commencing.

Development and Demonstration of Advanced Carbonization

Principal Investigator: Felix Paulauskas, ORNL
(865) 576-3785; fax: (865) 574-8257; e-mail: paulauskasfl@ornl.gov

Other Primary Participants:

Robert E. Norris, Ken Yarborough, Mike Kaufman, Terry White, John Caughman, ORNL; Truman Bonds, ReMaxCo Technologies, LLC

Accomplishments

- Demonstrated effective improvements in effluent removal. (FY 2012)
- Completed design for scale-up to five-tow processing, and upgrade is underway. (FY 2012)
- Improved cooling techniques for hardware without detrimental effects to properties. (FY 2012)
- Correlated system modeling with energy deposition and tow spacing options. (FY 2012)

Future Directions

- Optimize cost versus performance tradeoffs.
- Conduct process stability and durability analyses.
- Incorporate alternative precursors into new process capability.
- Develop technical specification for 25-tonne-per-year scale-up as the next step in the pathway to commercialization.
- Develop partnerships for technical collaboration in scale-up and commercialization.

Technology Assessment

- Target: Develop and demonstrate alternative methods for carbonization of stabilized CF precursors having potential to reduce energy and cost in carbonization by more than 30%.
- Gap: Conventional carbonization requires significant expenditure of energy and requires extensive furnace maintenance resulting in high processing costs.
- Gap: High temperature furnaces have significant thermal inertia requiring long start-up and shut-down times limiting mid-process changes and adjustments and adding expense in resolving problems.

Introduction

This project seeks to develop, demonstrate, and commercialize a scaled energy-efficient advanced conversion technology to enable manufacturing of CF that is technically and economically viable in industrial markets. Industrial applications critical to efficient energy production and use (transportation, wind energy, infrastructure, and oil drilling applications) are attractive for lower cost CF where aircraft grade CF properties are not required. This project is co-funded by the Vehicle Technologies Office (VTO) and the Advanced Manufacturing Office in DOE's Office of Energy Efficiency and Renewable Energy. The project aims to optimize MAP, speeding up the process while simultaneously increasing the volume (tows) processed. This work builds upon previous work at ORNL (Paulauskas and Spruiell, 2004; Paulauskas et al., 2002). The team will evaluate the overall energy usage of the hardware and materials systems to determine the energy and cost efficiency of the technology.

The production cost of commercial grade CF is about equally split between raw materials and the conversion process; therefore, it is necessary to reduce both the cost of the precursor as well as the cost to convert it to carbon fiber. While we are pursuing synergistic work on the low cost precursor with Dow Chemical under the Advanced Manufacturing Office, this work focuses on developing a low cost conversion process. Conventional conversion employs a thermal pyrolysis process

that is slow and energy and space intensive. ORNL demonstrated that microwave energy combined with plasmas (MAP) can be used as a means to rapidly convert PAN precursor fibers into finished CFs. This process can occur under shorter residence times (about 1/3 of the conventional residence time). This project focuses on demonstrating the scale-up of the MAP process to further reduce the manufactured cost of CF and the energy used to produce them by up to 50%.

Approach

Previously, we demonstrated the carbonization of a single 50,000 filament tow at 5 m/min (less than 1/2 the conventional residence time), and 3 × 50,000 filament tows at 1 m/min. Currently, the system is not sufficiently robust to sustain these rates and volumes. Therefore, this project aims to further scale up the process while also improving the robustness of the process. The principal tasks of this portion of the project are as follows.

- Evaluate materials, sealing, and atmospheric pressure solutions.
- Estimate the energy requirement for various scales.
- Conduct system modeling to guide hardware design and process development.
- Determine preferred microwave/plasma parameters and profiles necessary to minimize residence time.
- Scale to more than five large tows of 24,000 or more filaments.
- Demonstrate nonstop operation of at least 8 h, indicating potential for weeklong production scenarios.
- Develop information necessary to produce a robust advanced technology carbonization unit to be built and operated in the ORNL CFTF.

The goal here is to define technical specifications and process design for scaling this technology to semi-production scale consistent with the 25-tonne-per-year capability at the ORNL CFTF. Validation of the robustness includes demonstrating fiber property and uniformity, system continuous operation, and scalability to five or more large tows, with a strategy for scaling to production levels. We will also verify through models the economic feasibility in production so that we can successfully transition the technology to industry for commercialization.

Results and Discussion

In 2011, continuous operations exceeding an hour resulted in variability along the tow of less than ±15%. Programmatic goals for tensile strength and modulus were met for two of the three tows processed concurrently. We completed a preliminary energy and mass balance for the MAP line for a line speed of 24 in./min. In order to provide insight into how geometry impacts performance with respect to scaling up the process, we modeled the MAP line with CST Microwave Studio, a 3D electromagnetic finite element code. The model includes the material properties of the waveguide, vacuum tube, and tows and we use it to optimize the effect of varying the iris size on the electric field distribution. Additionally, we studied the electric field variance as the system was scaled up from one to three tows. Although the 3D modeling provided some insight into expected energy deposition and preferential size and spacing of the waveguide ports, validation of the model was not as close as desired, leading to less reliance on this approach for scaling from three to five tows. We developed a unique dielectric measurement system. This system provides material properties for better understand the interaction physics (microwave coupling versus temperature) in the processing environment (White et al., 2004).

We completed several hardware upgrades and these upgrades result in improved fiber properties. The upgrade involves adapting rollers/winders, adding creel parts, and upgrading the new cross. The most significant upgrade for the MAP is the use of a larger (25%) vacuum tube to accommodate a larger number of tows in the plasma chamber without touching either the wall or other tows. Shakedown testing revealed that increased power for a given pressure is required to stabilize the plasma—an expected effect as the power density is lower with the increased cross section. However, the higher power shows a significant improvement in realized mechanical properties. Future runs will include the demonstration of a continuous operation (2 h) while maintaining seal integrity resulting in adequate plasma processing pressure. Continuous operation will now be demonstrated over an 8 h window while maintaining plasma processing pressure.

Previously the buildup of tar in the foreline, mesh filters, and vacuum pumps reduced pumping efficiency after only a few hours of processing. This buildup contributes to a lack of robustness in the process and needs to be corrected. Initial trials involved attempts to filter the tar effluent utilizing an in-house designed and constructed trap, fitted with a commercial filter. **Figure 4** illustrates this system. This approach enabled a vacuum for sufficiently longer times. This solution worked well by enabling the collection of most of the tar into the trap.

Initial studies using the larger tube resulted in a “hot spot” which caused melting of the tube in that region. Attempts to mitigate the “hot spot” with air cooling appears to solve the melting problem without impacting the mechanical properties of the carbon fiber.

Use of the larger tube enabled achieving both the strength and modulus goals. The properties from a selection of MAP runs are shown in **Figure 5**.

Previous work to process three tows simultaneously resulted in non-uniform properties in one of the three tows. However, computer modeling indicated that the microwave absorption should be uniform despite the presence of the other tows. We observed that the tow farthest from the location where the radio frequency power is coupled into the plasma chamber shows the weakest properties. This result supports the hypothesis that the falloff of the electric field may be the primary factor in the drop off of the properties. We are studying how to place fibers in the tube to mitigate this effect.



Figure 4. Commercial filter trap installed on the MAP vacuum line.

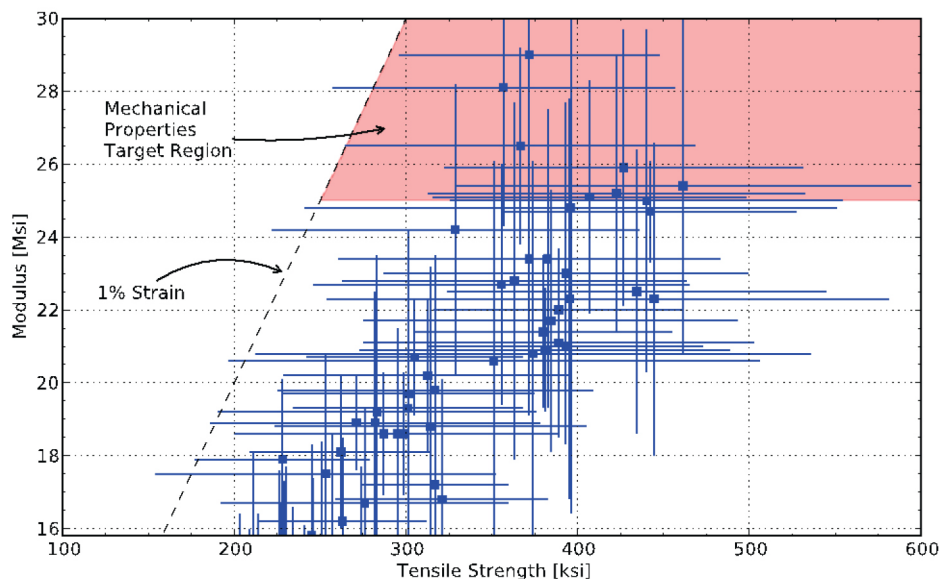


Figure 5. Mechanical properties from selected MAP runs. Fiber properties in the shaded region meet or exceed programmatic targets. The data are from single-filament mechanical testing, which tends to yield relatively large data ranges in each sample group.

Atmospheric Plasma

One way to reduce the buildup of the tar effluent is to transform the fiber in atmospheric plasma instead of vacuum plasma. Initial feasibility studies using atmospheric pressure plasma torch to carbonize the fiber was only partially successful. An alternative approach we are also considering is to utilize a glow discharge technique. A contractual agreement for work on the CF carbonization process has been completed with ReMaxCo, an ORNL subcontractor with extensive background and experience in the area of atmospheric plasma processing for CF oxidation, and initial hardware design and fabrication are underway. We are undertaking initial feasibility studies of an atmospheric approach.

Industrial partners include suppliers of microwave generator and vacuum systems. In addition, existing manufacturers of CF conversion equipment and others interested in entering this business have expressed interest in this technology. At this point, we do not feel it is appropriate to commit to specific partners, especially considering we have not resolved the potential for atmospheric plasma approaches and specifics of multichamber versus single chamber MAP approaches. We will pursue engaging industry partners after the specific technical solution is clearer. We anticipate this activity taking place during the last half of FY 2013.

The goal for this work is to have technical specifications and design for scaling this technology to semi-production scale consistent with the 25-tonne-per-year capability at the ORNL CFTF. We intend to have demonstrated adequate hardware improvements, operational experience, production performance in meeting fiber property targets and uniformity, system robustness in continuous operation, and scalability to process five or more large tows simultaneously.

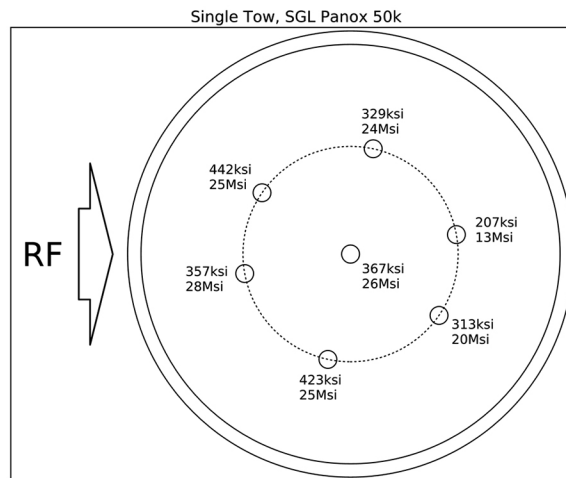


Figure 6. Mechanical properties from the MAP tow location experiment. The arrow indicates from which direction the power is coupled into the plasma chamber.

Technology Transfer Path

During the latter portion of this work, ORNL will formally evaluate potential partners and partnership arrangements for scaling the technology to a preproduction-scale demonstration comparable with the 25-tonne-per-year scale currently being implemented at the CFTF in Oak Ridge. A deliverable of this project is technology documentation adequate for specifying the equipment in this size range. Equipment and process details can be demonstrated and discussed with potential partners allowing for development of collaborative proposals for moving to the next scale level and eventual commercialization. ORNL will solicit input from various commercial sources as to interest in this area and work with the DOE program offices to formalize planning for acquiring adequate resources for the following phases of this work.

Conclusions

We continue to make strides in understanding and addressing issues associated with the durability and scaling of the MAP process. Significant tools have been put in place to assist with the hardware development, including a system model. In addition to implementing the larger chamber, work is being conducted to develop models which correlate the effects of tow placement in the system with the resultant fiber mechanical properties that are achieved. We procured feed rollers and winders and significant portions of the creel are complete.

Pilot Line Upgrade

Principal Investigator: Robert E. Norris Jr., ORNL
(865) 576-1179; fax: (865) 574-8257; e-mail: norrisrejr@ornl.gov

Primary Participants: Felix Paulauskas, Ken Yarborough, Soydan Ozcan, ORNL

Accomplishments

- Completed final engineering for the major upgrade to the ORNL pilot line to enhance throughput, controls, flexibility, and other capabilities; contractual work for completing the upgrade is in progress. The upgrade more than doubles the material throughput and allows for the production of higher volumes of finished CF to support VTO projects. Before the upgrade, the line could run two tows while holding appropriate tension, producing 2 lbs CF/day. The upgrade doubles the line speed and allows tensioning of six tows, increasing daily possible production to 12 lb. It also provides far greater capability for multiple tension zone control during conversion, better tension monitoring, and overall enhanced data (time/temperature/tension) collection.
- Completed adaption and installation of hardware for surface treatment and sizing post-treatment units. Although design and construction were executed independent of the balance of the pilot line upgrade, the conventional surface treatment unit is fully compatible with the other hardware and was integrated into the test facility.
- Procured and installed all fiber handling equipment including multiple braking and stretching units, multiple tension monitoring units, tow spreading devices, and fully integrated controls and data monitoring equipment. Upgrade will be checked out and fully commissioned in late FY 2012 and early FY 2013.

Future Directions

- The pilot line upgrade enables ORNL to demonstrate fully integrated precursor conversion with flexibility in stretching and facilitates ORNL capability to demonstrate continuous production capacity at small scale. The pilot line will be more useful and cost effective in demonstrating complete conversion recipes (temperature/time/tension) for a variety of precursors. This represents a key step between demonstration that a precursor can be converted to CFs when an approximate conversion recipe has been demonstrated in the Precursor Evaluation System (PES) and provides confidence a precursor material is ready for the considerable investment required for large-scale demonstration at the CFTF, along with the more precise conversion recipe needed as a starting point for that work.
- The combination of the ORNL PES, ORNL Small Pilot Line, and ORNL CFTF will be operated as part of an integrated strategy where PES continues being the workhorse for day-to-day alternative precursor formulation and development iterations, the pilot line serves as the tool for demonstrating continuous conversion recipe fine-tuning and the proving ground prior to large-scale demonstration, and CFTF demonstrates large-scale manufacturability and provides adequate quantities of fiber for end user product development.

Technology Assessment

- Target: Increase the material throughput of the pilot line to provide needed quantities of material to VTO.
- Target: Increase the tensile strength of fiber produced on the pilot line to match properties that are achievable with the precursor and fiber evaluation line.
- Gap: Before the upgrade the pilot line was not capable of practically providing the quantities of CF indicative of truly continuous processing needed by VTO for technology validation.
- Gap: The current pilot line does not produce CF with properties equal to that achievable on smaller lines due to a lack of precise tensioning in the oxidative stabilization ovens.

Introduction

The CF pilot lines facilitate the evaluation of materials and processes for the low cost carbon fiber projects. This line plays a key role in advancing technology development and providing critical information necessary for planning and executing production scale-up. The use of this facility includes evaluation of alternate precursor convertibility, production of fibers for evaluation by automotive composites manufacturers and other interested parties, and new concept evaluations. Completion of this task upgrades the output of CF from 2 to 12 lbs/day and, more importantly, increases the tensioning control enabling in-depth study of continuous processing effects of temperature and tension versus time. This allows us to (1) develop continuous conversion recipes for each precursor; (2) determine maximum practical fiber properties for each potential precursor candidate, (3) conduct optimization of properties versus critical production parameters to optimize product performance versus conversion costs, and (4) evaluate potential production issues (exotherm sensitivity or environmental concerns for example) and validate manufacturability of each precursor candidate with low investment in labor and raw materials to mitigate risks in transitioning to CFTF scale-up.

Approach

ORNL's conventional pilot line enables the production of 3,000- to 50,000-filament tows. It is useful for making small quantities of fiber for tow and composite evaluations. It can also be used to oxidize or carbonize tows under conventional processes. Minimum material requirements for evaluation on the pilot line are hundreds of feet of 3,000 filament or greater tows, and startup time for the high temperature carbonization furnace is about 1 shift. A significant upgrade to this system is currently being completed. Although ORNL has already effectively increased the nameplate speed rating from 8 to 16 in./min, the upgrade essentially doubles the line speed to a current nameplate capability of 30 in./min (with potentially even greater capability if needed) and provides tensioning for up to six tows rather than the one or two tows for which it has been used in the past. It also allows for more precise tensioning control in multiple independently controlled zones, which provides the capability for significant increases in the strength of CF from alternative precursors and/or much more tailorable property control to demonstrate costs versus performance tradeoffs.

Results and Discussion

Better understanding of the precursor evaluation system (PES) and its capabilities has facilitated minor upgrades recently, including a three zone high temperature carbonization furnace capable of reaching temperatures over 1,500°C. This unit has a longer heating zone and much better capability to tailor the heating progression than the single zone furnace we had been using. A second improvement is the addition of an oxidation oven with fully integrated but independently controlled tensioning sections. These upgrades allowed for the development of greater property control (and ultimately higher strength fiber) from textile precursors but could not be mimicked in the pilot line due to the low level of tension control available in the pilot line. The pilot line upgrade provides the capability for production of fiber achieving the same mechanical property values in volumes that will allow for initial composite evaluation.

The PES allows conversion process development at laboratory scale where individual process stages (e.g., each of four stages of oxidation and two or more stages of carbonization) are used to process small amounts of material from a few grams and single or few filaments up to single large tow levels, while the pilot line transitions closer to preproduction demonstration scale, with multiple tow and fully integrated continuous process development. Although the pilot line has proven to be a useful tool, it has limitations we are working to address, including the following which are part of the upgrade.

- The original pretreatment system was based on a simplistic system designed specifically to eliminate crimp (not typically needed in processing most of our developmental precursors) resulting in nonuniform processing; the system has been removed from routine operation.
- The oxidation stages previously lacked capabilities for progressive, controlled stretching to enhance overall properties via molecular orientation or provide tension compensation for heat-induced relaxation. Capabilities added for multiple independently controlled stretching zones in oxidation are the centerpiece of the upgrade.
- The original tension controls were marginal and not very flexible, and the fiber transport system was limited in speed without the capacity to increase speed, increase number of passes, or bypass potentially superfluous processes.

Additional passes have been added, which allows us to run at higher speeds for the equivalent residence time. A modern drive system capable of higher speeds with more precise control has been installed to take advantage of the additional flexibility.

- With the exception of oven temperatures, no monitoring of process parameter (tension, speed, stretching, etc.) capabilities and no automated data acquisition system to capture and analyze data were present on the original system. Overall control, monitoring, and data acquisition have been upgraded.

ORNL has been working extensively with a well-established company specializing in fiber movement features to design and implement a major pilot line upgrade. The upgraded system, scheduled for completion in mid-FY 2012, will be capable of implementing the individual and collective process steps as developed on the PES. The following major items are part of the upgrade.

- Additional free-roller systems, as shown in Figure 7, have been added to the oxidation system providing five to six passes in each oxidation oven versus the previous configuration where three passes per oven were typical.
- Seven controllable stretch units have been added to the four-oven oxidation system allowing for independently controlled stretching zones in oxidation. Stretch units are controllable based on speed and speed ratios versus a selectable master or baseline stretch unit.
- Three controllable stretch units have been added to the two-furnace carbonization and surface treatment system as shown in Figure 8 allowing for two independently controlled tensioning zones in carbonization.



Figure 7. Free-roller systems as installed between oxidation ovens.

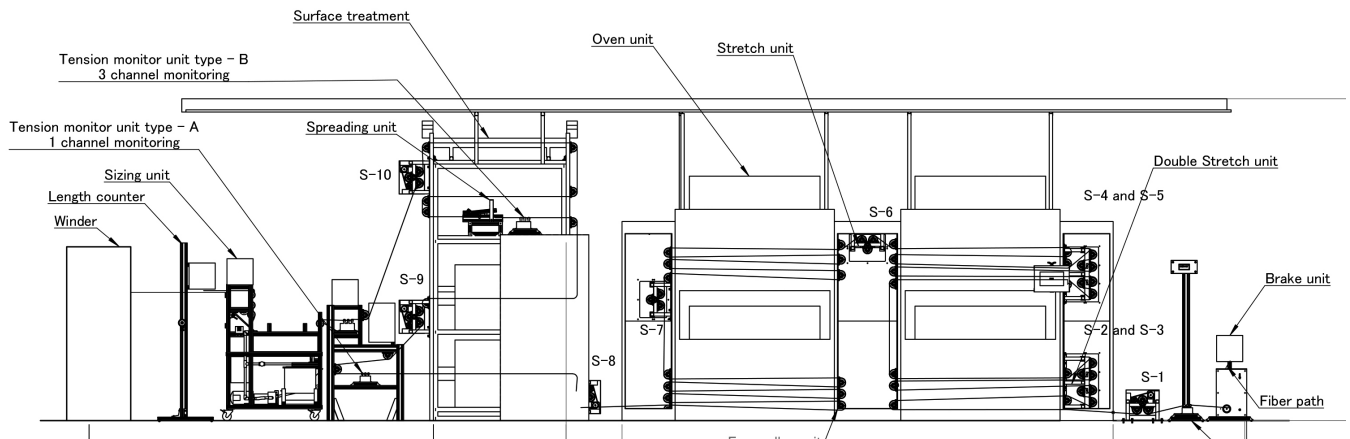


Figure 8. Depiction of multiple stretch zones and fiber paths.

- Multiple movable tensioning measurement devices are provided for independent tow tension measurements.
- Although drive speed is controllable, a speed measurement/yardage counter system is provided for production rate confirmation.
- Provision has been made for integration of ORNL designed surface treatment units (based on ORNL developed gas phase technology as shown in Figure 9) and sizing units (as shown in Figure 10).

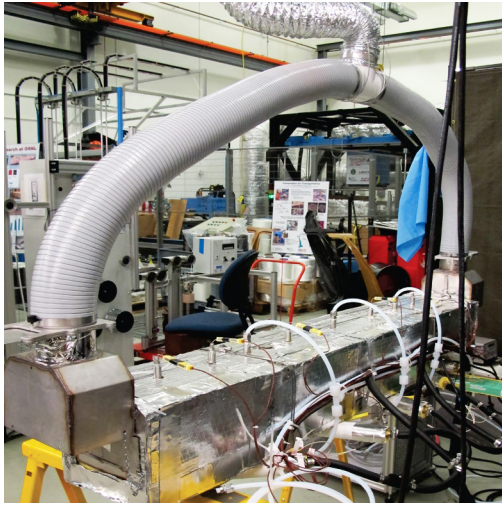


Figure 9. ORNL gas phase surface treatment unit for pilot line.



Figure 10. ORNL sizing unit.

The upgraded system will now be able to produce significantly higher quantities of CF with greater precision, repeatability, and certainty for the process parameters used. The upgraded pilot line will be capable of producing fiber with mechanical properties that match those developed in the precursor and fiber evaluation laboratory with the same precursor. Also, because of the similarity in approach, the pilot line processing will be very compatible with production technology for tows being deployed in the 25-tonne-per-year CFTF scheduled for completion in FY 2013 and is a critical link in scaling technologies from the precursor and fiber evaluation to the CFTF.

Technology Transfer Path

The pilot line is a critical tool for scaling up the development of new processing and conversion technologies for CF. This upgrade will speed the development of polyolefin and textile grade precursors and serve as a critical link in the commercialization paths for the advanced oxidation and MAP carbonization technologies.

Conclusions

The pilot line continues to function as an essential tool for the validation of new precursor technologies, having been used for the textile PAN precursor. Important upgrades to the pilot line are being completed to provide higher speed capability, additional stretching capability, enhanced surface treatment and sizing capabilities, and enhanced controls and data acquisition systems. The line speed has been doubled, the number of tows that can be simultaneously processed has been increased from two to six, and the amount of tension control on each tow will be significantly enhanced allowing for the production of CFs matching those available in the smaller precursor and fiber evaluation laboratory and providing an appropriate tool for qualifying precursors for demonstration at semi-production scale in the ORNL CFTF that will be coming online in FY 2013.

Conclusions

This project comprises three separate tasks that are aimed at developing technologies to lower the cost of CFs, making them more attractive to the automotive industry. The fibers must have a minimum strength of 250 ksi and a minimum modulus of 25 Msi and be compatible with automotive grade resin systems. Two alternative production methods are under development. In the development of a more rapid oxidative stabilization process, several important objectives were met that produced valuable knowledge on the scaled-up advanced oxidation process. We are now completing the work necessary to design a pilot-scale unit under that task. At the conclusion of this project, the researchers will be positioned to procure, install, test, and operate a pilot-scale plasma oxidation module in an advanced technology pilot line. The targeted outcome for the advanced carbonization portion of the project is to have technical specifications for scaling this technology to semi-production scale

consistent with the 25-tonne-per-year capability at the Oak Ridge CFTF. Important upgrades to the pilot line were completed which include a sixfold increase in CF production capability. This increases the daily production capacity from 2 to 12 lbs of large tow CF. It also includes improved tow tensioning during oxidative stabilization and carbonization allowing for better fiber production.

Presentations/Publications/Patents

Patents

Paulauskas, et al. *Apparatus and Method for Carbon Fiber Surface Treatment*. US Patent 8,227,051 B1, issued July 24, 2012.

Paulauskas, et al. *Rapid Oxidation of Polymeric Fibers for Producing Flame Retardant Fibers*. 13/163,134 filed in June 2011.

References

Paulauskas, F. L. Temperature-Dependent Dielectric Measurements of Polyacrylonitrile Fibers. Presented at SAMPE 2004, Long Beach, CA, May 16–20, 2004.

Paulauskas, F. Advanced Oxidation & Stabilization of PAN-Based Carbon Precursor Fibers. Presented at the DOE Annual Merit Review, Washington, June 9, 2010; LM-006.

Paulauskas, F. L.; Spruiell, J. Structure and Properties of Carbon Fibers Produced Using Microwave-Assisted Plasma Technology: Part 1. Presented at SAMPE 2004, Long Beach, CA, May 16–20, 2004.

Paulauskas, F. L.; Yarborough, K. D.; Meek, T. T. Carbon Fiber Manufacturing via Plasma Technology. US Patent 6,372,192 B1, April 16, 2002.

Roth, J. R. *Industrial Plasma Engineering, Volume 2: Applications to Nonthermal Plasma Processing*; Institute of Physics Publishing: Philadelphia, 2001; Chapter 15.

White, S. M.; Spruiell, J. E.; Paulauskas, F. L. Fundamental Studies of Stabilization of Polyacrylonitrile Precursor, Part 1: Effects of Thermal and Environmental Treatments. Presented at SAMPE 2004, Long Beach, CA, May 16–20, 2004.

C. Carbon Fiber Technology Facility – Oak Ridge National Laboratory

Field Technical Monitor: C. David Warren
Oak Ridge National Laboratory
1 Bethel Valley Road, Oak Ridge, TN 37831
(865) 574-9693; fax: (865) 574-6098; e-mail: warrencd@ornl.gov

Principal Investigator: Lee McGetrick
Oak Ridge National Laboratory
1 Bethel Valley Road, Oak Ridge, TN 37831
(865) 574-0302; e-mail: mcgetricklb@ornl.gov

Collaborators: Craig Blue, Ray Boeman, Claus Daniel, Cliff Eberle, Bob Norris

Technology Area Development Manager: Carol Schutte
U.S. Department of Energy
1000 Independence Ave., S.W., Washington, DC 20585
(202) 287-5371; fax: (202) 856-2476; e-mail: carol.schutte@ee.doe.gov

Contractor: Oak Ridge National Laboratory (ORNL)
Contract No.: DE-AC05-00OR22725

Executive Summary

This project aims to scale and transition low cost carbon fiber (CF) technology through the ORNL Carbon Fiber Technology Facility (CFTF). This project is cofunded by the DOE Vehicle Technologies Office (VTO) and the Advanced Manufacturing Office (AMO). It supports the DOE Office of Energy Efficiency and Renewable Energy's (EERE's) technology deployment agenda, specifically with respect to advanced lightweight materials in high volume energy applications.

Activities in FY 2012 were primarily focused on CFTF development, staffing, training, and readiness assessments. These activities included development of facility- and equipment-specific operating procedures and work packages; development of environmental, health, safety, security, and quality plans and procedures; development and implementation of training for CFTF staff on these plans and procedures; establishment of a preventive maintenance and equipment calibration program; and completion of readiness assessments before commissioning and transition to operations.

Accomplishments

- Developed a potentially patentable wireless, tablet-based work control and training system.
- Hired 22 qualified staff members through a rigorous recruitment and evaluation program in collaboration with Roane State Community College (RSCC). All staff meet the requirements to be in compliance with export control regulations.
- Developed a robust set of procedures (including export control) and an advanced manufacturing training system by which they were implemented.
- Completed a management readiness assessment to ensure safe and reliable CFTF operations.
- Partnered with Dow and Ford to secure a \$9M award for low cost polyolefin-based CF scale-up, funded by AMO under the Innovative Manufacturing Initiative.

Future Plans (postcommissioning)

- Tune the CF production process using polyacrylonitrile (PAN) precursor.
- Produce limited quantities of PAN-based CFs at CFTF production rate and specification requirements.
- Tune the melt spun precursor fiber production process.
- Produce polyolefin and lignin precursor fibers at CFTF as part of a follow-on project.
- Demonstrate conversion of alternative carbon fiber precursors at a semi-production scale.
- Obtain industry- or academia-based certification for the CF technician training system (e.g., similar to the American Composites Manufacturers Association Composites Technician Certification).

Technology Assessment

- Target: Demonstrate alternative precursor materials can be produced through melt spinning and converted into low cost CF at a semi-production scale.
- Target: Demonstrate that nontraditional lower cost processes for converting precursors into CF can be scaled to industrially viable levels.
- Gap: CF is too expensive for many automotive and other industrial applications, and the cost of the precursor contributes 51% of the CF cost. The cost of current production processes account for the remainder of the costs.
- Gap: While ORNL research has shown that CF can be produced from lower cost precursors and alternative production methods, there is no facility available to U.S. industry to prove the scalability of this research.

Introduction

ORNL has performed research for many years to demonstrate that, at a laboratory scale, CFs can be produced using alternative precursors such as textile grade PANs, polyolefins, and lignins. ORNL has also been performing research to develop lower cost methods for converting precursors into CF. To commercialize this technology, it is necessary to prove viability of these processes at a larger scale in collaboration with industry. CFTF offers a unique, highly flexible, highly instrumented CF line for demonstrating advanced technology scale-up and producing market-development volumes of prototypical CFs. CFTF has unique capabilities with the flexibility to process a range of feed stocks and product forms that is unmatched anywhere in the world. The CFTF will bridge the “valley of death” between laboratory research and commercial scale deployment of low cost CF technologies, thus filling a critical need for promoting industrial competitiveness for the manufacture of CF in this nation.

When complete, the semi-production-scale facility will be capable of producing up to 25 tons of CF each year. This estimate is based on processing with 24k PAN precursor in tow format. In addition to a conventional conversion line, CFTF will have a melt spun precursor fiber production line with a rated capacity of 65 tons per year. The 42,000 ft² facility has the capacity for future expansion, including the addition of an advanced technology conversion line.

A wide range of activities necessary to prepare for CFTF operation are funded under this project. Tasks are cofunded by VTP and AMO and support EERE’s efforts to transition technologies to industry, specifically with respect to cost-effective CF for composite materials in high volume energy applications. These tasks include the development of facility- and equipment-specific operating procedures and work packages; development of environmental, health, safety, security, and quality plans and procedures; development and implementation of training for CFTF staff on these plans and procedures as well as export control; and completion of a readiness assessment before equipment start-up and commissioning.

Approach

A CFTF operations organization was established within ORNL's Energy and Environmental Sciences Directorate in early calendar year 2012 to prepare for operations at CFTF. Initially a director and operations manager were selected to plan and organize the ramp-up and readiness preparations.

A vision was developed in which ORNL would leverage the ongoing relationship with RSCC's Advanced Materials Training and Education Center (AMTEC), a technician training program developed jointly between RSCC and ORNL. The AMTEC program is targeted toward regional unemployed and underemployed adults with a desire to learn new skills in advanced manufacturing. Targeting the pool of AMTEC graduates and attendees through a series of job fairs and multiple interviews, we selected 19 technicians and began the training program in July 2012. During this same time frame, three shift managers were hired and operating procedures development and training activities were begun.

The goal is for CFTF to be recognized as a manufacturing demonstration facility and an advanced technology commercialization asset to this nation. Therefore, the process and programs implemented to support CFTF operations have been carefully developed keeping the latest technologies and needs of industry in mind. The results of these efforts have produced a highly professional, well-qualified operations team with the capabilities for critical thinking and innovation that will be necessary to support the process development and commercialization goals of ORNL's CF program.

Demonstration projects at CFTF will commence in 2013. Results from a research and development standpoint are not reported in this annual report. However, major activities taking place in FY 2012 to prepare the facility for operations have included the completion of construction and equipment design, fabrication, testing, and installation. Major efforts toward staffing, training, program planning, and procedure development have been completed in expectation of start-up and commissioning of the facility, which will commence operation in October 2012.

Results and Discussion

Significant progress has been made since staffing in June and July 2012. Numerous procedures and plans have been developed for the facility and for each unit of operation (e.g., creel, ovens, furnaces, winders, etc.) with the exception of the melt spinner. CFTF-related documents and procedures are organized on a server and are available through a web-based application. The screen shots in [Figures 1 and 2](#) provide insight into how the information is organized.

To implement the procedures, CFTF management developed a sophisticated training system that serves two purposes: (1) to train the current staff of new hires and (2) to provide a workforce development capability that can be shared with industries that may commercialize technologies demonstrated at CFTF. The training system features a wireless, tablet-based, real-time system for providing procedures, logging technician observations, and capturing a wealth of data related to process development. Based on enthusiastic feedback on the system from industry partners, an invention disclosure will be filed for this technology with the anticipation of a patent to follow.

Technicians will use iPad checklists ([Figures 3 and 4](#)) in the field to guide and record activities while monitoring the CF line. The checklists will serve as aids and include important information such as safety warnings and requirements. They will also allow the technicians to initiate maintenance actions with the touch of a screen.

In preparation for the transition to operations that will follow commissioning in FY2013, a Management Readiness Assessment was started during the month of September to assess readiness of the project team to proceed into the commissioning phase. The commissioning phase will require three-shift operations. At the direction of the Major Item of Equipment (MIE) project federal project director, and as required by DOE O 413.3B, a second Readiness to Operate Assessment will be conducted for closeout of the MIE project after site acceptance testing and commissioning are completed, just before requesting CD-4 (critical design step 4) approval from DOE. [Figure 5](#) depicts the CFTF project phases, the anticipated progression of the project, and the timing for each of the assessments.

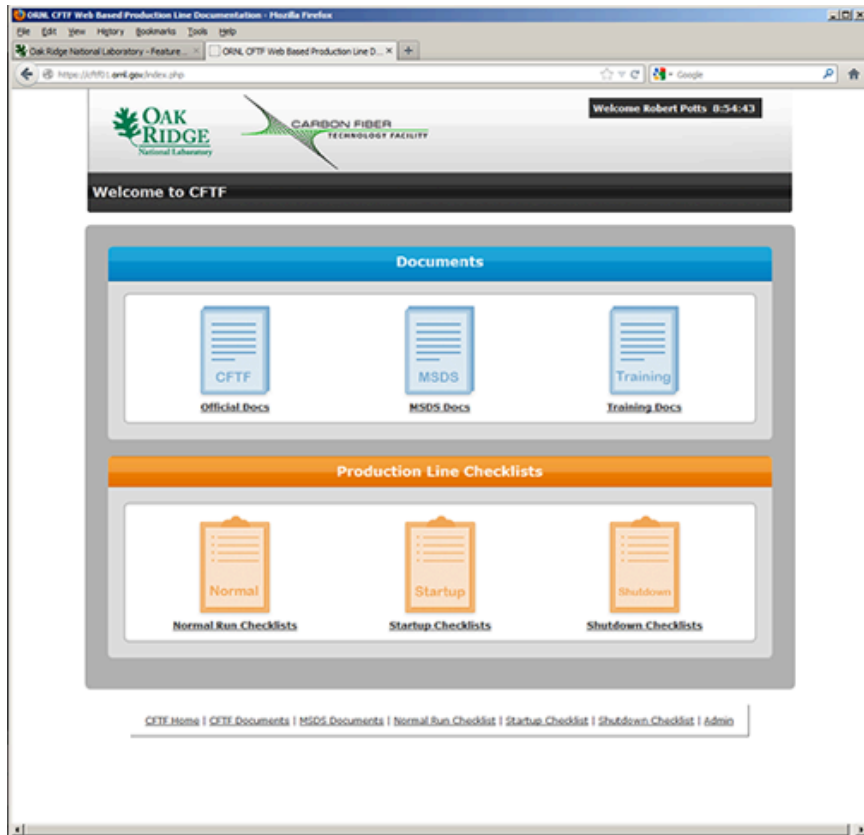


Figure 1. Welcome screen for CTF web-based document access.

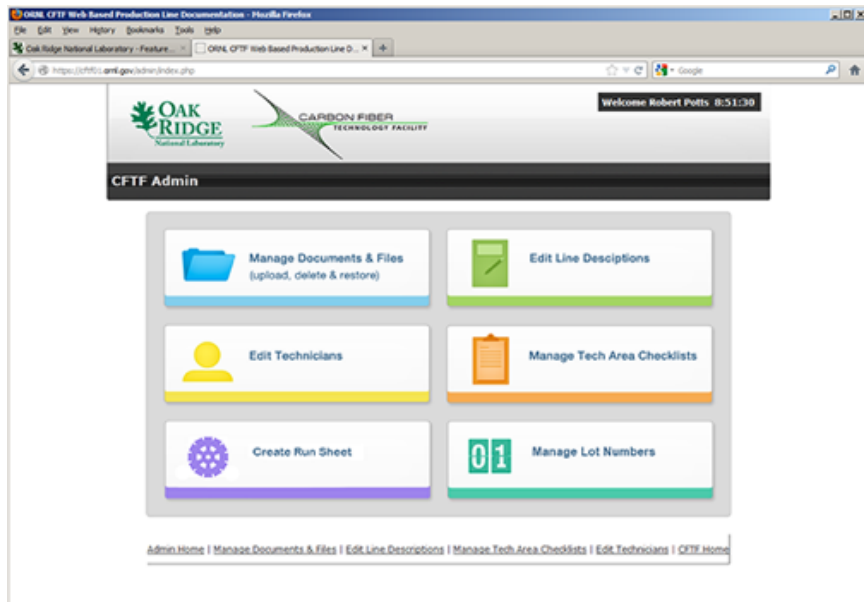


Figure 2. CTF document creation and management menu.

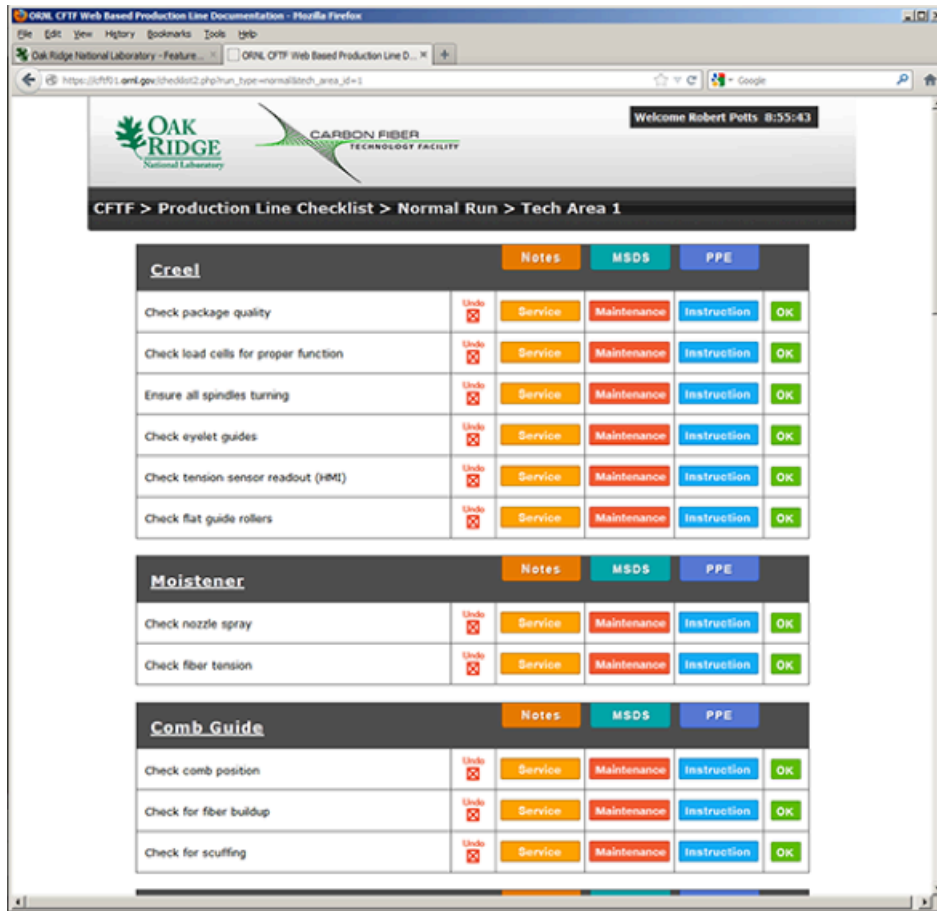


Figure 3. Technician checklist screen for CF production line upstream unit operations.

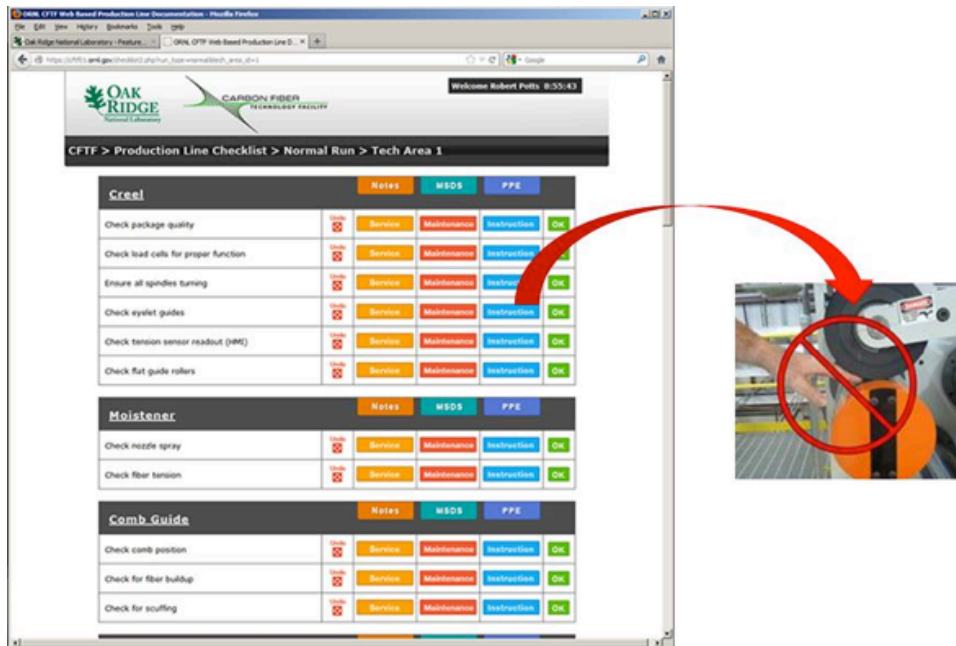


Figure 4. Checklist selection of a video illustrating a safety requirement.

Project Timeline

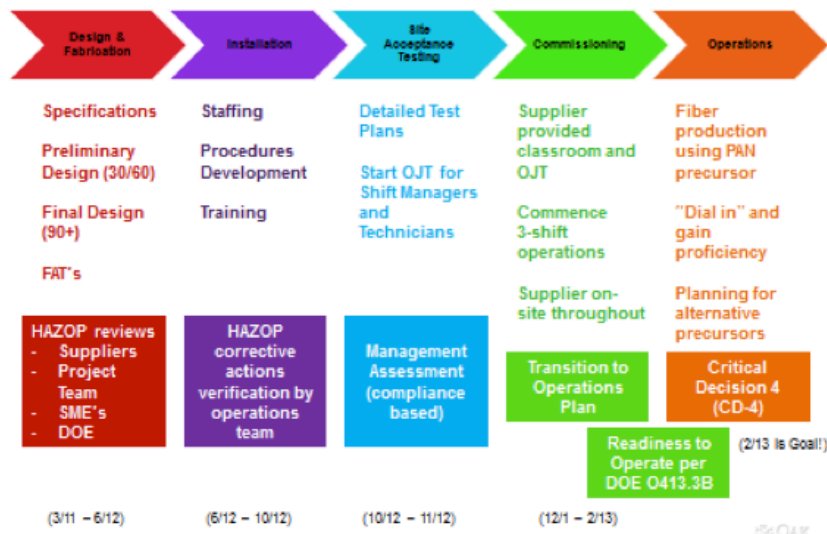


Figure 5. CFTF MIE project timeline, with operational assessments, some of which are funded by this project, shown in lower boxes.

The management assessment, which will be completed and a report issued in October 2012, included an in-depth look across a broad spectrum of functional areas including environment, safety, and health; work control; operations; engineering; maintenance; and quality (Table 1). As outlined in the plan, the assessment team is made up of a group of ORNL independent senior level management system owners and subject matter experts.

Table 1. Management assessment matrix

Activity	Subject matter expertise								
	Laboratory operations	Safety	Environmental protection	Performance analysis, quality	Facilities development	Security	Export control	Research and development	
Work control and planning including hazards analysis	✓	✓							
Transition to operations	✓							✓	
Interface with research	✓							✓	
Worker safety and health		✓							
In-process testing				✓					
Quality assurance, including software	✓			✓					
Training and qualification		✓		✓					
Human performance elements		✓							
Environmental protection, waste management, and air quality			✓						
Configuration management					✓				
Equipment calibration				✓	✓				
Human performance of control panels, valves, and piping		✓			✓				
Project management program and maintenance	✓				✓				
Project turnover process/project execution plan/acceptance criteria	✓				✓				
Third party interfaces/remote location uniqueness	✓							✓	
Emergency preparedness			✓			✓			
Export control							✓		
Access control						✓			
Physical security						✓			
Intellectual property							✓		

Technology Transfer Path

Although not explicitly funded as part of the CFTF project, successful transfer and commercialization of low cost CF technology for achieving U.S. energy and economic benefits is the overarching objective of CFTF. Toward that end, ORNL is working hard to identify potential partners and create effective partnerships, with emphasis on CF users such as composites fabricators and original equipment manufacturers (OEMs), that can generate market pull in high volume energy applications. We frequently host visits by potential industrial partners throughout the supply chain from multiple end use industries.

We have had some notable successes in building partnerships with organizations that will use CFTF for scaling toward commercial deployment. In June, AMO selected proposals from three industrial partners that plan to scale at CFTF for Innovative Manufacturing Initiative awards.

1. Dow Chemical Company was awarded \$9M for “Scale-up of Novel Low-Cost Carbon Fibers Leading to High-Volume Commercial Launch.” This project is focused on scaling and deployment of polyolefin-based CFs with initial application in the automotive industry. Ford Motor Company and ORNL are partners in the project, with semi-production scaling at CFTF being a critical project task.
2. “Low-Cost Bio-Based Carbon Fiber for High Temperature Processing” was selected as an alternate project slated for future funding, hopefully beginning in FY 2013. A vertically integrated project team, including a biorefiner, a materials manufacturer, and multiple component manufacturers, will develop and scale lignin-based CFs with initial focus on functional (nonstructural) applications. Semi-production scaling at CFTF is also a critical task in this project.
3. “Low-Cost In Situ Composite Processing” was also selected as an alternate project slated for future funding. This project is led by an OEM with interests in multiple energy industries. It will include scaling at CFTF, with the production of several fiber sublots with different posttreatments. Surface treatment and sizing approaches that are most suitable for specific resins and composite applications will be determined.

In addition to the aforementioned project awards that will use CFTF, we are also engaged in detailed discussions with CF equipment manufacturers about the potential for validating equipment and process designs and/or operator training at CFTF. Currently we are developing the statement of work for one such partner and discussing potential needs with others.

Finally, ORNL has committed \$2.2M to a Laboratory Directed R&D initiative focused on lignin-based carbon fibers. A key objective of this work is to enable ton-scale production of lignin-based carbon fibers at CFTF in FY14. All of these awarded, pending, or potential projects aim to commercialize low cost CF technology by demonstrating technology scalability and/or producing market development materials at CFTF.

Conclusions

CFTF bridges the gap to enable effective transition of low cost CF technology from the research laboratory to U.S. industrial deployment and commercialization. Key CFTF strategies are (1) demonstrate advanced low cost CF technology scalability, (2) produce materials needed for low cost CF market development, and (3) develop the skilled workforce that is needed to enable U.S. industrial deployment. This project funds the execution of these key CFTF strategies.

CFTF is scheduled to start up in FY 2013. Equipment procurement, installation, and commissioning is funded by a capital project. Expense funds are directed to the development, staffing, training, and readiness assessments required to establish operational readiness. In FY 2012, we hired and trained 22 staff members, developed and implemented robust work control systems and procedures, conducted initial assessments of progress toward operational readiness, and started resolution of the assessment findings and recommendations.

ORNL’s CF-related industrial and educational partnerships have advanced significantly because of CFTF. Many of the newly hired technicians were trained through our educational partnership with RSCC. We have secured one scale-up project with three others pending, all led by different industrial partners and most including multiple industry partners from different parts of the value chain. We are engaged in various levels of discussion with several other current and/or potential industrial partners regarding potential scaling projects at CFTF.

ORNL is on schedule and budget in our preparations for CFTF start-up. We are well positioned for a successful start-up with qualified staff and robust protocols that are now being fine-tuned for approval. We have secured scale-up projects with multiple low cost precursors and committed partners. We continue to have enthusiastic engagement of current and potential industrial partners with prospects for additional scale-up projects to be booked during FY 2013.

Presentations/Publications/Patents

No presentations or publications were released during this reporting period. We hosted numerous potential industrial partners and collaborators who toured CFTF during the reporting period. In the coming fiscal year, presentations on CFTF will be made at the National Educators’ Workshop at Ivy Tech Community college in Fort Wayne, Indiana, and at the Carbon Fibers 2012 Conference in San Diego, California. We also expect to submit an invention disclosure and begin the patent election/application process for a patent on our wireless, tablet-based system for work control and training.

D. Development and Commercialization of a Novel Low-Cost Carbon Fiber – Zoltek Companies, Inc.

Principle Investigator: George Husman, Chief Technology Officer
3101 McKelvey Road
St. Louis, Missouri 63044
(314) 291-5110; e-mail: george.husman@zoltek.com

Technology Area Development Manager: William Joost or Carol Schutte
U.S. Department of Energy
1000 Independence Ave., S.W., Washington, DC 20585
(202) 287-6020; fax: (202) 856-2476; e-mail: william.joost@ee.doe.gov

Contractor: Zoltek Companies, Inc.
Contract No.: DE-EE0005394

Executive Summary

The objectives of this project are to develop and commercially validate a low cost carbon fiber meeting the target cost of \$5.00/lb. and target properties of strength > 250,000 pounds per square inch (psi), modulus of elasticity > 25,000,000 psi, and strain-to-failure > 1%. This project is a joint development effort of Zoltek Companies, Inc. and Weyerhaeuser Company. The bases of this development are innovative, patent pending technology for wet-spinning of lignin/PAN blended polymer precursor fibers combined with modifications to existing commercial precursor and carbon fiber manufacturing processes. This approach, which combines the fiscally conservative use of existing carbon fiber infrastructure, with the innovative development of a new low cost, renewably based lignin precursor material, provides the greatest chance of near term commercial adoption and a line of sight to low cost carbon fiber suitable for light-weighting automotive structures as well as other energy efficient applications.

This project builds upon and accelerates pre-award (Phase 0) joint efforts by Zoltek Companies, Inc. and Weyerhaeuser Company to develop low cost carbon fiber precursor technology based on wet spinning of lignin/PAN polymer blends. The objectives of Phase 1 are to optimize this precursor technology and carbon conversion parameters to achieve a precursor fiber with maximum lignin content that converts to a carbon fiber exceeding the defined property requirements. The final objective of Phase 1 is to validate the scale up of this technology to full scale commercial production using existing spinning and carbon fiber manufacturing facilities. Phase 2 objectives are to develop improved precursor chemistries to provide higher carbon conversion ratio and higher rate carbon conversion to achieve further cost reduction. In addition, every process step within polymerization, spinning, and carbon conversion will be analyzed and optimized for improved efficiencies and reduced energy consumption. The final objective of Phase 2 is to validate the scale up of the improved precursor technology to full scale commercial production using manufacturing facilities that have been modified for operational efficiency and energy reduction.

Accomplishments

- During FY 2012 large numbers of solution studies have been performed to determine best parameters for solution spinning of lignin/PAN polymer blends to produce precursor fibers with good morphology and properties required for producing carbon fiber.
- A large data base of thermal properties has been generated to determine the chemical reaction behavior of lignin/PAN precursor fibers to understand the oxidation / stabilization process required to produce carbon fiber. This data includes differential scanning calorimetry (DSC), thermal gravimetric analysis (TGA), and dynamic mechanical analysis.

- Guided by the solution and spinning studies and the thermal analyses data, a large number of lignin/PAN precursor fibers have been produced under varying conditions on laboratory and pilot scale spinning lines and subsequently oxidized under varying conditions on pilot scale oxidation line. These precursor fibers and oxidized fibers have been fully characterized for physical, chemical and mechanical properties and have also been examined using scanning electron microscopy to assess fiber morphologies.
- Oxidized fibers achieving good morphologies and properties have been successfully carbonized to produce carbon fibers. 25% and 35% lignin containing carbon fibers have been produced exceeding the target mechanical properties for this project.
- In preparation for a commercial scale validation of the lignin/PAN precursor and carbon fiber technologies, 10,000 pounds of high purity lignin polymer have been produced, commercial scale polymer mixing equipment has been developed and readied for production operation, and a commercial scale spinning line has been prepared for the commercial trial to be accomplished in FY 2013.

Future Directions

- Additional laboratory scale and pilot scale optimization will be accomplished to refine all processing parameters for success of commercial scale validation.
- Commercial scale validation of technologies will be performed during first calendar quarter 2013. Approximately 22,000 pounds of 35% lignin/PAN precursor fiber will be produced, leading to production of approximately 10,000 pounds of carbon fiber. This fiber will be put into various intermediate product forms and made available to automotive OEMs and Tier 1 molders for evaluations.
- Following commercial scale validation, Phase 2, Commercial Scale-up Development, will proceed. This phase will start with detailed process modeling and cost modeling focused on defining cost reduction opportunities beyond just materials substitution of lignin for PAN. These studies will define process changes as well as equipment and facilities modifications required to approach the cost target for this project. This will lead to modifications of existing commercial processing equipment and facilities for lignin manufacturing, precursor fiber manufacturing, and carbon fiber manufacturing. These manufacturing modifications will be implemented and started to produce commercial product.
- Final task of the project will be full scale validation and characterization of commercial carbon fiber produced from lignin/PAN precursor fiber.

Technology Assessment

- Target: Achieve \$ 5.00/pound carbon fiber from renewable (non-petroleum based) raw materials.
- Gap: The approach of this project is to develop precursor fibers from lignin/PAN polymer blends utilizing existing wet spinning technologies and commercial equipment. Solution chemistry limits this approach to 45% lignin (renewable) content, but this is a significant step forward toward using renewable materials for producing carbon fiber. This will also result in lower energy consumption and CO₂ emissions for carbon fiber production.
- Gap: Material substitution alone cannot achieve the cost target. Phase 2 of this project will focus on carbon fiber manufacturing and additional energy consumption efficiencies to further reduce costs and approach the cost target.
- Target: Achieve a low cost carbon fiber with tensile strength > 250,000 psi and tensile modulus > 25,000,000 psi.
- Gap: Precursor spinning behavior with lignin/PAN polymer blends is significantly different than 100% PAN. Phase 1 of this project has demonstrated the ability to spin the lignin-containing precursor fibers, but achieving good morphologies in these fibers (no macro-voids) capable of achieving carbon fibers with target properties has proven technically challenging.
- Gap: FY 2012 studies have developed approaches to achieve desired morphologies by changing molecular weight and polydispersity of the PAN polymer. Carbon fiber mechanical properties exceeding target values of this project have been demonstrated at pilot scale. These pilot scale precursor polymer, spinning, and carbon fiber conversion studies will be continued in early FY 2013 leading the commercial scale validation during 1st calendar quarter 2013.

Introduction

The objectives of this project are to develop and commercially validate a low cost carbon fiber meeting the target cost of \$5.00/lb. and target properties of strength > 250,000 psi, modulus of elasticity > 25,000,000 psi, and strain-to-failure > 1%. This project is a joint development effort of Zoltek Companies, Inc. and Weyerhaeuser Company. The bases of this development are innovative, patent pending technology for wet-spinning of lignin/PAN blended polymer precursor fibers combined with modifications to existing commercial precursor and carbon fiber manufacturing processes. This approach, which combines the fiscally conservative use of existing carbon fiber infrastructure, with the innovative development of a new low cost, renewably based lignin precursor material, provides the greatest chance of near term commercial adoption and a line of sight to low cost carbon fiber suitable for light-weighting automotive structures as well as other energy efficient applications.

This project builds upon and accelerates pre-award (Phase 0) joint efforts by Zoltek Companies, Inc. and Weyerhaeuser Company to develop low cost carbon fiber precursor technology based on wet spinning of lignin/PAN polymer blends. The objectives of Phase 1 are to optimize this precursor technology and carbon conversion parameters to achieve a precursor fiber with maximum lignin content that converts to a carbon fiber exceeding the defined property requirements. The final objective of Phase 1 is to validate the scale up of this technology to full scale commercial production using existing spinning and carbon fiber manufacturing facilities. Phase 2 objectives are to develop improved precursor chemistries to provide higher carbon conversion ratio and higher rate carbon conversion to achieve further cost reduction. In addition, every process step within polymerization, spinning, and carbon conversion will be analyzed and optimized for improved efficiencies and reduced energy consumption. The final objective of Phase 2 is to validate the scale up of the improved precursor technology to full scale commercial production using manufacturing facilities that have been modified for operational efficiency and energy reduction.

Initial feasibility of technology was demonstrated during Phase 0 in FY 2011, prior to award of this project. Phase 1 was initiated at the beginning of FY 2012 when this project was awarded. The efforts accomplished during Phase 1 have been focused on developing full understanding of polymer and polymer solution behaviors, spinning technologies and parameters for producing blended lignin/PAN precursor fibers, oxidation chemistry and kinetics of reaction to achieve stabilized lignin/PAN fibers capable of producing high performance carbon fibers, and validation of pilot scale produced carbon fibers with mechanical properties meeting or exceeding target values. The final milestone for Phase 1 will be commercial scale validation of the technologies developed. This will be accomplished early in FY 2013. The accomplishments of FY 2012 are described in more detail in the remainder of this report.

Approach

The approach used for this project consists of a logical sequence of series and parallel tasks focused on achieving the project objectives. These tasks develop and validate the required technologies through a classical building block approach from lab scale through pilot scale to full scale commercial demonstration. Descriptions of tasks performed during the Phase 1 of project are outlined below:

Task 1 – Cost Model Development: Perform detailed analyses of each process step from raw materials purchase through polymerization, spinning, and conversion to assess cost and operational and energy efficiencies. Develop a simple cost model that clearly identifies cost drivers and opportunities for cost reductions, providing focus to technical efforts of the project

Task 2 – Polymerization & Solution Studies: Evaluate modified PAN chemistries and molecular weights for optimized lignin/PAN solutions and spinning behaviors.

Task 3 – Lab and Pilot Scale Spinning: Develop and validate spinning parameters at lab scale leading to spinning of larger tow precursor fibers at pilot scale for batch and continuous oxidation studies.

Task 4 – Pilot Scale Oxidation and Carbonization Development: Perform pilot oxidation and carbonization studies leading to selection of candidate product and process conditions for full scale development and validation.

Task 5 – Analytical Studies: Perform thermal analysis, chemical analysis, microscopy, mechanical and physical property testing at all stages of development.

Task 6 – Commercial Scale Readiness: Design, fabricate and install large scale lignin/PAN mixing equipment. Prepare commercial spinning line for full scale validation.

Task 7 – Large Scale Lignin Production: Produce of 10,000 pounds of high purity lignin polymer at Weyerhaeuser pilot facility to be used for full commercial scale validation of lignin/PAN precursor fiber and resulting carbon fiber.

Results and Discussion

Task 1 – Cost Model Development:

A baseline unit costing model, developed for all components of the Zoltek PAN-based process (polymerization, precursor spinning and conversion to carbon fiber), has been assembled into a spreadsheet format to serve as the basis for a comparison of the total manufacturing costs of carbon fiber derived from 100% PAN copolymer versus various lignin/PAN blends. First validation of the model for lignin/PAN carbon fiber production will be accomplished during the commercial scale validation at the completion of Phase 1 in early FY 2013. This model will be used to define tasks to be accomplished during Phase 2 of the project.

Preliminary indications are that material substitution alone cannot achieve the cost target. Phase 2 of this project will focus on carbon fiber manufacturing and additional energy consumption efficiencies to further reduce costs, approaching the cost target of the project.

Task 2 – Polymerization & Solution Studies:

Early solution studies identified that lignin caused a reduction in solution viscosity when added to PAN spinning solutions. It was further determined in spinning studies that in order to spin lignin/PAN precursor fibers with good morphologies (no macro-voids), with lignin contents above 25% and capable of producing carbon fiber, that it was necessary to use higher molecular weight PAN polymer to provide higher solution viscosities for spinning. A series of studies were performed using various molecular weight PAN polymers in order to determine optimum spinning performance. These initial studies were done with PAN polymers produced in lab scale reactor. When this polymerization was scaled up to commercial reactor, producing polymer with tighter molecular weight distribution, it was determined that this tighter poly-dispersity changed solution diffusion characteristics. These effects will be further evaluated early in FY 2013 and have led to a delay in the commercial scale validation to the first calendar quarter of 2013.

Task 3 – Lab and Pilot Scale Spinning:

Throughout FY 2012, a large number of lab scale and pilot scale precursor fiber spinning trials were completed in order to define optimum spinning conditions using the polymer solutions developed in Task 2. These precursor fibers were fully characterized for physical, chemical, and mechanical properties and behaviors, and those with good properties and morphologies were taken forward to pilot scale oxidation and subsequent carbonization studies. As a result, a large data base and understanding of lignin/PAN precursor fiber spinning parameters and behaviors have been developed. Detailed data from these studies have been reported in quarterly progress reports.

Task 4 – Pilot Scale Oxidation and Carbonization Development:

A pilot scale oxidation line was commissioned at the start of FY 2012 and was used throughout the year to perform oxidation studies on precursor fibers developed in Task 3. These oxidized fibers were fully characterized for physical, chemical, and mechanical properties and behaviors, and those with good properties and morphologies were taken forward to subsequent carbonization studies. As a result, a large data base and understanding of lignin/PAN precursor fiber oxidation parameters and chemistry have been developed. Detailed data from these studies have been reported in quarterly progress reports.

As a result of these studies, lignin/PAN precursor fiber properties and processing conditions combined with oxidation processing parameters have been defined that result in pilot scale carbon fibers exceeding the target mechanical properties of this project. Carbon fibers with tensile strengths > 300,000 psi and tensile modulus > 30,000,000 psi have been demonstrated and reproduced. These results, together with the results from polymerization, solution, spinning results obtained in Tasks 2 and 3, will lead to the commercial scale validation early in FY 2013.

Task 5 – Analytical Studies:

Dozens of optical and scanning electron microscopy pictures have been produced and evaluated to assess morphologies of precursor fibers, oxidized fibers and carbon fibers produced from various material combinations and processing conditions. Similar numbers of DSC tests have been performed to assess oxidation behavior of precursor fibers, helping to guide oxidation processing studies. In addition, TGA, x-ray diffraction studies, FTIR spectroscopy, thermal mechanical analyses, and other analytical tests have been used throughout the project to provide understanding of materials and processes being developed and to guide the experimental development efforts. Details of these analytical procedures and results are presented in the quarterly progress reports.

Task 6 – Commercial Scale Readiness:

Large scale polymer solution mixing equipment has been designed, fabricated, and installed in preparation for the commercial scale validation. Also a commercial spinning line has been prepared for the commercial scale validation. These facilities are ready for this commercial scale validation milestone, currently scheduled for the first calendar quarter 2013. A commercial carbon line will be scheduled and used for this validation test.

Task 7 – Large Scale Lignin Production:

Ten thousand pounds of high purity lignin polymer were produced by Weyerhaeuser in their pilot facility in New Bern, South Carolina, to be used for full commercial scale validation of lignin/PAN precursor fiber and resulting carbon fiber. In addition, Weyerhaeuser has continued to develop new technologies for increased purity lignin polymer and has begun to develop designs and plans for a commercial scale lignin production facility, in preparation for the Phase 2 commercialization phase of the project.

Technology Transfer Path

Approximately 22,000 pounds of 35% lignin/PAN precursor fiber and subsequently 10,000 pounds of carbon fiber will be produced as the technology validation milestone at the end of Phase 1 of the project. This fiber will be put into various intermediate product forms and made available to automotive OEMs and Tier 1 molders for evaluations. These evaluations will include molding of panels for mechanical properties tests as well as molding demonstrations of representative automotive parts. Intermediate product forms evaluated will include carbon fiber sheet molding compound, carbon fiber prepregs for compression molding, carbon fiber fabrics for resin transfer molding, and carbon fiber tows with thermoplastic sizings for thermoplastic direct compounding demonstrations.

A similar validation will be done at the end of Phase 2 of the project demonstrating the performance of the fully commercialized lignin/PAN precursor and carbon fiber technology. After successful validation of the Phase 2 commercial product, this innovative low cost, high performance lignin/PAN carbon fiber product will be available for sale to the worldwide automotive industry as well as for use in other markets such as wind energy.

Conclusions

During FY 2012, a large volume of materials, processing, and analytical studies have been performed to develop the necessary knowledge and data base for the successful commercialization of a novel low cost carbon fiber based on wet spinning of lignin/PAN blended polymer precursor fibers. The results of these studies, data, and knowledge are leading to the first technology validation milestone in early 2013 that will demonstrate commercial scale production of a 35% lignin-containing precursor fiber and subsequent carbon fiber. Further, the results developed during this fiscal year have defined the technical approaches to achieving a 45% (maximum possible) lignin-containing precursor and carbon fiber. The logical building block approach taken in this project has resulted in development of a detailed understanding of materials and process parameters that can be easily scaled from laboratory to pilot scale to full commercial scale production.

Results demonstrated in this fiscal year have shown that mechanical properties of a 35% lignin-containing carbon fiber can exceed the target properties for this project. Initial cost modeling has clearly indicated that the Phase 2 commercialization phase is required to approach the cost target of \$5.00/pound. Materials substitution of lignin for PAN will get part of the way

toward this target, but improvements in production throughput and energy efficiencies must be developed to attempt to achieve the cost target.

A high level of interest has been expressed by automotive OEM and Tier 1 and Tier 2 manufacturers. The full scale validation of the technologies developed during this fiscal year will lead to application verification and acceptance of this novel low cost carbon fiber technology by these manufacturers. Completion of Phase 1 and successful development and validation of commercial manufacturing technologies in Phase 2 will allow immediate and wide scale production implementation for automotive and other applications.

Presentations/Publications/Patents

Presentations:

Husman, G. Development and Commercialization of a Novel Low-Cost Carbon Fiber. Presented at the 2012 DOE Vehicle Technologies Office Annual Merit Review, May 14-18, 2012, Washington, D.C.

Husman, G., Carbon Fiber Composites-Low Cost Materials and Manufacturing Options. Presented at the Society of Plastics Engineers Automotive Composites Conference and Exhibition, September 11-13, 2012, Troy, MI.

A one-slide status of this project was presented at the SAE 2012 World Congress and Exhibition on April 24, 2012.

A presentation on this project was given at the 2nd International Lignin Biochemicals Conference, June 21, 2012, Toronto, Canada.

Patents:

Bissett, P. J., Herriott, C. W. Lignin/Polyacrylonitrile-Containing Dopes, Fibers, and Methods of Making Same. U.S. Patent Application 12828054, published January 5, 2012.

4. United States Automotive Materials Partnership LLC Cooperative Research

A. Advanced Metals

Optimization Of High-Volume Warm Forming For Lightweight Sheet Alloys (AMD 905)

Principle Investigator: Nia Harrison
Ford Motor Company
Ford Research and Innovation Center
2101 Village Road
MD 3135
Dearborn, MI 48121-2053
(313) 805-7426; Fax: (313) 390-0514; e-mail: nharri31@ford.com

Principle Investigator: Jugraj Singh
Chrysler Corporation LLC
Materials Engineering
Mail Code 482-00-13
800 Chrysler Drive
Auburn Hills, MI 48326-2757
(248) 512-0029 Fax: (248) 576-7490; e-mail: js329@chrysler.com

Principle Investigator: Ravi Verma
General Motors Corporation
GM, R&D and Planning
Mail Code 480-106-224
30500 Mound Road
Warren, MI 48090-9055
(24) 807-4188, Fax: (586) 986-9260; e-mail: ravi.verma@gm.com

Contractor: U.S. Automotive Materials Partnership
Contract No.: DE-FC26-02OR22910

Abstract/Executive Summary

Traditional warm forming of aluminum refers to sheet forming in the temperature range of 200°C to 350°C using heated, matched die sets similar to conventional stamping. Non-isothermal warm forming refers to a prescribed temperature difference between the die and the sheet, which has also been known to show enhanced formability characteristics within aluminum sheet. Phase 2 of the AMD905 project utilizes the optimized non-isothermal warm forming parameters determined in Phase 1 for the development and construction of a full-scale door inner. Extensive thermal and formability studies were conducted to guide the design of the die face and blank shape. Following construction of the die, manual and automated forming trials were conducted at two Magna facilities. The manual trial verified concept feasibility and identified areas of the die that required modifications prior to the automated trial. The automated trial was used to demonstrate process

repeatability, cycle time, and the formability window while the forming cell included demonstrations of pre-heating, automation, and formability. Successful parts were formed with a sheet temperature in the window of 250°C +/- 10°C with a room temperature die face using material from two material suppliers in two orientations. This work has demonstrated the sufficient formability achieved by non-isothermal warm forming of a one-piece door panel in a production environment that is consistent with conventional stamping.

Objectives

1. Conduct non-isothermal forming trials to demonstrate optimized warm forming process with production supplier partner.

Accomplishments For 2012

1. Engineered the door inner die using traditional die construction practices optimized for aluminum sheet.
2. Demonstrated a low-cost warm forming process which requires minimal die heating based on thermal simulation analysis recommendations.
3. Demonstrated a minimized wrinkling and cracks through radii and draw bead modifications while preserving the part complexity based on finite element analysis recommendations.
4. Demonstrated an aluminum design that achieved a weight savings of ~5 lbs (or 40%) over the EDDQ-steel original (~13 lbs).

Future Directions

This project is now complete. If additional funding were available, the team would recommend the next step toward commercialization would be to demonstrate a full-scale run-at-rate production cell of the low cost warm forming process of the door inner panel at a supplier partner facility.

Technology Assessment

- Target: Attain craftsmanship levels in aluminum similar to steel.
- Gap: Run-at-rate production cell has not been established to verify thermal simulation predictions.

Introduction

Successful completion of two projects on warm forming (ADM307 and AMD602) have shown that this technology can be used as a cost-effective method of manufacturing complex 3-dimensional panels from both aluminum and magnesium sheet alloys. This current project was aimed at investigating non-isothermal methods of warm forming to further optimize the process in terms of production robustness and total cost. By controlling temperature locally on different elements of the die as well as the blank, the formability of these alloys can be significantly improved while also reducing process complexity and cost. Enhanced formability characteristics within aluminum sheet has been observed when there is a prescribed temperature difference between the die and the sheet (Kim et al., 2006; Daoming and Ghosh, 2004; Tebbe and Kridli, 2004). The phase 1 non-isothermal warm forming work provided suitable evidence that a full scale part would be achievable with respect to depth of draw and stretch and suggested that the recommended approach to warm forming only required a warm sheet and a room temperature die. The current project transferred the appropriate non-isothermal forming conditions based on the recommendations of the simulation studies concluded in FY 2011 to the design, construction, and prove-out of a Focus door inner (Figure 1). This non-isothermal approach is significantly cheaper than traditional warm forming proposals due to the elimination of heating elements within the die. Die performance was validated through forming trials and post-formed analyses.

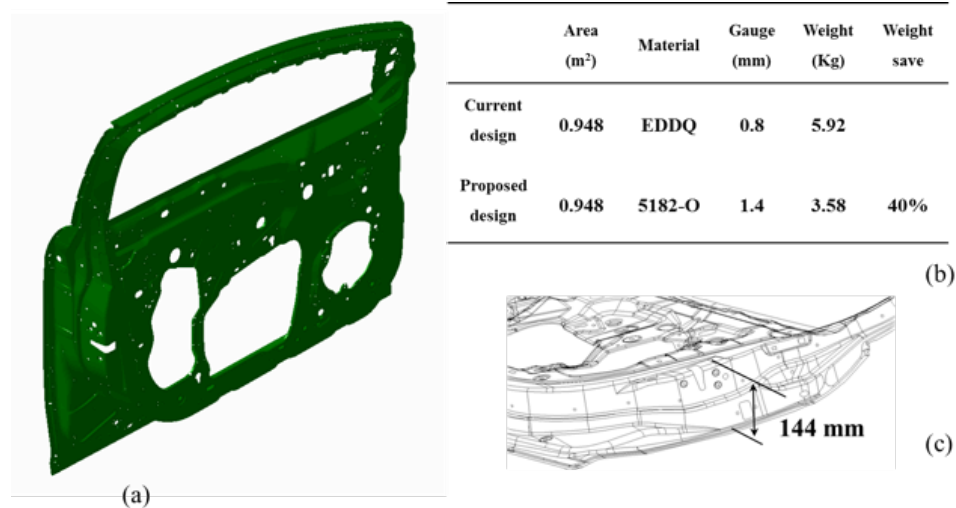


Figure 1. This image depicts the (a) Ford Focus door inner, (b) material comparison and potential weight save, and (c) the maximum draw depth.

Production Trial

Material Preparation

Sheet aluminum blanks from two alloy suppliers were used in this study. Both suppliers were asked to supply a nominal gage of 1.5 mm. Coil width was selected so as to be able to stamp panels in the rolling direction as well as 90 degrees to the rolling direction. A solid lubricant was used to enhance formability and reduce friction between the sheet and the die. The Fuch's Forge Ease 278 lubricant, diluted 1:4 with isopropyl alcohol, was used for the forming trials. Lubricant was applied with a roller on both sides of the blanks, and was allowed to dry at room temperature.

Automated Forming Trials

Final forming trials were conducted at Magna's Canadian research facility, Promatek located in Brampton, Ontario. A conduction pre-heater was used to heat the blanks. The blank was moved from the loading station to the furnace robotically using a Fanuc 2000i robot. The robot was fitted with a custom designed and fabricated end-effector using suction cups, capable of operating at elevated temperatures which gripped the sheet. The blank was left inside the furnace for 180 seconds to reach the desired warm forming temperature, and then moved to the die using the same end-effector. Cycle time from the moment the blank left the furnace to the end of the forming operation was approximately 15 seconds. Formed panels were manually retrieved from the die. The warm forming parameters used during the forming trials are given in Table 1. An aerial schematic of the forming cell is shown in Figure 2.

Table 1. Warm forming parameters for forming trials.

Blank Temperature	200°C - 300°C
Blank Heating Time	180 sec
Die Temperature	~25°C
Press Tonnage	1475 tons
Cushion Pressure	270 tons

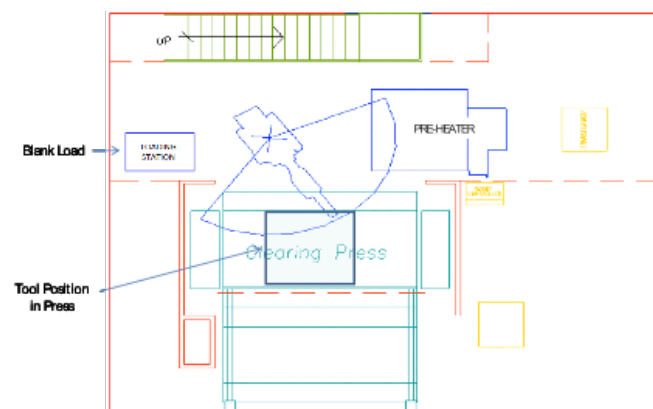


Figure 2. Schematic of production cell lay-out.

Forming Trial Results

Initial trials were done in increments of 25°C starting from a blank temperature of 200°C and going up to 300°C. At 250°C the first successfully formed panel was achieved (Figure 3). Good panels were formed from both the supplier alloys. In general, trials with blanks oriented 90 degrees (T-direction or transverse) from the rolling direction (L-direction or longitudinal) also produced good stampings. However, when the blank temperature was raised to 275°C, good results were produced only when the blank was oriented in the L-direction. Stampings for the T-direction suffered minor splitting. At 300°C, no good panels could be formed. Subsequent trials were conducted to further refine the warm forming window by changing the temperature by smaller increments of 10°C. The results on these smaller increments indicated that the lower bound of the forming window could be reduced, and thus successful parts could be drawn at 240°C. The results of these trials are fully captured in Figure 4. The optimum warm forming window representing both aluminum sheet suppliers was determined to be between 240°C to 260°C.

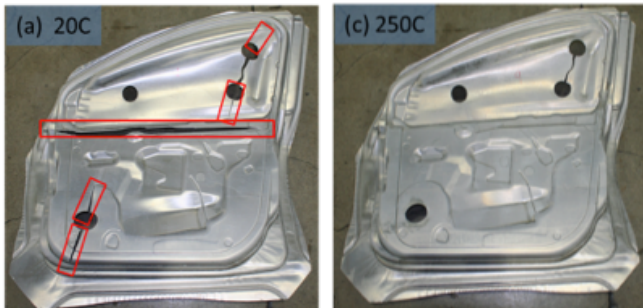


Figure 3. Door inner panels formed at room temperature and warm formed at 250°C.

Blank Temperature ↓	Supplier 1		Supplier 2	
	Longitudinal	Transverse	Longitudinal	Transverse
200°C	Fail	Fail	Fail	Fail
225°C	Fail	Fail	Fail	Fail
230°C	Fail	Not Tested	Pass	Not Tested
240°C	Pass	Pass	Pass	Pass
250°C	Pass	Pass	Pass	Pass
260°C	Pass	Pass	Pass	Pass
270°C	Fail	Not Tested	Fail	Not Tested
275°C	Pass	Fail	Pass	Fail
280°C	Fail	Not Tested	Fail	Not Tested
300°C	Fail	Fail	Fail	Fail

Legend	Pass	Fail	Not Tested
--------	------	------	------------

Figure 4. Warm forming window for 5182-O aluminum alloy sheet marked as dashed blue line box.

Post Forming Analysis

White Light Scanning for Dimensional Analysis

Two panels from one supplier, one with the blank oriented along the rolling direction (RD) and the other oriented in the transverse direction, were selected to study dimensional accuracy of the panels. The panels were washed using a low-foaming liquid acid cleaner (such as Citrajel by Alconox) to remove the lubricant and then prepped for the white light scan. The scanned digital data was overlaid on die computer-aided design (CAD) surfaces for analysis. Both panels showed very similar behavior with respect to where the deviation from CAD occurred. The panel with the blank aligned in the longitudinal showed slightly worse dimensional accuracy than the transverse blank. Deviation of the panel from the CAD surface up to 5 mm was evident.

Thinning Analysis

The warm formed panels were analyzed for thinning using an ultrasonic precision thickness measurement device, the Model CL5, manufactured by GE Inspection Techniques. Panels formed at 250°C from both suppliers were studied. Each panel was marked at 5 critical locations and material thickness was measured along a straight line in 5 mm increments. Percent thinning was then calculated based on original blank thickness. Maximum thinning noted at various locations was in the range of 10% to 20%. No significant difference was observed between the materials supplied from the two suppliers used in this study. It should be noted that some deviations can be attributed to locating differences of the panels when measured. Additionally, these measurement results are reflective of a single panel from each supplier and could potentially show even less deviation between suppliers if multiple panels were studied.

Post-formed Material Properties

The door inner panels warm formed at 250°C from both suppliers were tested for post-formed properties. Samples of as-received (AR) sheet/blanks were also tested for comparison. Tensile testing was performed at room temperature per the ASTM-E8 standard using subsize specimens. Testing was done using an SFM-20 United testing tensile machine using EP-1 extensometer (1 in. extensometer, 25 mm gage length), with a constant crosshead speed of 0.5 inch/min. The bar chart shown in Figure 5 shows a direct comparison of the strengthening behavior of warm forming of the doors formed from Supplier 1 and Supplier 2 material. The horizontal line marks the yield strength of the AR sheet (~139 MPa).

All locations show strength increases for both alloys which are primarily due to work hardening, the common strengthen mechanism in 5xxx-series alloys, when compared to the AR sheet. However, the results shown here do not take into account any relaxation of material properties due to part exposure to a paint bake cycle.

FEA Modeling Comparison

Overall, a reasonable correlation between finite element analysis (FEA) and the door inner was observed. Some notable observations are captured in Figure 6. The flagged areas, like the top left corner (Fig. 6a), were problematic when iterating in simulation toward a solution as well as in reality. Both the die and the blank had to be significantly modified in that corner to prevent splitting. There was also one persistent split prediction in simulation, Fig. 6e, that was not present in the formed panel. This could be reflective of the material properties used. Another problem was slight wrinkling, Fig. 6b and c, which was observed in reality and reasonably predicted by simulation. However, it is believed that this level of wrinkling was no more significant than that shown by the extra-deep drawing quality material. Finally, edge cracking predictions in relief windows were correct in most cases. However, the upper right window shown in Fig. 6d was predicted to be safe but in reality demonstrated intermittent edge cracking.

Conservative assumptions of isothermal FEA for non-isothermal warm forming of 5182 aluminum alloy demonstrated reasonable accuracy and proved to be a useful tool for upfront feasibility analysis. Using substantially lower blank temperature in simulation offsets model simplifications and imperfections and allows for an additional factor of safety. A more sophisticated coupled non-isothermal thermo-mechanical model for this strain-rate sensitive material is expected to substantially improve simulation accuracy and prediction quality.

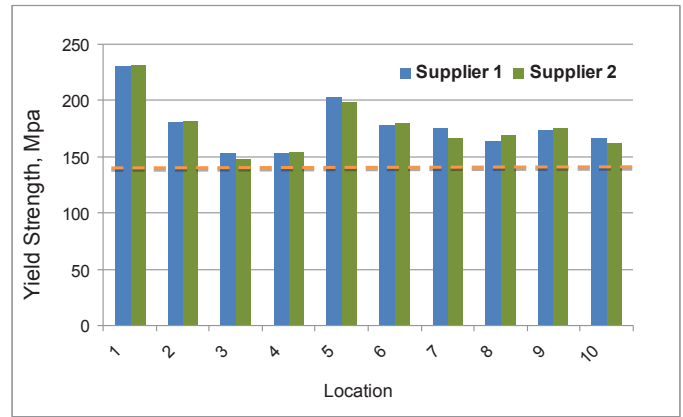


Figure 5. Bar chart showing yield strength behavior of doors formed from Supplier 1 and Supplier 2 material.

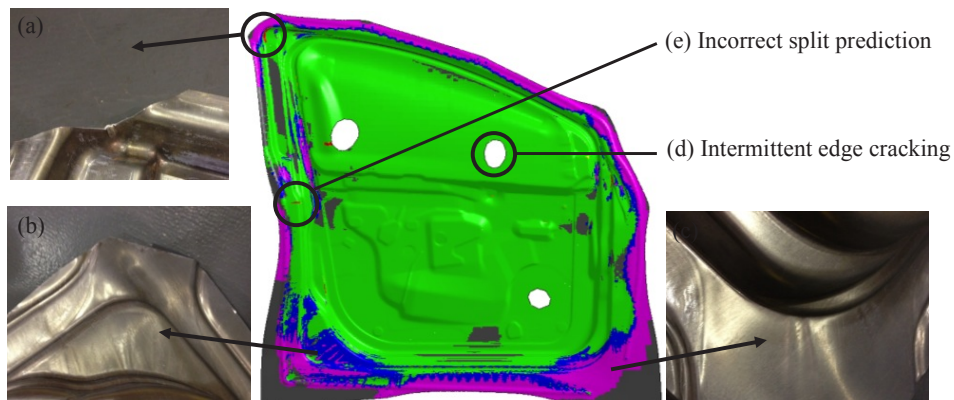


Figure 6. Comparison of the FEA to formed panel.

Technology Transfer Path

The optimized warm forming process is more cost competitive with traditional stamping due to the removal of heaters and controls and likely more attractive for components that require significant draw like the door inner by OEMs. A part made by this process with aluminum in comparison to steel could have a weight savings of ~40%. An additional benefit of this process is the reduction of forming operations from five to four given that a part like the door inner can be produced in a single draw without a re-strike operation; this implies capital equipment savings. For these reasons, there is a high probability that the optimized warm forming process (non-isothermal warm forming) could be adopted by OEMs and suppliers for the forming of various aluminum components in future efforts toward achieving mass savings.

Conclusions

A great deal of this work was focused on the upfront engineering of the door inner die. The die then was crafted for optimum material flow and designed to achieve a steady-state production process. The forming trials demonstrated part formability, process repeatability, and cycle time of the optimized warm forming process. Post-formability analysis demonstrated the dimensional accuracy of the process and commonality of alloy formability with respect to thinning and increased tensile yield. While there are some areas to further study with respect to non-isothermal warm forming, the work completed through this project demonstrates a high level of application readiness for those interested in embracing this advanced approach to sheet forming as a mean of achieving weight savings.

Presentations/Publications/Patents

1. Harrison, Nia; Ilinich, Andrey. Optimization of High-Volume Warm Forming for Aluminum Sheet (USCAR - AMD095 Project Review), North American Deep Drawing Research Group Symposium, Oakland University, Rochester, MI., 2012.
2. Harrison, Nia. Optimization of High-Volume Warm Forming for Lightweight Sheet Alloys. DOE Annual Merit Review, Washington, D.C., 2012.
3. Singh, Jugraj. Warm Forming of Lightweight Metals. International Automotive Body Congress Conference, Troy, MI., 2012.
4. Harrison, Nia; Ilinich, Andrey; Friedman, Peter; Singh, Jugraj; Verma, Ravi. Optimization of High-Volume Warm Forming for Lightweight Sheet Alloys. SAE World Congress, Detroit, MI., 2013. *paper accepted*.

References

- Daoming, L., Ghosh, A.K., Biaxial Warm Forming Behavior of Aluminum Sheet Alloys. *Journal of Materials Processing Technology*, **2004**, *145*, 281-293.
- Kim, H.S., et al., Determination of Proper Temperature Distribution for Warm Forming of Aluminum Sheet Materials. *Journal of Manufacturing Science and Engineering*, **2006**, *128*, 622-633.
- Tebbe, P.A., Kridli, G.T. Warm Forming of aluminum alloys; an overview and future directions. *International Journal of Materials and Product Technology*, **2004**, *21*, 24-40.

Magnesium Front End Research And Development (Phase II - AMD904)

Principle Investigator: Alan A. Luo, General Motors Research & Development Center
(248) 912-8254; fax: (586) 986-9204; e-mail: alan.luo@gm.com

Principle Investigator: Mei Li, Ford Motor Company
(313) 206-4219; fax: (313) 323-1129; e-mail: mli9@ford.com

Principle Investigator: Stephen D. Logan, Chrysler Group LLC
(248) 512-9485; fax: (248) 576-7490; e-mail: sl16@chrysler.com

Technology Area Development Manager: William Joost
U.S. Department of Energy
1000 Independence Ave., S.W., Washington, DC 20585
(202) 287-6020; fax: (202) 856-2476; e-mail: william.joost@ee.doe.gov

Contractor: United States Automotive Materials Partnership LLC (USAMP)
Contract No.: DE-EE0003583

Abstract/Executive Summary

This report summarizes activities for USAMP AMD904, “Magnesium Front End Research and Development, Phase II,” for the time period October 1, 2011, through March 31, 2012 (at which time all technical work on the project was concluded). Three of the project’s eight tasks had technical activities during this period, all other work having been largely concluded with the exception of documentation, and preparations for the 3-country review meeting occurring in June 2012. Task 2.0 (Design, Build and Test) was largely logistical in nature, providing for acquisition, storage, transport and mechanical testing of “demonstration” structures. Task 2.3 (Fatigue and Durability) oversaw the mechanical testing of the two families of structures and provided analysis of results. Task 2.4 (Corrosion and Surface Treatment) oversaw both coupon testing of advanced coatings for magnesium, but also cyclic corrosion testing of pretreated and painted structures from a commercial processor. This report summarizes these various activities and relevant results.

Accomplishments

- A total of 211 magnesium demonstration structures were fabricated during this project, including 120 structures joined by friction-stir linear (lap) welding, 54 structures joined using only self-piercing rivets, and 37 structures joined using a combination of self-piercing rivets (SPRs) with adhesive bonding. Additionally 20 structure “kits” consisting of piece parts for the structure (i.e., shock tower, upper and lower rails, steel test plate and aluminum spacers and SPAC® nuts were provided to the international partners (China and Canada) for their own studies of joining and corrosion protection. The Canadian partners received 16 additional painted structures for environmentally assisted fracture testing, and Chinese partners received two additional uncoated friction-welded structures for corrosion pretreatment studies using the micro-arc oxidation process.
- Fifty-six of the manufactured “demonstration” structures underwent various mechanical tests during the time period of this report; these tests including static strength in three principal axes of loading, constant amplitude fatigue tests in three orthogonal axes, “real world” fatigue loading on the principal vertical axis, and “real world” multi-axis fatigue testing. Two major features emerged from the entire body of testing: 1.) that friction-stir welding showed a propensity for fatigue crack initiation associated with the remnant “pin hole” caused by withdrawal of the stir pin within the body of the structure at the conclusion of the weld, and 2.) that it was difficult to produce failures in the vicinity of SPR joints through conventional loading of the structure, even with “drilling out” of adjacent rivets in order to focus the applied stress at one or more remaining rivets. Agreement of actual and predicted fatigue failures at riveted joints using computer-aided engineering was therefore poor.
- A total of 24 uncoated and coated structures were made available for OEM cyclic corrosion testing. Three different test protocols were employed and a method of comparing intrinsic corrosion rates with respect to the base magnesium alloys

of construction was developed. The “painting” process applied to completed structures included a pretreatment of Henkel Alodine® 5200 and PPG 590-534 cathodic electrocoat. The coating process was conducted by a commercial supplier of electrocoated components (B.L. Downey).

- The investigation of an alternating current (AC)-direct current (DC)-AC electrochemical method to assess the corrosion prevention capability for various pretreatments and polymeric topcoats to magnesium alloys was completed at North Dakota State University. These studies included a statistically designed experiment to determine relative influence of base metal alloy, pretreatment, topcoat material and topcoat thickness using several different response function measurements of coating breakdown. As has been previously hypothesized by the Task 4 team, the pretreatment process is a significant contributor to corrosion resisting performance of the coating system.
- USAMP in association with Forming Simulation Technologies, LLC, has provided for the incorporation of a new material model (MAT_CAZACU_BARLAT_MAGNESIUM) to be incorporated into the library of constitutive materials equations for LS-DYNA®, specifically applied to die-cast AM60B. USAMP partners will have exclusive access to this function for a limited time period until it is made generally available by LS-DYNA®.

Future Directions

- This project concluded all technical work on March 31, 2012. In August 2011, the USAMP was notified of DOE Award DE-EE0005660, also directed toward magnesium-intensive front end demonstration structures. Much of the background information obtained in this project is expected to carry over to this new effort – in particular the structural design employing a central AM60B super-vacuum, die cast “shock tower,” as well as upper and lower rail structures of materials (to be determined), including advanced wrought alloys of magnesium, as well as typical current automotive structural materials including galvanized high-strength, low-alloy steel and wrought aluminum.

Technology Assessment

- Target: Develop a “demonstration” structure for exhibiting the capabilities of various enabling materials technologies (e.g.; component fabrication, joining and surface treatment) for manufacturing, as well as providing a means to assess durability (including ultimate loads, fatigue and corrosion resistance) of a model magnesium-intensive subassembly, as might eventually be employed in automotive manufacturing.
 - Achievement: The structure, as designed for this work, achieved the original objective.
- Target: Improved CAE modeling of die-cast AM60B in high strain rate (crash) was demonstrated for LS-DYNA using new material models developed by this project.
 - Achievement: Validation took the form of close matching of predictive and actual deformations of model structures (crush boxes) from prior work. These improved deformation models for die-cast AM60B have been made available to the CAE community of the three OEMs.
 - Gap: Crashworthiness modeling capability for current wrought magnesium alloys selected. Materials of construction for the current demonstration, particularly wrought alloys of AM30 and AZ31 are not amenable to accurate CAE crash analysis (e.g., by LS-DYNA) in high-rate deformation due to issues of both tensile/compressive yield point asymmetry and intrinsic textures introduced by the several forming processes. This is a fundamental technical challenge for current wrought magnesium alloys in general.
- Target: Predictive capability for fatigue failures at joints in assembled structures. The design intent for the “demonstration” structure was to focus mechanical failures (e.g., overload and fatigue) at joints formed either by SPRs or friction-stir linear welding. The approach was predicated on first establishing durability behaviors of the joint types themselves on coupons of well-defined geometry (e.g., lap shear or ‘T’ peel), and then seeking CAE formalisms which permitted the calculation of local stresses at joints in more complex structures – viz. the “demonstration.” In this manner, there is an ability to determine the relevant local stresses leading to joint failure.
 - Achievement: Testing and correlation studies were completed.
 - Gap: At this point, predictive capability for joint failure in fatigue (particularly SPRs) is poorly correlated with experimentation. Although correlation is somewhat better for linear friction stir welds (i.e., within an order of

magnitude for certain geometries), there still remains an issue of the remnant pinhole as a fatigue initiator. There are technical approaches to negate this feature, but as of yet, not verified. The capability to focus failures at joints has not been realized, and durability studies still indicated some failures occurring in the base metals.

- Target: Corrosion protection capability for assembled “demonstration” structures that meets or surpasses OEM cyclic corrosion test requirements for body structures.
 - Achievement: For this target, a commercial supplier (B. L. Downey Co., of Broadview, IL) was enlisted to provide metal cleaning, pretreatment with Henkel Alodine®5200, and topcoating with PPG 590-534 electrocoat. OEM cyclic corrosion tests were conducted on these structures. Alternative coating providers were also engaged, however, satisfactory coatings were not produced in time for corrosion measurements to be conducted.
 - Gap: Galvanic corrosion at coated SPRs is evident in OEM cyclic tests of coated structures. This suggests work still to be done on satisfactory surface treatments to steel fasteners as may be used. A corrosion phenomenon associated with difficulty in removal of organic lubricant layers from wrought materials was observed but not overcome within this project’s time frame. Peculiarities of the electrocoat process with regard to magnesium alloy materials were also observed and not fully understood within the time frame of the project.
- Target: Predictive capability for the performance of surface treatment “systems” for the corrosion protection of magnesium. Even a relatively small number of potential surface processes (e.g., metal cleaning, pretreatment and topcoating) can yield a myriad of possible combinations yielding differing corrosion protective capabilities.
 - Achievement: Early failure of several coating systems were predicted by the AC-DC-AC method and confirmed by later testing.
 - Gap: Corrosion protection evaluation methodology. A simple, rapid, reliable, inexpensive and transportable technology is required to rapidly assess long-term coating systems performance for magnesium alloys.

Introduction

Details of this project have been previously reported and are not reviewed here. A review article by Luo et al., appearing in *Light Metal Age* magazine of April 2012, provides a snapshot of the project and its history. The objectives of the current work were to construct and test multiple copies of “demonstration” structures which serve as the platform for enabling manufacturing technologies for magnesium-intensive automotive substructures. The balance of this report covers several details of the testing procedures and their outcomes following production of the demonstration structures.

Approach

The approach to this project is included in the review paper cited above. In general, a two-pronged approach was developed: 1.) continuation of “knowledge based” disciplines such as fatigue; durability; corrosion; and noise, vibration, and harshness and 2.) the advancement of particular manufacturing technologies as could be incorporated in actual magnesium-intensive substructures. The manufacturing enablers included, for example: advanced die-casting processes for magnesium, warm sheet forming, extrusion, joining technologies (friction stir welding and SPRs) and surface finishing. Additionally, a “logistics” function was initiated to handle piece parts and final assemblies, including a serialization system much like the vehicle identification numbers for actual automobiles. The “knowledge” disciplines largely incorporated testing and analysis of mechanical strength and corrosion resistance for comparison with predicted characteristics.

Results and Discussion

Task 2.0 – Design, Build and Test. Logistics for piece parts, fabrication of tooling, inventory of fabricated structures and testing were all handled by Cosma Engineering, Troy, MI. Some 211 structures were fabricated using both friction-stir welding and laser-assisted SPRs in roughly equal quantities. Structures were either designated for mechanical testing “as fabricated” or were dispatched for corrosion protective coatings, either through B. L. Downey (Broadview, IL), PPG

Industries (Euclid, OH) or Luke Engineering (Wadsworth, OH). All mechanical testing (overload and fatigue) was conducted by Exova, Ltd., of Mississauga, ON (Canada). A number of completed structures still remain with Cosma Engineering in storage.

Task 2.3 – Durability and Fatigue. Figure 7 illustrates the structure layout and coordinate axes nomenclature for the various mechanical tests. A fixture “block” was designed to mount to the shock tower cap, with provisions for attachment to mechanical actuators in a test frame arrangement as shown in Figure 8.

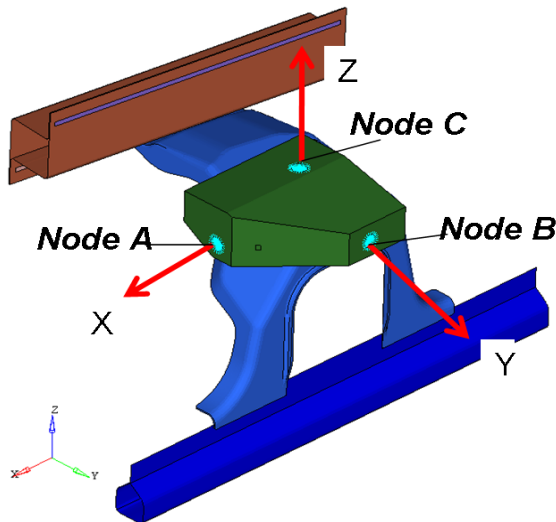


Figure 7. Coordinate axes and layout arrangement for demonstration structure mechanical testing.



Figure 8. Mechanical test rig with actuation affixed to the demonstration structure (Exova).

For fatigue testing, a compliant spacer was employed on the underside of the shock tower cap to both resist fretting at the point of attachment to the shock tower, and to assure a more distributed application of the loading to the structure itself. Testing consisted of overloading to failure in each of the three principal axes, for each version of the structure as indicated by the proposed testing layout of Table 2. The overload values were intended to provide a starting point for later fatigue measurements for the same principal axis used for the overload. Loads for fatigue testing were selected as a fraction of the load-to-failure value determined from the static overload tests. Constant amplitude tests were conducted for at least one level in each of the principal axes. Since the “Z” direction of Figure 7 is the most likely severe loading direction for a similar actual part as might be used, there was a greater focus of attention on these measurements, with most number of replicates.

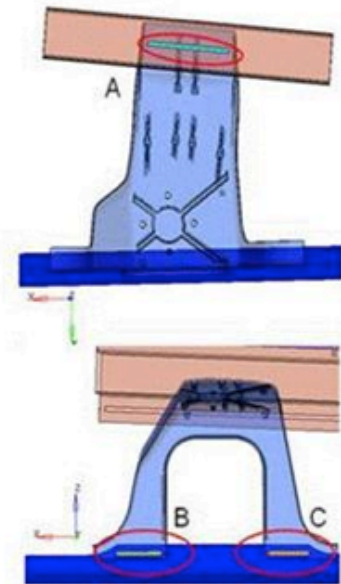
Table 2. Original mechanical testing schedule for demonstration structures.

Joining method	Overload			Fx			Fy			Fz			Combined
	Fx	Fy	Fz	C1	C2	V.A	C1	C2	V.A	C1	C2	V.A	
FSLW	2	2	3	1		1	2		2	4	4	4	2
SPR	2	2	3							4	4	4	2
SPR + Adhesive			1							1	1	1	1

Table 3 and inset figures illustrate predicted and observed fatigue failures of friction stir weldments for these structures as tested in the constant amplitude mode. Failures were only observed for the joint between the sheet-formed upper rail (box) and the shock-tower. In general, the life predictions, based on transformation of lap-shear data for friction welds to 3D finite element models for this particular joint were within an order of magnitude of the measured values. On the other hand, fatigue loading applied to the ‘X’ and ‘Y’ axes did not result in failures within the time frame of the experiments as shown.

Table 3. Comparison of predicted and measured cycles to failure for friction-stir linear welds at locations on the demonstration structures as shown in the inset figures.

Load	Sample	Location A		Location B		Location C	
		Test (cycle)	Prediction (cycle)	Test	Prediction (cycle)	test	Prediction (cycle)
7.26 KN	358	5815	2399	no failure	84	no failure	19
	315	5000					
	330	5000					
5KN	375	11328	8455	no failure	671	no failure	155
	382	9300					
2kN	340	100000	187000	no failure	109132	no failure	25269
	316	375000					



Task 2.4 Corrosion and Surface Treatment. Both friction stir linear welding and SPR (with and without adhesive bonding) demonstration structures were subjected to surface treatment processes for corrosion protection after assembly. The stipulation for processing of the SPR structures was that all component parts were also pretreated prior to assembly using Henkel Alodine® 5200, which was to aid in both the laser preheating process as well as adhesive bonding. SPR component parts were pretreated by the B.L. Downey Company of Broadview, IL. The final surface protection treatments were as follows:

- 1.) Alodine® 5200 pretreatment with PPG 590-534 cathodic electrocoat – B.L. Downey, Broadview, IL
- 2.) PPG XBond® 4000 pretreatment with either PPG P 6000 CX or 590-534 electrocoat, as provided by PPG Industries, Euclid, OH.
- 3.) MagPass® pretreatment with PPG (either P 6000 CX or 590-534) produced jointly by Luke Engineering of Wadsworth, OH and PPG Industries.

For the SPR structures, it will be noted that a second pass through Alodine® 5200 resulted due to the pretreatment step for the component parts. Downey had adapted their processing line so as to avoid the usual deoxidation step on these structures, resulting in a potentially more robust pretreatment layer.

By the conclusion of technical work, PPG had been unable to treat structures in time for corrosion testing by the OEMs. A number of unexpected problems that had not been seen with previous coupon coating had occurred during coating of the actual demonstration structures at both Luke Engineering and PPG. Luke Engineering was unable to implement MagPass® particularly on the sheet-formed rail, and PPG had a number of difficulties in applying the electrocoat, also noticeably on the sheet-formed box. Downey was able to provide coated structures, however, the appearance of the sheet-formed rail suggested a possible e-coat “rupture” phenomenon which results when gas evolution during the coating breaks through the depositing polymer layer. The Downey coatings on the die casting and extrusion parts, however, appeared normal. Luke was only able to produce MagPass®-coated upper rails by manually removing the smut layer following the deoxidation step in phosphoric acid. This phenomenon is being attributed to a “baking” of the sheet-forming lubricant onto the surface during warm forming, which was not easily removable by the cleaning and processing steps of MagPass®. Further study of this effect is planned for the follow-on project.

The OEM corrosion test cycles employed for evaluation of the coated assemblies included GMW-14872 (GM), L-467 (Ford) and SAE J-2334 (Chrysler). Details of exposure times, electrolyte composition, temperatures and relative humidity are summarized in Table 4.

Table 4. Summary of OEM cyclic corrosion test conditions.

Test Feature	Units	OEM and Test Designation		
		Chrysler SAE J2334	Ford L-467	GM GMW14872
Electrolyte				
NaCl	wt %	0.5	0.5	0.9
CaCl ₂	wt %	0.1	0	0.1
NaHCO ₃	wt %	0.075	0	0.075
Liquid immersion or spray cycle				
Relative humidity	%	100	100	45
Temperature	°C	N/A	25	25
Time	hours	0.25	0.25	8
Drying/Drain Off				
Relative humidity	%	50	70	30
Temperature	°C	60	50	60
Time	hours	15.75	18	8
Humidity Exposure				
Relative humidity	%	100	95	100
Temperature	°C	50	25	49
Time	hours	8	5.75	8
Duration				
(this experiment)	weeks	24		10
	cycles	120	30	56

The corrosion exposures here were further complicated by the desire to complete technical work on this project by March 31, 2012, which in some cases did not permit full test exposures as would normally be specified by the manufacturers. Uncoated structures (e.g., friction stir welded (FSW) structures) exposed to all of the OEM cycles exhibited observable corrosion product, especially for the sheet-formed box of AZ31, which has typically shown poor corrosion resistance. In some instances, the galvanized steel test plate affixed to the shock-tower cap exhibited white corrosion product (due to the zinc) as well as red rust at cut edges.

Some of the visual test results are compared in Figure 9. In general, for all OEMs, the sheet-formed rail (AZ31) seemed to exhibit the least resistance to corrosion attack, while the die-cast shock tower was typically better in resisting formation of visible magnesium corrosion product. Corrosion product was typically seen at the “head” end of self-piercing rivets, and usually resulted in coating delamination and increased local attack in that area.

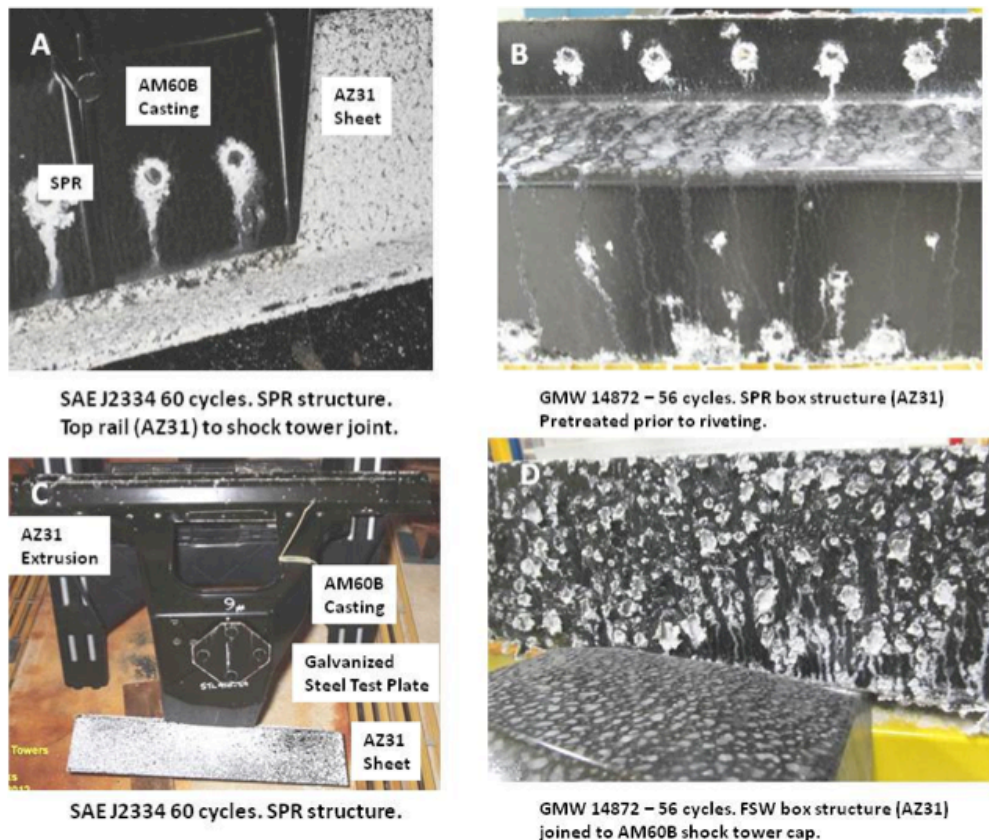


Figure 9. Visual comparison of several OEM cyclic tests of structures coated by B.L. Downey using the Henkel Alodine 5200 pretreatment and PPG 590-534 cathodic electrocoat topcoat.

In the SAE J2334 testing (Chrysler), the pretreated AZ31 box structure joined with SPRs actually appeared worse in visual corrosion than did the FSW assembly, which had no prior pretreatment before joining. The SPR box structure and joints with AM60B are illustrated in Fig. 9-A and C. Conversely, GMW14872 yielded an opposite result inasmuch as the FSW assembly showed markedly more general corrosion than did the riveted assembly, which had received the additional pass through Alodine® 5200. The riveted assembly did, however, exhibit the localized attack at the rivets as mentioned previously. The riveted structure following 56 cycles of GMW14872 is shown in Fig. 9-B, while the friction welded structure is shown in Fig. 9-D.

The relatively poor showing by the Downey-processed AZ31 was later found to have been forewarned by the coatings evaluation studies at North Dakota State University. Unfortunately, given the processing issues with PPG and Luke Engineering, there were no alternative coatings on demonstration structures to evaluate for comparison. North Dakota State had been tasked with continuing study of an AC-DC-AC electrochemical method to deduce breakdown of organic coatings on pretreated magnesium surfaces (Song et al., 2011). This was particularly challenging, since many of the coating combinations developed (i.e., metal pretreatment and polymeric topcoating) were resistant to efforts to promote breakdown by application of the cathodic DC bias which is a requisite for this approach. An alternative approach developed during this work, however, employed non-electrically biased exposure to more concentrated salt solutions according to ASTM B-117 (i.e. 5% sodium chloride) which prompted measurable decay of the low-frequency coating impedance in a greater number of coating systems, permitting some form of ranking. Work at North Dakota State also revealed a lack of correlation between polymer undercutting attack with corresponding de-adhesion of paint layers (i.e., ‘scribe creepback’) versus moisture ingress through polymer topcoats resulting in more uniform corrosion of the underlying metal.

Figure 10 illustrates the relative breakdown characteristics under the AC-DC-AC protocol for two B.L. Downey-coated test plates of AZ31 and AM60B, as well as more durable coatings of MagPass® with the powder epoxy topcoat on AZ31 and AM60B at two different thickness levels. The initial AC impedance of the MagPass®-treated coupons seemed to be unaffected by variables of substrate and coating thickness, and furthermore was not degraded by cathodic polarization, even up to as much as 8 volts. The electrocoated coupons from Downey, on the other hand showed immediate breakdown under cathodic polarization of 5 volts, the coating on AM60B being slightly more durable than the AZ31. The SAE J2334 electrolyte, detailed in Table 4, was employed in these measurements.

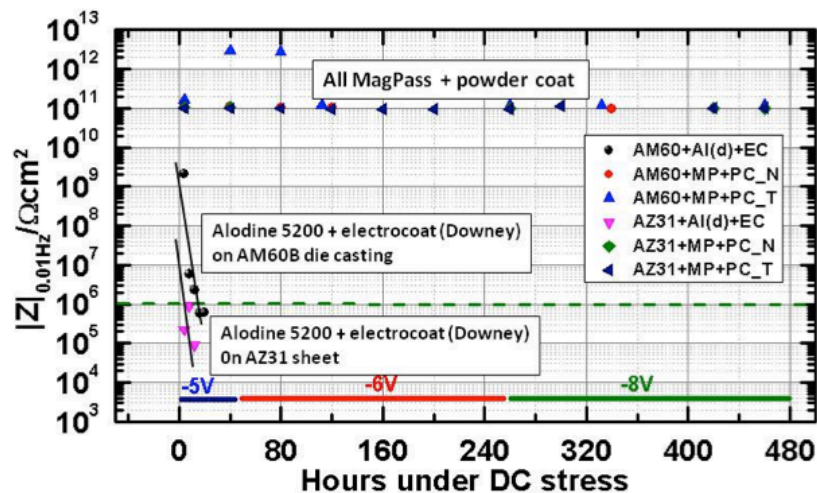


Figure 10. Comparison of AC-DC-AC EIS breakdown behavior of electrocoated (B.L. Downey Co. processing) vs powder coated materials with a MagPass pretreatment.

The necessity for probing at least two mechanisms for coating breakdown and corrosion protection can be seen from Figure 11, which contrasts the AC-DC-AC results from the “benchmark” process, used on the Ford F-150 radiator surround, with coupons identified as “baseline” which represented an attempt to recreate this process in the laboratory. The ‘benchmark’ process was tailored for AM50, and includes metal deoxidation with acetic acid, pretreatment with Alodine®5200, extensive baking and degassing, epoxy powder coat, followed by a lengthy thermal fusion step (Balzer et al., 2003). A limited number of samples of this process on AZ31 remained from prior work. Figure 11 illustrates two contrasting behaviors of the benchmark and baseline process on AZ31. The AC-DC-AC results suggest more rapid degradation of the baseline coating on both AM60B and AZ31, with the coating on AZ31 actually being slightly more durable in this protocol. The ‘benchmark’

process on AZ31, produced from the actual process line showed no proclivity for breakdown under the cathodic voltages applied, using the SAE J2334 electrolyte. This situation, itself, was unlike the breakdown of the same coating at -4 V, using ASTM B-117 electrolyte as observed previously (Song et al., 2011). Scribe undercut measurements on just AZ31 following exposure to 74 cycles of SAE J2334, on the other hand, suggested less durability of the benchmark process when compared to the laboratory baseline. Thus, a particular coating system may be durable to moisture ingress but fail due to undercut attack. This result was an unexpected turn of events and implies that coating systems must be subjected to more than a single test protocol in comparing overall behaviors.

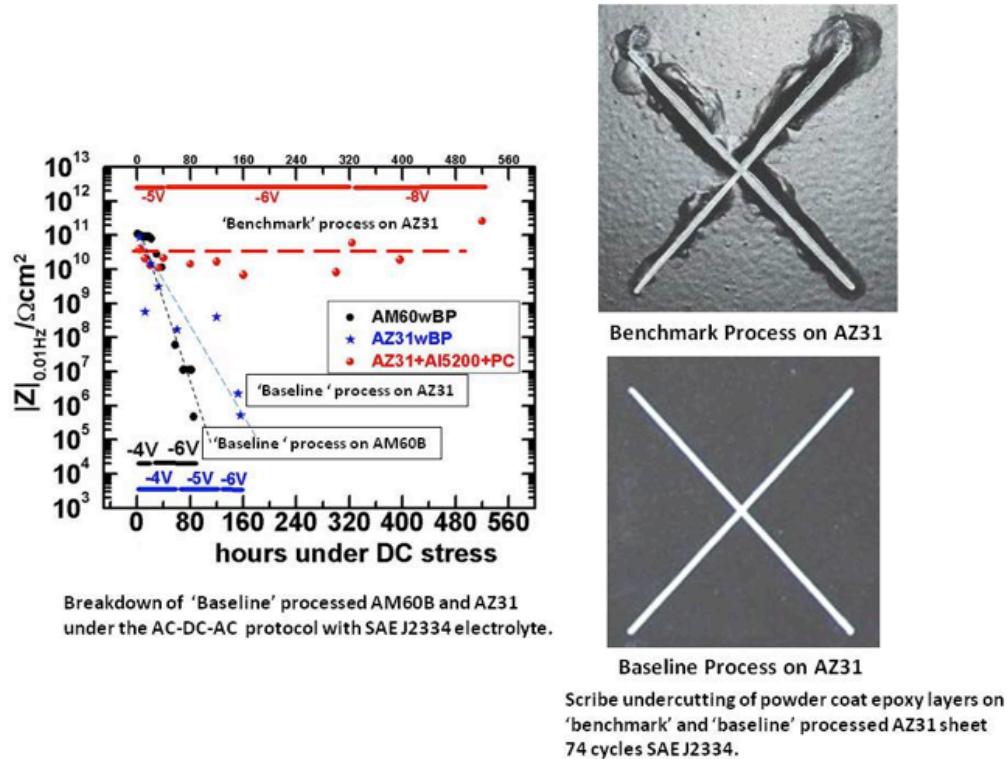


Figure 11. Comparison of AC-DC-AC performance of 'benchmark' and 'baseline' processes employing Alodine 5200 and powder epoxy topcoat, with scribe undercut results after 74 cycles of SAE J2334.

Technology Transfer Path

The outcomes of efforts in Task 2.1 (Crashworthiness), i.e., material models for deformation of AM60B in high strain-rate situations, have been integrated into the LS-DYNA library and are available to the technical community using this software.

Performance information on the laser-assisted SPR process has been acquired and details of implementation of this process reside with the supplier, Henrob Corporation. The strength of SPR joints in magnesium intensive structures was shown to be excellent, and prompts further investigations as to elimination of the galvanic corrosion concerns, and alternatives to laser processing.

FSW is available in the marketplace, and presumably, data from this project encourages its further development as a viable joining technique for magnesium-to-magnesium joints.

The super vacuum die cast process will continue development under the aegis of CANMET in Hamilton, ON, with technical support of prototype tooling and vacuum hardware from USAMP.

The USAMP inaugurated the first U.S. implementation of the MagPass® pretreatment process, which is now available from Luke Engineering. Peculiarities of the cathodic electrocoat process for certain grades (e.g., AZ31 warm-formed sheet) are now appreciated and suggest opportunities for further developments.

Conclusions

In the concluding period of this project, emphasis was on conduct of mechanical testing and corrosion performance of the assembled and coated demonstration structures. These activities produced considerable data which are only highlighted in this report. Efforts on magnesium-intensive demonstration structures will continue in the follow-on project.

Presentations/Publications/Patents

Luo, A. A., Quinn, J.F., Wang, Y.-M., Lee, T.M., Verma, R., Wagner, D.A., Forsmark, J.H., Su, X., Zindel, J., Li, M., Logan, S.D., Bilkhu, S., McCune, R.C., “The USAMP Magnesium Front End Research and Development Project”, *Light Metal Age*, April 2012, pp. 54-58.

Zhu, F., Chou, C.C., Yang, K.H., Chen, X., Wagner, D., Bilkhu, S. and Luo, A.A., “Calibrating Material Parameters to Model the Thin-Walled Components Made of Die Cast AM60B Magnesium Alloy”, *International Journal of Crashworthiness*, **2012**, 17 (5), pp. 540-552.

H.A. Patel, H.A., Rashidi, N., Chen, D. L., Bhole, S.D., and Luo, A. A., “Cyclic Deformation Behavior of a Super-Vacuum Die Cast Magnesium Alloy”, *Materials Science and Engineering A*, **2012**, 546, pp. 72-81.

Zhu, F., Chou, C.C., Yang, K.H., Chen, X., Wagner, D. and Bilkhu, S., “Application of AM60B magnesium alloy material model to structural component crush analysis,” *International Journal of Vehicle Safety* (in press).

Jiang, C.; Hunt, J.; Su, X.; Forsmark, J.; Khoshrovaneh, A.; Quinn, J.; Zhang, L. Fatigue Performance of Magnesium Alloys - Self-Piercing Riveted Joints. In *Proceedings of Sheet Metal Weld Conference XV*; American Welding Society, **2012**.

Carlson, B.; Verma, R.; Yuan, W; Szymanski, B. Friction Stir Welding of a Magnesium AZ31 Sub-Assembly. In *Proceedings of Sheet Metal Weld Conference XV*; American Welding Society, **2012**.

References

Balzer, J.S., Dellock, P. K., Maj, M. H., Cole, G.S., Reed, D., Davis, T., Lawson, T. and Simonds, G., “Structural Magnesium Front-End Support Assembly,” Society of Automotive Engineers, Warrendale, PA, **2003**, Paper 2003-01-0186.

Song, S., McCune, R. C., Shen, W., and Wang, Y.-M., “Use of an AC/DC/AC Electrochemical Technique to Assess the Durability of Protection Systems for Magnesium Alloys,” in *Magnesium Technology, 2011, Magnesium Technology 2011*, Wim Sillekens, Sean R. Agnew, Suveen N. Mathaudhu, and Neale R. Neelameggham, eds., **2011**, The Minerals, Metals and Materials Society, Warrendale, PA, pp. 531-535.

Integrated Computational Materials Engineering (ICME) For Magnesium (AMD703)

Principle Investigator: Mei Li, Ford Motor Company
(313) 206-4219; fax: (313) 323-1129; e-mail: mli9@ford.com

Principle Investigator: Alan A. Luo, General Motors Research & Development Center
(248) 912-8254; fax: (586) 986-9204; e-mail: alan.luo@gm.com

Technology Area Development Manager: William Joost
U.S. Department of Energy
1000 Independence Ave., S.W., Washington, DC 20585
(202) 287-6020; fax: (202) 856-2476; e-mail: william.joost@ee.doe.gov

Contractor: United States Automotive Materials Partnership LLC (USAMP)
Contract No.: DE-EE0003583

Abstract/Executive Summary

This project, begun in 2007, concluded all technical work in January 2012. The project fostered a “community of practice” in the field of integrated computational materials engineering (ICME), specifically of magnesium and its alloys. The vision for the project was to create such a community with sufficient breadth to cover a wide range of topics from atomistic and first principles calculations through metal forming by die casting, sheet stamping and extrusion. The tangible objective for outcomes of the effort was the “magnesium front end” of the companion USAMP AMD604 and 904 projects. Achievements over the entire period of performance included atomistic calculations of defect energies in the β -phase of Mg17Al12, vacancy-solute energies of rare-earth elements in magnesium, development of self-optimizing tools for computer calculation of phase diagrams (CALPHAD), improved constitutive equations for metal stamping and extrusion, and measurement of mechanical properties, including fatigue, for a precipitation strengthened die-cast alloy (AZ91). Members and suppliers to the team met regularly over the period of work, and a special symposium, devoted to magnesium ICME, was hosted at an annual meeting of The Minerals, Metals and Materials Society in 2010. Reports and research results are archived in the USAMP “Vroom” collaborative web center, as well as the SharePoint web site hosted by Mississippi State University.

Accomplishments

- Conducted a review of all task area accomplishments in October, 2011.
- Completed “beta” site testing of the extensible self-optimizing phase equilibrium infrastructure (ESPEI) tool with Carpenter Technologies (Materials Informatics).
- Completed first principles atomistic modeling of rare earth solutes in magnesium (Northwestern University).
- Completed “phase field” modeling of the strengthening effect of β -phase precipitates in AZ91D die cast alloy (University of Michigan and Ford).
- Completed the yield strength model development for AZ91 die cast alloy (University of Michigan and Ford)
- Collaborated with Mississippi State University to generate predicted and actual mechanical failures of the AZ91D shock tower component part, in both monotonic loading and fatigue.

Future Directions

- This project concluded all technical work on January 31, 2012.
- The USAMP Magnesium Front End project with DOE (DE-EE0005660) includes an ICME task which will develop modeling of the precipitation strengthening and deformation behavior of aluminum 6061-T6, as will be incorporated in

the lower “rail,” determination of processing-structure-property relationships for a new extrusion alloy and continued analysis of the die-cast shock tower component part in both monotonic loading and fatigue – specifically for providing useful failure models to the OEM participant companies in USAMP.

Technology Assessment

The ICME of magnesium alloys is not characterized so much by a singular target, as it is in building a framework which develops databases and methodologies, with the broad objective of rapidly improving the quality and performance of objects at the engineering level, by employing scalable processing/structure/property relationships originating even at the atomic scale. In this regard, ICME will always be a “work in progress,” building on successive levels of achievement over a period of time, as data and methods are acquired. AMD703 was able to touch on only a portion of the broader challenge for application of magnesium alloys to the engineering challenges of automotive lightweighting, typified by the Magnesium Front End R&D (MFERD) coalition. Comments on achieved targets and remaining gaps are contained in the following breakdown by task area subject matter.

Target Subject and Status	Gaps Remaining
Task 1. Cyberinfrastructure: Hardware and software platforms established at Mississippi State and made available to the technical community.	Despite an initial influx of data, the scientific and technical community has been slow to build a substantial and useful repository for physical data as well as background and developmental reports from the various activities.
Task 2. First principles calculations, thermodynamics, phase diagrams and diffusion: There have been active individual activities in all sub disciplines. The ESPEI tool is a valuable addition to CALPHAD and received beta testing through this project.	Thermodynamics, diffusion and phase equilibria are a continual challenge in the development of new alloys and their processing. Correlation of calculated alloy behavior with actual experimental data is even more difficult to realize. The “gap” in this case is that neither computational nor experimental data exists for all possible combinations of constituents as may exist in any new alloy formulation.
Task 3 - Processing-Structure-Property Relationships for Extruded Magnesium Components: USAMP provided the “double top hat” extrusion profile and tooling access for modeling at Mississippi State University.	Extrusion, like sheet forming, involves the tension/compression asymmetry of magnesium, as well as texture generation and dynamic recrystallization – all of which influence final mechanical properties of extruded structures. Improved alloys are needed to reduce the influences of these factors on extruded magnesium components.
Task 4 - Processing-Structure-Property Relationships for Sheet Magnesium Components: USAMP conducted sheet forming of a stamped pan structure and employed constitutive equations of deformation which had been developed by Mississippi State University and the University of Virginia for the specific materials (AZ31). Forming predictions based on the improved constitutive equations for forming were found to be accurate and useful for the warm-forming operation.	Development of sheet alloys with less tension/compression yield point asymmetry and less texturing during the forming process. Development of sheet alloys that are formable at room temperature.
Task 5 - Processing-Structure-Property Relationships for Die-cast Magnesium Components: USAMP developed computer models for the die-casting process for the super vacuum die cast (SVDC) shock tower, including improvements in porosity due to the vacuum process. These analyses provided a starting point for calculation of multi-stage fatigue failure by Mississippi State. The project has also supported microstructural development in casting of AZ91D where precipitation of the β -phase is important for matrix strength.	Computational techniques for determination of both gaseous and shrink porosity in die castings are still evolving, and are a particular challenge due to the chaotic nature of die casting. While technologies such as SVDC may help in minimizing gaseous porosity and improve ductility, shrinkage porosity cannot be avoided, and likely limits the achievement of optimum fatigue resistance for die-cast magnesium objects.

Task 6 - Multi-Attribute Design Optimization: USAMP did not have a contribution to this task, all work being done at Mississippi State.	N/A
Task 7 - Multi-Stage Fatigue Modeling: USAMP has supported microstructural and mechanics studies of fatigue for die cast magnesium through several projects at the University of Michigan and Mississippi State. For AZ91 and AM60 die-cast alloys, porosity is the major microstructural feature limiting fatigue performance. Predictive capability for estimation of fatigue life of homogeneous, bulk materials in components is at a nominal state of development and will likely be refined as parameters relating fatigue damage to microstructural features are developed.	The greater gap exists for non-homogeneous material – e.g., die castings with variable distribution of porosity, or joint areas such as weldments and fasteners, where computer-aided engineering methods are less accurate in prediction of fatigue failure.

Introduction

Integrated Computational Materials Engineering (ICME) is a coordinated framework to develop computational approaches to materials engineering that extend over a range of length scales from the quantum level to the scale of engineering objects. It is the broad goal of ICME to provide a computational infrastructure to generate predictive approaches to the processing-structure-properties relationships in engineering materials and objects, beginning with the physical metallurgy at the atomic level. The approach, itself, is sufficiently broad that it covers many subdisciplines and research organizations working collectively. A national effort, “The Materials Genome Initiative,” seeks to develop the infrastructure and approach to the topic on the scale of grand scientific challenge, in spirit much like the human genome of years past. The work reported here has attempted to launch a smaller framework, in the spirit of ICME, aimed specifically at the physical metallurgy and processing of magnesium and its alloys.

USAMP AMD703 was launched in 2007 as a companion project to AMD604, MFERD with a focus on national and international efforts devoted to ICME of magnesium alloys. The USAMP project maintained a linkage with a similar project headquartered at the Center for Advanced Vehicular Studies at Mississippi State University, as well as efforts in China and Canada. The cooperation with Mississippi State University involved common meetings, technical discussions and sharing of materials and data, where appropriate. The cooperation with Canada and China took place in the form of the annual “3-country” MFERD meetings. The USAMP project also collaborated with researchers at the Oak Ridge National Laboratory in studies of diffusion in magnesium alloys, and with researchers at Pacific Northwest National Laboratory in the organization of data structures for ICME.

Approach

USAMP ICME of Magnesium Project (AMD703) was organized into seven Tasks as follows:

Task 1 - Cyberinfrastructure,

Task 2 - Calculated Phase Diagrams (CALPHAD), Diffusion Infrastructures and Database,

Task 3 - Processing-Structure–Property Relationships for Extruded Magnesium Components,

Task 4 - Processing-Structure–Property Relationships for Sheet Magnesium Components,

Task 5 - Processing-Structure–Property Relationships for Die-cast Magnesium Components,

Task 6 - Multi-Attribute Design Optimization, and

Task 7 - Multi-Stage Fatigue Modeling.

Results and Discussion

1. ESPEI (Materials Informatics, LLC) For the time period of this report, ESPEI was advanced by beta-site evaluation mainly through companies such as Thermo-Calc (a program participant in ICME) and Carpenter Technologies (also brought into the ICME effort specifically to evaluate ESPEI). **Figure 12** illustrates the conceptual framework for this software product, which simplifies the organization and management of thermodynamic data from various sources, which may then be used in the computer calculation of phase equilibria (CALPHAD).

Overall Infrastructure of ESPEI

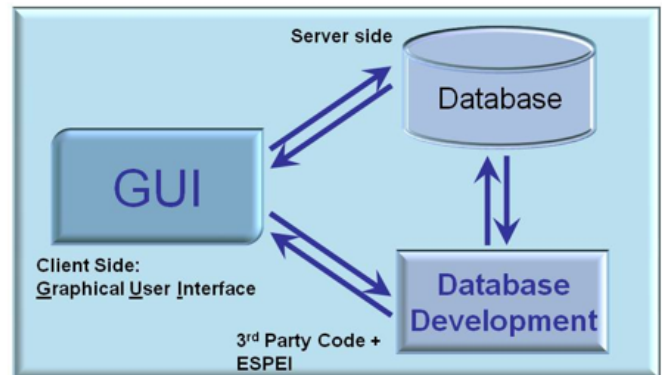


Figure 12. Conceptual layout showing the incorporation of ESPEI in thermodynamic database development for the computer calculation of phase equilibria.

2. Precipitation Strengthening of AZ91D. (University of Michigan – J. E. Allison) The focus of this work was on the development of a model for the strengthening of die-cast alloy AZ91D based on the precipitation of the β -phase ($Mg_{17}Al_{12}$) during solidification and also by heat treatment. (A separate study at the University of Michigan, under J. W. Jones, had explored the fatigue properties of AM60B and AZ91D as influenced by heat treatment.) In the current work, the microstructural features of as-cast and heat treated (solution treatment + aging) of AZ91D as produced for the project by the SVDC process, were studied by a variety of microstructural characterization tools, including optical microscopy, electron microscopy, crystallographic and elemental analysis using X-ray and energy loss spectroscopies.

Figure 13 compares the microstructural appearances of the β -phase as it is generated either discontinuously during the original solidification step (primarily at α -phase boundaries), or continuously (primarily in grain interiors) following the solution/quench/age sequence. The continuously precipitated particles are generally much finer in scale than those occurring through the discontinuous precipitation.

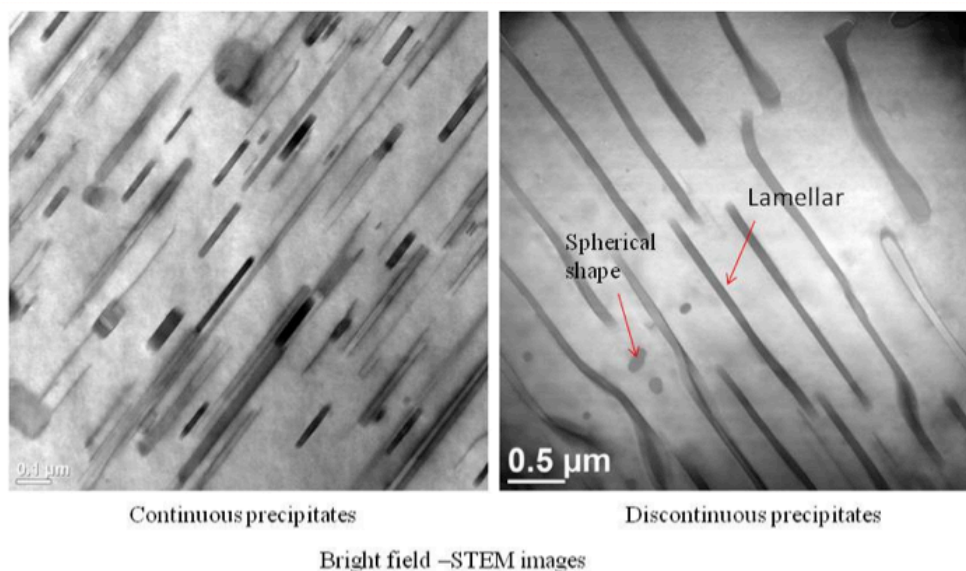
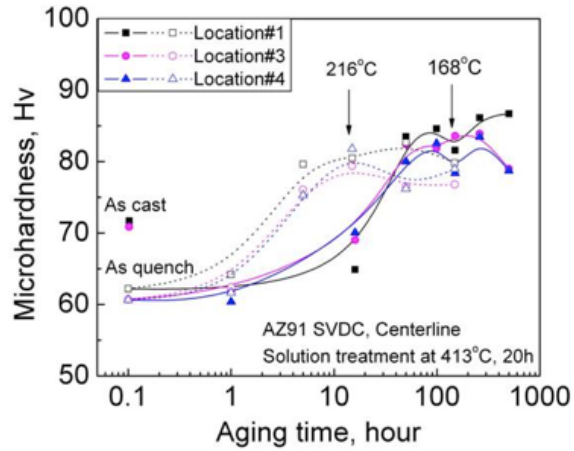


Figure 13. Comparison of TEM images of continuous and discontinuous precipitates of the β -phase ($Mg_{17}Al_{12}$) occurring in super-vacuum die cast AZ91D.

The effect of precipitation after solution treatment and quenching can be seen from Figure 14 which illustrates the development of hardness as a function of aging time for two different temperatures of investigation.

- 413°C, 20 h in argon → water quench → aging at 168°C or at 216°C.
- Peak occurs after 50 h at 168°C or after 5 h at 216°C.

Figure 14. Response of SVDC AZ91D to aging treatments at temperatures shown.



3. Fracture and fatigue behavior of a component part using multi-stage modeling. This work was conducted collaboratively between USAMP, the University of Michigan (J. W. Jones) and Mississippi State University. The objective of the study was the prediction of the locus of fracture for the three-dimensional object, viz. the AZ91D magnesium shock tower, based on microstructural, processing and deformation behavior as determined from finite element analysis. In a sense, this exercise represents a culmination of the ICME concepts wherein engineering-scale behavior is determined from a succession of analyses beginning at the microstructural level. Figure 15 illustrates the manner in which the shock tower was fixture, along with an actual image of the load frame and the MagmaSoft® computer rendering of the likely density of porosity within the structure.

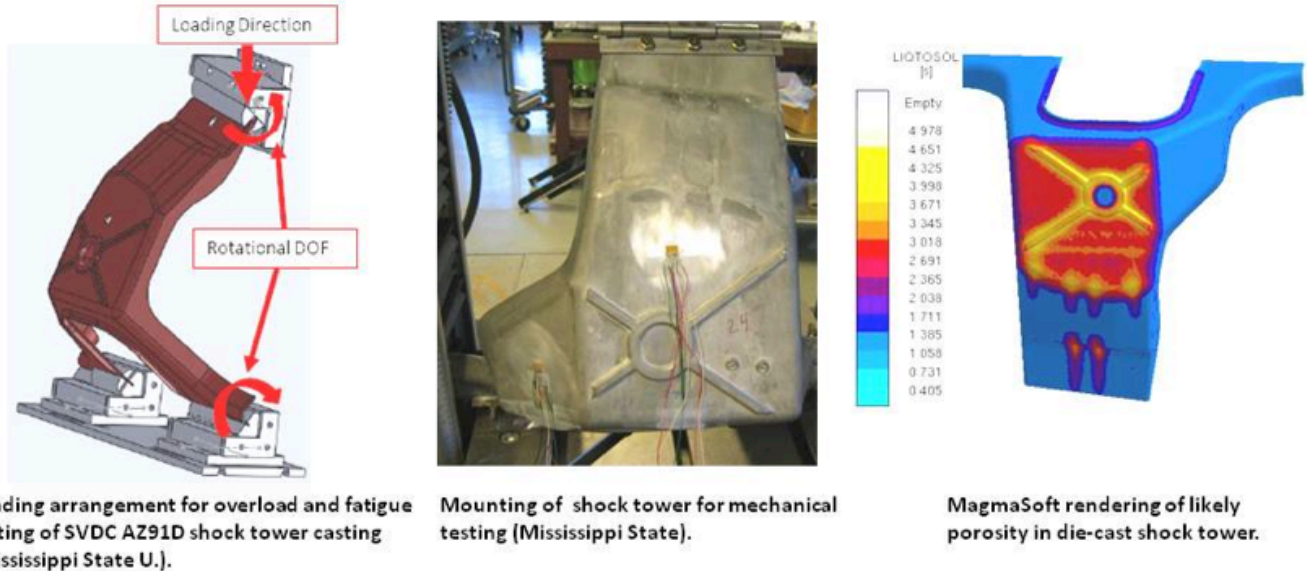


Figure 15. Fixturing arrangement for AZ91D shock tower and image of instrumented component (Mississippi State University). MagmaSoft® rendering of porosity density in the as-cast shock tower structure.

Figure 16 illustrates the finite element model for the shock tower component showing the locations of the likely failure point based on yield criteria (von Mises stress) and the location of greatest porosity from the casting process. The actual failure in monotonic loading is rather seen at point ‘A’ which is inferred from a damage generation model as would be used in ICME, coupled with use of the finite element method to determine the discrete stress/strain tensors and the porosity mapping from MagmaSoft®.

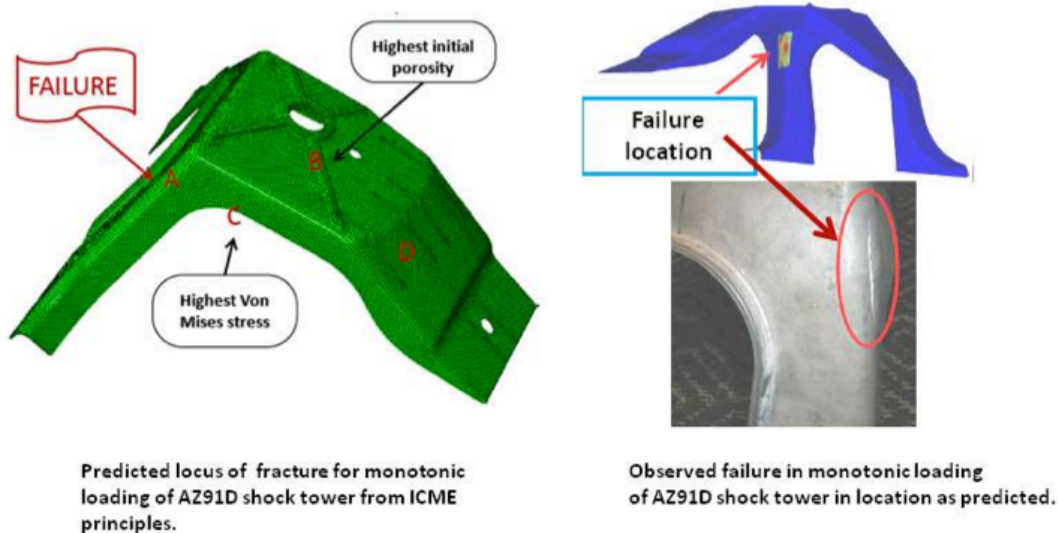


Figure 16. Prediction of the locus of failure under monotonic loading per Figure 15 of the AZ91D shock tower structure using ICME principle for damage evolution, coupled with computer modeling of the porosity distribution and finite element prediction of the stress and strain tensors under load.

Cyclic loading of the structure (e.g., fatigue) also results in ICME predictions of failure locus that are counterintuitive to both a pure materials science approach based on the extent of porosity as well as the von Mises yielding criteria in both compression and tension in reversible loading. Figure 17 illustrates the predicted failure location using ICME principles and the actual location of the first fatigue cracking from experimentation. In this regard, ICME methods have provided an insight beyond what may have been gleaned from classical materials characterization and finite element methods alone.

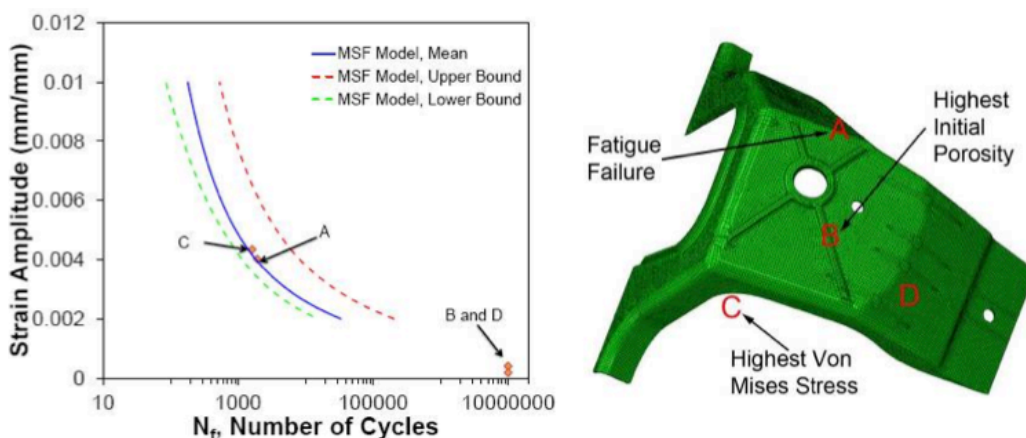


Figure 17. Strain amplitude vs. cycles to failure prediction curves from multi-scale fatigue modeling developed by Mississippi State, and locus of fatigue failure in the AZ91D shock tower as measured in the laboratory.

Technology Transfer Path

The various Task Team results outlined above are retained and are available to interested persons through the Mississippi State University SharePoint web site, for which a user account must be created. As suggested previously, ICME is not a single research outcome, but rather a framework of data and formalisms permitting characterization of engineering structures, predicated on knowledge extending down to the atomic level. ICME advances not always so much from solution of individual problems as it does from continuous expansion of data and methodologies which may be applied to a variety of engineering problem.

One enduring contribution of this effort is the ESPEI, which can be made part of Thermo-Calc, a computer-based calculation tool for phase diagrams. ESPEI was beta tested as part of this project and can be made available by the Materials Informatics Company, which developed the software under this project.

Summary

This report concludes USAMP AMD703. Over the course of five years, the project, through its various participants and suppliers, launched an effort directed toward the ICME of magnesium alloys and populated the technical literature and relevant databases with information and procedures from the work. Because ICME is also a “framework,” the project has fostered important collaborations extending basic knowledge at the atomic and microstructural level to a world of actual engineering structures, viz. the magnesium front end and its “demonstration” version. Additionally, the project has supported graduate and post-doctoral scientists in the emerging field of ICME, who may then carry the lessons learned on to similar pursuits. The project has enlisted the support of a major professional and technical society The Minerals, Metals and Materials Society in the effort, and presumably this will further advance the envisioned framework for years to come.

Presentations/Publications/Patents

Rettberg, L.H., Jordon, J.B., Horstemeyer, M.F., and Jones, J.W. “Low-Cycle Fatigue Behavior of Die-Cast Mg Alloys AZ91 and AM60,” *Metallurgical and Materials Transactions*, (in press), 2011

Agnew, S. R. “Developing a mechanism-based understanding of the forming characteristics of wrought Mg alloys,” presentation to the Mechanical Engineering Dept., North Carolina State University, Raleigh, NC, Oct. 21, 2011.

Saal, J.E. and Wolverton, C. “Solute–vacancy binding of the rare earths in magnesium from first principles,” *Acta Mater.*, **2012**, *60*, p. 5151.

Saal, J.E. and Wolverton, C. “Thermodynamic Stability of Mg-Y-Zn Long-Period Stacking Ordered Structures,” *Scripta Mater.*, **2012**, *67*, p.798 .

Shin, D. and Wolverton, C. “The effect of native point defect thermodynamics on off-stoichiometry in β -Mg₁₇Al₁₂,” *Acta Mater.*, **2012**, *60*, p. 5135.

B. Non-Destructive Evaluation

Principle Investigator: Leonid C. Lev, PhD
GM R&D
30500 Mound Rd
Warren, MI 48090
(248)807-3961; e-mail: leo.lev@gm.com

Principle Investigator: Prof. LianXiang Yang, Ph.D.
Oakland University,
Mechanical Engineering Department
2200 N. Squirrel Road, Rochester, Michigan 48309-4401
163 DHE;
(248) 370-2283; Fax: (248) 370-4416; e-mail: yang2@oakland.edu

Technology Area Development Manager: William Joost
U.S. Department of Energy
1000 Independence Ave., S.W., Washington, DC 20585
(202) 287-6020; fax: (202) 856-2476; e-mail: william.joost@ee.doe.gov

Contractor: United States Automotive Materials Partnership LLC (USAMP)
Contract No.: DE-EE0003583

Abstract/Executive Summary

A new, hybrid method for measuring the size of resistance spot weld nuggets nondestructively has been developed. It involves experimental measurement of the displacements on the weld surface using shearographic technique and numerical processing of the data using finite element method (FEM). The FEM model that produces the displacements similar to those observed in experiment has the same shape and size of the weld nugget.

A novel shearographic technique using a large shearing amount has been proposed. Several loading methods have been investigated, including vibration with an indenter attached to a piezoelectric transducer, thermal heating with a heat gun and a flash lamp, and electromagnetic force. A non-contact and easy to control device, generating electromagnetic force to excite the weld sample was developed. A two-dimensional axisymmetric model of the weld, used in the proposed numerical approach, provided good correlation between the size of the weld nuggets predicted nondestructively and measured destructively.

The proposed hybrid approach shows strong potential for development into an online NDE tool for detecting weld defects during automotive assembly.

Accomplishments

- A new hybrid nondestructive evaluation procedure based on shearographic measurements and finite element modeling has been developed to measure the size of the nuggets of automotive resistance spot welds. A large numbers of samples with different nugget sizes have been measured nondestructively using the developed procedure. The results were compared with direct measurements; good correlation has been obtained (FY 2011-2012).
- A novel shearographic technique with large shift to measure the surface displacements directly without numerical integration has been proposed and validated (FY 2011).
- The effect of the excitation method has been analyzed. The methods that were compared included vibration using an indenter attached to a piezoelectric transducer, thermal heating using a heat gun and a flash lamp and electromagnetic force (FY 2011-2012).

- An error-minimization procedure based on FEM has been developed and validated (FY 2011).
- A non-contact and easy to control device generating electromagnetic force to excite the sample has been developed (FY 2012).

Future Research Directions

This project has been completed. However, if additional funding is made available, the following aspects of the proposed technique will be developed:

- Further development of shearographic technique. Shearographic techniques have been successful in acquiring the derivatives of the surface displacements. A novel shearographic technique has been proposed to obtain the off-plane displacement directly, without numerical integration. Additional work will characterize the precision and accuracy of the proposed technique.
- A prototype of an electromagnetic force exciter has been developed. The device is capable of providing electromagnetic force by a controllable solenoid. A production-intent prototype of the exciter will be developed and evaluated.
- A new numerical minimization approach has been proposed. Its robustness, accuracy and rate of convergence will be evaluated.

Technology Assessment

- Target: The feasibility of a nondestructive test for resistance spot welds has been demonstrated. The test, capable of measuring the size of the weld nuggets has been proposed. The developed approach eliminates the need for a manual “chisel test” and enables in-line inspection of the spot welds.
- Gap: A production-intent prototype of the proposed test has to be developed, including exciter and software suitable for mathematical interpretation of the results.

Introduction

Despite intensive efforts over the last few years, there has been little progress in development of sensory systems for monitoring the quality of resistance spot welds (Todd et al., 1994). The main quality control tests used in industry are still destructive tests: chisel test and peel test (Cullen et al., 2008). As a result, excessive welds are used to ensure secure fastening of the vehicle, leading to increase in vehicle weight and cost.

The goal of this project was to demonstrate the feasibility of a hybrid approach, combining shearographic measuring technique and a numerical algorithm to determine the size of weld nuggets. In the first step, the shearographic technique is used to measure displacements on the surface of the weld caused by the controlled excitation. In the second step, the nugget size is determined by developing the FEM model of the weld that produces the same displacements as measured experimentally. As this approach required solution of an ill-posed inverse mathematical problem, a special procedure has been developed.

Approach

The experimental shearography setup with a beam splitter is shown in [Figure 1](#). A charge coupled device camera was used to record the shearogram. The camera lens was carefully selected to bring the entire sample into the field of view of the camera and to maximize its effective resolution.

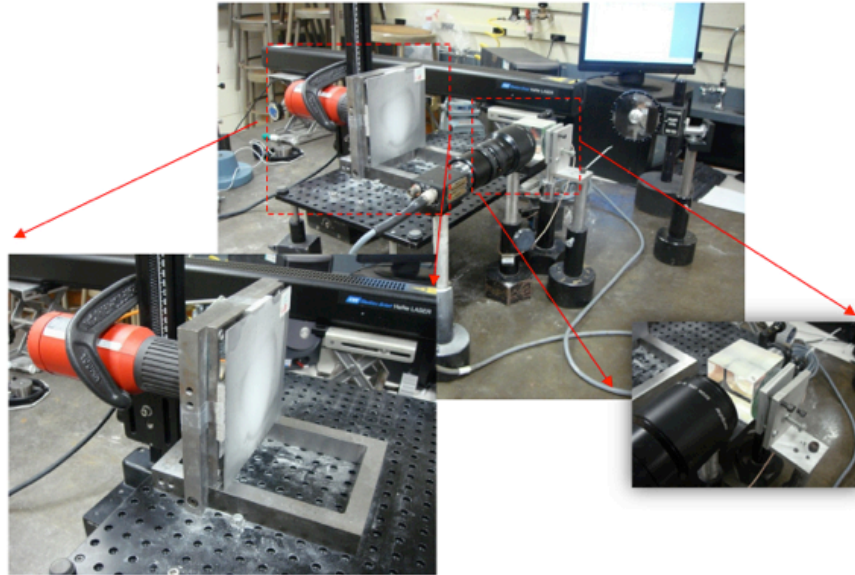


Figure 1. Experiment setup. The sample is attached to a rigid frame and subject to thermal load using a heat gun (the red cylindrical object).

The loading methods investigated included:

- static loading,
- bending,
- thermal loading,
- dynamic loading, and,
- special loading methods.

Shearography measures the first derivative of surface displacements; the direction of the derivative depends on shearing direction. To determine the displacements around the weld, two shearographic measurements are required: one with shearing in x-direction and another with shearing in the y-direction. Examples of the shearograms (fields with constant displacement gradient) are shown in Figure 2 and Figure 3.

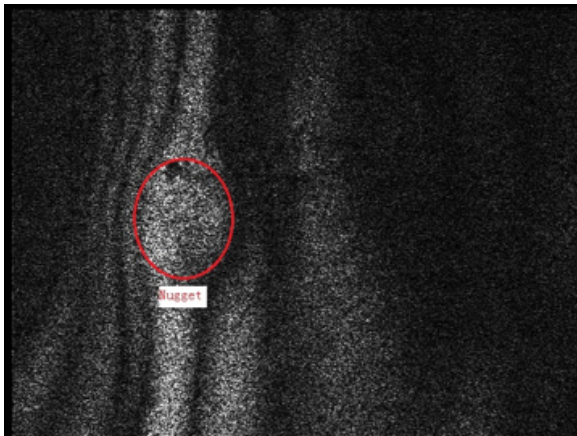


Figure 2. Shearogram with x shearing direction. Excitation frequency: 434Hz

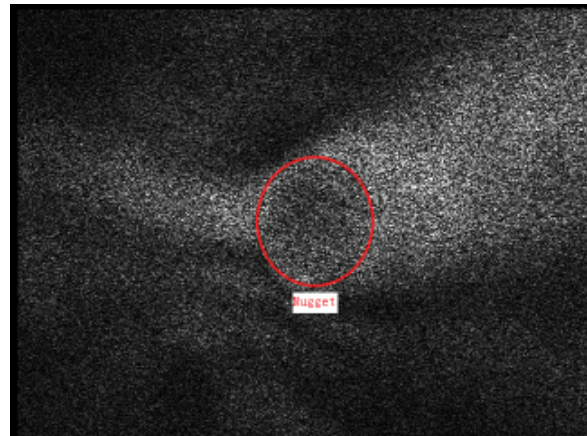


Figure 3. Shearogram with y shearing direction. Excitation frequency: 434Hz

The image in Figure 2 shows the shearogram with vibration excitation with the derivative in the x-direction, i.e., the shearing direction is parallel to the direction of vibration. The white area in the red circle is the “node line” and indicates the nugget area as predicted. The image in Figure 3 is the shearogram with vibration excitation with the shearing perpendicular to the direction of vibration.

A novel shearographic technique, so called large shearing shearography, has been proposed in the current work to measure the off-plane displacement w . In the proposed technique, the shearing distance is much larger than in the original shearography technique, as seen in Figure 4. The difference between the two techniques is illustrated in Figure 5.

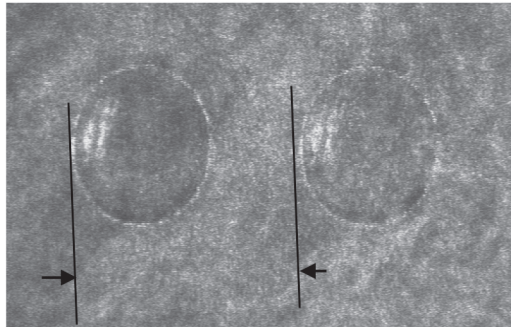


Figure 4. Image captured by a shearographic camera with large shearing.

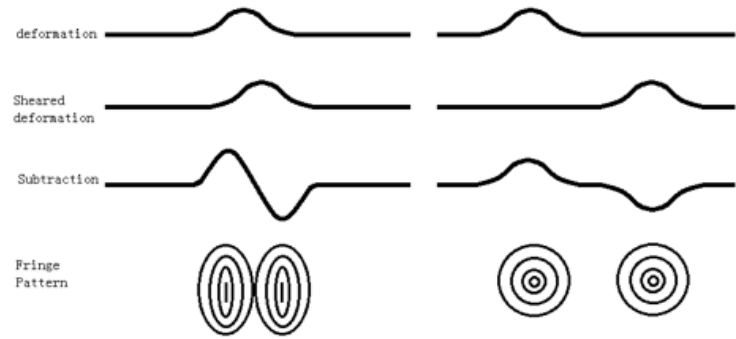


Figure 5. Differences between typical shearography and large shearing shearography.

Numerical Model Development

A mathematical model was formulated to solve the ill-posed inverse problem. The solution sought was required to satisfy both the experimental measurements and the theoretical foundation of the problem. A numerical algorithm was proposed to solve the inverse problem by minimizing the deviation between the theoretical prediction and the experimental measurements. The algorithm was tested using several examples in which the experimental measurements were simulated by the data from a separate finite element analysis.

Finite Element Analysis

In the experimental study, one of the loading methods involved a cone capable of exerting a magnetic force to pull the small plate away from the larger one as shown in Figure 6.

In this technique, one plate is loaded while the other should be free of obstruction so it is exposed to the laser light. An FEM simulation was performed to find the off-plane deflection of a weld coupon consisting of one 150 mm × 150 mm × 1.2 mm steel plate welded to a 100 mm × 100 mm × 1.2 mm steel plate with a $\phi 5$ mm nugget.

The geometric parameters for the two-dimensional axisymmetric model used in the numerical study are shown in Figure 7. The boundary and loading conditions are:

- outer edge of the larger circular plate (bottom plate) is constrained completely,
- the smaller circular plate (top plate) is to be pulled away, and
- the total applied load is 100 N applied at the outer edge of the top plate.

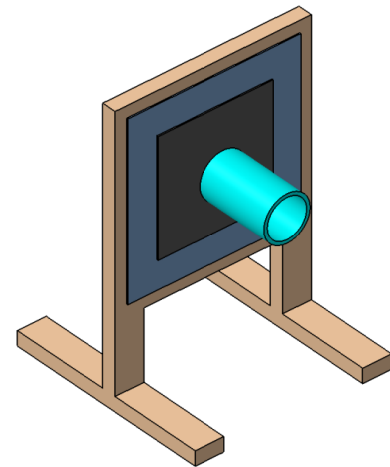


Figure 6. A magnetic force is placed in front of the smaller plate to pull it away from the larger plate. The force maybe introduced using a solenoid.

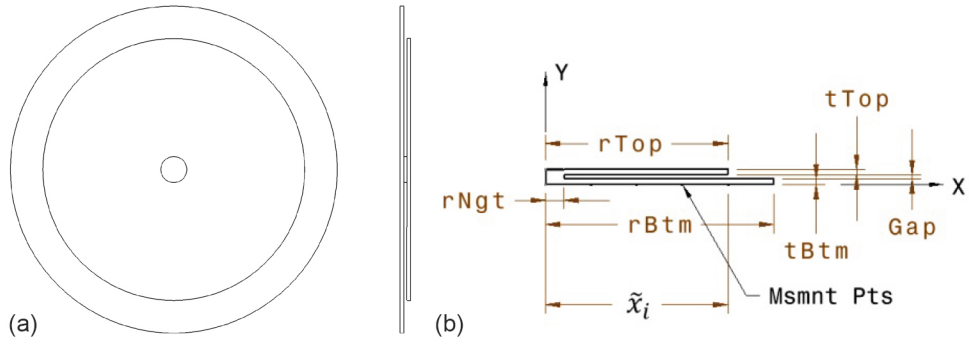


Figure 7. Projection views of the weld sample, (b) axisymmetric model with geometric parameters and locations of measurement points \tilde{x}_i .

Mathematical Formulation, Genetic Algorithm and Numerical Test

Let the radius of the weld nugget be r_N , the y-displacement at the measurement points with x-coordinate of \tilde{x}_i be \tilde{v}_i , and the calculated displacement at the measurement points be v_i . The inverse problem for the hybrid approach is formulated as a minimization as given below.

$$\min_{r_N} [\text{err}] = \min_{r_N} \sum_{i=1}^n \|v_i - \tilde{v}_i\|^2 \quad (1)$$

A genetic algorithm (Deb, 2001; Steuer, 1986) was used to solve the minimization problem. The algorithm was extensively tested. Sensitivity of the found weld nugget size to initial guess and errors in experimental measurements has been investigated.

Results and Discussion

Since the positions of the welds may vary, the location of the fringes on the shearograms may vary as well. However, as shown in Figure 8, the trend can be observed in the fringe pattern depending on the nugget size.

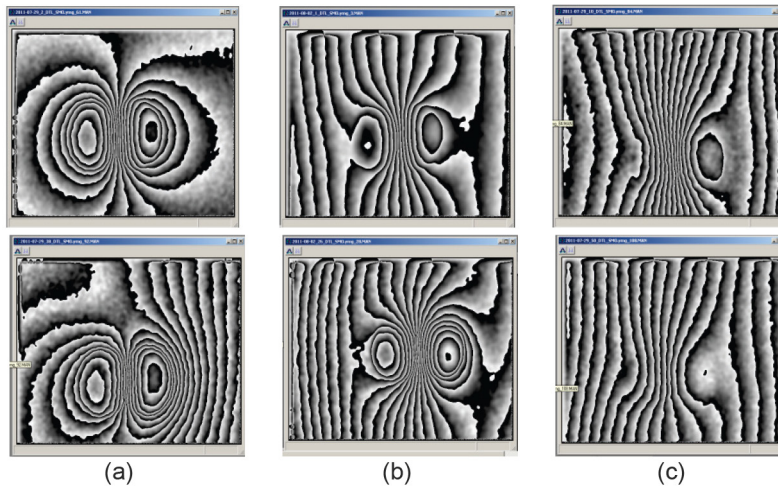


Figure 8. Results from shearogram: (a) sample with 6-mm nugget, (b) sample with 4-mm nugget; (c) sample with 2-mm nugget.

The nugget size is indicated by the red ellipses in Figure 9.

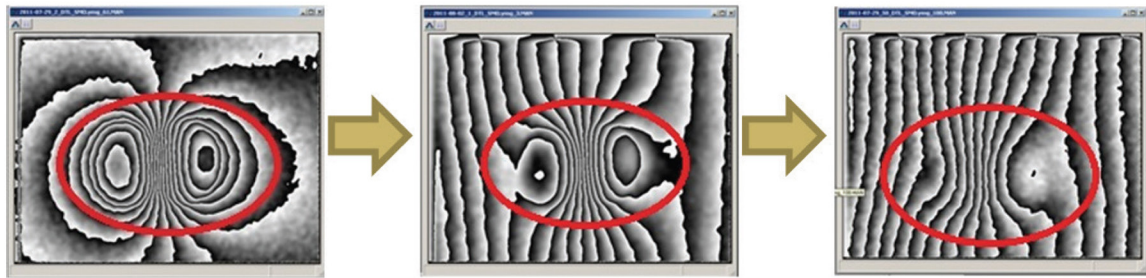


Figure 9. Nugget areas indicated by red ellipses.

To compare the results of the nondestructive measurements with the results of direct measurements, the coupons were peeled apart, measured and photographed. An example of the samples is shown in Figure 10, where each gradation of the scale is equal to 0.5 mm.

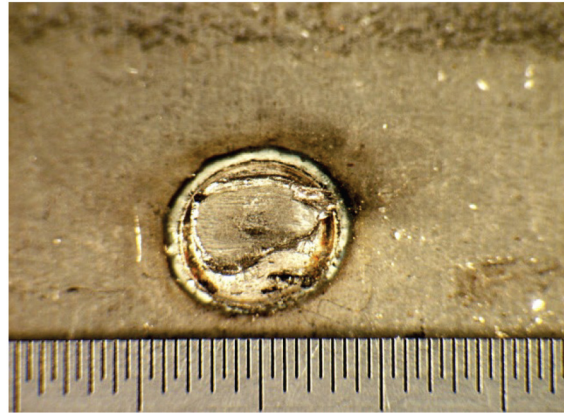


Figure 10. Sample 3A4.

Using the scale in the photographs, the size of the weld nuggets can be estimated. Table 1 summarizes the sizes and shapes of the thirteen samples. It is seen that the sample welds have different shapes: rectangle, C-shape, triangle, and circle.

Table 1. Sizes and shapes of thirteen weld samples.

No.	3A4	3A9	3B1	3B3	3B9	3C1	
Actual, mm	6 × 3	4.5	2 × 12	2 × 12	3.5	3.0	
Shape	Rect	Circ	C-Shape	C-Shape	Tria	Tria	
Optical, mm	3 × 4	4 × 3	4 × 3	3 × 4	4 × 4	4 × 4	
Shape	Rect	kidney	kidney	kidney	unclear	unclear	
	3C5	5A1	5A5	5B1	5B4	5C2	5C9
	3.0	5.0	5.5	3.0	3.0	2.5	2.5
	Tria	Circ	Circ	Circ	Circ	Circ	Circ
	3 × 4	5 × 5	5 × 4	4 × 4	3 × 4	3 × 3	3 × 3
	unclear	kidney	kidney	kidney	Rect	Square	Square

It can be observed that, except the three samples with shaded cells, the results of nondestructive evaluation of the weld nuggets are in a good agreement with directly measured weld nugget sizes.

Technology Transfer Path

In this project, the feasibility of a hybrid NDE method has been demonstrated. The approach can serve as a basis for a successful production tool, capable of evaluating the quality of spot welds in automotive structures. If additional funding were available, a production-intent prototype would be developed, leading to development of a dedicated in-line weld inspection station, to be implemented at one of the assembly plants. The developed NDE technique could assess the quality of 100% of the vehicle's welds, enabling the design of lighter yet stronger automotive structures at lower cost.

Conclusions and Future Directions

The proposed NDE technique shows promising results in evaluating the nugget sizes of resistance spot welds. The inverse problem of determining the weld nugget size from known boundary and loading conditions and additional optical surface measurement is formulated as a minimization problem which can be solved using a genetic algorithm. The proposed algorithm is tested using a number of examples with simulated experimental data. It was found that

- The initial guess of the weld nugget size has little influence on the proposed numerical algorithm;
- Analogous to other numerical schemes for ill-posed inverse problems, use of excessive experimental measurements would hamper the performance of the numerical algorithm;
- For the experimental data containing random noise and distorted experimental data the algorithm correctly predicts the trend—larger deflection with smaller weld nugget size.

Current study demonstrates that integration of a shearographic technique and the numerical method forms a powerful tool for determining weld quality.

Presentations/Publications/Patents

The following manuscript has been submitted to 2012 SAE World Congress.

- Xu, Nan; Xie, Xin; Yang, Lianxiang; and Gu, Randy Nugget Size Measurement In Spot Weld Using Shearography, *SAE Int. J. Mater. Manf.*, **2012**, 5(1), 96-101. Also presented in SAE World Congress 2012, April 2012, Detroit, Michigan.

The following abstract in the numerical algorithm has been submitted to EngOpt 2012.

- Gu, Randy J.; Yang, Lianxiang; Xu, Nan; Xie, Xin; Harmon, George; and Lev, Leonid, Determination of Weld Nugget Size Using an Inverse Engineering Technique, submitted to EngOpt 2012, 3rd International Conference on Engineering Optimization, Rio De Janeiro, Brazil. (withdrawn, to be submitted to SAE World Congress 2013)

A manuscript in the numerical algorithm is in preparation for submitting to a journal (e.g., *Inverse Problems in Science and Engineering*) for possible publication.

References & Bibliography

Beck, J. V.; Blackwell, B.; St. Clair, Jr., C. R.. *Inverse Heat Conduction—Ill-Posed Problems*, Wiley-Interscience: New York, 1985.

Cullen, J. D.; Athi, N.; Al-Jader, M.; Johnson, P.; Al-Shamma'a, A. I.; Shaw, A.; El-Rasheed, A. M. A. Multisensor fusion for online monitoring of the quality of spot welding in automotive industry. *Measurement*, **2008**, 41(4), 412–423.

Deb, K. *Multi-Objective Optimization using Evolutionary Algorithms*, John Wiley & Sons, 2001.

Gu, R. J.; Barber, G. “Determination of True Dimensional Quality and Build Errors Using Coordinate Measurement Data,” *ASME Journal of Manufacturing Science and Engineering*, **1999**, 121, 749–755.

MATLAB, version R2009b; The Mathworks, Inc., Natick, MA.

Mortenson, M. E. *Geometric Modeling*, John Wiley & Sons, 1985.

Steinchen, Wolfgang; Yang, Lianxiang. *Digital Shearography: Theory and Application of Digital Speckle Pattern Shearing Interferometry*, SPIE: Bellingham, WA, 2003.

Steuer, R. E. *Multiple Criteria Optimization: Theory, Computations, and Application*. John Wiley & Sons, Inc.: New York, 1986.

Tikhonov, A. N.; Arsenin, A. V. *Solutions of Ill-Posed Problems*. Winston: Washington, D.C., 1977.

Todd, Robert H.; Allen, Dell K.; Alting, Leo. *Manufacturing Processes Reference Guide*, Industrial Press Inc.: New York, 1994.

5. Crosscutting

A. Demonstration Project for a Multi-Material Lightweight Prototype Vehicle — Vehma International of America, Inc.

Principle Investigator: Tim Skszek
Vehma International of America, Inc.
1807 East Maple Road; Troy, MI 48084
(248) 786-2584; e-mail: tim.skszek@vehmaintl.com

Principle Investigator: Matthew Zaluzec, Ph.D.
Ford Motor Company – Research and Innovation Center
2101 Village Road; Dearborn, MI 48121
(313) 337-1098; e-mail: mzaluzec@ford.com

Technology Area Development Manager: Carol Schutte
U.S. Department of Energy
1000 Independence Ave., S.W.; Washington, DC 20585
(202) 287-5371; fax: (202) 856-2476; e-mail: carol.schutte@ee.doe.gov

Contractor: Vehma International of America, Inc.
Contract No.: DE-EE0005574

Abstract

The Multi-Material Lightweight Vehicle (MMLV) includes engineering, design, prototype build, and component/vehicle-level validation testing of a “new passenger vehicle design architecture.” The MMLV design facilitates extensive use of lightweight and high strength materials, resulting in environmental and fuel economy benefits associated with up to a **50% reduction in weight relative to a CY 2002 baseline Federal Motor Vehicle Safety Standards-compliant steel vehicle architecture**. This effort is in response to the Clean Energy Dialogue Action Plan of 2009 between the United States and Canada.

The MMLV project will produce two designs (Mach-I & Mach-II) based on a manufacturer’s production-intent vehicle and the common “new” lightweight body structure architecture. The Mach-I design will define a “new” passenger car vehicle architecture, using materials and processes that are commercially available or demonstrated using currently available materials and manufacturing processes. The lightweight body structure, chassis, bumper and closure components associated with the Mach-I vehicle design will be prototyped and integrated with the other advanced lightweight vehicle systems, including lightweight advanced powertrain; suspension; interior; seating; heating, ventilation and air conditioning (HVAC); steering; occupant safety; lighting and glass systems. The advanced lightweight vehicle will represent all of the comparative elements of the baseline vehicle and vehicle subsystems that fall within the acceptable range of the functional safety requirements using original equipment manufacturer’s (OEM) standard experimental procedures.

The Mach-II design will utilize advanced materials and manufacturing processes that have known potential but require further research and development to resolve processing and materials-related issues prior to commercialization. The Mach-II design will demonstrate the benefits that can be achieved if promising new materials and process technologies can be successfully commercialized.

Accomplishments

- The MMLV target matrix and virtual test plans have been developed and published.
- Architectural freeze of MMLV designs for body in white (BIW), cab in white (CIW), and suspension structures (FY 2012).
- Mach-I design 50% completed (FY 2012).
- Concept release of BIW, CIW and suspension structures (FY 2012).
- Lightweight aluminum/steel body design with over 30% weight reduction completed (approximately 96 kg) (FY 2012).
- Lightweight aluminum/steel closure design with over 30% weight reduction completed (approximately 30 kg) (FY 2012).
- Lightweight aluminum chassis/suspension design with over 30% weight reduction completed (approximately 34 kg) (FY 2012).
- Self-piercing rivet gun study performed on the BIW and closures (FY 2012).
- High-pressure die castings used in the BIW, CIW and suspension designs reviewed, optimized, and quoted by production sources (FY 2012).
- Initial computer aided engineering (CAE) tests completed for global stiffness, local stiffness, and durability. Full-vehicle crash analysis has 40% of tests complete (FY 2012).
- MMLV bill of materials developed and maintained (FY 2012).
- Formability studied and simulated on high-risk stampings (FY 2012).
- Reviewed and assessed designs and recommended changes to improve manufacturability (FY 2012).
- Suppliers identified and quoted prototype support of sheet and cast materials, joining and fastening technologies, and coatings/corrosion protection (FY 2012).
- Mass tracking document developed, mass status tabulated and published (FY 2012).
- The joint identification matrix established including details for all joints in the MMLV structure (FY 2012).
- A dimensional control strategy developed for the BIW, closures, and suspension structure designs (FY 2012).
- The MMLV powertrain decision confirmed (FY 2012).
- Lightweight carbon fiber composite seats with over a 35% weight reduction designed (approximately 8 kg on each of the front seats and 12 kg on the rear seat) (FY 2012).
- Lightweight instrument panel with over a 35% weight reduction designed (approximately 8 kg) (FY 2012).
- MuCell® interior trim weight reduced saving two to four kilograms (approximately 10%) (FY 2012).
- Specialized brake rotors saving over 10 kg designed (approximately 20%) (FY 2012).
- Lightweight wheels and tires coupled with the elimination of the spare tire saving over 35 kg designed (approximately 35%) (FY 2012).
- Multiple spring technologies investigated for a potential weight saving of approximately six to eight kilograms for all four coil springs (FY 2012).
- Lightweight glazing systems investigated for a potential weight saving of over 11 kg (approximately 35%) (FY 2012).

Future Directions

- Run full vehicle and trimmed-body CAE analysis for safety; noise, vibration and harshness (NVH); and durability analyses to ensure the supplied parts meets the same performance as the baseline manufacturer's production intent vehicle while minimizing mass.
- Further refine closures and chassis component designs to meet stiffness, strength, and durability performance criteria of the baseline production intent vehicle's future while minimizing mass.
- Finalize the material suppliers and consequently material grades and sheet thickness.
- Finalize the joining suppliers and consequently joint development.
- Make common the joint identifications to perform the BIW assembly with minimum number of self-pierce riveting (SPR) guns.
- Mach-I design 100% complete 1/14/2013.
- Order the long lead tooling and material ordered for prototype build by 1/4/2013.
- Determine further mass reduction of interior and powertrain designs in three categories: (1) include in prototype vehicles, (2) include in design of possible prototype, and (3) include in design of possible prototype with available funds and engineering resources. Review parts list from baseline manufacturer's production intent vehicles to identify further weight reduction opportunities among components weighing one to five kilograms.

Technology Assessment

- Target Mach 1 Design: Achieve between 37 to 40% mass reduction as compared to the CY 2002 baseline vehicle.
- Gap: Current design is at 20% mass reduction as compared to the CY 2002 baseline vehicle. Mass reduction development is continuing with updated CAE crash analysis, but using currently available funding for producing five vehicles has limited the possible mass reduction. Additional mass reduction components could be realized in a high volume engineered production vehicle where all components can be scrutinized for weight reduction opportunities.
- Technology target: Magnesium sheet and castings could be used to a greater degree in the MMLV Mach I design, but magnesium alloys currently available have specific challenges in stamping and, when used in the load path, have strength that is strain-rate dependent. Further development and processing of magnesium and magnesium alloys will allow increased usage in the future.
- Technology target: In many cases, BIW, closure, and suspension structure targets are stiffness-driven in order to maintain a customer-accepted level of NVH, ride and handling performance. If the structure designs were strength-driven and stiffness was not the primary target, weight reduction opportunities would be greater using the same aluminum alloys that are currently specified for MMLV Mach I designs.
- Target Mach 1 Design: Achieve advanced light weight vehicle that meets the comparative elements and engineering performance of the baseline vehicle and vehicle subsystems fall within the acceptable range of the functional safety requirements using OEM standard experimental procedures.
- Gap: Initial assessment shows that there is no gap at this time

Introduction

Due to government regulations on vehicle fuel economy over the next several years, the automotive industry is always looking at weight reduction initiatives to increase vehicle mileage. Reduction in overall vehicle weight is one of the best ways to reduce the overall vehicle fuel economy. Developments in body and chassis designs using aluminum material and high strength steels have given the automotive industry tools to help with this vehicle weight reduction. Developments in powertrain efficiency and downsizing, along with advances in interior trim materials and glazing, have also reduced the weight of components in automotive vehicles. Combining all of these production intent technologies in the design of one vehicle should provide a directional weight target that should be attainable in the near future with some cost increase while meeting all engineering performance metrics and customer expectations.

Approach

For body and closures, design techniques were used with aluminum material as the main weight reduction enabler. Dual phase (DP) and ultra-high strength steels (UHSS) chosen as the material in the major crash load paths, see Figure 1, for maximum energy absorption and strength considerations.

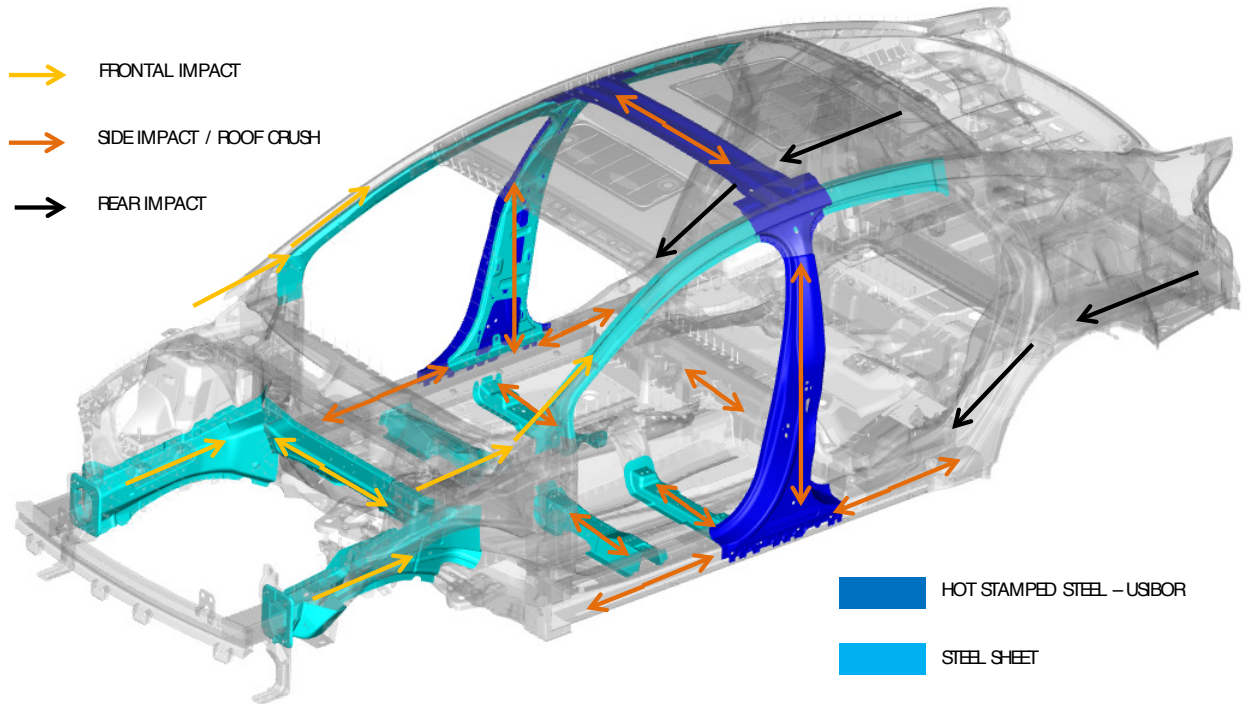


Figure 1. Major crash load paths.

Assembly techniques for joining aluminum and aluminum/steel were developed using production intent methods. SPR, as shown in Figure 2, were targeted as the main joining method for assembly since it could be applied on similar and dissimilar material joints.

Flow drills, screws and single-sided rivets will also be used on a limited as needed basis. For chassis, design techniques include aluminum castings/extrusions and a Metal Inert Gas-welded assembly as a main weight reduction enabler.

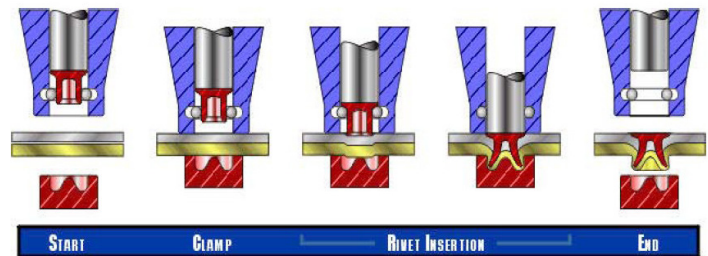


Figure 2: Self-pierce riveting process.

The BIW structure and chassis was refined to meet the global-local stiffness and the modal performance of the baseline manufacturer's production-intent future vehicle while minimizing the mass working towards a more viable concept design. Formability studies of the critical stampings and castings were performed to confirm feasibility of the design put forth by the engineers. The assembly process was drafted and a plan was developed to assemble the vehicle for both prototype build and production intent. The dimensional strategy was developed defining the major A – B datums. Slip planes were defined for assembly feasibility at the module level. Material suppliers were engaged to assure availability of the proposed material grades in steel and aluminum. Joining and fastening suppliers were engaged to develop the joining strategy for the multi-material BIW structure.

The MMLV prototype vehicles will be powered by a 1.0 liter I-3 gasoline engine equipped with direct injection and a turbo charger. This down-sized and boosted engine will be coupled with a six-speed manual transmission for the drivable prototype vehicles. The Mach I design includes a lightweight automatic transmission for equivalence with the 2002 baseline vehicle. However, electrical system incompatibilities and timing would make including the automatic transmission in the drivable prototype vehicles prohibitively costly. The 1.0 liter I-3 engine coupled with a six-speed manual transmission will be a future

high volume production powertrain making integration electronics and calibration feasible within the time frame and funding available for the MMLV prototype vehicle. The driveline system will be front wheel drive. Lightweight half shafts are being investigated for drive train application.

Additional areas of weight reduction will be considered and are discussed below.

Results and Discussion

BIW, Closure, Chassis

In FY 2012, a design concept including the BIW, closures, and structural chassis was created for an MMLV based on the following: current manufacturer's production sedan weight distribution, material strategy, weight strategy, cost, assembly strategy, dimensional plan, slip planes, and joining strategy. CAE virtual analysis was conducted to help optimize the weight of the design concept to validate and release a prototype design for vehicle build. Three stages of analysis were conducted to optimize the BIW, closures, and chassis design: (1) NVH analysis for vehicle structure on BIW, closures, and chassis; (2) fatigue analysis using the current loading aspects of the current manufacturer's production vehicle; and (3) engineering analysis of front, side, and rear safety impact requirements. For the fatigue analysis stage, direction was to assume 20% reduction in durability loads due to a reduced-weight vehicle. The performers for this project discussed and finalized preset targets for all CAE analysis based on current vehicle or current manufacturer's directional requirements.

The MMLV design for BIW, closures and chassis meet all of the targets set forth for the project at this time for Stage 1 and 2. Stage 3 structural impact analysis is ongoing and will be complete by the first quarter of FY 2013 possibly allowing an additional mass reduction to the BIW structure.

Powertrain, Driveline, Interior, and other Systems

The powertrain selection has been finalized as discussed in the "Approach" above.

Interior and other systems weight reductions include but are not limited to lightweight carbon fiber composite seats, lightweight instrument panel with carbon fiber cross car beam, selected reduced weight MuCell® interior trim, lightweight brake rotors, lightweight wheels and tires, lightweight coil springs, and lightweight glazing systems.

The climate control and electrical systems may have little or no meaningful weight saving potential. Since future anticipated vehicle requirements call for more electrical content and customer features, dual zone HVAC, heated seats, larger and faster entertainment systems, etc., current technologies are few for lightweighting the electrical or HVAC systems. Weight savings may possibly be associated with reducing content and features such as removing the solenoid and baffles that provide dual zone HVAC. These opportunities are being assessed.

Technology Transfer Path

The technology integration of this project will be applied by manufacturers such as Ford Motor Company on near future product platforms. Additionally, this technology will be applied by global suppliers such as Magna International on future OEM development projects and production intent designs for automotive and heavy trucks.

Conclusions

The project is successfully providing lower weight design alternatives that significantly reduce weight compared to the CY 2002 baseline vehicle while still meeting the functional safety requirements, durability expectations and NVH performance as evaluated through CAE analysis.

The next major step in this project will be to finalize a design for release to build prototype vehicles for physical testing and validation.

Presentations/Publications/Patents

The following Executive level reviews were held within the reporting period:

August 24th, 2010 - Project Review Meeting – MMLV presentation to Paul Mascarenas, Vice President Research, and Chief Technical Officer, Ford Motor Company.

October 23rd, 2012 – Global Technology Meeting – MMLV overview presented to Raj Nair, Vice President Product Development, Ford Motor Company (6 Vice Presidents reporting to Raj Nair were present at the review meeting) giving the project maximum exposure within Ford's executive ranks.

October 30th, 2012 – Executive Board Technical Review Meeting - The MMLV project was presented by the Magna/VEHMA team to Ford senior management (Vice President and Chief Engineer Level attendees).

B. Safety Data and Analysis — Lawrence Berkeley National Laboratory

Principal Investigator: Tom Wenzel
Lawrence Berkeley National Laboratory
1 Cyclotron Road, 90R4000 ; Berkeley, CA 94720
(510) 486-5753; e-mail: TPWenzel@lbl.gov

Technology Area Development Manager: Carol Schutte
U.S. Department of Energy
1000 Independence Ave., S.W., Washington, DC 20585
(202) 287-5371; e-mail: carol.schutte@ee.doe.gov

Contractor: Lawrence Berkeley National Laboratory (LBNL)
Contract No.: DE-AC02-05CH11231

Abstract/Executive Summary

In FY 2012 LBNL prepared two draft preliminary reports (Wenzel 2011a, 2011b) in support of the proposed joint rulemaking for fuel economy and greenhouse gas emission standards for 2017 to 2025 light-duty vehicles. The first preliminary report replicated the National Highway Traffic Safety Administration's (NHTSA's) updated logistic regression analysis of the relationship between vehicle mass and U.S. societal fatality risk per vehicle miles traveled (VMT; Kahane 2011, 2012). The results of this collaborative effort with NHTSA were used to provide input assumptions concerning maximum mass reduction allowed by vehicle type in the NHTSA Volpe Model used to evaluate the costs and benefits of Corporate Average Fuel Economy (CAFE) stringency levels, for the Notice of Proposed Rulemaking (NPRM). LBNL also assessed the sensitivity of NHTSA's results to the data used and the variables included in the regression models, and analyzed the relationship between mass and fatality risk by vehicle make and model, after accounting for all the control variables NHTSA used in their regression models. The second preliminary report was an analysis of the relationship between mass and societal casualty (fatality plus serious injury) risk per crash, using data on police-reported crashes from 13 states. The analysis used similar methods as NHTSA's preliminary analysis to allow comparison of the effects of mass and footprint reduction on the two measures of risk, fatalities per VMT and casualties per crash. Four peer reviewers provided comments on LBNL's preliminary reports (SRA 2012). LBNL incorporated those comments in the final reports, which were published in August 2012 (Wenzel 2012a, 2012b).

Accomplishments

- Using a dataset prepared by NHTSA, replicated NHTSA's estimates (Kahane 2011, 2012) of the effect of mass and footprint reduction on U.S. fatality risk per ten billion VMT. Assessed the sensitivity of NHTSA's results to subsets of the data used, and to changes in the variables included in the logistic regression models. Prepared a preliminary report (Wenzel 2011a) for inclusion in the docket for the NPRM for fuel economy/tailpipe greenhouse gas emission standards for 2017 to 2025 light-duty vehicles. The results of this collaborative effort with NHTSA were used to provide input assumptions concerning maximum mass reduction allowed by vehicle type in the NHTSA Volpe Model used to evaluate the costs and benefits of CAFE stringency levels.
- Using data on police-reported crashes from thirteen states, estimated the effect of mass and footprint reduction on casualty (fatality plus serious incapacitating injury) risk per crash. Analyzed the causes of differences based on whether risk is measured as fatalities per VMT or as casualties per crash. Assessed the sensitivity of the results to changes in the data used, and to changes in the variables included in the logistic regression models. Prepared a preliminary report

(Wenzel 2011b) for inclusion in the docket for the NPRM for fuel economy/tailpipe greenhouse gas emission standards for 2017 to 2025 light-duty vehicles.

- Updated the analyses in the two preliminary reports to include updated VMT data by vehicle model, and data on crashes in 2008 for six additional states. Responded to comments from four peer reviewers on the two preliminary reports (SRA 2012). Incorporated these responses, as well as responses to comments by NHTSA, Environmental Protection Agency, and DOE staff, into the final versions of the two reports (Wenzel 2012a, 2012b).
- Provided formal comments on NHTSA's final report analyzing the effect of mass and footprint reduction on U.S. societal fatality risk per VMT, as well as the language summarizing the analyses in the Preamble of the final rule.
- Prepared four articles summarizing the results of the two reports, which were submitted for publication in peer-reviewed archival journals.

Future Directions

- Continue to examine several aspects of the relationship between vehicle mass and footprint and fatality risk per VMT or casualty risk per crash.
- Analyze annual vehicle odometer data from the Texas vehicle emission inspection program to understand how driving activity changed in response to the economic downturn, and increased gas prices, in 2008. The reduction in driving likely contributed to the large decline in fatalities in 2008.

Introduction

NHTSA finalized its logistic regression analysis update of its 2003 and 2010 studies of the relationship between vehicle mass and U.S. societal fatality risk per VMT (Kahane 2011, 2012). The new study updates the previous analyses in several ways: updated Fatality Analysis Reporting System (FARS) data from 2002 to 2008 for model year (MY) 00 to MY07 vehicles are used; induced exposure data from police reported crashes in several additional states are added; a new vehicle category for car-based crossover utility vehicles (CUVs) and minivans is created; crashes with other light-duty vehicles are divided into two groups based on the crash partner vehicle's weight, and a category for all other fatal crashes is added; and new control variables for new safety technologies and designs, such as electronic stability controls (ESC), side airbags, and methods to meet voluntary agreement to improve light truck compatibility with cars, are included. LBNL replicated the 2012 final NHTSA analysis, and examined the data in slightly different ways to get a deeper understanding of the relationship between vehicle weight/footprint and safety (Wenzel 2012a).

LBNL finalized its second analysis that compares the logistic regression results of the NHTSA analysis of U.S. fatality risk per VMT with an analysis of 13-state casualty risk per crash (Wenzel 2012b). This analysis differs from the NHTSA analysis in two respects: first, it analyzes risk per crash, using data on all police-reported crashes from 13 states, rather than risk per estimated VMT; and second, it analyzes casualty (fatality plus serious injury) risk, as opposed to fatality risk. There are several good reasons to investigate the effect of mass and footprint reduction on casualty risk per crash. First, the data can be used to isolate the two components that influence whether a person is killed or seriously injured in a crash: how well a vehicle can be driven (based on its handling, acceleration, and braking capabilities) to avoid being involved in a serious crash (crash avoidance), and, once a serious crash has occurred, how well a vehicle protects its occupants from fatality or serious injury (crashworthiness). Use of the state crash data allows the separate analysis of the effect of mass or footprint reduction on crash frequency (the number of crashes per VMT) as well as crashworthiness (the number of fatalities or casualties per crash). Second, drawing both the outcomes (fatality or casualty) and the measure of exposure (police-reported crashes) from the same dataset minimizes any bias that might be introduced by drawing the outcomes or exposure from a different dataset. Third, extending the analysis to include serious or incapacitating injuries reduces the statistical uncertainty of analyzing just fatalities per crash. In addition, a serious incapacitating injury can be just as traumatic to the victim and her family, and costly from an economic perspective, as a fatality. Limiting the analysis to the risk of fatality, which is an extremely rare event, ignores the effect vehicle design may have on reducing the large number of incapacitating injuries that occur each year on the nation's roadways.

Approach

For its analysis NHTSA used FARS data on fatal crashes for MY00 to MY07 light-duty vehicles between 2002 and 2008. NHTSA used a subset of nonculpable vehicles in two-vehicle crashes from police-reported crash data from 13 states as a measure of induced exposure; these records provide distributions of on-road vehicles by vehicle year, make, and model, driver age and gender, and crash time and location (day vs. night, rural vs. urban counties, and high-speed roads). Each induced exposure record is then given a registered vehicle weighting factor, so that each induced exposure record represents a number of national vehicle registrations; the sum of the weighting factors equals the number of vehicles registered in the country. Each record is also given a VMT weighting factor, based on vehicle year, make/model, and age, using odometer data provided by R.L. Polk; for its final 2012 analysis NHTSA updated these weighting factors to reflect VMT from the 2001 National Household Travel Survey. The data can be used to estimate U.S. fatality risk per registered vehicle or VMT.

NHTSA compiled a database of the following vehicle attributes, by model year, make and model: curb weight and footprint (wheelbase times track width), as well as the presence of all-wheel drive and automated braking systems. NHTSA added several new variables for new safety technologies and designs: ESC, four types of side airbags, and two methods to comply with the voluntary manufacturer agreement to better align light truck bumpers to make them more compatible with other types of vehicles.

To reflect changes in the vehicle mix since the 2003 study, NHTSA added a third vehicle category, car-based CUVs and minivans. It also added two new crash types, for a total of nine: crashes with other light-duty vehicles are divided into two groups based on the crash partner vehicle's weight, and all other fatal crashes (involving more than two vehicles, etc.). The analysis involves running a logistic regression model with total crash fatalities as the dependent variable for each of the nine crash types and the three vehicle types, for a total of 27 regressions. Because all fatalities in the crash are used, the risks reflect societal risk, rather than just the risk to the occupants of the case vehicle. The induced exposure cases are weighted by the number of vehicle registrations and the annual mileage, so that the models are estimating the effect of changes in the control variables on U.S. fatalities per VMT.

Rather than reporting coefficients for the variables of interest (curb weight and footprint) from a single regression model across all crash types, NHTSA reports a weighted average of the coefficients from the nine regression models run for each of the nine crash types. NHTSA uses a "baseline" distribution of fatalities across the crash types, to represent the expected distribution of fatalities in the 2017 to 2025 timeframe of the new CAFE and greenhouse gas (GHG) emission standards. Similar to the 2003 study, NHTSA derives the baseline fatalities from MY04-09 vehicles in crashes between 2004 and 2008. NHTSA then adjusts this baseline distribution downward to account for the assumption that all vehicles in the 2017-2025 timeframe will have ESC installed. The assumptions used for this adjustment are taken from a NHTSA analysis that found that ESC reduces fatal rollovers by 56% in cars and 74% in light trucks; fixed-object impacts by 47% in cars and 45% in light trucks; and other non-pedestrian crashes by 8% in both cars and light trucks. These assumptions treat CUVs and minivans as light trucks rather than cars. This "post-ESC" distribution of fatalities by crash type is then multiplied by the regression coefficients for each crash type to create the weighted average effect of each control variable on risk.

For our analysis of fatality and casualty risk per crash, we used all of the police-reported crashes from thirteen states, both for the number of fatalities or casualties, and for the measure of exposure, the total number of reported crashes. To the extent possible, we used the same assumptions as in the NHTSA analysis, in many cases using the same SAS programs. However, it was necessary to diverge from the NHTSA analysis in several respects. The most important of these is the need to control for differences among the states in what types of crashes are reported to police and included in the databases. Risks per crash vary substantially by state, because of either different definitions of "incapacitating," "serious," or "major" injuries, or different reporting requirements or reporting bias in certain states. For this reason it is crucial to account for state reporting requirements when analyzing risks per crash using state crash databases. Therefore, we replaced the single variable for high-fatality states (HIFAT_ST) that NHTSA used for its analysis of U.S. fatalities per VMT with 12 variables identifying each state except Florida for our analysis of fatality and casualty risks per crash.

Results and Discussion

The effect of mass reduction on risk that NHTSA calculated in 2012 is much smaller than in its 2003 and 2010 studies; NHTSA estimates that a 100-lb reduction in mass for lighter-than-average cars would lower societal fatality risk per VMT by only 1.55%. The estimated effect on heavier cars, light trucks, and CUVs/minivans is even smaller, and statistically-significant in only two of the four cases. NHTSA attributes this reduction in the importance of mass reduction on safety to the phase-out of relatively light cars that had unusually high fatality risk, an observed improvement in how light, small cars are driven which reduces their tendency to be involved in serious crashes, and voluntary improvements made to light trucks to improve their compatibility with other vehicles. The 2012 NHTSA analysis finds that reducing vehicle footprint by one square foot while holding mass fixed is estimated to increase fatality risk per VMT by 1.87% in cars and 1.72% in CUVs and minivans (the effect on risk in light trucks is even smaller and not statistically significant).

Rather than relying on the confidence intervals output by the logistic regression models, NHTSA estimates the uncertainty around its point estimates using a jack-knife technique that accounts for the sampling error in the FARS fatality and state crash data. These uncertainty estimates are larger than the confidence intervals output by the logistic regression models included in this report. As a result, in its report NHTSA finds that only the 1.55% increase in risk from mass reduction in lighter than average cars is statistically significant.

LBNL was able to replicate NHTSA's results, and found that:

- NHTSA's (reasonable) assumption that all vehicles will have ESC installed by 2017 slightly **increases** the detrimental effect of mass reduction, but slightly **decreases** the detrimental effect of footprint reduction, on risk in cars, CUVs and minivans. This is because NHTSA projects ESC to substantially reduce the number of fatalities in rollovers and crashes with stationary objects, and mass reduction appears to reduce risk, while footprint reduction appears to increase risk, in these types of crashes, particularly in cars and CUVs/minivans.
- Many of the control variables NHTSA includes in its logistic regressions are statistically significant, and have a much larger estimated effect on fatality risk than vehicle mass. For example, installing torso side airbags, electronic stability control, or an automated braking system in a car is estimated to reduce fatality risk by about 10%; cars driven by men are estimated to have a 40% higher fatality risk than cars driven by women; and cars driven at night, on rural roads, or on roads with a speed limit higher than 55 mph are estimated to have a fatality risk over 100 times higher than cars driven during the daytime on low-speed non-rural roads. While the estimated effect of mass reduction may result in a statistically-significant increase in risk in certain cases, the increase is small and is overwhelmed by other known vehicle, driver, and crash factors.
- Vehicle mass and footprint are correlated, but only strongly for passenger cars. NHTSA includes both variables in their regression models, introducing the possibility that multi-collinearity may create biased results. When footprint is allowed to vary along with weight (i.e., the regression model accounts for weight but not footprint), mass reduction results in a larger estimated increase in risk for cars and CUVs/minivans than when footprint is held constant. Similarly, when mass is allowed to vary along with footprint, footprint reduction results in a larger estimated increases in risk for cars, but a smaller estimated increase in risk for CUVs and minivans. To isolate the effect of mass reduction from footprint reduction on risk, NHTSA estimates the effect of mass reduction on risk for deciles of vehicles with similar footprint. Mass reduction does not consistently increase risk across all footprint deciles for any combination of vehicle type and crash type. **Risk increases with decreasing mass in a majority of footprint deciles for 12 of the 27 crash and vehicle combinations, but few of these increases are statistically significant. On the other hand, risk decreases with decreasing mass in a majority of footprint deciles for 5 of the 27 crash and vehicle combinations; in some cases these risk reductions are large and statistically significant.**
- Logistic regression methods do not have a statistic, such as the model R^2 in a linear regression model, to measure how much variability in risk by vehicle model is explained by the control variables included in the model. Analysis of pseudo- R^2 and R^2 from a linear regression model suggests that much of the variation in risk remains unexplained, even after accounting for many important vehicle, driver, and crash variables. After accounting for all of the variables in NHTSA's logistic regression model, except for vehicle mass and footprint, we find that the correlation between estimated fatality risk by vehicle model and mass is very low. There also is no significant correlation between the residual, unexplained risk and vehicle weight. **These results indicate that, even after accounting for many vehicle, driver, and crash factors, the variation in risk by vehicle model is quite large and unrelated to vehicle weight.** The large

remaining unexplained variation in risk by vehicle model could be attributable to other differences in vehicle design, or how drivers who select certain vehicles drive them. It is possible that including variables that account for these factors in the regression models would change the estimated relationship between mass or footprint and risk.

- NHTSA's estimates are sensitive to the definition of risk, and changes in the data and variables used in its regression models. LBNL compared the results from NHTSA's "preferred" model with 19 alternative regression models. The estimates for cars were particularly sensitive to the choice of regression model used; mass reduction in cars is associated with a larger increase in risk if footprint is allowed to vary with mass, vehicle manufacturer (including five luxury brands) is included in the regression model, or fatal crashes involving drivers who had been drinking, using drugs, or had poor driving records are excluded from the analysis. On the other hand, mass reduction in cars is associated with smaller increases, and in some cases small reductions, in risk when risk is defined as fatalities per crash, stopped vehicles rather than non-culpable vehicles are used as the induced exposure cases, track width and wheelbase are used instead of footprint, and median household income is included as a control variable.
- For its baseline fatalities NHTSA assumed that all new vehicles will have ESC installed by 2017, which will reduce the fraction of fatalities in rollovers and crashes with stationary objects, and thus will increase the estimated detrimental overall effect of mass reduction, but decrease the estimated detrimental overall effect of footprint reduction, on risk. However, other recent trends that are likely to continue through 2017 may also affect the distribution of crashes in that year. For example, side airbags in cars will likely reduce the fraction of fatalities in side-impact crashes, and better alignment of light truck bumpers with those of other vehicles appears to reduce the risk imposed on car occupants, at least in side impact crashes. However, it appears that mass reduction has less of an estimated detrimental effect on risk when cars are struck in the side than when they are involved in frontal or rear-end crashes, so any future reduction in fatalities in car side impact crashes will not necessarily influence the relationship between mass and risk. And it is not clear whether full adoption of side airbags or compatibility measures for light trucks will reduce fatality risk when light-duty trucks, CUVs or minivans are struck in the side.
- Finally, in part because of high gas prices and the poor economy, households have been purchasing smaller and lighter vehicles in the last decade. For example, the explosion of CUVs appears to have led to a reduction in the market share of minivans, cars, and in recent years (MY05 to MY07) sport utility vehicles (SUVs) and pickups. It is likely that these trends would continue, even in the absence of stronger CAFE and GHG emission standards. Any future market shifts from SUVs or pickups to cars or car-based CUVs and minivans will result in much larger reductions in fatality risk than the relatively small increases in risk expected from mass or footprint reduction. For example, we estimate that a large-scale shift in the market share of pickups and SUVs to CUVs, minivans, and cars will reduce overall fatalities by over 3%.

We compared the results from NHTSA's 2003, 2010, and 2012 analyses with our 19 alternative model specifications. NHTSA's 2012 analysis of a simultaneous reduction in mass and footprint (i.e., excluding a control variable for footprint in the regression model) results in a smaller estimated increase in fatalities than in NHTSA's 2003 analysis, particularly for lighter cars and light trucks. Similarly, the 2012 analysis estimates a smaller increase in risk with mass reduction when footprint is held constant (i.e., when a control variable for footprint is included in the regression model), compared to NHTSA's 2010 study. The results of the alternative model specifications examined in the final LBNL 2012 report are, in nearly all cases, lower than the results of the 2003 NHTSA report, and often lower than the results of NHTSA's 2010 and 2012 analyses.

LBNL's second study used police-reported crash data from 13 states to examine the relationship between vehicle mass reduction and the two components of risk per VMT, the number of crashes per VMT (crash frequency) and the fatality or casualty risk per crash (crashworthiness/crash compatibility). The effects from the two components, crash frequency and crashworthiness/compatibility, roughly add together to result in the overall effect on fatality risk per VMT. Mass reduction is estimated to increase crash frequency in all five vehicle types, with larger estimated increases in lighter-than-average cars and light-duty trucks. As a result, mass reduction is estimated to have a more beneficial effect on casualty risk per crash than on fatality risk per VMT, and on fatality risk per crash than on fatality risk per VMT. Mass reduction is associated with decreases in casualty risk per crash in all vehicles except lighter cars; in two of the four cases these estimated reductions are statistically significant, albeit small. Footprint reduction is associated with increases in crash frequency in cars and light trucks, but with a small decrease in crash frequency in CUVs/minivans; footprint reduction does not have a statistically significant effect on fatality risk per crash, and only for casualty risk per crash or light trucks. For cars and light trucks, lower mass is associated with a more beneficial effect on fatality risk per crash than on casualty risk per crash, while lower footprint

is associated with slightly more detrimental effects. The effect is opposite for CUVs/minivans: lower mass is associated with a more beneficial effect, while lower footprint is associated with a more detrimental effect, on casualty than fatality risk per crash.

The association of mass reduction with 13-state casualty risk per VMT is quite consistent with that NHTSA estimated for U.S. fatality risk per VMT, although we estimate the effects on casualty risk to be more detrimental than the effects on fatality risk, for all vehicle types. The association of footprint reduction also is similar, with 13-state casualty risk per VMT slightly more beneficial than U.S. fatality risk per VMT for cars and CUVs/minivans, while 13-state casualty risk is substantially more detrimental than U.S. casualty risk for light-duty trucks.

As with U.S. fatality risk per VMT, the estimated effect of mass reduction on 13-state casualty risk per crash is much smaller than the estimated effect of the other vehicle, driver, and crash control variables. There are several unexpected results for some of the control variables in our regressions: side airbags in light trucks and CUVs/minivans are estimated to reduce crash frequency; ESC and anti-lock braking systems (ABS) are estimated to reduce risk once a crash has occurred; and all-wheel drive and brand new vehicles are estimated to increase risk once a crash has occurred. In addition, male drivers are estimated to have essentially no effect on crash frequency, but are associated with a statistically significant increase in fatality risk once a crash occurs. And driving at night, on high-speed or rural roads, are associated with higher increases in risk per crash than on crash frequency. These unexpected results suggest that important control variables are not being included in the regression models. For example, crashes involving male drivers, in vehicles equipped with all-wheel drive, or that occur at night on rural or high-speed roads, may not be more frequent but rather more severe than other crashes, and thus lead to greater fatality or casualty risk. And drivers who select vehicles with certain safety features may tend to drive more carefully, resulting in vehicle safety features designed to improve crashworthiness or compatibility, such as side airbags, being also associated with lower crash frequency.

Our analysis of vehicle models indicates that, although casualty risk tends to increase as mass decreases, there is even lower correlation between mass and casualty risk per crash as fatality risk per VMT, even after accounting for differences in other vehicle attributes, driver age and gender, and crash times and locations. And there is also little correlation between mass and the remaining casualty risk per crash not explained by the variables included in the regression models.

As with our analysis of U.S. fatality risk per VMT, sensitivity tests using different measures of risk, different control variables, or excluding certain cases results in large changes in the estimated effect of mass reduction on 13-state casualty risk per crash, particularly for cars. In particular, accounting for vehicle manufacturer (including five luxury brands) results in a nearly 1% estimated increase in casualty risk per crash from mass reduction in cars, while not accounting for the state in which the crash occurred, including vehicle purchase price, or replacing footprint with track width and wheelbase results in an estimated 1 to 2% decrease in casualty risk per crash from car mass reduction.

Conclusion

The 2012 NHTSA and LBNL studies conclude that the estimated effect of mass reduction while maintaining footprint on societal U.S. fatality risk per VMT is small, and statistically non-significant for all but the lightest cars. Although the estimated effects are sensitive to what variables and data are included in the regression analysis, in nearly all cases the effects are less, in some cases dramatically less, than reported in the 2003 NHTSA study. The reports also find that the estimated effects of other control variables, such as vehicle type, specific safety technologies, and crash conditions such as whether the crash occurred at night, in a rural county, or on a high-speed road, on risk are much larger, in some cases two orders of magnitude larger, than the estimated effect of mass or footprint reduction on risk. Finally, the LBNL reports show that after accounting for the many vehicle, driver, and crash variables NHTSA used in its regression analyses, there remains a wide variation in risk by vehicle make and model, and this variation is unrelated to vehicle mass.

Casualty risk per crash is not necessarily a better metric than fatality risk per VMT for evaluating the effect of mass or footprint reduction on risk; rather, it provides a different perspective in assessing the benefits or drawbacks of mass and footprint reduction on safety in vehicles. However, it does allow the risk per VMT to be separated into its two components, crash frequency and risk per crash. Our analysis indicates that much of the estimated detrimental effect of mass or footprint reduction on risk can be attributed to the tendency for crash frequency, rather than crashworthiness/compatibility (risk once a crash has occurred), to increase as vehicle mass or footprint decreases. It is unclear why lower vehicle mass is associated with higher crash frequency, but lower risk per crash, in the regression models. It is possible that including variables that

more accurately account for important differences among vehicles and driver behavior would reverse this relationship. For example, adding vehicle purchase price substantially reduces the estimated increase in crash frequency as vehicle mass decreases, for all vehicle types; in the case of heavier-than-average cars, mass reduction is estimated to slightly decrease crash frequency. On the other hand, it is also possible that over thirty years of improvements in vehicle design to achieve high crash test ratings have enabled manufacturers to use clever vehicle design to mitigate the hypothetical safety penalty of low mass vehicles.

Although the purpose of the NHTSA and LBNL reports is to estimate the effect of vehicle mass reduction on societal risk, this is not exactly what the regression models are estimating. Rather, they are estimating the recent historical relationship between mass and risk, after accounting for most measurable differences between vehicles, drivers, and crash times and locations. In essence, the regression models are comparing the risk of a 2600-lb Dodge Neon with that of a 2500-lb Honda Civic, after attempting to account for all other differences between the two vehicles. The models are **not** estimating the effect of literally removing 100 lbs from the Neon, leaving everything else unchanged. In addition, the analyses are based on the relationship of vehicle mass and footprint on risk for recent vehicle designs (MY 2000 to 2007). These relationships may or may not continue into the future as manufacturers utilize new vehicle designs and incorporate new technologies, such as more extensive use of strong lightweight materials and specific safety technologies.

Presentations/Publications/Patents

Wenzel, Tom. *Assessment of NHTSA's Report "Relationships Between Fatality Risk, Mass, and Footprint in Model Year 2000-2007 Passenger Cars and LTVs"*. LBNL-5696E; Lawrence Berkeley National Laboratory: Berkeley, CA, 2011a.

Wenzel, Tom. *An Analysis of the Relationship between Casualty Risk per Crash and Vehicle Mass and Footprint for Model Year 2000-2007 Light-Duty Vehicles*. LBNL-5695E; Lawrence Berkeley National Laboratory: Berkeley, CA, 2011b.

Wenzel, Tom. *Assessment of NHTSA's Report "Relationships Between Fatality Risk, Mass, and Footprint in Model Year 2000-2007 Passenger Cars and LTVs"*. LBNL-5698E; Lawrence Berkeley National Laboratory: Berkeley, CA, 2012a.

Wenzel, Tom. *An Analysis of the Relationship between Casualty Risk per Crash and Vehicle Mass and Footprint for Model Year 2000-2007 Light-Duty Vehicles*. LBNL-5697E; Lawrence Berkeley National Laboratory: Berkeley, CA, 2012b.

Systems Research and Application Corporation. 2012. Peer Review of LBNL Statistical Analysis of the Effect of Vehicle Mass & Footprint Reduction on Safety (LBNL Phase 1 and 2 Reports), EPA-420-R-12-020; U.S. Environmental Protection Agency, 2012.

References

Kahane, C.J. *Vehicle Weight, Fatality Risk and Crash Compatibility of Model Year 1991-99 Passenger Cars and Light Trucks*. DO HS 809-662; NHTSA: Washington, DC, 2003.

Kahane C.J. *Relationships Between Fatality Risk, Mass, and Footprint in Model Year 1991-1999 and Other Passenger Cars and LTVs*. Final report included in the *Corporate Average Fuel Economy for MY 2012-MY2016 Passenger Cars and Light Trucks Final Regulatory Impact Analysis*, NHTSA: Washington, DC, 2010.

Kahane, C.J. *Relationships Between Fatality Risk, Mass, and Footprint in Model Year 2000-2007 Passenger Cars and LTVs*. NHTSA-2010-0152-0023; preliminary report prepared for the National Center for Statistics and Analysis, NHTSA: Washington, DC, 2011.

Kahane, C.J. *Relationships Between Fatality Risk, Mass, and Footprint in Model Year 2000-2007 Passenger Cars and LTVs*. DOT HS 811 665; final report prepared for the National Center for Statistics and Analysis, NHTSA: Washington, DC, 2012.

This report is being disseminated by the Department of Energy. As such, this document was prepared in compliance with Section 515 of the Treasury and General Government Appropriations Act for Fiscal Year 2001 (Public Law 106-554) and information quality guidelines issued by the Department of Energy.

This document highlights work sponsored by agencies of the U.S. Government. Neither the U.S. Government nor any agency thereof, nor any of their employees, makes any warranty, express or implied, or assumes any legal liability or responsibility for the accuracy, completeness, or usefulness of any information, apparatus, product, or process disclosed, or represents that its use would not infringe privately owned rights. Reference herein to any specific commercial product, process, or service by trade name, trademark, manufacturer, or otherwise does not necessarily constitute or imply its endorsement, recommendation, or favoring by the U.S. Government or any agency thereof. The views and opinions of authors expressed herein do not necessarily state or reflect those of the U.S. Government or any agency thereof.

DOE/EE-0902 April 2013
Printed with a renewable-source ink on paper containing
at least 50% wastepaper, including 10% post consumer waste.

U.S. DEPARTMENT OF
ENERGY | Energy Efficiency &
Renewable Energy

For more information
eere.energy.gov

